UNIVERSITY OF SOUTHAMPTON

FACULTY OF ENGINEERING, SCIENCE AND MATHEMATICS

SCHOOL OF ELECTRONICS AND COMPUTER SCIENCE

A NANOSTRUCTURED POROUS SILICON BASED DRUG DELIVERY DEVICE

by Chien Fat Chau

A thesis submitted for the degree of Doctor of Philosophy

October 2009

UNIVERSITY OF SOUTHAMPTON

ABSTRACT

FACULTY OF ENGINEERING, SCIENCE AND MATHEMATICS
SCHOOL OF ELECTRONICS AND COMPUTER SCIENCE

Doctor of Philosophy

A NANOSTRUCTURED POROUS SILICON BASED DRUG DELIVERY DEVICE

by Chien Fat Chau

Targeted and controlled delivery of therapeutic agents on demand is pivotal in realising the efficacy of many pharmaceuticals. The design and fabrication of a novel, electrically-addressable, porous structure-based drug delivery device for the controlled release of therapeutic proteins and peptides, are described in this thesis.

The initial prototype microdevice design incorporates a porous polysilicon (PPSi) structure as a drug reservoir. Two alternative methods were investigated to fabricate the PPSi structure: i) the chemical stain etching method; ii) a reactive ion etching (RIE) method through a masking template. Random pores, with irregular pore shape and size in the micro- to mesoporous regime (< 50 nm), were obtained using the stain etching method but this method suffered from poor reproducibility and non-uniformity. Two novel RIE approaches were investigated to fabricate ordered PPSi structures; two different masking templates were investigated – a porous anodic alumina (PAA) and a metal mask with hexagonally arranged holes produced by a novel nanosphere lithography (NSL) technique. A quasi-ordered PAA template with pore diameters in the region of 50 nm was fabricated but was not suitable for the subsequent proposed RIE process. By using the NSL technique, quasi-ordered PPSi structures with tapered pore profiles, were obtained. This is the first demonstration of the fabrication of PPSi with ordered pores of sizes in the macropore range of ~ 370 nm.

A revised silicon-based prototype microdevice was designed and fabricated. The microdevice incorporates a nanostructured, quasi-ordered porous silicon (PSi) as a drug reservoir and an integrated heater and temperature sensor as an active control mechanism. The PSi structure was fabricated using a modified NSL technique and a Bosch-based RIE process. Hexagonally arranged cylindrical pores with diameters between ~75 nm and ~120 nm, and depths in the range of ~330 nm and 500 nm, were obtained. The novel fabrication techniques investigated here are simple and versatile; both p-type and n-type PSi structures have been successfully fabricated.

Proof-of-concept studies, using the revised prototype drug delivery microdevices, suggested that the nanostructured PSi would be suitable for the passive release of an intermediate-sized (~23 000 Dalton) model protein. It is envisaged that the microdevice has the potential to deliver osteoinductive growth factors, on demand, to the site of fracture, in a controlled and sustainable manner, as a first step to an intelligent therapeutic system for skeletal regeneration.

Contents

List of Figures

List of Tables

Declaration of Authorship

I, Chien Fat Chau

declare that the thesis entitled

A Nanostructured Porous Silicon based Drug Delivery Device

and the work presented in the thesis are both my own, and have been generated by me as the result of my own original research. I confirm that:

- this work was done wholly or mainly while in candidature for a research degree at this University;
- where any part of this thesis has previously been submitted for a degree or any other qualification at this University or any other institution, this has been clearly stated;
- where I have consulted the published work of others, this is always clearly attributed;
- where I have quoted from the work of others, the source is always given. With the exception of such quotations, this thesis is entirely my own work;
- I have acknowledged all main sources of help;
- where the thesis is based on work done by myself jointly with others, I have made clear exactly what was done by others and what I have contributed myself;
- parts of this work have been published as in **Appendix F Publications**.

Signed:……..

Date: 8 October 2009

Acknowledgements

Firstly, I would like to thank my supervisor, Dr. Tracy Melvin, for her continuous support and guidance throughout this work, for her understanding and encouragement during the frustrating periods, and for her exceptional advice and assistance in completing my thesis. It has been an incredible experience working in a multi-disciplinary environment, and I could not thank her more for providing this opportunity throughout my PhD studies. My special thanks to Prof. Michael Kraft for his fine comments and advice during the ninth-month and transfer viva; and for the use of his STS Pegasus ASE™ DRIE machine which is indispensable in realising the porous silicon structure. I'm also indebted to Dr. Eleanor Tarbox for her enormous help in proof-reading some of the chapters in this thesis. Thanks also to Tristan Temple and Nicolas Perney for their fine comments and critical feedbacks on Chapter 5 and 6, and Chapter 7, respectively.

Thank you to the School of ECS for funding my PhD studies, the Nano research group who has supported me all the way through and the ORC who has allowed me to use their facilities and offices after the fire. My thanks also to my employer, Universiti Tenaga Nasional, for granted me the opportunity to pursue my studies.

After the fire, I have spent almost 12 months at the University of Manchester using the cleanroom facility and the SPM/AFM laboratories. For this, I must thank Prof. Bruce Hamilton for accommodating me during the difficult period, for his support and constructive advice throughout my work at Manchester, and not forgetting his hospitality during my stay. My thanks also go to Eric Whittaker and Mal McGowen, who have been enormously helpful in training and assisting me in the SPM labs and the cleanroom, respectively. Not forgetting, the members of Prof. Hamilton's group, especially Nasir who was kind enough to share with me the secret in fabricating porous anodic alumina and places to get authentic curries, and Nikos for showing me the AFM and the PL system. In addition, I would like to thank the School of ECS for awarding the Alleviation Fund which made this visit possible.

The fabrication of porous silicon drug delivery device could not be made possible if not for the continuous effort from people of the Nanofabrication Laboratory at the Chalmers University of Technology, Sweden to fabricate the silicon membrane, despite major issues and setbacks during the process. Special thanks to Göran Alestig for planning, coordinating and overseeing the entire fabrication work and his hospitality during my stay; and to Johan Andersson for his persistent effort and intuitive creativity in overcoming the challenges faced during the fabrication.

I really enjoyed and appreciated the friendly environment working in the cleanrooms across the campus at Southampton. Hence, I would like to acknowledge the members of Innos™, especially Jean Humphrey for her guidance and vital help on many critical occasions prior to the fire, Tony Blackburn and Mohamad Harun for advice on photoresist, Janet Bonar and Mir Mokthari for getting my fabrication batches running and completed swiftly after the fire, and Nasser Afshar for support in mask layout. In addition, my gratitude for the technical support and assistance from Dave Sager, Neil Sessions and Neil Fagan at the ORC Dairybox temporary cleanroom, and Zondy Webber at the Nanomaterials Rapid Prototyping Facility over at Physics.

I must also thank Graham Ensell for constructive discussion and advice during the design and development of the porous polysilicon device and silicon membrane; people at the School of Chemistry, in particular, Mamdouh Abdelsalam for discussion on self-assembly of nanospheres, and Prof. Tom Brown and his team – James Richardson for showing me the UV/Vis spectrophotometer and the spectrofluorimeter, Rachel and Dorcas for helping with the freeze drying; Ken Frampton and his team at the Mechanical Workshop for the machining of the Teflon trough; and Prof. Feodor Ogrin and Evgeny Sirotkin at the University of Exeter for generous demonstration of the self-assembly of nanospheres using the Teflon trough.

I would also like to acknowledge the contribution from Ben Mills for diffraction pattern and complex refractive index measurement using the ultrafast soft X-ray; Christoph Kaminski for designing and fabricating some parts of the porous polysilicon drug delivery devices which have been extensively used in many parts of the early development work of this research; and Salina Mohmad for help with the early work on stain etching of porous polysilicon devices.

My gratitude to the members in Tracy's group, especially graduates Ben and Manouchehr for their continuous motivation and invaluable discussion on topics not limited to the project; the past and present post-docs Huabin, Suzanne, Nic, Samson, Liqin, Patrick, Matt and Lucy for their help and support in the Biolab and Cell Culture Lab; and fellow PhD candidates Chris, Mukhzeer, Tim, Daniel and Katrin. It has been a pleasant learning experience working with all of you.

I would like to thank the many good friends that I've met here, to name a few, Biswajit, Song Ni, Lit Ho, Bee Leong and Khatijah for their fine encouragement; and fellow PhD students and graduates at the now Nano research group, Tristan, Stuart, Kian, Xiaoli, Gareth, Petros, Mehdi, Yufeng, Badin and Mohammad.

Above all, I would like to thank my parents, my parents-in-law and my loving wife, Janice for their understanding, endless patience and encouragement when it was most required.

List of Symbols

α	–	Temperature coefficient of resistance of material [K^{-1}]
A_{280}	–	Absorbance at 280 nm [a.u.]
A_{495}	–	Absorbance at 495 nm [a.u.]
C	–	Specific heat capacity [$J \cdot kg^{-1} \cdot K^{-1}$]
C_F	–	Concentration of fluorophore [$mg \cdot mL^{-1}$]
CF	–	Correction factor [1]
$C_{M,FLUOS}$	–	Molar concentration of FLUOS [M]
$C_{M,Papain}$	–	Molar concentration of Papain [M]
C_P	–	Concentration of protein [$mg \cdot mL^{-1}$]
C_{Papain}	–	Concentration of Papain [$mg \cdot mL^{-1}$]
d_{int}	–	Interpore spacing or pitch size [nm]
d_p	–	Mean pore diameter [nm]
ε	–	Molar absorption coefficient [$L \cdot mol^{-1} \cdot cm^{-1}$]
e^-	–	Number of electrons exchanged in silicon dissolution process [1]
$\varepsilon^{1\%}$	–	Molar absorption coefficient [$L \cdot g^{-1} \cdot cm^{-1}$]
ε_{FLUOS}	–	Molar absorption coefficient of FLUOS [$L \cdot mol^{-1} \cdot cm^{-1}$]
ε_{Papain}	–	Molar absorption coefficient of Papain [$L \cdot mol^{-1} \cdot cm^{-1}$]
$flc1hs$	–	COMSOL Heaviside function
h	–	Porous layer thickness [nm]
h^+	–	Number of holes exchanged in silicon dissolution process [1]
h_c	–	Natural convective heat transfer coefficient [$W \cdot m^{-2} \cdot K^{-1}$]
$I(\lambda)$	–	Fluorescent intensity curve [a.u.]
J_{ep}	–	Current density at V_{ep} [$mA \cdot cm^{-2}$]
k	–	Thermal conductivity [$W \cdot m^{-1} \cdot K^{-1}$]
l	–	Path length of cuvette [cm]
$[\lambda_a, \lambda_b]$	–	Sub-intervals of $I(\lambda)$ [nm, nm]
λ_{EM}	–	Emission wavelength [nm]
λ_{EX}	–	Excitation wavelength [nm]
μ_n	–	Mobility of electrons [$m^2 \cdot V^{-1} \cdot s^{-1}$]
μ_p	–	Mobility of holes [$m^2 \cdot V^{-1} \cdot s^{-1}$]
MR	–	Molar reaction ratio [1]

MW	–	Molecular weight [Dalton]
MW_F	–	Molecular weight of fluorophore [Dalton]
MW_P	–	Molecular weight of protein [Dalton]
MW_{Papain}	–	Molecular weight of Papain [Dalton]
n	–	Average number of holes required to dissociate one atom of silicon [1]
P_{theory}	–	Theoretical porosity [%]
q	–	Magnitude of electron charge [C]
ρ	–	Resistivity [Ω·cm]
ρ	–	Density [kg·m^{-3}]
R	–	Resistance [Ω]
ρ_0	–	Resistivity at reference temperature [Ω·m]
R_0	–	Initial resistance at reference temperature [Ω]
R_s	–	Sheet resistance [Ω/sq]
R_{s_exp}	–	Expected sheet resistance based on simulation [Ω/sq]
R_{s_mea}	–	Measured sheet resistance [Ω/sq]
R_{s_rev}	–	Simulated sheet resistance from a revised simulation [Ω/sq]
R_{s_sim}	–	Simulated sheet resistance [Ω/sq]
σ_{Heater}	–	Electrical conductivity of the heater [S·m^{-1}]
S_{HS}	–	Slope of the COMSOL's Heaviside function [1]
T	–	Temperature [K]
T_0	–	Reference temperature [K]
t_i	–	Incubation time (in stain etching) [s]
t_{ON}	–	Heater on-time used in COMSOL simulation [s]
V_{dd}	–	Actuation voltage [V]
V_{ep}	–	Electropolishing voltage in electrochemical etching of silicon [V]
V_F	–	Volume of fluorophore [mL]
V_{in}	–	Input voltage to COMSOL simulation [V]
V_P	–	Volume of protein [mL]
ζ_{int}	–	Interpore distance proportionality constant [nm·V^{-1}]
ζ_{p}	–	Pore diameter proportionality constant [nm·V^{-1}]

List of Abbreviations

a.u.	–	Arbitrary unit
ACS	–	Absorbable collagen sponge
AFM	–	Atomic force microscopy
ASE®	–	Advanced Silicon Etch
bFGF	–	Basic fibroblast growth factor
BHF	–	Buffered hydrofluoric acid
BioMEMS	–	Biomedical microelectromechanical systems
BMP	–	Bone morphogenetic protein
BSA	–	Bovine serum albumin
BSE	–	Backscattering electrons
C_4F_8	–	Octafluorocyclobutane
CCS	–	Constant current source
CF_4	–	Tetrafluoromethane
CHF_3	–	Trichloromethane
CL	–	Cathodoluminescence
CMC	–	Carboxymethyl cellulose
CMPS	–	Carboxylate-modified polystyrene
DAQ	–	Data acquisition
DBR	–	Distributed Bragg reflector
DC	–	Direct current
DCM	–	Dichloromethane
DI	–	De-ionised
DMF	–	Dimethylformamide
DMM	–	Digital multimeter
DMSO	–	Dimethyl sulfoxide
DNA	–	Deoxyribonucleic acid
DRIE	–	Deep reactive ion etching
ECR	–	Electron cyclotron resonance
EDP	–	Ethylenediamine pyrocatechol
EDX	–	Energy-dispersive X-ray
EL	–	Electroluminescence
FEA	–	Finite element analysis
FEGSEM	–	Field emission gun scanning electron microscopy
FFT	–	Fast Fourier transform

FIB	–	Focused ion beam
FITC	–	Fluorescein isothiocyanate
FLUOS	–	5(6)-Carboxyfluorescein *N*-hydroxysuccinimide ester
FNA	–	Fuming nitric acid
GI	–	Gastrointestinal
HF	–	Hydrofluoric acid
HNO_3	–	Nitric acid
ICP	–	Inductively coupled plasma
IFN-α	–	Interferon α-2b
IPA	–	Isopropanol
IR	–	Infrared
IUPAC	–	International Union of Pure and Applied Chemistry
KOH	–	Potassium hydroxide
LF	–	Low frequency
LPCVD	–	Low pressure chemical vapour deposition
LTO	–	Low temperature oxidation
MCM	–	Mobil Crystalline of Materials
MEMS	–	Microelectromechanical systems
MWCO	–	Molecular weight cut-off
nDS	–	Nanochannel drug system
NHS	–	*N*-hydroxysuccinimide
NI	–	National Instruments™
NMP	–	*N*-methylpyrrolidone
NSL	–	Nanosphere lithography
NSOM	–	Near-field scanning optical microscopy
NTX	–	Naltrexone
OT	–	Optical thickness
% v/v	–	Percent volume per volume
PAA	–	Porous anodic alumina
PDMS	–	Polydimethylsiloxane
PGA	–	Poly(glycolic acid)
PL	–	Photoluminescence
PLA	–	Poly(lactic acid)
PMGI	–	Polymethylglutarimide
PMMA	–	Poly(methyl methacrylate)
PPSi	–	Porous polysilicon
PSD	–	Pore size distribution
PSG	–	Phosphosilicate glass
PSi	–	Porous silicon
PSPD	–	Position-sensitive photodetector
PTFE	–	Polytetrafluoroethylene
RF	–	Radio frequency
rh	–	Recombinant human

RIE	–	Reactive ion etching
RMS	–	Root mean square
rpm	–	Revolutions per minute
SAM	–	Self-assembled monolayer
SBA	–	Santa Barbara Amorphous
SBF	–	Simulated body fluids
sccm	–	Standard cubic centimetres per minute
SDS	–	Sodium dodecyl sulphate
SEM	–	Scanning electron microscopy
SF_6	–	Sulphur hexafluoride
Si_3N_4	–	Silicon nitride
SIMS	–	Secondary ion mass spectrometry
SiO_2	–	Silicon dioxide
SOI	–	Silicon-on-insulator
SPM	–	Scanning probe microscopy
STM	–	Scanning tunneling microscopy
SVDP	–	SIMS-Verified Dual Pearson model
TCR	–	Temperature coefficient of resistance
TEM	–	Transmission electron microscopy
TGF-β	–	Transforming growth factor-β
THF	–	Tetrahydrofuran
TMAH	–	Tetramethyl ammonium hydroxide
UHV	–	Ultra high vacuum
UV	–	Ultraviolet
UV / Vis	–	Ultraviolet / visible
w/v	–	Weight in volume
wt%	–	Weight percent
XRD	–	X-ray diffraction

Chapter 1

Introduction

1.1 Background and Motivations

Fractures, as a result of congenital deformities, trauma or tumour resection, or degenerative diseases such as osteoporosis and degenerative disc disease, represent a major and growing global public health issue. The socioeconomic burden of traumatic or osteoporotic bone fractures is high and likely to rise with the increasing elderly population (aged ≥ 65 years) from the current 323 million to 1 555 million by the year 2050 [1]. It has been estimated that in 1990 there were 1.66 million hip fractures worldwide; this is estimated to increase to 6.26 million in 2050 [1], inline with the demographic changes. In the United Kingdom, there are more than 70 000 hip fractures every year and the number is estimated to increase to 101 000 by the year 2020 [2]. Osteoporotic fractures cost the UK £1.7 billion annually [1], while the combined health and social care costs of hip fractures alone, in the UK, were estimated at £726 million per annum in 2000 [3]. The lifetime risk of any fracture was found to be 53.2 % and 20.7 %, among women and men in the UK aged 50 years, respectively [4]; hence, one in two women and one in five men over the age of 50 in the UK will have an osteoporotic fracture in their remaining lifetime. These numbers are greater than the lifetime risk of coronary heart disease (46 % for a 50-year-old woman [1]) and substantiate the need for innovative strategies to manage fracture incidences.

From the clinical perspective, the treatment of fractures remains a challenge in orthopaedic surgery. Fracture healing and bone formation is a complex physiological process involving a cascade of cellular events [5, 6]. Even under optimum clinical condition, 5 % to 10 % of all fractures (reported cases in the United States) progress to delayed union or non-union [7]. These complications often result in the patients required a surgical re-intervention. Currently, the primary tissue engineering approach to improve impaired healing, accelerate bone regeneration and restore skeletal condition includes the utilisation of i) osteoinductive growth factors, ii) osteogenic cells (mesenchymal stem cells, osteoprogenitor cells and osteoblasts), iii) osteoconductive scaffolds, and the provision of a iv) mechanically stable environment; collectively, these four factors are known as the diamond concept in facture healing [6]. The utilisation of growth factors from the transforming growth factor-β (TGF-β) superfamily, especially the bone morphogenetic proteins (BMPs), is the most intensively studied and shows the most promising potential to enhancement in skeletal regeneration.

In 1965, Marshall R. Urist first described the phenomenon of osteoinduction or the ability to induce bone formation at an ectopic (non-bone) site [8], following his seminal discovery of local *de novo* bone formation after intramuscular implantation of demineralised bone matrix in rabbits [9]. He later ascribed the phenomenon of osteoinduction to the presence of a protein in the bone matrix, which he termed *bone morphogenetic protein* [10]. Since then, the biological activity and the clinical application of BMPs have been extensively investigated and reviewed [11-17]. Of the more than sixteen different human BMPs identified, at the present time, only two engineered or recombinant human BMPs (rhBMPs), rhBMP-2 and rhBMP-7, are available for clinical use, in restricted orthopaedic indications, based on the positive evaluation by a number of large prospective, randomised controlled trials [18-20]. The rhBMP-7, also known as osteogenic protein-1 (OP-1), is commercially available as OP-1® Implant[1] (Stryker Biotech, US) for the treatment of tibial non-union. The rhBMP-2 is commercially available as InductOs® (Wyeth, UK) or INFUSE® Bone Graft[2] (Medtronic Spinal and Biologics, US) in combination with an absorbable collagen sponge (ACS) as the carrier. INFUSE® Bone Graft was regulatory approved

[1] OP-1® Implant, http://www.stryker.com/en-us/products/Orthobiologicals/Osteoinductive/OP-1/OP-1Implant/index.htm (*last accessed Jul. 2009*).
[2] INFUSE® Bone Graft, https://www.infusebonegraft.com/ (*last accessed Jul. 2009*).

for the treatment of lumber fusion (in combination with LT-CAGE® fusion cage), open tibial fractures (with an intermedullary nail fixation), and as an alternative to autogenous bone grafts for sinus augmentations and for localised alveolar ridge augmentations [15].

One of the factors that limit the extended use of BMPs in orthopaedic therapy is the dose-dependent of BMPs in the induction of bone formation [14]. The dose of BMPs must overcome a threshold level for effective osteoinduction; however, too high of a dose beyond this threshold results in rapid osteoinduction that eventually results in direct intramembranous ossification. The dose-response curve, of BMPs, also becomes steeper in larger animal models due to a relatively rapid systemic clearance of BMPs in higher species [14]. The efficacy of BMPs is thus dependent on the ability to provide and retain the required level of BMPs, at the rate needed to effect the local sculpting of the fracture repair.

Currently, the predominant delivery system of BMPs, for skeletal regeneration, involves incorporation of the BMPs with appropriate biomaterials (or carriers) either covalently or non-covalently. Several carrier materials have been developed [14, 21-24] and these can be broadly categorised into the following:

I) Natural polymer carriers, such as collagen, chitosan and alginate. These materials are highly biocompatible, bioresorbable and can be modified into many configurations with variable residence time. The disadvantages, however, include sourcing and processing of these materials, and their possible immunogenicity and disease transmission [21]. Thus far, collagen-based carrier is by far the most widely used. Collagen formulations include gelatine, demineralised bone matrix and fibrillar collagen [21]. The clinically approved carrier, for the delivery of rhBMPs, is a type-I bovine collagen, either as an ACS (used with INFUSE® Bone Graft and InductOs®) [24] or as a particulate bone-derived collagen matrix (used with OP-1® Implant) [21].

II) Inorganic materials, such as calcium phosphate cements, calcium sulphates cements and bioglass. These materials can be produced in various forms and can mimic the natural bony structure. Calcium

phosphate and its variants, such as synthetic hydroxyapatite (crystalline calcium phosphate) and tricalcium phosphate, are osteoconductive and have been used as bone graft substitutes [25]. However, due to the high temperature manufacturing process, the incorporation of BMPs into these materials is less effective; commonly this is achieved, post fabrication, by adsorption, surface coating or mixing with additional carrier or in microspheres [21].

III) Synthetic polymer materials, such as poly(lactic acid) (PLA), poly(glycolic acid) (PGA) and their copolymers. These materials are widely used in medical implants and drug delivery systems as they are biodegradable (via hydrolysis, cellular degradation or enzymatic pathways [8, 21]) and biocompatible [8, 22]. The disadvantages of some synthetic polymers are a potential decrease in local pH, bulk degradation and adverse host tissue reactions that may result from the residual molecules from the polymerisation process (such as catalysts and solvents) [8, 21].

IV) Composites of the above materials to optimise the benefits of each material. For instance, the calcium phosphate can be added to natural polymers to enhance their mechanical stability [26].

Most of these carrier systems are designed to mimic the porous bone matrix, which is the natural delivery system of BMPs. The incorporation of the BMPs in these carrier materials is achieved either by encapsulation during the fabrication of the carrier materials or by adsorption post fabrication. Hence, the release of BMPs is mostly by diffusion and desorption of BMPs, which often accompanied by the bio-degradable of the carrier materials. The release of BMPs is thus passive and dependent upon the physical and chemical interaction between the material, the BMPs and the surroundings; when the loading process was performed by post-fabrication adsorption, the released BMPs typically follow an initial burst profile. Although the exact pharmacokinetics of BMPs release required for an optimum bone growth remains to be elucidated [8], an active means of controlling the release of the BMPs seems to be advantageous. In this way, either a sustained or a pulsatile release profile can be potentially achieved, with a precise dosage and frequency, during the therapeutic period thus providing an optimum osteoinduction. Advanced

drug delivery systems, which are realised using the microfabrication techniques derived from microelectromechanical systems (MEMS), offer the potential of such an actively controlled release profile. In addition, these microdevices could be integrated with sensors for monitoring the bio-chemical activities at the site of implant or measuring the release rate of BMPs. It is envisaged that such a monitoring system can provide a timely feedback of the healing rate and thus appropriate dose can be adjusted via telemetry. Microfabricated drug delivery devices have been intensively investigated and some promising approaches can potentially pave the way for the use of certain biopharmaceuticals. Some of the current state-of-the-art microfabrication-based drug delivery systems are reviewed in Chapter 2.

1.1.1 Bone Morphogenetic Protein-2 (BMP-2)

Bone morphogenetic protein-2 (BMP-2) is one of the multi-functional growth factors from the TGF-β superfamily that plays significant roles in the proliferation, differentiation and other functions in many cell types. BMP-2, as a potent osteoinductive growth factor, is best-known for its ability to induce *de novo* bone and cartilage formation. The mature BMP-2 is a homodimeric protein consisting of two 114-residues monomers representing the C-terminal sequence of a long precursor protein of 396 amino acids [27]. BMP-2 consists of seven cysteine residues, like all members of the TGF-β superfamily, with six of the cysteines form the intra-polypeptide disulfide bonds and one cysteine (Cys78) contributes to an inter-chain disulfide bridge, therefore conserving the cystine-knot folding motif [27, 28]. BMP-2 has a molecular weight of about 26 000 Dalton [27], with dimensions of 7.0 nm x 3.5 nm x 3.0 nm [28]. The two-dimensional ribbon model of human BMP-2 is depicted in Figure 1.1 (a), which identifies the dimeric protein structure as chain A (in cyan) and chain B (in green), the inter-polypeptide disulfide bonds (in yellow) and the inter-chain disulfide bridge (in red). The solvent-accessible surface model, as depicted in Figure 1.1 (b), shows an elongated S-shaped molecule of 7 nm in length [29]. The recombinant-form of BMP-2, rhBMP-2 showed little reduction in biological activity, after being heat-treated for 8 hours at 70 °C (based on *in vitro* assay data) [30].

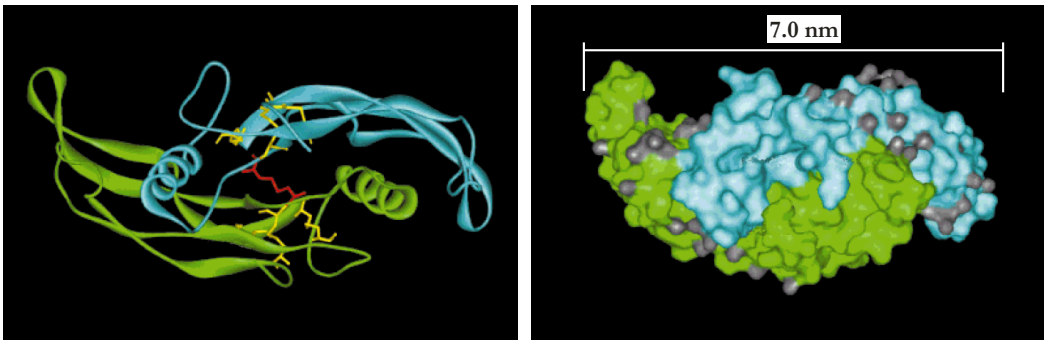

(a) (b)

Figure 1.1: Two dimensional computer-generated (a) ribbon model and (b) solvent-accessible surface model of dimeric human BMP-2. Colour scheme: cyan – chain A; green – chain B; yellow – disulfide bonds of the cystine-knots between Cys14-79, Cys43-111, Cys47-113; red – inter-chain disulfide bridge at Cys78; grey – water molecules (reprinted from [29]).

1.2 Aims and Scope of Work

Implantable drug delivery devices, for site-specific, controlled delivery of therapeutic agents, especially biopharmaceuticals, have significant potential for a wide range of clinical applications. In skeletal regeneration, the delivery of the osteoinductive growth factors to the site of fracture, in a controlled and sustainable manner, has been regarded as the key factor to improve the efficacy of BMPs. Hence, the aim of this research is to create, by microfabrication, novel electrically-addressable drug delivery devices, which can be used for the controlled release of proteins and peptides. The longer term's aim, beyond the scope of this thesis, is to demonstrate the potential of this technology for the controlled delivery of rhBMP-2 on human mesenchymal stem cells for the formation of bone, as a first step to an intelligent therapeutic system for skeletal regeneration.

The design and fabrication of a prototype of such a drug delivery device, which incorporates a porous structure as a drug reservoir and an integrated electro-thermal actuation mechanism for the controlled release of the drug, are the aims of this thesis. The device packaging to prevent bio-fouling, and the interface circuitry for a pre-programmed or telemetry control to the active control mechanism, are not part of the work presented in this thesis. However, it is envisaged that the device can be feasibly packaged, as illustrated in Figure 1.2, within the metal plate or the

intramedullary rod that is commonly used to hold the fracture in place. The interface circuitry can be designed and assembled post-fabrication of the device.

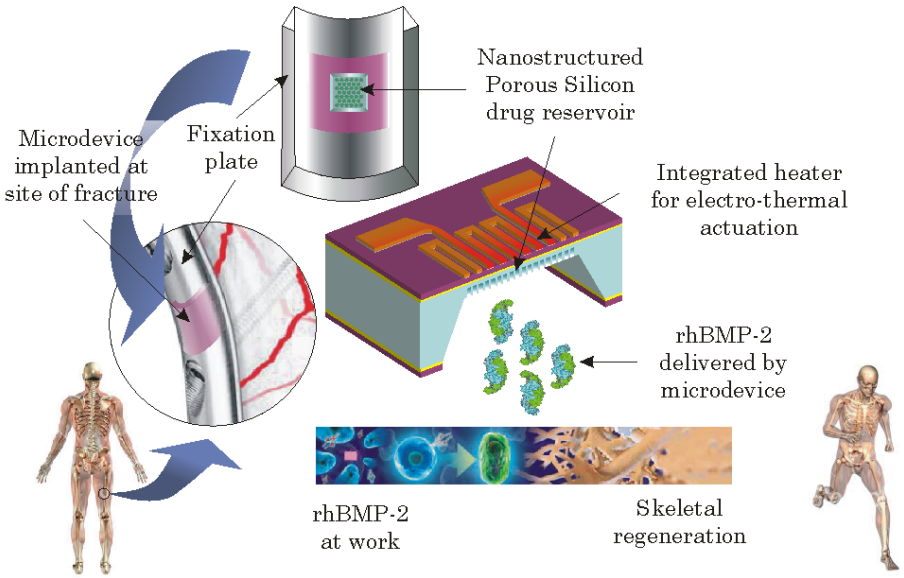

Figure 1.2: Conceptual illustration demonstrating the working principle of the envisaged integrated porous silicon membrane drug delivery device.

1.3 Summary of Main Achievements

A number of original contributions were achieved during this research, and these are outlined briefly as follows:

Three alternative approaches to fabricate a porous polysilicon (PPSi) structure were investigated, which include the chemical stain etching method, a templating approach that uses a porous anodic alumina (PAA) and reactive ion etching (RIE), and another templating approach that uses nanosphere lithography (NSL) technique and the RIE process. The stain etching method produced PPSi structures with random order of pore arrays, while the two templating methods created quasi-ordered PPSi structures. Although the quasi-ordered PPSi exhibited a tapered profile, this is the first demonstration of the fabrication of PPSi with ordered pores and a pore sizes in the macropore range of ~ 370 nm.

A novel fabrication technique, using a modified NSL technique and an improved, Bosch-based RIE process, to realise a quasi-ordered, vertical, cylindrical porous silicon (PSi) structure, with pore diameter in the region of 100 nm, was successfully demonstrated. The fabrication technique is versatile and pores with various sizes and periodicities can be feasibly tuned. It is a "materials general" nanofabrication technique and has been successfully demonstrated on both p-type and n-type silicon substrates. Ordered PSi with pores in 100 nm diameter range has been difficult to achieve using conventional electrochemical etching method.

A drug delivery device, which incorporates a nanostructured, quasi-ordered PSi structure as a drug reservoir and an integrated heater and temperature sensor as an active control mechanism, was designed and successfully fabricated. Preliminary investigation, using a model protein, suggested that the nanostructured PSi improves the passive release of the protein.

1.4 Organisation of Thesis

A two-part literature review is presented next. The current state-of-the-art drug delivery system derived from microfabrication technologies is first examined. These include microdevices that are aimed for oral administration, transdermal drug delivery and BioMEMS-based implantable drug delivery devices. The next half of the chapter reviews the properties of PSi and the application of PSi in the field of drug delivery. The fabrication techniques to produce PSi are briefly discussed.

In Chapter 3, the design and fabrication of a PPSi-based drug delivery prototype device is presented. The fabrication of PPSi structures using the stain etching method is described. The evaluation and optimisation of the stain etching conditions, followed by the characterisation of the porous structures, are discussed.

As a result of the poor reproducibility of the stain etch method to produce PPSi structures, alternative, more reliable methods to form orderly porous structures with pore sizes in the low, macropore regime (~ 50 nm to 100 nm) were evaluated. In Chapter 4 and 5, the potential and feasibility of using two templating

methods to fabricate ordered PPSi structures is described. In specific, Chapter 4 describes the work carried out at the University of Manchester using self-organised PAA as a masking template for RIE methods to create ordered PPSi. The fabrication of the test structures is discussed.

Chapter 5 presents another templating approach which combines the NSL technique and the RIE technology. The NSL technique relies on the self-assembly properties of polymer nanospheres; by using a RIE process to reduce the size of nanospheres, followed by evaporation of metal thin films and subsequent removal of nanospheres, a masking template with hexagonally arranged, non-close-packed nanoholes was created. Subsequent RIE process via this masking template transferred the nanoholes' pattern into polysilicon to realise PPSi structures. The challenge and limitations of the fabrication method are also discussed.

The design and fabrication of a PSi membrane-based drug delivery device are detailed in Chapter 6. The design and process development of the silicon membrane, the PSi drug reservoir, and an integrated heater and temperature sensor, is first described. A thermal analysis, using finite element modelling, to investigate the theoretical operating range of the integrated heater and temperature sensor, is presented. The fabrication and characterisation of the microdevice is then discussed. This includes the fabrication of the silicon membrane carried out at Chalmers University of Technology, the fabrication of the nanostructured PSi, as the drug reservoir, using the NSL technique described in Chapter 5, and the fabrication of the integrated heater and sensor using a lift-off method. The calibration and functionality characterisation of the integrated heater and temperature sensor conclude the chapter.

Chapter 7 details "proof-of-concept" studies of the loading and release of a model protein from the PSi membrane drug delivery device. The investigation focuses on the passive release of the model protein into de-ionised water, in a constant temperature environment.

Finally, Chapter 8 concludes the thesis by summarising the overall achievements of this research, followed by suggestions for future work.

Chapter 2

Microfabricated Drug Delivery Devices: A Literature Review

2.1 Introduction

Drug delivery, in simplistic terms, refers to the method or process of introducing pharmaceuticals into the human body to achieve a therapeutic effect. Synergism between the pharmacology of drugs and its route of administration is key to efficacious and cost effective therapies [31]. Therapeutic agents often have an optimum spatial and temporal range within which maximum therapeutic benefit is obtained [32]. Below this optimum range, the therapeutic effect could not be achieved; while above this optimum range, adverse effects such as fatal toxicity may be encountered. The effective delivery of a drug, to realise its designed therapeutic effect, is of both scientific and economic importance.

Conventional drug delivery systems, which are predominantly based on oral delivery or intravenous injection, only offer moderately efficient treatment. Drugs administered orally or intravenously, in general, produce a "burst effect" [33] release profile, as depicted in Figure 2.1, which is consistent with first-order kinetics, meaning that there is a high plasma level of drugs above optimum therapeutic range, immediately after the initial administration. This is followed by a rapid, often exponential fall below the optimum therapeutic range [34]. Hence, because the time at the optimum therapeutic window may be short, the therapy can be inefficacious.

In contrast, controlled release is used to provide a sustained plasma level of drugs over a period of time, such that the concentration of the therapeutic agent is maintained at the optimum range consistent with zero-order kinetics [34]. Moreover, controlled release devices can also be used for pulsatile delivery of a drug, if necessary, for certain treatments, such as in the delivery of insulin or growth factors, where sustained release fails to mimic the body's natural response [35, 36].

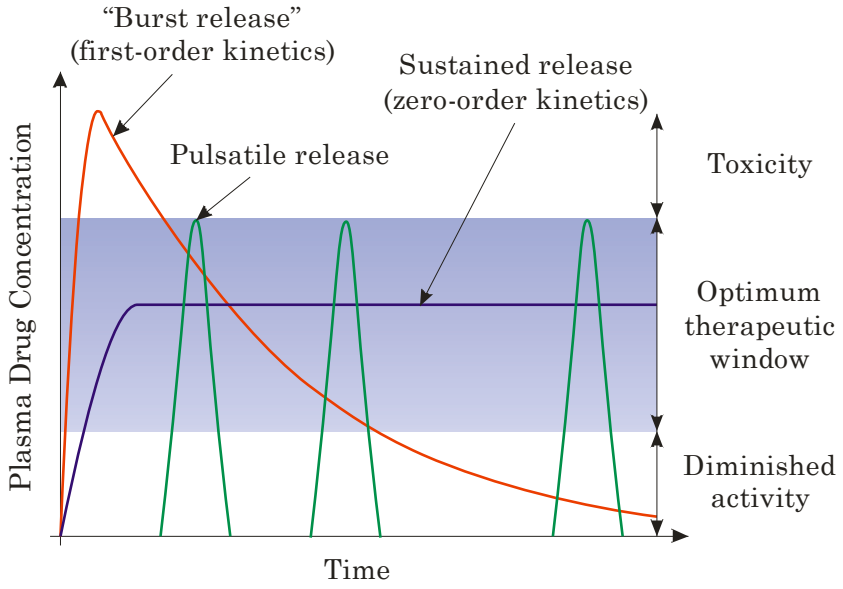

Figure 2.1: Exemplary plasma drug concentration, as a function of time, for conventional "burst effect" release profile (red) and controlled release with sustained delivery (blue) or pulsatile delivery (green) (adapted from [32]).

In addition, orally administered drugs often have a reduced bioavalability due to gastrointestinal (GI) degradation and hepatic first-pass metabolism [37, 38]. Routine hypodermic injection to diabetic patients, for instance, causes an unacceptable level of pain and, hence, the quality of treatment is poor. Many of the newly discovered drugs are increasingly based on recombinant proteins, monoclonal antibodies and nucleic acids [39]. These biopharmaceuticals require novel delivery routes straight to a specific or a targeted site. Along with a need for better patient compliances and cost effective therapeutic care, drug delivery technologies may need to be redesigned. Modern drug delivery systems, therefore, require combined consideration of several factors including the characteristic properties of drugs, route and nature of administration, mechanism and pharmacokinetic of release and the

ability of site specific targeting. To achieve these goals, novel drug delivery systems are required.

Advances in microsystems technology (also known as microelectromechanical systems, MEMS) have enabled the fabrication of highly precise and reproducible miniaturised structures and devices [40-42] that can be on the same size scale as the biological entity. These microfabrication techniques use a broad range of established technologies developed by the microelectronics industry. This ability to fabricate microstructures for biological applications is especially compelling and perceived by many to be one of the approaches needed to rise above the challenges faced in the drug delivery industry, as evident by the increase in the new developments reported recently [33-36, 43-57]. These approaches could be broadly categorized into biomedical MEMS (BioMEMS) based drug delivery microdevices [33-36, 43-50], which combine microfluidic (especially micropump technology), electronics and micromachining and offer the possibility for the implant route; and nanoparticles based drug delivery vehicles [33, 50-57], which use liposomes, polymer or microfabricated particles as carriers for targeted drug delivery and is relatively new in development.

In particular, microfabricated drug delivery devices used as implants are envisaged to be revolutionary to the field of therapeutic care [58, 59]. With the ease of integration of microelectronics and biosensing systems, implantable microdevices are capable of providing personalised and ultimately the responsive controlled release of therapeutic agents. This can be achieved either by a pre-programmed release profile, by using a telemetry system to provide wireless controlled release or by feedback from integrated biosensors to provide timely and precise dosage as required by the human body [59]. These enormous potentials rightly translate into greater challenges in the design consideration of the implantable microdevices. The materials used in fabricating microdevices need to be biocompatible, the delivery mechanisms need to be reliable and reproducible, and there is also a need for an effective fail safe mechanism to avoid dose-dumping upon device failure.

Porous silicon (PSi) is considered as one of the emerging and promising materials in drug delivery technology. It is biocompatible and can be made bioinert, bioactive or biodegradable depending on its microstructural properties (such as

porosity and pore morphology), which can be tailored with microfabrication techniques [60, 61]. The porous structure is ideal for entrapping therapeutic agents, and biodegradable PSi can be safely dissolved into the human body [62] at the same time bringing along the therapeutic agents. PSi, in particulate forms, has been used as a drug delivery vehicle [54, 55] and the integration of PSi as a drug reservoir of an implantable microdevice could be advantageous.

The following review first examines the contribution of microsystem technologies in three of the major drug delivery approaches – oral delivery, transdermal delivery and implantable devices. Current example microdevices are presented and the microfabrication techniques involved are briefly discussed. In view of the potential of PSi in drug delivery technology, the properties of PSi are next examined. Existing examples of the use of PSi for drug delivery applications and the fabrication techniques are then discussed.

2.2 Microdevices for Drug Delivery

Microfabrication technology is instrumental in developing novel approaches for drug delivery. The ability to miniaturise structure or devices to the same feature size of living cells prompted enormous interest and subsequently countless efforts both from the academia and industry [33-36, 43-55]. These contributions are summarised here into three major areas: micromachined microparticles for oral drug delivery, microneedles for transdermal drug delivery and implantable microchips for localised delivery.

2.2.1 Micromachined Particles for Oral Drug Delivery

Oral administration of drugs remains the preferred route of delivery due to its non-invasive nature and ease of self-administration. However, oral drug delivery in general provides only moderately efficient treatment [37, 38]. Orally administered drugs are subjected to both an acidic and enzymatic environments in the stomach and a physical barrier in the intestine before being absorbed. Once absorbed, these

drugs enter the hepatic portal system and experience metabolism by the liver before being circulated throughout the body. By this time, the concentration of the drugs has been greatly reduced; hence this leads to low oral bioavailability of the drug and consequently a degraded therapeutic effect. Due to this degradation in the GI tract and by hepatic first pass metabolism, oral administration is generally not a viable route for biopharmaceuticals such as proteins, peptides, DNA and vaccines [33, 63]. These biopharmaceuticals are naturally broken down into smaller molecules by the GI tract, and nearly all macromolecules would have been destroyed or marginally absorbed into the system.

A number of approaches are currently being developed to address the problem of degraded bioavailability in orally administered drugs. These include using protective coatings such as lipids and polymers, bioadhesive agents, permeation enhancers and protease inhibitors [33]. Drug-eluting micro- and nanoparticles have been used for site-specific and targeted delivery of therapeutic agents either by oral administration or intravenous injection [33]. These microparticles are often made from natural or synthetic polymers and can be specially designed to be pH and temperature sensitive [64]. However, due to the manufacturing method used, these microparticles, in general, are spherical and polydisperse in size. This has a number of implications – the spherical geometry inherently limits contact to the cell surface and the drug is often released in all directions; the size polydispersity on the other hand, results in variance in drug loading [64].

Microfabrication technology, on the other hand, offers an alternative approach to addressing some of the challenges faced by oral drug (in particular, peptides and proteins) delivery systems. Micromachined particles encapsulating macromolecular drugs, for instance, have been investigated as a new drug delivery method [33, 36, 49, 50]. Unlike the conventional synthesised microparticles, micromachined particles can be manufactured with precise control over size, shape, aspect ratio and surface features [33, 50]. These microparticles can thus be designed to be flat, thin and disc-shaped, such as the one depicted in Figure 2.2, to optimise the flow of the microparticles within the GI tract and maximise the contact area with cells or intestinal walls [65]. The general concept of using micromachined particles for oral drug delivery [33] is as follows:

i) Microparticles are first filled into enterically coated capsules for protection during passage through the acidic environment of the stomach.

ii) Once in the upper intestines, the enteric capsule is designed to dissolve, hence releasing the microparticles. These microparticles are typically coated with bioadhesive agents (such as lectin) on one side to ease binding to the surface of the epithelial cells of the intestines. This intentionally orientates the microparticles towards the target intestinal lining, and hence limits the exposure of the coated peptide or protein to enzymatic degradation.

iii) The reservoir contents in the microparticles are hydrated and have a high local concentration of permeation enhancer (and, if needed, enzyme inhibitors) which allows the transport of macromolecules through intestinal barriers.

iv) The microparticles are then designed to effectively be cleared from the GI system; the macromolecules enter the bloodstream below epithelial cells and into systemic circulation.

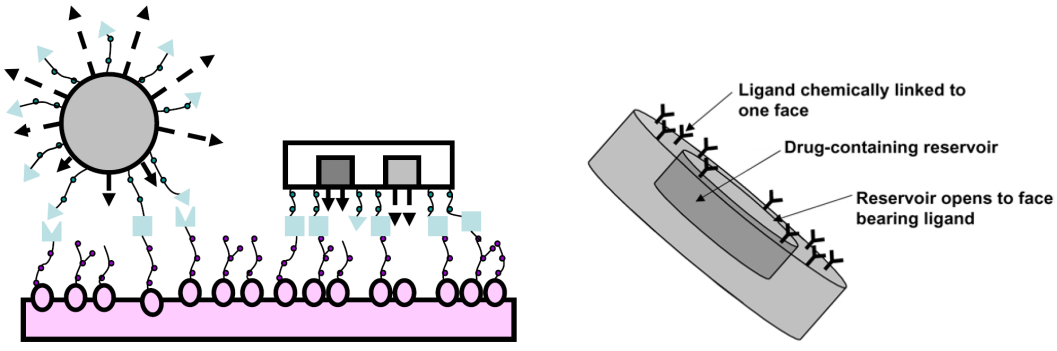

(a) (b)

Figure 2.2: Conceptual illustration showing (a) the contact area of conventional spherical drug delivery microparticles compared to that of micromachined particles (reprinted from [63]); and (b) a typical micromachined particles with some key features (reprinted from [33]).

One of the groups actively involved in the development of micromachined particles for oral drug delivery is the group of Desai[3]. Microparticles of various materials, such as polymers [63, 66, 67] and silicon dioxide (SiO_2) [65], have been fabricated using a combination of a micro-moulding technique and photolithography and etching processes. These square-shaped microparticles, as depicted in Figure 2.3, ranged between 50 μm and 150 μm and consist of a square recess of various sizes defining the reservoirs. Surface modifications were carried out to provide viable covalent bonding to biological molecules, specifically for conjugation of avidin-biotin-lectin binding. These reservoirs were then filled with an aqueous polymeric drug solution, using a microinjection technique, before being detached from the substrate. Different polymers can be used to provide various drug release rate and time. Recently, the group incorporated hydrogel into the reservoir for a responsive drug delivery system [64]. The *in vitro* studies of permeation of drug (chemotherapeutic camptothecin) through a Caco-2 epithelial monolayer demonstrated a significantly improved permeation with drug filled in microparticles as compared to drug filled into hydrogel alone and free drug.

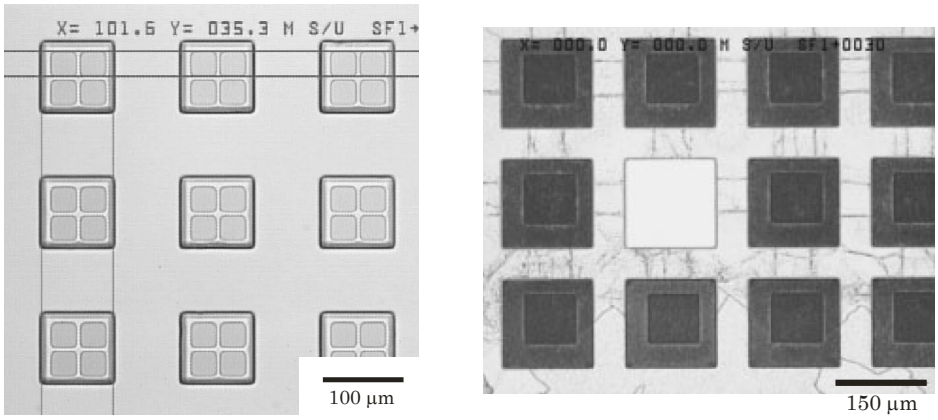

(a) (b)

Figure 2.3: Micromachined particles developed by Desai's group. Plane-view SEM micrographs of (a) SiO_2 microparticles of 100 μm x 100 μm with four-wells reservoirs of 35 μm x 35 μm each (reprinted from [65]); and (b) poly(methyl methacrylate) (PMMA) microparticles of 150 μm x 150 μm with single-well reservoirs of 80 μm x 80 μm. One of the PMMA microparticles is shown released from the substrate (reprinted from [67]).

[3] Tejal A. Desai, Professor in Physiology, University of California San Francisco, USA. http://physio.ucsf.edu/desai/ (*last accessed Jul. 2009*).

Apart from SiO_2 and polymers, porous silicon (PSi) has also been used as material for the fabrication of microparticles [68, 69]. PSi is biocompatible and biodegradable [60], and the size of the pores can range from nanometers to micrometers. Hence, PSi microparticles can be used as a drug delivery vehicle for various sizes of therapeutic agents, as demonstrated by Salonen *et al.* [70]. After loading or entrapping drugs into the pores, PSi microparticles can be delivered to the target site. The drugs can be released by diffusion to the surroundings, assisted by biodegradation of PSi. In fact, based on a similar principle, a multistage delivery system has been recently proposed and demonstrated [71]. The core of the system is the micrometer-sized PSi particles with mesoscale size pores (between 2 nm and 50 nm) which act as the first stage delivery vehicle. With proper surface chemistries, one or more smaller particles (second stage nanoparticles), such as therapeutic nanovectors and imaging contrast nanoparticles, can then be loaded in the first stage mesoporous silicon particles. Consequently, the mesoporous silicon particles reduce the system uptake of the second stage nanoparticles, hence providing a better chance for the second stage nanoparticles to accomplish their intended tasks. Quantum-dots and single-walled carbon nanotubes have been used as second stage nanoparticles in this study [71], where intravenous injection is proposed as the administration route of the mesoporous silicon particles.

2.2.2 Microneedles for Transdermal Drug Delivery

Although oral administration of drugs is the preferred route, there are times when it is not feasible due to poor bioavailability of therapeutic agents as a result of degradation in the GI tract and hepatic first pass metabolism [37, 38]. The common alternative is to inject the drugs intravenously. In addition to the pain caused to the patients, intravenous injection requires trained medical personnel to avoid infection and injury, hence rendering self-administration difficult.

An alternative and possibly more appealing approach is by transdermal drug delivery, which offers the possibility of painless controlled release over time. Transdermal drug delivery refers to the administration of a drug through the skin, (specifically the epidermis layer) into the bloodstream via diffusion to achieve a systemic delivery, although some transdermal approaches are meant for topical delivery [72-74]. Apart from reducing the aforementioned issues faced by oral and

intravenous routes of administration, transdermal drug delivery with controlled release requires relatively smaller amounts or doses of drug to achieve the desired therapeutic effect, and is thus more cost effective. In addition, transdermal delivery can allow the administration of drug with short biological half-lives and in a narrow therapeutic window [74] due to its closer vicinity to the target site. Therefore, transdermal delivery of drugs could potentially lead to reduced side effects due to the reduced peak plasma level and lower fluctuations in plasma levels of these drugs [75].

A transdermal route of administration is, however, often limited to the transport of therapeutic agents with low molecular mass (typically < 500 Dalton), high lipophilicity and low potency [76]. One of the reasons for these limitations is the poor penetration of therapeutic agents through the stratum corneum – 10 μm to 20 μm thick, "hard" outermost layer of the skin. There are a number of strategies currently explored to enhance the permeation of drugs through the stratum corneum. These approaches [75-79] endeavour to affect the physicochemical properties of stratum corneum either by means of chemical enhancer, physical enhancer (such as microneedles), electric (by iontophoresis or electroporation), ultrasound (by sonophoresis), thermal or laser radiation.

Among the approaches developed to enhance transdermal drug delivery, physical enhancement using microfabricated arrays of micrometer dimensions needles (microneedles) has been one of the more actively researched methods [45, 80-82]. Microneedles can be designed and precisely fabricated such that the microneedles are long, and robust enough to penetrate the stratum corneum, and thus create holes that are feasible for transport of drug molecules. At the same time, the length of the microneedles is short enough to avoid the nerves and blood vessels mostly found in the dermis layer, hence avoiding pain and bleeding. In addition, unlike other approaches, microneedles have been used to deliver larger and more hydrophilic molecules, including proteins, DNA and nanoparticles [83, 84]. Microneedle technology is also envisaged to provide efficacious vaccine delivery; the dendritic cells, which are responsible for the immune response, are located in the epidermis layer, and hence could be better targeted by using microneedles [85].

In general, microneedles could be categorised as either in-plane or out-of-plane, based on whether the microneedles are either parallel or normal to the substrate, respectively. In addition, microneedles are also recognised by the shapes, notably either solid or hollow. The materials used to fabricate microneedle arrays include silicon, metal and more recently polymer. Most silicon microneedles are fabricated using a series of MEMS technology processes including deposition, photolithography, wet chemical etching and reactive ion etching (RIE); while polymer microneedles are typically micro-moulded. Currently, there are four strategies to deliver therapeutic agents into the skin [83]: i) by piercing the skin using the microneedles, followed by application of a drug patch; ii) by dry coating drug onto the microneedles and inserting into the skin for subsequent dissolution of the coated drug; iii) by delivering through a hollow channel of microneedles; and iv) by encapsulating drug within the biodegradable polymer forming the microneedles, followed by insertion into the skin and dissolution of the polymeric microneedles along with the drugs.

2.2.2.1 In-plane Microneedles

With the advancement in the planar integrated circuit microfabrication technology, in-plane microneedles were the earlier type of microneedles developed, as the length and shape of the microneedles can be easily defined by photolithography. In fact, in-plane microneedles had been developed as early as the 1970s by Wise *et al*., but were initially used as neural microprobes for biopotential recording [86]. Microchannels were later incorporated into the improved version of the neural microprobes, allowing the delivery of a chemical into the central nervous system of guinea pigs for studies of spontaneous neural responses [87]. The trapezoidal microchannels, as depicted in Figure 2.4, were fabricated by anisotropic etching into the silicon substrate using ethylenediamine pyrocatechol (EDP) via an array of chevron-shaped, boron-doped silicon masks. The microchannels were then sealed by thermal oxidation and low pressure chemical vapour deposition (LPCVD) of multilayers of dielectrics materials. Polycrystalline silicon (polysilicon) interconnects and metal contact pads were integrated for recording of neural responses. The shank of the microneedles was defined by deep boron diffusion prior to sealing and a final etch in EDP to release the structure. Microneedles with one to four delivery channels have been fabricated in this way, with the lumen ranging from 10 μm to 32 μm wide and a

depth of 15 μm. The microneedles have a width of 58 μm to 74 μm and a length of 4 mm.

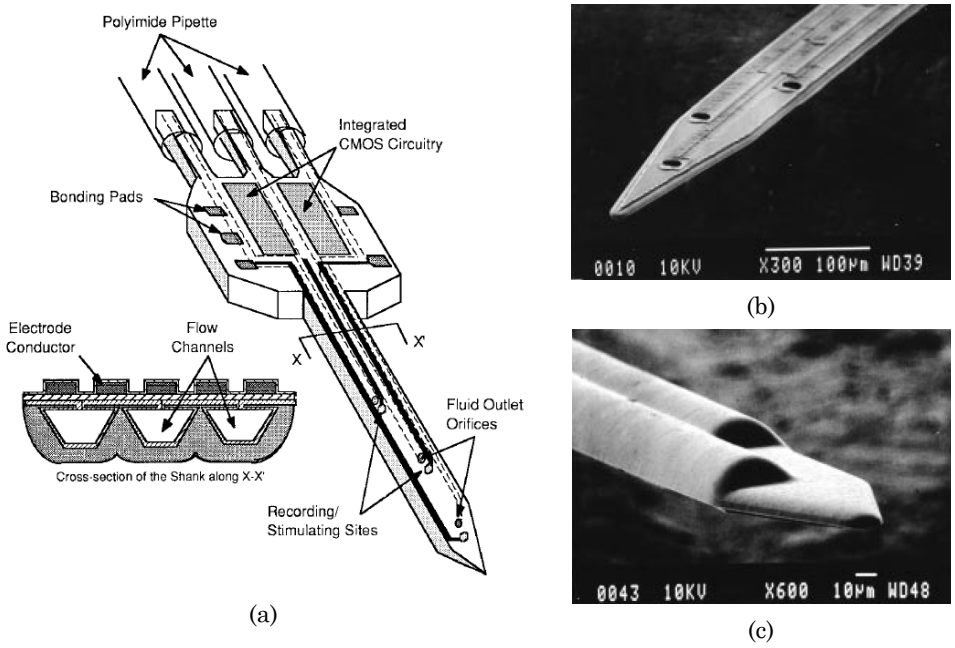

(a) (b) (c)

Figure 2.4: In-plane microneedles for chemical delivery at the cellular level developed by Wise *et al.* (a) A conceptual drawing of a three delivery channel microneedle probe with recording and stimulating electrodes. (b) – (c): SEM micrographs of the (b) micromachined three delivery channel microneedle with recording sites; and (c) back of a two delivery channel microneedle (reprinted from [87]).

Instead of etching into the bulk silicon to form the microchannels, Lin and Pisano used sacrificial layers (combined phosphosilicate glass (PSG) and low temperature silicon oxide (LTO)) by surface micromachining to define the microchannels [88]. By depositing a layer of silicon nitride (Si_3N_4) over the sacrificial layers and subsequent removal of these sacrificial layers, in-plane microhypodermic needles of 1 mm to 6 mm in length with lumens of 9 μm high and 30 μm or 50 μm wide have been realised. Polysilicon heater strips were integrated at the proximal ends of the microneedles to generate bubbles to pump fluid down the lumen.

In an attempt to form a more complex, responsive drug delivery system, microneedles have been integrated with microsensors or microactuators. Zahn *et al.* demonstrated that by incorporating an on-chip MEMS micropump, sustainable continuous drug delivery could be achieved [89]. The proof-of-concept polysilicon microneedles, with a micropump fabricated by micromolding demonstrated a water flow rate of ~ 1.0 $nL \cdot s^{-1}$ with continuous pumping for more than 6 hours.

2.2.2.2 Out-of-plane Microneedles

In contrast to the in-plane microneedles, which are mostly hollow, the out-of-plane microneedles are mostly solid due to the ease of microfabrication. One of the first microneedles to demonstrate enhancement in transdermal drug delivery was reported by Prausnitz[4] and his research group [90], who have since been at the forefront of developments in microneedles for transdermal drug delivery. The microneedle arrays reported were fabricated using RIE of silicon to form an array of out-of-plane, conical microneedles. Each microneedle is approximately 150 μm long with a base diameter of ~ 80 μm; 400 of these microneedles formed a 20 x 20 array in a 3 mm x 3 mm area, as depicted in Figure 2.5 (a). The single mask RIE process used was based on the "black silicon" method [91], with modified parameters such that deep vertical etching with controlled mask undercut could be achieved, hence forming sharp silicon spikes. Using these microneedles to create holes in human cadaver skin, the permeability of calcein through the skin has been reported to increase by up to 25 000-fold post insertion [90]. Further studies on the pain caused by these microneedles concluded that essentially no pain was experienced by the 12 human subjects [92]. Recently, these microneedles have been used with a

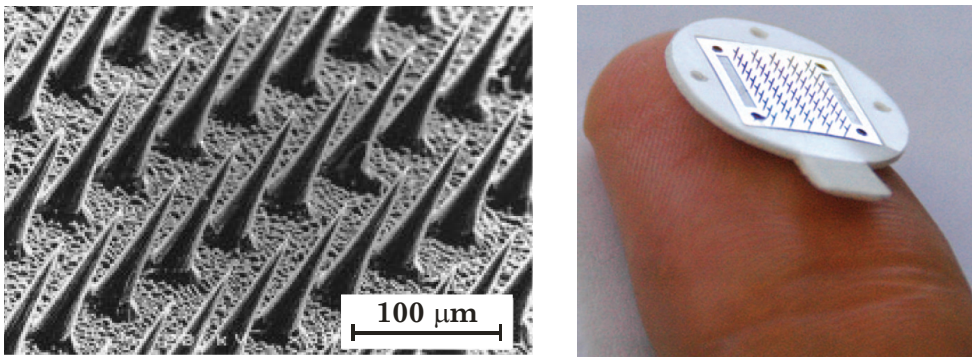

(a) (b)

Figure 2.5: Solid, out-of-plane silicon microneedles array by Prausnitz's group. (a) SEM micrograph showing a section of the 400 microneedles in an area of 3 mm x 3 mm (reprinted from [90]). (b) Digital image showing a 5 x 10 array of microneedles patch resting on a tip of a human thumb (reprinted from [93]).

[4] Mark R. Prausnitz, Professor of Chemical and Biomedical, and the Emerson Lewis Faculty Fellow, Georgia Institute of Technology, USA, http://www.che.gatech.edu/drugdelivery (*last accessed Jul. 2009*).

transdermal patch for delivery of naltrexone (NTX), which is a hydrophilic, skin-impermeant, potent mu-opioid receptor antagonist used to treat opiate and alcohol dependence [93]. In a human proof-of-concept study, healthy volunteers who were pre-treated with the microneedles array demonstrated steady-state plasma concentrations within 2 hours of patch application and were maintained for at least 48 hours. In comparison, volunteers who did not go through the pre-treatment of microneedles showed undetectable drug plasma levels post-patch application.

By using a two-step RIE process, Stoeber and Liepmann demonstrated that arrays of hollow out-of-plane silicon microneedles, as depicted in Figure 2.6 (a), could be fabricated [94]. The first RIE (substrate etch through) was used to create the lumen of the microneedle by deep RIE of the silicon substrate using the Bosch process [95]. The substrate was turned over and an isotropic RIE was carried out to define the shape of the microneedles. A wet chemical etch was also carried out to smoothen the surface of the microneedles. In order to prevent tissue clogging on the tip of hollow microneedles, Griss and Stemme fabricated the fluidic opening at the sides of the microneedles instead, as depicted in Figure 2.6 (b) [96]. Hollow microneedles with a complex out-of-plane structure and flow profiles have also been developed by NanoPass Tech. Ltd.[5] and the University of Twente [97]. The MicronJet needle, which is essentially a standard syringe mounted with arrays of MicroPyramids, similar to that depicted in Figure 2.6 (d), has been developed for intradermal administration of drugs, proteins and vaccines. Another company currently pursuing microneedles technology as transdermal drug delivery system is Zosano Pharma™ Inc.[6]. The Macroflux® technology, which uses stainless steel, out-of-plane microprojection arrays has been developed since 2001 [98] and is currently in Phase II clinical trials for treating osteoporosis using a parathyroid hormone (hPTH 1-34). The Macroflux® technology has been previously demonstrated to provide bolus release of oligodeoxynucleotides [98] and ovalbumin [99, 100] in a hairless guinea pig.

[5] NanoPass Technologies Ltd., Israel. http://www.nanopass.com/ (*last accessed Jul. 2009*).

[6] Zosano Pharma™, Inc. (previously Macroflux Corp., spinoff from ALZA), Fremont, CA, USA. http://www.zosanopharma.com/ (*last accessed Jul. 2009*).

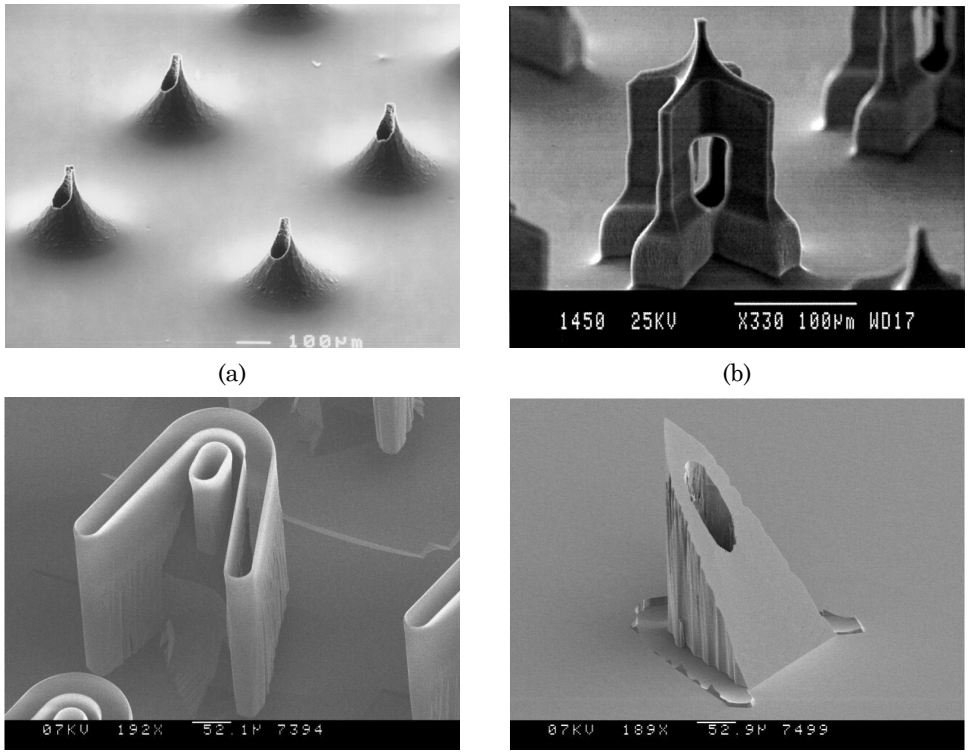

(a) (b)

(c) (d)

Figure 2.6: Micromachined hollow out-of-plane silicon microneedles. SEM micrographs of (a) an array of hollow microneedles by Stoeber and Liepmann (reprinted from [94]); (b) side-opened microneedles fabricated by Griss and Stemme (reprinted from [96]) and (c) – (d) hollow microneedles fabricated by Gardeniers *et al*. (reprinted from [97]).

Biodegradable Microneedles

More recently, due to the increased concern of broken microneedles causing possible undesirable infections, microneedles have been fabricated using biodegradable materials [83, 101-109]. Prausnitz and his team have been working on polymer-based biodegradable microneedles [83, 101-105] and, recently, demonstrated that by micro-moulding biocompatible, water soluble polysaccharide (carboxymethyl cellulose (CMC) or amylopectin), solid, out-of-plane, conical or pyramidal (with a base of 300 μm in width over microneedle length of 600 μm to 800 μm) microneedle arrays could be fabricated [101]. The microneedle arrays encapsulated with model drugs, in this case, sulforhodamine B, bovine serum albumin (BSA) and lysozyme, have been shown to be strong enough for insertion into cadaver skin and spontaneously (within minutes) dissolved to release the model drugs either by bolus or sustained delivery, as demonstrated in Figure 2.7. In this way, no sharp biohazardous waste has been left on the skin surface.

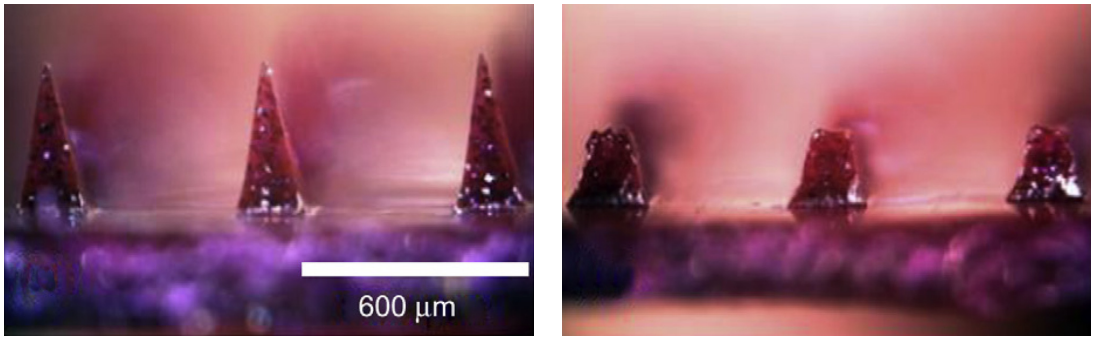

(a) (b)

Figure 2.7: Self-dissolving polymer based microneedles by Prausnitz's group. The brightfield microscope images show the CMC pyramidal microneedles (a) prior to and (b) 1 minute after insertion into pig cadaver skin (reprinted from [101]).

In contrast, Tay and his team anodised the tips of solid, out-of-plane silicon microneedles thus making them porous [107-109]. Porous silicon has been known to be biocompatible and biodegradable [60]; this approach is also advantageous as the porous silicon tips can, at the same time, be used to carry drugs.

2.2.3 Implantable Microchips for Localised Delivery

Similar to microneedles technology, implantable microdevices provide an alternative route of administration which addresses the issues faced by oral delivery and intravenous injection. Implantable microdevices (microchips) are preferred for therapies that require controlled release over the therapeutic period, which is typically achieved by daily or weekly intravenous injection [34]. These microchips can be strategically implanted into the human body or placed just under the skin (subcutaneously), hence eliminating the need for frequent injections and avoiding pain or risk of infection. In addition, when placed near the specific site where the drug is needed, these microchips offer the potential of site-specific localised delivery, an attractive therapeutic effect particularly for treatment using potent drugs, such as in chemotherapies of cancer patients [110]. The typically high concentration of the drugs required can be administered at the site, while keeping the systemic level low, hence reducing adverse side effects as compared to by systemically administered the drugs in high dose. It is also more cost effective, as the amount of drug used is less. Most implantable microchips are also designed for controlled release either by active control (potentially with sophisticated microelectronics systems) or passive release.

Hence, the dose level and dose frequency could be personalised and precisely regulated for the therapeutic needs.

Implantable microchips could be broadly categorised into microfluidic and non-microfluidic based devices. Microfluidic based drug delivery devices often incorporate active components such as micropumps and microvalves [111, 112]; while non-microfluidic based microchips may use either active or passive release mechanisms [32, 34, 43, 46, 47, 113]. Non-microfluidic based microchips do not typically consist of moving parts, hence reducing the adverse effect caused by malfunction of these components.

2.2.3.1 Microfluidic based Microchips

Drug delivery devices derived from the microfluidic technology [42, 114] often incorporate micropumps, microvalves and flow channels as the basic components. These components, combined with flow sensing, have been well-known to provide accurate, nano- to pico-litre volume liquid metering and dispensing [115]. Hence, in principle, microfluidic based microchips are able to provide a controlled release of accurate quantities of pharmaceuticals on demand, possibly by telemetry or feedback from biosensors that could be integrated into the device. While most non-microfluidic based, controlled release, microchips rely on the diffusion of drugs as a result of the concentration gradient, microfluidic based microchips (mostly actuated by a micropump) depend on the pressure gradient from the surroundings. This is advantageous as the diffusion rate of most molecules, in general, is relatively slower than the flow rate that is able to be generated from micropumps. The pressure gradient is typically created by either pressurising the drug reservoir, by osmotic action or by direct actuation of micropumps with various methods [111, 112]. As with other drug delivery technology, there are some concerns and challenges to be addressed especially on microchips intended for implantation. The specific design considerations relating to microfluidic based microchips include i) reduction of biofouling; ii) biocompatibility with the drugs and the surrounding tissue; iii) the need for external sources and high power consumption; and iv) the safety and reliability of moving parts within the microfluidic system [111, 112].

The group of Woias[7] at the Institute of Microsystem Technology (IMTEK), Germany is one of the many academic research groups working in the development of micropumps. Recently, based on their experience in micropump technology, the group has been focusing on developing a fully integrated drug delivery system, so-called "active microport" which strives to address some of the challenges faced by most implantable microchip technologies [116]. The microport is envisaged to offer a freely programmable release profile within a low flow drug delivery regime. The core of the system is a two-stage piezoelectrically actuated micropump specifically developed to deliver a pulsatile flow of liquid drug with high resolution volumetric dosing, at the same time being small, demand less power and be easy to fabricate [117, 118]. The resolution of the micropump is determined by the voltage controlled stroke volume, which currently can be preset between 10 nL and 200 nL [116]. The high resolution volumetric dosing has been facilitated by the low backpressure dependency (up to 30 kPa within a low flow regime of (0.1 to 50) $\mu L \cdot min^{-1}$), which is

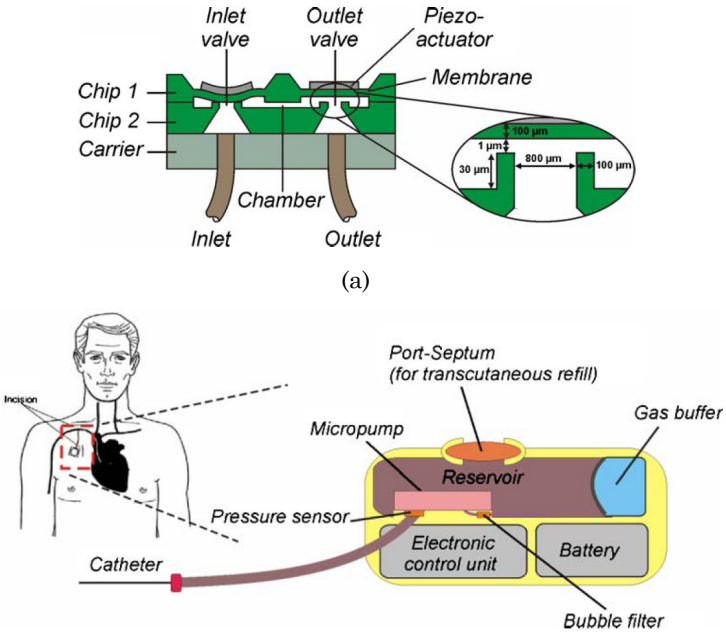

Figure 2.8: Active microport developed by the group of Woais.The conceptual drawing of (a) the two-stage piezoelectrically driven micropumps and (b) the microport (reprinted from [116]).

[7] Peter Woias, Professor, Chair for Construction of Microsystem, University of Freiburg, Germany. http://www.imtek.de/konstruktion/index_en.php (*last accessed Jul. 2009*).

the susceptibility of the flow rate to an increase in the static pressure at the outlet of the micropump [118]. This feature ensures a constant flow rate, and coupled with an integrated pressure sensor to monitor the flow rate, the system potentially is able to address the problem of varying pressures caused by the changing blood or tissue pressure – an imperative consideration to ensure safety and reliability of an implantable microchip system. In comparison, one of the commercial micropumps developed by Debiotech S. A.[8] can only provide a constant flow rate up to 20 kPa backpressure (within low flow regime up to 33 $\mu L \cdot min^{-1}$), with a constant stroke volume of 160 nL [119]. The disposable Nanopump™ utilises piezoelectric actuation with a reciprocating membrane, and achieves the backpressure independency by means of a "double limiter concept". Its predecessor, MIP implantable micropump which was developed for implantable drug delivery system, is larger in size and more complex in design with similar accuracy and reliability [120]. Currently, the Nanopump™ is developed to provide continuous subcutaneous insulin infusion for a week. Other marketed insulin infusion devices include the leading MiniMed Paradigm® developed and marketed by Medtronic Inc.[9]. The insulin pump can be wirelessly linked to the REAL-Time System which measures the glucose level continuously, hence providing real-time monitoring and management of insulin uptake. Medtronic's SynchroMed® II Drug Pump, on the other hand, is a fully implantable intrathecal drug delivery system for managing severe chronic pain or treating severe spasticity.

Most of the micropump based microchips discussed thus far, require some forms of external power source for actuation. In contrast, micropumps that are based on osmotic pressure, such as one developed by Su and Lin [121], could release the drug without the need for mechanical or electrical sources. The two-part prototype device, as depicted conceptually in Figure 2.9, is composed of an osmotic microactuator at the bottom, bonded to polydimethylsiloxane (PDMS) microfluidic components consisting of reservoir, delivery channel and delivery port at the top. The PDMS microfluidic components were cast from an SU-8 mould, while the bottom osmotic microactuator was fabricated from cellulose acetate using the hot embossing technique [121].

[8] Debiotech S.A., Lausanne, Switzerland. http://www.debiotech.com/ (*last accessed Jul. 2009*).

[9] Medtronic Inc., Minneapolis, MN, USA. http://www.medtronic.com/ (*last accessed Jul. 2009*).

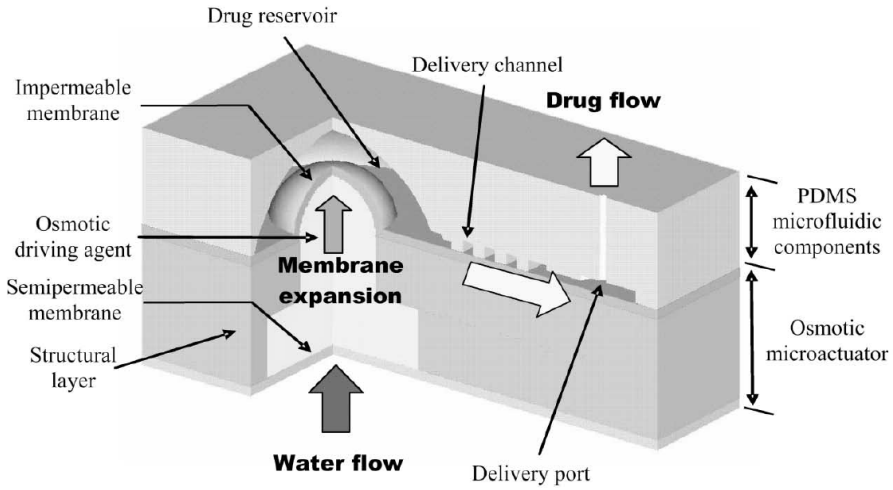

Figure 2.9: Conceptual illustration of the osmosis actuated micropump for drug delivery developed by Su and Lin (reprinted from [121]).

Due to a concentration gradient across the semipermeable membrane at the bottom of the osmotic microactuator, water from the surrounding aqueous environment is drawn through the membrane into the chamber filled with the salt, hence the actuating membrane is deflected and this forces the liquid drug, stored in the reservoir, to be dispensed though the delivery channel to the delivery port. The device is capable of inducing pressure up to 25 MPa, and this is believed to be sufficient to overcome the pressure from surrounding cells or tissue, during operation, and hence deliver a total drug volume of 2 μL at a constant rate of 0.2 $\mu L \cdot h^{-1}$ for an operation period of 10 hours [121].

Other simpler osmotically driven micropump-based drug delivery devices include a biodegradable prototype [122] and a commercial implant, Viadur®. The biodegradable device developed by Ryu *et al.* was fabricated by micro-moulding and thermal assembly of 85/15 poly(L-lactide-co-glycolide) sheet [122]. The *in vitro* release of basic fibroblast growth factor (bFGF) was regulated at 40 nanogram per day, on average, over four weeks. The commercial device, Viadur® is developed by Durect Corp.[10] via the DUROS® technology and was distributed by Bayer HealthCare Pharmaceutical[11] before being phased out in April 2008 [123]. The implantable, 44 mm long, 3.8 mm diameter cylindrical device with titanium casing, delivers leuprolide acetate for 1 year to manage symptoms associated with advanced

[10] Durect Corp. (spinoff from ALZA), Cupertino, CA, USA. http://www.durect.com/ (*last accessed Jul. 2009*).

[11] Bayer HealthCare Pharmaceuticals, Wayne, NJ, USA. http://www.bayerviadur.com/ (*last accessed Jul. 2009*).

prostate cancer. By attaching a micro-catheter, the DUROS® technology can be modified to allow site-specific local drug delivery [124].

2.2.3.2 Non-microfluidic based Microchips

One of the earliest demonstrations of controlled drug delivery using an implantable microchip has been reported by Langer[12] and co-workers [32, 125]. The microreservoirs-based microchip has been used for the controlled release of microgram quantities of either single or multiple substances in a pulsatile manner, potentially on demand. In these studies, model chemical substances, sodium fluorescein and radioactive calcium chloride ($^{45}CaCl_2$) were loaded into separate reservoirs capped with thin gold membranes. The release mechanism was based on the electrochemical dissolution of the gold membrane in the presence of chloride ions at the bias voltage, hence allowing the loaded chemical substances to diffuse into the surrounding medium.

The proof-of-concept prototype microchips used in the studies, as depicted in Figure 2.10 (a), were 17 mm x 17 mm x 310 μm in size and contained 34 reservoirs [125]. The 480 μm square reservoirs, providing volume of ~ 25 nL each, were chemically etched from the back of the silicon wafer using potassium hydroxide, through a photolithographically patterned silicon nitride etch mask, forming the typical anisotropically etched square pyramidal voids with silicon nitride membranes. Gold electrodes of 300 nm thick, patterned using the lift-off method were deposited over the silicon nitride membranes. A passivation silicon dioxide layer of 600 nm thick was deposited, patterned and etched using electron cyclotron resonance (ECR) enhanced RIE. This serves as electrical isolation and protection to some portions of the electrodes. The silicon nitride membrane underneath the gold membrane was then removed using the ECR-enhanced RIE. An aqueous solution of liquid polyethylene glycol and model chemical substances were loaded using inkjet printing and a microsyringe pump capable of dispensing nanolitre solution or gel. The reservoirs were then covered with thin adhesive plastic and sealed with waterproof epoxy.

[12] Robert S. Langer, Institute Professor and Professor of Chemical Engineering & Biological Engineering, Massachusetts Institute of Technology, USA. http://web.mit.edu/langerlab (*last accessed Jul. 2009*).

By applying an electrical potential of +1.04 V (with respect to the saturated colomel reference electrode) to the gold membranes, release of the chemical substances was detected within a few minutes, with a typical 70 % of the chemical released within 30 min [125]. The release studies also demonstrated the ability to activate each reservoir individually, hence creating the possibility for designing complex release profiles. Currently, the microreservoirs-based microchip technology is developed by MicroCHIPS Inc.[13]. The improved microchip, as depicted in Figure 2.10 (b) and (c), contains a better release mechanism using electro-thermal effect [126], an electronics control and telemetry circuitry, and a biocompatible packaging. The device is currently in preclinical trials for treating prostate cancer using model polypeptide leuprolide [127, 128] and treating osteoporosis using human parathyroid hormone (hPTH 1-34) [129].

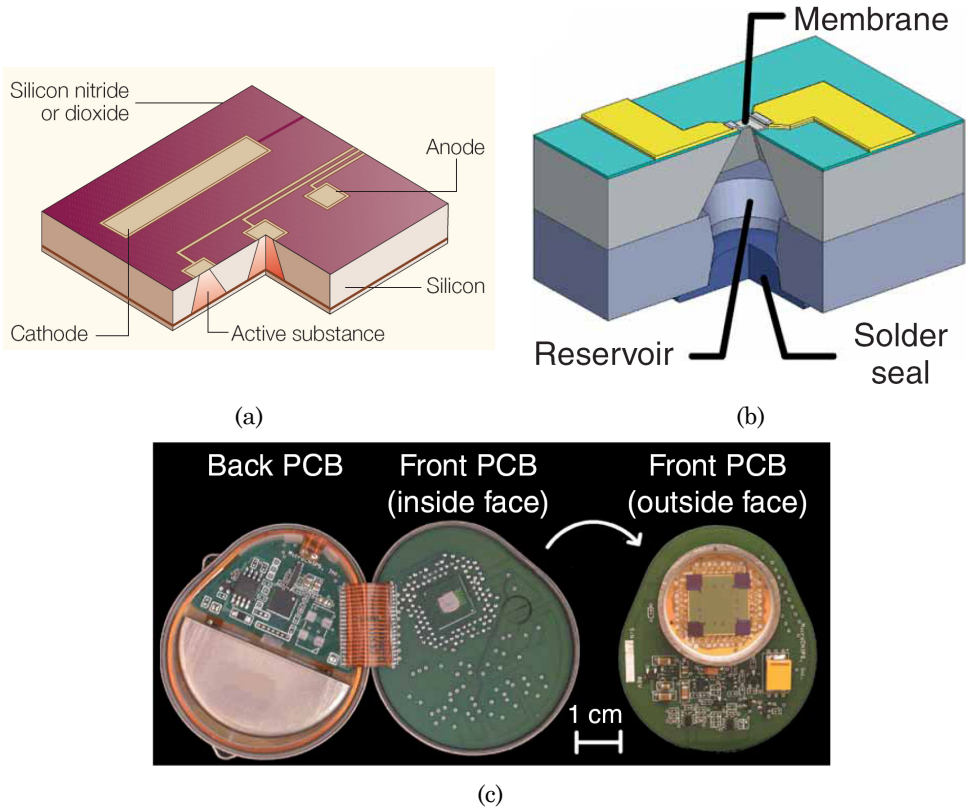

Figure 2.10: Implantable microchip for controlled release of drug by Langer's group and MicroCHIP Inc. (a) The conceptual illustration of the first prototype device (reprinted from [125]) and (b) the improved device. (c) Photographic images of the device complete with electronics components and packaging ((b) and (c) reprinted from [128]).

[13] MicroCHIPS, Inc. (spinoff from Massachusetts Institute of Technology), Bedford, MA, USA. http://www.mchips.com (*last accessed Jul. 2009*).

In addition, by using a similar concept of "reservoir trapping" of drugs, Langer's group developed a biodegradable, polymer-based, multi-dose delivery microreservoir microchip [130]. Instead of using active control, the polymeric microchip relies on a passive release mechanism without the need for external sources and triggers. The 1.2 cm diameter, 480 μm to 560 μm thick prototype used in the study was fabricated from poly(L-lactic acid) using compression moulding technology. The device was microinjected with ~ 150 μm thick, biodegradable poly(D,L-lactic-co-glycolic acid) membranes of different molecular masses covering the 36 reservoirs to control the release of various chemicals (radiolabelled dextran, human growth hormone or heparin) *in vivo*. The passive release relies on the pure diffusion of the drugs and can be tailored to a preset rate by careful design and selection of various parameters including the size and polymer composition, the number and volume of the reservoirs, and the thickness and composition of the membrane.

By using surface and bulk silicon micromachining processes, Ferrari[14] and co-workers developed silicon nanoporous [131] and nanochannel [132] microchips for sustained drug delivery. These microchips are based on a single dose, passive release concept to the delivery of liquid drugs following a zero-order kinetic. The nanoporous microchip implant, NanoGATE consists mainly of a nanopore membrane, as depicted in Figure 2.11 (a) and (b), which was fabricated using a series of key process step to create sacrificial SiO_2 layer sandwiched between silicon and polysilicon [131]. Upon removal of the sacrificial SiO_2 layer, nanopores could be realised with a pore width essentially defined by the thickness of the sacrificial SiO_2 layer. *In vitro* diffusion kinetics of model antitumor agent human recombinant interferon *α–2b* (rhIFN- *α*) and fluorescein isothiocyanate (FITC)-labelled BSA loaded into nanopore membranes with 20 nm and 13 nm pore width, respectively, demonstrated a non-Fickian[15] behaviour [131]. *In vivo* studies using the NanoGATE implant with 13 nm pore membrane loaded with radio-labelled BSA (^{125}I-BSA) demonstrated sustained

[14] Mauro Ferrari, Professor and Director of the Research Center for NanoMedicine at the Brown Foundation Institute of Molecular Medice, Chair of the Department of Biomedical Engineering, the University of Texas Health Science Center; Professor of Experimental Therapeutics, University of Texas M.D. Anderson Cancer Center; Professor of Bioengineering, Rice University; Professor of Biochemistry and Molecular Biology, University of Texas Medical Branch; and President of Alliance for NanoHealth, USA. http://nanomed.uth.tmc.edu/ (*last accessed Jul. 2009*).

[15] Fick's laws of diffusion relate diffusion to the concentration field and are typically used to solve for the diffusion coefficient.

release over a period of 45 days post insertion [131]. More recently, the group developed and fabricated a proof-of-concept nanochannel drug system (nDS) using fusion bonding of two silicon wafers, encapsulating nanochannels which were formed by similar SiO_2 sacrificial layer technique prior to the bonding [132]. rhIFN -α was released using these passive release microchips (nDS1, 100 nm channel size) and the *in vitro* result demonstrated the bioactivity of IFN-α on both host immune cells and a human melanoma cell line [133]. Future nDS microchips are envisaged to be integrated with on-board electronics to allow pre-programmed (electro-osmotically driven, nDS2) and remote-activated (nDS3) drug delivery.

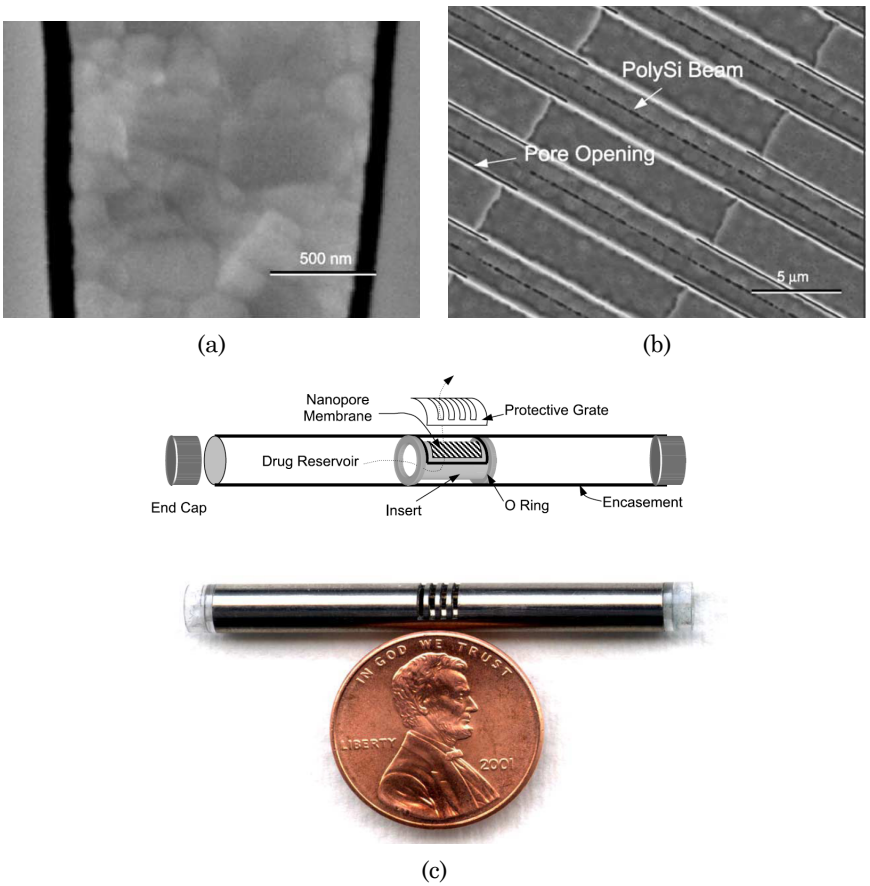

Figure 2.11: Implantable NanoGATE microchips developed by Ferrari's group. (a) Cross-sectional view SEM micrograph of the membrane with 50 nm pores separated by silicon and polysilicon; (b) Plane-view SEM micrograph of the membrane showing 45 µm long pores separated by 10 µm long anchors; and (c) Implant device fitted with nanopore membrane. Top: Conceptual drawing of the device. Bottom: Photograph of the actual prototype in relation to a US 1 cent coin (all images reprinted from [131]).

Implantable microchips drug delivery technology is still in an early development stage. The major challenges faced by these technologies are the safety and reliability, and biofouling and biocompatibility. There is also a need for an

effective fail safe mechanism that can protect the patient when the device fails, which potentially could lead to fatality as the stored drugs could be dose-dumped into the body. The delivery mechanism needs to be reliable and reproducible in maintaining its drug delivery performance over the therapeutic period, or at least a reasonable period of time to justify the need for surgery to place or remove the implant. The implantable microchips need to be biologically, chemically and physically stable. Hence, the materials used to fabricate the implantable microchips need to have the same requirements and be compatible with the drugs and surrounding biological environment so that the microchips are non-inflammatory, non-antigenic and non-carcinogenic. Ideally, an implantable drug delivery microchip should also be easy to use by both the patient and the health professional, flexible and programmable in setting up the dosing requirement, implantable under local anaesthesia, small and light, efficient in consuming power and ultimately have some sort of feedback or monitoring mechanism for a responsive drug delivery system. Once these challenges have been satisfactorily addressed, the true potential of the implantable microchips will be realised.

2.2.4 Summary

Novel approaches in drug delivery, which benefitted from the advancement in microfabrication technology, were discussed with a focus on three major areas: micromachined particles for oral drug delivery, microneedles for transdermal drug delivery and implantable microchips for localised delivery.

Micromachined particles, which are often designed to be flat and disc-shaped, as depicted in Figure 2.2, can be fabricated with precise control over size, shape, aspect ratio and surface features. This way, optimum flow within the GI tract and maximum contact area with the intestinal walls could be potentially achieved. Polymers [63, 64], SiO_2 [65] and PSi [68-70] microparticles have been demonstrated to deliver therapeutic agents and model drugs, albeit mostly *in vitro*. These micromachined particles, which mostly rely on passive release, are more appropriate for applications where sustainable, localised delivery is required.

The use of microneedles is a promising drug delivery technology, firstly because it resembles the hypodermic needles used in intravenous injection. They also

offer better permeability for a breadth of biopharmaceuticals, hence potentially providing greater bioavailability compared to other transdermal delivery approaches. Out-of-plane microneedles, including solid [90] (see Figure 2.5), hollow [94] (see Figure 2.6 (a)) and porous-tip [107] silicon microneedles, require relatively straight-forward fabrication processes; while polymer-based biodegradable microneedles, mainly developed by Prausnitz and co-workers [83, 101-105], potentially reduce the risk of infection caused by broken silicon or stainless steel microneedles. Thus far, the drug delivery devices utilising microneedles, such as the MicronJet needle [97] or the Macroflux® transdermal patch [100], are already in clinical trials. In order to fully realise the potential of self-administration using microneedles for transdermal drug delivery, the safety and ease of use, of these microneedles-based devices, need to be improved.

Microfabricated implantable microchip devices could eventually incorporate all the benefits of microsystem technology. With the integration of microelectronics and biosensing systems, implantable microdevices are capable of providing personalised and ultimately responsive controlled release of therapeutic agents. Release mechanisms, with both active control [116, 125] and passive release [121, 122, 130-132], have been demonstrated using microfabricated microchips. However, at the same time, these microchips are the most challenging in terms of design and implementation. A microfluidic-based implantable microchip which uses a micropump, such as one depicted in Figure 2.8, for instance, requires an external source to drive the micropump. In addition to the needs for biocompatibility and reduction of biofouling, the micropump poses safety and reliability issues, as the moving parts could potentially fail and hence, unintended, adverse release of drugs (dose-dumping) could occur. In contrast, the microdevice developed by Langer's group (see Figure 2.10) is more interesting and promising. It does not require any moving parts and the concept of reservoir trapping of drugs and electrical dissolution of the capping membrane, is an attractive approach. The sealable reservoir with the capping membrane used in the study [125], however, is potential for dose-dumping upon failure; accidental removal of the sealing or the capping membrane could adversely release the drug. Perhaps, using a porous media, such as porous silicon as the drug reservoir could better entrap the therapeutic agent without the need for an external valving mechanism. This proposition is, thus, explored extensively and served as the basis of this study.

2.3 Porous Silicon as an Emerging Material in Drug Delivery Technology

Porous silicon (PSi) has been well-known for its unique luminescent properties since the demonstration of its visible photoluminescence at room temperature almost simultaneously by Canham[16] [134] and by Lehman and Gösele [135]. Since then, there have been growing efforts in understanding the various aspects of PSi, including its fabrication methods, characterisations and applications, as shown by the increased amount of literature on PSi [136, 137]. In 1995, Canham also demonstrated the bioactivity and biocompatibility of PSi [60], and thus initiated various studies to develop PSi for biomedical applications [61, 136]. In the field of drug delivery, PSi has been mainly used as a vehicle or a carrier for the therapeutic agents [54, 55]. The following review first examines the properties of PSi, in particular its micro-structural, photoluminescence and biochemical properties. The applications of PSi in the field of drug delivery are then investigated. Lastly, the approaches used to fabricate PSi are briefly examined.

2.3.1 Properties of Porous Silicon

Porous silicon has various properties that make it uniquely attractive for many applications, in particular its large surface area to volume ratio for the application in biochemical sensing [138, 139]; its photoluminescence properties for optical [140-142] and optoelectronics applications [143, 144]; and its bioactivity and biocompatibility for implantable biomedical applications [61, 136]. Here, some of the interesting properties, along with some recent findings are summarised.

2.3.1.1 Micro-structural Properties

The unique physical and structural properties of PSi have been the subject of interest since the postulation of the quantum size confinement as the origin of visible light emission from PSi [145, 146]. The ability to determine and control these

[16] Leigh T. Canham, Professor & Chief Scientific Officer, Intrinsiq Materials Ltd. UK. http://www.intrinsiqmaterials.com/ (*last accessed Jul. 2009*).

physical properties, using established fabrication processes, has also attracted interest in the applications of biochemical sensing [138, 139] and biofiltration [61, 147].

Fundamentally, the microstructure of PSi can be characterised by the pore sizes and their distribution, the pore types and shapes, the porosity and surface area, although other aspects such as the skeleton size, pore morphology, pore spacing, and many more parameters have also been extensively examined [137, 148]. Many of these parameters are not always easy to obtain, and thus far various techniques – electron microscopy [149-152], gas adsorption-desorption analysis [153-155], X-ray investigations [156-158] and many more [159-162], have been used to investigate certain aspects of the microstructure characteristics of PSi.

In classifying the microstructure of PSi, guidelines by the International Union of Pure and Applied Chemistry (IUPAC) on the characterisation of porous solids have been generally adopted [163, 164]. The IUPAC defines a 'pore' as a cavity, channel or interstice with depth exceeding its width [163]. The pore size is hence generally accepted as the width or "the distance between two opposite walls" of the pore [163]. The ranges of pore size exhibiting characteristic adsorption properties defined by IUPAC [164] are summarised in Table 2.1 and this is widely used to classify PSi. Most of the PSi structures studied thus far are in the micro- to mesopore regime, although recently there has been an increased interest in the macroporous silicon structure. In practice, the mesopore sized PSi structures are readily obtained by typical electrochemical (anodisation) or chemical (stain) etching of silicon; while microporous silicon is mostly associated to anodisation using highly concentrated hydrofluoric acid (HF). Macroporous silicon, on the other hand, is conventionally fabricated by anodisation of silicon with predefined starting pits [165, 166]. The macropores formed this way are ordered with a typically cylindrical shape, but the pore sizes are limited to the range of 0.2 μm to 20 μm due to limitations in the fabrication and formation mechanism [165, 167]. On the other hand, the term "nanoporous silicon" has also been used in the literature to loosely describe PSi with a pore width in the nanometer regime (<1 μm) [168, 169].

Classification	Pore Width (nm)
Micropore	≤ 2
Mesopore	2 – 50
Macropore	≥ 50

Table 2.1: IUPAC classification of pore size.

The pore size alone does not always provide a complete understanding of the morphology of a porous structure. To better understand the microstructure of the PSi, the geometrical shape and the size distribution of the pore should also be investigated [170]. However, it is not always possible to distinguish the types and shapes of pores as typical anodisation or stain etching of silicon tends to produce irregular and poorly-defined pores. This is especially the case for microporous silicon. In principle, however, there are several types and shapes of pore that can be formed. Most meso- and macroporous silicon structures (or layers) consist of pores that are closed at one end (blind) and interconnected or branched to some degree, as depicted in Figure 2.12. Through pores, which are open at both ends, are often associated to free-standing PSi membrane and are useful in biofilteration application. Closed or isolated pores are less typical but could be realised via a capping process which minimises the ageing of the PSi [171].

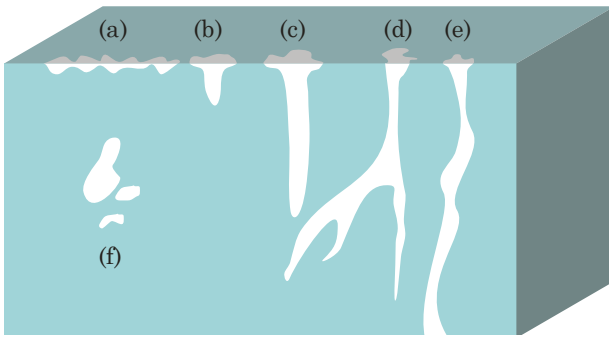

Figure 2.12: Conceptual illustration of (a) a rough surface and the types of pores: (b) and (c) blind or dead-end, (d) interconnected or branched, (e) through pore and (f) closed or isolated pores (adapted from [170]).

The most common pore shape observed in electrochemically formed PSi is cylindrical with varying degrees of branching. Mesoporous silicon also exhibits gradual decrease in pore size with depth, resulting in a funnel-like shape; while some macroporous silicon structures have been demonstrated to exhibit a thin surface porous film of smaller pore size [172], resulting in ink-bottle shape morphology. Crystallography of the wafers can also affect the pore shape – <100>-

oriented silicon wafers have been demonstrated to produce square cross-sectional pores; whereas <111>-oriented wafers exhibit triangular shaped pores [173].

The pore size distribution (PSD) has also been used as one of the more quantitative parameters to characterise a PSi structure. The PSD of PSi with meso- to macropore size regimes can be determined by using high resolution transmission (TEM) and scanning electron microscopy (SEM). These techniques provide direct observation of pore morphology and microstructural characteristics [149-152]. However, as the observed area using these techniques is limited, only the pore sizes within the field of view can be determined, hence may not entirely represent the PSD of the PSi structure. A more common method, especially in determining the size distribution of mesopores, is by analysing the adsorption isotherms of gases at low temperature [153-155]. Combined with spectroscopic ellipsometry [161], a non-destructive measurement of PSD could be obtained.

The porosity of PSi has been reported to range from 4 %, observed in macroporous layers, to above 95 %, observed in mesoporous materials [170]. Porosity can be measured by gravimetric and optical techniques [174], and the potential applications associated with different porosity ranges are depicted in Table 2.2. The specific surface area or the area of solid surface per unit mass of PSi, on the other hand, is generally inversely proportional to the porosity of the PSi layer [175].

Void Content (%)	Porosity	Potential Applications
0 – 30	Low	Microcapacitors, wafer bonding, tissue binding
30 – 70	Medium	Micromachining, sensors, silicon-on-insulator
70 – 100	High	Light emitting diode, anti-reflective coating, non-linear optics

Table 2.2: Classification of porosity and its associated potential applications (reprinted from [170]).

2.3.1.2 Luminescence Properties

By far, the most studied property of PSi is its luminescent behaviour [137, 176, 177]. The great interest was primarily a result of poor luminescence of bulk silicon due to its indirect bandgap. PSi, on the other hand, emits visible light at room temperature, hence making it a potentially ideal material for integration into optoelectronics. Photoluminescence (PL) [134, 145, 158, 176, 178-189], cathodoluminescence (CL) [190, 191], electrolumiscence (EL) [192-197] and chemiluminescence [171, 198] of PSi

have been extensively studied and the existence of these luminescences in different spectral regions is summarised in Table 2.3.

Spectral Range	Peak Wavelength (nm)	Luminescence Band Label	PL	CL	EL
UV	~ 350	*UV*-band	Yes	Yes	No
Blue – green	~ 470	*F*-band	Yes	Yes	No
Blue – red	400 – 600	*S*-band	Yes	Yes	Yes
Near IR	1100 – 1500	*IR*-band	Yes	No	No

Table 2.3: Porous silicon luminescence band (reprinted from [137]).

Canham showed that the layers of freshly anodised silicon with high porosity exhibits a highly efficient PL in the visible range (the *S*-band) [134]. The first of such spectra published are depicted in Figure 2.13 (a), which shows a typical trend of PL in PSi, as a function of anodisation time. As the single layer PSi is continuously anodised from 1 hour to 6 hours, the porosity increases from 70 % to 80 % with a colour change of surface appearance, from dark golden brown through gold to yellow. The resultant yellow layer glows bright red at room temperature when illuminated by a 514.5 nm Ar laser. The corresponding PL is shifted from the near infrared (IR) to the visible region with a significant increase in the intensity. A similar blue shift was later observed on aged PSi samples [137], as depicted in Figure 2.13 (b).

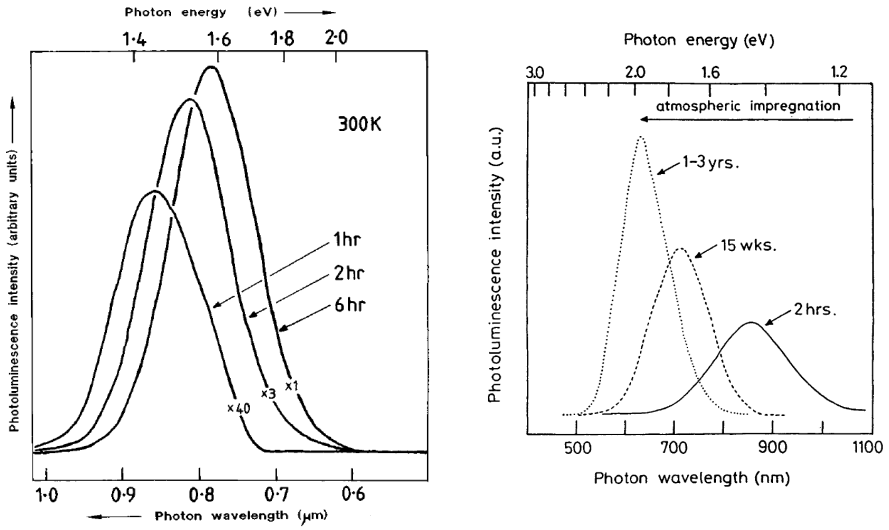

(a) (b)

Figure 2.13: Room temperature PL spectra observed by Canham (a) when freshly anodised silicon was probed with a 200 mW unfocused 514.5 nm Ar laser in air and amplified by the relative gains indicated. The p-type silicon was anodised in 40 % aqueous HF for the times indicated (reprinted from [134]); and (b) when a 11.6 μm thick PSi layer with 77 % porosity was excited at 325 nm, following extended air exposure for the indicated times (reprinted from [199]).

Many models have been proposed to explain the origin of PL in the PSi [137], as depicted in Figure 2.14, but the two models that have been broadly accepted are the quantum confinement effect in crystalline silicon and the highly localised defects states. Recently, Godefroo *et al*. proposed that both the quantum confinement effect and the localised defects states actually involved in certain aspect of PL [200]. By using high magnetic fields, they postulated that localised defects are the dominant source of light in nanocrystalline silicon. By passivation with hydrogen to remove these defects, the PL then originates from quantum-confinement states; subsequent UV illumination, however, reintroduced the defects making them the origin of the light again.

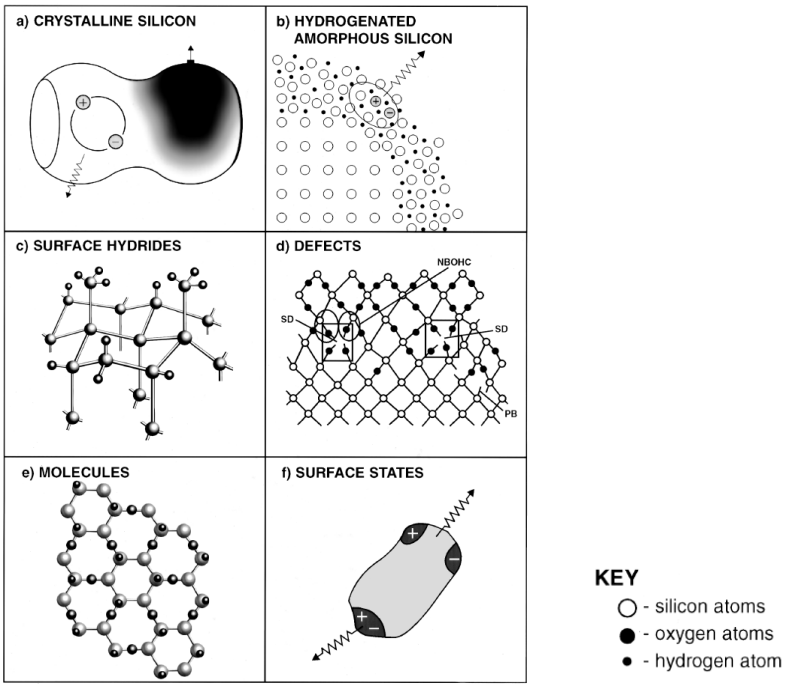

Figure 2.14: The six groups of models proposed to explain the PL from PSi. Detailed discussion of these models can be found in [137].

Porous silicon that is optically uniform has been demonstrated to exhibit a Fabry-Pérot thin film interference effect when illuminated by visible light [201]. In a PSi film, the Fabry-Pérot interference fringes observed in a reflectivity spectrum correspond to the constructive and destructive interference from light reflected at the air / PSi layer and PSi / bulk silicon interfaces. By taking the Fourier transform of the reflectivity spectrum, the optical thickness (OT), which is the product of the effective refractive index and the thickness of the film [201] can be extracted. When the refractive index of the PSi changes, for instance due to introduction of a molecule

by absorption, a red spectral shift in these fringes occurs [55], as depicted in Figure 2.15. Conversely, a blue shift in the spectrum can be observed when the process is reversed. Both the refractive index and the thickness of the PSi film, and thus the effective OT, can be reliably controlled by electrochemical etching process, hence making this method useful for *in-situ* biosensing [141, 202, 203] and drug loading and release monitoring [55, 204].

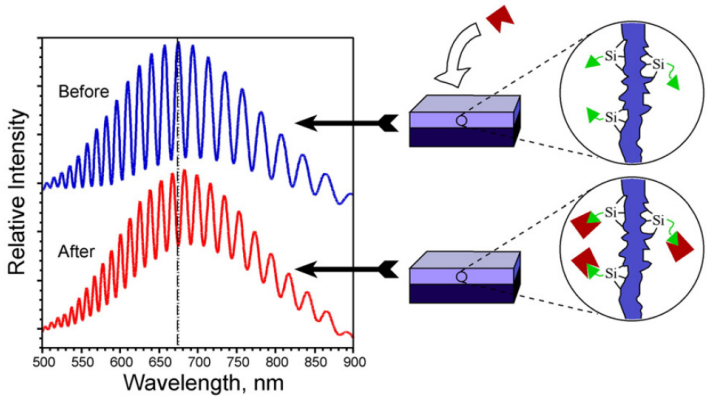

Figure 2.15: Schematic illustration demonstrating the red shift of the Fabry-Pérot interference fringes in a reflectivity spectrum from a PSi layer upon introduction of a molecular species into the porous structure. The reverse process yields a blue shift in the spectrum instead (reprinted from [55]).

2.3.1.3 Porous Silicon as a Biomaterial

Biocompatibility, in simplistic terms, is the ability of a biomaterial to co-exist and interface with the human body without "eliciting any undesirable local or systemic effects in the recipient" [205]. The human body typically responds to contact with synthetic materials by depositing proteins at the surface of the materials [206]. This biofouling effect can cause infection and biological rejection of devices implanted in the human body. Some materials such as polycarbonate and stainless steel are tolerated by the human body and are described as bioinert. Bulk silicon is relatively bioinert but PSi could be made bioinert, bioactive or biodegradable depending on the porosity and pore morphology [60, 61, 207]. Mesoporous silicon with high porosity was observed to dissolve in all the simulated body fluids (SBF); while medium porosity meso- and microporous silicon was found to be bioactive and slowly biodegradable [61]. No calcification was observed on macroporous silicon or PSi with very low porosity, suggesting that these materials are quite bioinert. A recent study

confirms that macroporous silicon shows marginal bioactivity, but this can be improved by surface functionalisation techniques [208].

Porous silicon hydrolyses under physiological environment and degrades into the human body as silicic acid (specifically, orthosilicic acid ($Si(OH)_4$)) [55], a natural form of silicon that is readily absorbed by the human body [209]. This makes PSi based implantable devices or drug vehicles attractive as these devices could be potentially dissolved and excreted by the body, hence no further surgery is required to recover the devices. Canham and co-workers investigated the dissolution of PSi under simulated physiological conditions [62] and electrical enhancement [210]. Mesoporous silicon were anodised to achieve different porosity levels: medium (60 %), high (80 %) and very high (88 %) porosity. The content of aqueous silicon (Si) released due to dissolution of PSi was measured using inductively coupled plasma optical emission spectroscopy [62]. At pH 7, mesoporous silicon with high and very high porosity showed an exponential increase in the release of Si over time (implying high biodegradability); while the increase in dissolution of PSi was also observed at higher pH and higher temperature. In a separate study, a PSi sample of 40.2 % porosity was found to dissolve when placed near to the electrode biased at – 6 V in a electrolyte (pH 7.6) [210]. The enhanced dissolution was believed to be due to the modulation of pH near the electrode when an electrical current is flowing, hence increasing the pH when negatively biased, while decreasing the pH when positively biased [210].

2.3.2 PSi for Drug Delivery and Therapeutic Applications

Since the demonstration of bioactivity and biocompatibility of PSi by Canham in 1995 [60], PSi has been increasingly used as drug delivery vehicles [54, 55]. The surface of PSi can be suitably modified [211, 212] to favour adsorption of therapeutic agents [136] and micron-sized PSi particles, pieces or thin films have been used to carry nanosized payload including drugs, such as the anticancer agent doxorubicin [213], steroid dexamethasone [204], ibuprofen and other model drugs [70, 214], imaging contrast nanoparticles [71] and biomolecules such as proteins [215, 216], peptides [216] and enzymes [217].

One of the earlier demonstrations of the use of PSi microparticles in drug delivery was reported by Foraker *et al.* [69]. In the study, FITC-labelled insulin was loaded into PSi particles (between (150 x 150 x 25) μm and (240 x 240 x 25) μm; pore size distribution of 20 nm to 100 nm) by capillary action and dried using vacuum drying or freeze-drying. The transport of both liquid and particle-encapsulated insulin across a differentiated human intestinal Caco-2 cell monolayer was investigated. In the presence of permeation enhancer (sodium laurate, C12), a nearly 10-fold increase in the permeability of FITC-insulin was reported from PSi particles, as compared to insulin in liquid form. Maximum insulin transport of 20 % per hour was achieved by incorporation of 0.337 μg sodium laurate per PSi particle with loading coverage at 25 % across the Caco-2 cell monolayer.

Moreover, PSi particles can be surface-treated by thermal carbonization or thermal oxidation and have been demonstrated to provide suitable surfaces for the loading of model drugs such as antipyrine, ibuprofen, griseofulvin, ranitidine and furosemide [70]. The modified surface has not only provided stability to the PSi particles, but also affected the affinity of the chemical substances towards the particles, as evidenced by the varied loading efficiencies. More importantly, based on the release experiments, the loading of these drugs into mesoporous silicon particles have been demonstrated to improve the overall dissolution of poorly dissolving drugs and reduce the pH dependency of the dissolution.

Porous silicon has also been used as a carrier for controlled delivery of doxorubicin anticancer agent [213]. The fabricated PSi consists of a macroporous layer of several microns deep, capped with a layer of 200 nm thick microporous silicon, as depicted in Figure 2.16. This unique structure enables loading of water soluble doxorubicin via the capillary effect, while the dissolution of the top layer of microporous silicon in a simulated physiological environment demonstrated a continuous release of doxorubicin that reached a plateau in 5 hours. The cytotoxicity of the released doxorubicin has been evaluated towards human colon adenocarcinoma cell lines LoVo and HT29, and suggested an appreciable and time-dependent anti-proliferation that is in-line with the doxorubicin release profile. The biocompatibility of the unloaded PSi structure was also investigated and showed no significant anti-proliferative effects in both LoVo and HT29 cell lines after 7 days exposure.

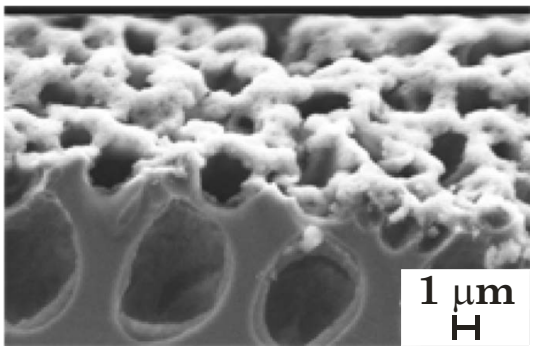

Figure 2.16: Cross-sectional SEM micrograph of the two-layer PSi structure produced by Vaccari *et al*. for controlled delivery of doxorubicin anticancer agent (reprinted from [213]).

Prestidge *et al*. demonstrated that a model protein, Papain (intermediate sized, ~ 23 000 Dalton hydrophilic protein) could be loaded into both anodised and stain etched PSi powders [215]. Freeze-drying has been used in the impregnation, solvent evaporation-based loading process, with pre-wetting of samples in methanol prior to loading process was carried out to improve the infiltration of Papain into the pores. They first observed a burst release of 22 % to 37 % and 35 % to 45 % of Papain from the electrochemically etched and the stain-etched PSi powder, respectively [215], indicating that a higher percentage of Papain was surface bound to stain etched PSi. The release of Papain over time was observed to be linear from electrochemically etched PSi; whilst stain etched PSi exhibited a more pseudo first order (exponential) release kinetic. These observed characteristics of loading and release behaviour are indicative of differences in porous structure and surface chemistry derived from the methods used to fabricate PSi. They have subsequently demonstrated that size and hydrophobicity of biomolecules, coupled with loading methodology, are some of the factors that influence the loading efficiency [216]. Both Gramicidin A (a small, ~ 1800 Dalton, hydrophobic peptide) and the larger Papain could penetrate the PSi layer to distances of > 60 μm, but Papain did not load as efficiently into the pores and has the higher tendency to bind to the surface.

Since the observation of the Fabry-Pérot interference effect in luminescent PSi layers [201], Sailor[17] and his research group have been exploiting this unique optical property of PSi for biosensing [141, 202, 203] and drug delivery applications [55, 204]. In one of the studies [204], Sailor's group demonstrated that the optical

[17] Michael J. Sailor, Professor of Chemistry and Biochemistry and Bioengineering, University of California, San Diego, USA, http://chem-faculty.ucsd.edu/sailor/ (*last accessed Jul. 2009*).

thickness (OT) (see also §2.3.1 – Luminescent properties) changed over time, as depicted in Figure 2.17, when a Fabry-Pérot PSi film was undergoing a pore size expansion process in a volume ratio of 9:1 HF: dimethyl sulfoxide (DSMO) etching solution. In this process, the DMSO acts as the slow oxidant agent, while the HF helps to dissolve the newly formed oxide and hence enlarges the pore width. The release of the loaded steroid dexamethasone from the hydrosilylated, pore expanded PSi samples into phosphate-buffered saline solution was found to be ~ 20 times slower than the unmodified freshly etched samples, observed by simultaneous UV absorbance spectrophotometry and optical reflectance spectrometry. The OT was also observed to be linearly correlated to the concentration of the released dexamethasone. In a separate study, Sailor's group has infused iron oxide magnetic nanoparticles of 30 nm diameter into PSi pieces [217]. Based on similar optical reflectance spectrometry, they were able to determine the amount (in nanogram quantities) of enzyme horseradish peroxidase that was loaded into the "magnetised" PSi pieces. Single PSi pieces could then be transported through air or a hydrocarbon liquid using an external magnetic field and have shown no loss in enzymatic activity after the transport.

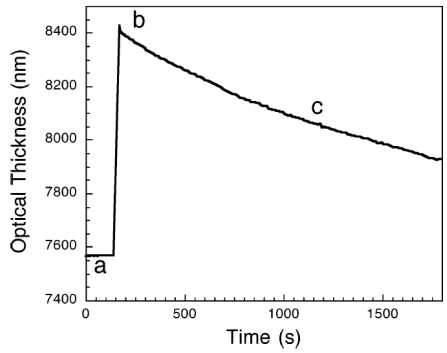

Figure 2.17: Change in optical thickness (OT) observed by Anglin *et al.* during the pore size expansion process of a PSi film. Point *a* represents the initial OT of the film in air (7570 nm). An increase in OT (to 8430 nm) at point *b* was observed upon the immersion of the PSi film into a HF: DMSO solution due to an increase in the effective refractive index of the film. As the HF gradually removed the formed oxide from the pores, a continuous decrease in OT was observed at point *c*. The porosity of the film was increased by ~ 10 % in this process (reprinted from [204]).

Using a similar concept, Koh *et al.* developed a free-standing distributed Bragg reflector PSi film (DBR PSi) for monitoring drug release within a smart patch intended for the application of transdermal drug delivery [218]. The as-prepared DBR PSi film exhibits a high reflectivity at 524 nm but when the film was covered by caffeine-impregnated PMMA layers a shift to 547 nm was observed, suggesting the

filling of the pores with the PMMA. Conversely, a blue shift was observed when the caffeine was released into a buffer solution. The DBR PSi / PMMA composite films are chemically stable and show no apparent degradation in their optical reflectivity after several days' exposure to aqueous HF or 3 M potassium hydroxide.

In other therapeutic applications, PSi has shown promising osteoconductivity for use as a cell interface for bone tissue engineering [219, 220]. In these studies, primary rat calvaria cells (osteoblasts) or the rat osteosarcoma cells (ROS 17/2.8 cell line) were seeded on the PSi substrates with various morphologies and sizes – straight macropores with pore width > 1 μm, branching mesopores with pore width ~ 50 nm and spongy micropores with pore width < 15 nm [219, 220]. It was observed that cells adhered to all three types of PSi, but only spread out well on a macroporous and micro-PSi substrate. In addition, the macro-PSi substrate demonstrated the highest viability after 4 hours of culture and this consistently

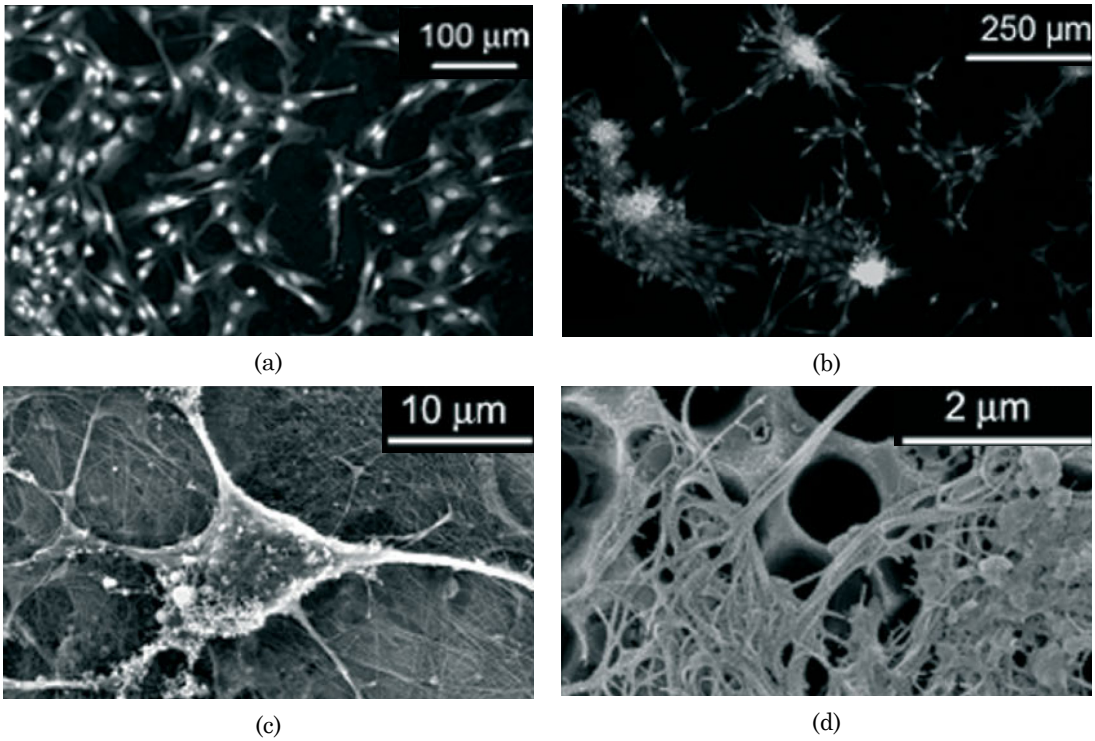

Figure 2.18: (a) – (b) Fluorescence microscope images showing the osteoblasts (stained by propidium iodide dye) on a macro-PSi surface (a) spread out after 18 hours of incubation; and (b) migrated, proliferated and clustered to form mineralizing nodules within 3 – 5 days of culture. (c) – (d) Plan view SEM micrographs showing the osteoblast and protein matrix on a macro-PSi substrate after one week of culture: (c) a mature osteoblast surrounded by fibrous mesh; and (d) fibrils with banding characteristics of type I collagen (reprinted from [219]).

increased after 5 and 7 days, as depicted in Figure 2.18. Moreover, macroporous silicon substrate demonstrated a higher level of transcription of three characteristic biomarkers of bone formation – alkaline phosphatase, osteocalcin and type I collagen. These results suggest that macroporous silicon is not toxic to osteoblasts and provides a favourable interface for osteoblasts growth and functionalisation.

In cancer treatment, PSi has been used as a brachytherapy device by pSivida Corp.[18]., a leading company in the biomedical applications of PSi. The Brachysil™ (32P-BioSilicon™), which comprises a combination of proprietary PSi particles and the isotope ^{32}Phosphorus, a proven anti-cancer therapeutic, has been demonstrated to be safe and well tolerated with a significant degree of antitumor efficacy during their Phase II clinical trials for inoperable primary liver cancer [221].

2.3.3 Fabrication of Porous Silicon

Porous silicon was first observed in the 1950s by the Uhlirs at Bell Laboratories, US during studies of electro-polishing of silicon and germanium in HF-based solutions [222]. They observed that silicon surfaces often developed a "matte black, brown or red deposit" during the process. Fuller and Ditzenberger then reported a similar "dark stain" surface appearance during chemical etching of silicon in a solution containing HF and nitric acid (HNO_3), without applying external bias [223]. Later, the anodised films first received a more detailed study by Turner [224]; while Archer further described the chemical stain etching of silicon [225]. However, it was not until a decade later, that Watanabe and co-workers described the porous nature of these anodised silicon surfaces, and hence evoked the term "porous silicon" [137, 226].

Since the demonstration of its visible PL at room temperature [134, 135], there have been significant efforts to improve the conventional anodisation and stain etching methods to produce PSi with various morphologies and physical characteristics [137, 148, 165, 227-229]; while at the same time, the development of novel fabrication approaches for specific applications have also emerged [230-238]. To date, however, anodisation or electrochemical etching of silicon remains the most

[18] pSivida Corp., Perth, Australia. http://www.psivida.com/ (*last accessed Jul. 2009*).

popular method used to produce PSi, simply because it has been well-studied and hence its reproducibility, even for processing of up to 200 mm wafers [168], has been greatly improved. In this process, silicon is etched by applying an external bias in a HF-based electrolyte, typically carried out in an etching cell made of highly acid-resistant polymer such as Teflon®. Aqueous or ethanoic HF electrolyte has been conventionally used, but organic solvent such as acetonitrile or dimethyl formamide (DMF) has also been mixed with HF, especially for the formation of meso- and macropores [165]. In general, there are three configurations of the etching cell: lateral or immersion cell, single-tank or o-ring cell and double-tank cell [227, 228]. The cathode is a mesh or rod made of HF-resistant and conducting material, typically platinum; while the silicon acts as the anode. Sometimes, a third reference electrode is also used. Any silicon surface in contact with the electrolyte will be made porous. Hence, a patterned layer of HF-resistant material, such as silicon nitride could be used to protect the areas not intended for anodisation.

The mechanism of pore formation during anodisation, including the pore initiation and pore propagation has long been scrutinised. Many factors have been proposed [239], but it has been generally accepted that quantum size effects are responsible for micropore formation [134, 135], while the formation of larger (meso- and macro-) pores is understood to be due to the electric field in the space charge region (known as the current burst model) [165, 229]. The dissolution chemistry itself has been generally agreed to follow the following reaction [227]:

$$\mathrm{Si} + 2 \cdot \mathrm{HF} + n \cdot h^{+} \rightarrow \mathrm{SiF_2} + 2 \cdot \mathrm{H^{+}} + \left(2 - n\right) \cdot e^{-} \tag{2.1}$$

$$\mathrm{SiF_2} + 2 \cdot \mathrm{HF} \rightarrow \mathrm{SiF_4} + \mathrm{H_2} \tag{2.2}$$

$$\mathrm{SiF_4} + 2 \cdot \mathrm{HF} \rightarrow \mathrm{H_2SiF_6} \tag{2.3}$$

where h^{+} and e^{-} are the exchanged hole and electron, respectively, and n is the number of charges exchanged during the elementary step. For n-type silicon, where holes are the minority carries, the hole injections are often assisted by illumination with white light to generate more electron / hole pairs [227]. The dissolution process itself is controlled by either monitoring the anodic current or potential. In general,

galvanostatic or constant current is preferred due to good reproducibility with a better control of both the porosity and thickness of PSi [227]. A typical current density – potential curve during the anodisation of silicon in aqueous HF electrolyte is depicted in Figure 2.19. Pores are typically formed during the initial rising current density where $0 < V < V_{ep}$ with V_{ep} denotes the potential at the smaller electro-polishing peak. The current density at this peak, J_{ep} is mostly dependent on the composition of the electrolyte [239]; beyond this, electro-polishing occurs and is characterised by the strong oxidation that forms an oxide layer on the surface. Electro-polishing is not observed when organic solvent is used in the electrolyte [165, 239].

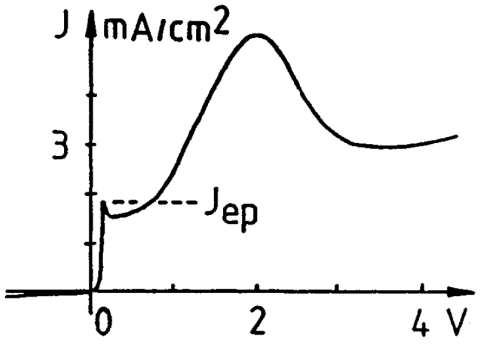

Figure 2.19: Typical current density – voltage curve during the anodisation of silicon (reprinted from [239]).

It is also well-studied that the current density, the electrolyte including the chemical composition, the concentration of HF, temperature and mechanical stirring; the resistivity, type and crystallographic orientation of wafer – determines many of the properties of PSi, in particular the pore size and distribution, the pore morphology, porosity, and photoluminescence [137, 177, 228, 240]. For instance, the pore density for PSi layers of different size regimes is influenced by the silicon substrate doping density, as depicted in Figure 2.20. The detailed parameters and assumptions used in this plot are discussed in [229]. Figure 2.21 and Figure 2.22 depict the examples of different pore morphologies as a function of anodisation current density, anodisation time and silicon doping density of n-type and p-type substrates, respectively.

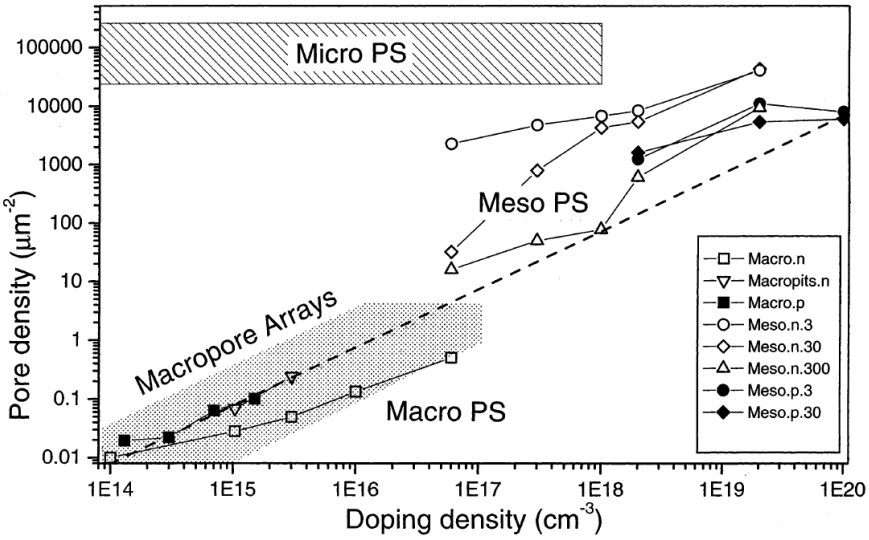

Figure 2.20: Pore density as a function of silicon doping density for PSi layers of different size regimes (reprinted from [229]).

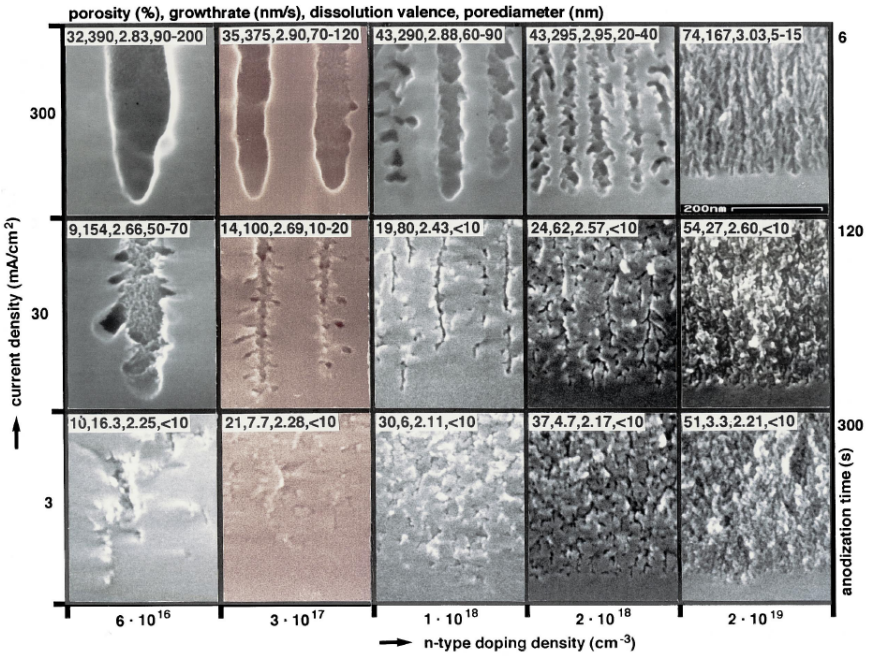

Figure 2.21: Cross-sectional view SEM micrographs showing the pore morphology at the interface between bulk and PSi for n-type <100> silicon substrate anodised galvanostatically in ethanoic HF electrolyte, as a function of current density, anodisation time and doping density (reprinted from [229]).

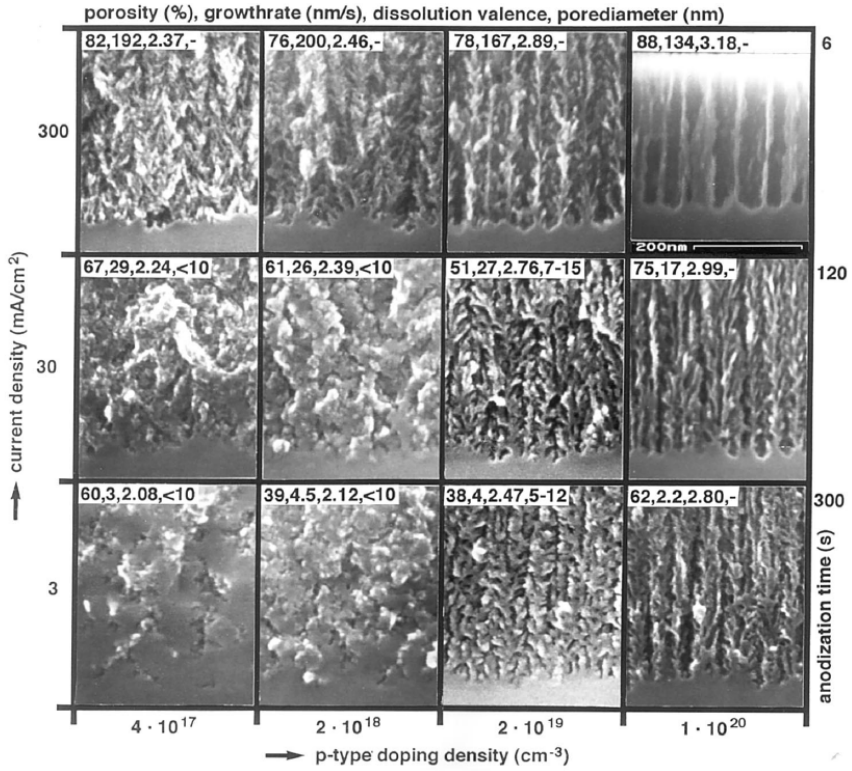

Figure 2.22: Cross-sectional view SEM micrographs showing the pore morphology at the interface between bulk and PSi for p-type <100> silicon substrate anodised galvanostatically in ethanoic HF electrolyte, as a function of current density, anodisation time and doping density (reprinted from [229]).

The chemical stain etch method is a simpler alternative to the anodisation process for the porosification of silicon [241]. Stain etching is based purely on chemical reaction and does not require complex experimental equipment to provide an external bias. The generation of holes is essential in the stain etching process, as it is in the anodisation process, and this is achieved by introducing strong oxidising agents [242, 243]. HNO_3 (sometimes with addition of sodium nitrate, $NaNO_2$) is most commonly used as the oxidant, although potassium permanganate ($KMnO_4$) and sodium chromate (Na_2CrO_4) [244] have been used as well. Non-uniform etching profiles are typical of stain etching due to bubble formation [180]. The possible thickness of PSi layer obtained by stain etching is often thinner than that produced by anodisation [245, 246]. These characteristics of stain etching may be the reasons behind a typically lower intensity in the photoluminescent emission observed in stain etched films [242, 244]. A more detailed review (see §3.2) and discussion on stain etching is presented in Chapter 3.

Other methods to fabricate PSi include variations of stain etching processes, such as introducing intense illumination during stain etching to generate more electron / hole pairs (known as photochemical [230] or laser-assisted [231] etching); using heat to induce stain etching process (known as hydrothermal etching) [232]; or using the vapour generated by stain etching of a metal or silicon (known as reaction-induced vapour-phase stain etching) [233]. Galvanic etching, which relies on internal current generated between silicon and a nearby noble metal immersed in HF-hydrogen peroxide (H_2O_2) based electrolyte, has also been used to produce PSi [234-237]. The internal current leads to a similar etching chemistry as in anodisation process, and thick (>10 μm) PSi layers could be formed this way. Relatively cylindrical macropores has also been produced when silver particles were used as the catalyst instead [238].

2.4 Conclusion

The use of microsystems technology, to develop novel approaches and microdevices for drug delivery by oral administration, transdermal delivery and implantation, were discussed. These novel techniques, which include micromachined polymer [63, 64] and silicon-based [65, 68-70] particles, biodegradable polymer-based [83, 101-105] and solid [90] and hollow [94, 96, 97] silicon out-of-plane microneedles and implantable microfluidic [116, 119, 121] and non-microfluidic [125, 130-132] based microchips, offer an alternative to the conventional drug delivery technologies. The aims are to improve the bioavailability of therapeutic agents, to provide a controlled (either sustainable or pulsatile) drug release and, ultimately, to realise a responsive drug delivery system for improved therapeutic care with better patient compliance.

Among the drug delivery microdevices studied, the implantable microchips offer the true potential of the benefit of microfabirication technologies. In particular, the non-fluidic based microchips [125, 130-132], which do not typically require moving parts (such as a micropump), offer a lower risk for dose-dumping upon device failure. The implantable microdevice depicted in Figure 2.10, developed by Langer and co-workers, is of particular interest. The concept, of trapping the drugs in individual reservoirs and later releasing the drugs in a controlled manner by

electrical dissolution of the capping membrane, is an attractive approach. However, the issue of dose-dumping remains; accidental removal of the capping membrane could still release the drug adversely.

A porous drug reservoir, with better entrapment and retention of the drugs, could offer a solution. Porous silicon (PSi) is an emerging material for drug delivery technology [54, 55], and is a good candidate to be used as the drug reservoir. PSi is biocompatible and can be made bioinert, bioactive or biodegradable depending on its microstructural properties (such as porosity and pore morphology) [60, 61, 207]. Various PSi structures, such as those depicted in Figure 2.21 and Figure 2.22, have been fabricated using electrochemical etching [137, 148, 165, 227-229] and other fabrication methods such as stain etching [241-243] and galvanic etching [234-237]. The porous structure is ideal for entrapping therapeutic agents and biodegradable PSi can be safely dissolved into the human body [62], thus introducing the therapeutic agents. The surface of PSi can also be suitably modified to favour adsorption of therapeutic agents [136, 239].

Thus far, micron-sized PSi particles, pieces or thin films have been used as drug delivery vehicles [54, 55] to carry nanosized payload including drugs, such as anticancer agent doxorubicin [213], steroid dexamethasone [204], ibuprofen and other model drugs [70, 214], imaging contrast nanoparticles [71] and biomolecules such as protein [215, 216], peptide [216] and enzyme [217]. However, there have been limited attempts to integrate PSi into a MEMS device for electrically-induced release of the drug. Therefore, a drug delivery microdevice incorporating a PSi drug reservoir is proposed and an attempt to fabricate the PSi structure using the stain etching method is discussed in Chapter 3.

Chapter 3

The Fabrication of a Porous Polysilicon Device using Stain Etching

3.1 Introduction

Microfabricated drug delivery devices, in particular implantable microdevices with integrated electronics, have the potential to offer responsive and controlled delivery of therapeutic agents. So far, none of these systems has included both porous silicon (PSi) structures for drug storage and delivery, and electronics components for controlled drug delivery. PSi is biocompatible and its porous structure is ideal for entrapping the therapeutic agents into the pores by the capillary effect. Hence, a novel drug delivery system with an integrated PSi drug reservoir is proposed. Passive release by the dissolution of biodegradable PSi and the desorption or diffusion of drugs' molecules could be used to provide a form of sustainable drug release. Here, as a prototype device, electro-thermal actuation is proposed as a mechanism for the active control in the release of the therapeutic agents [247]. By applying a current across a pair of electrodes and using the resistive porous silicon structure, it is envisaged that the entrapped drug could be released by local Joule heating.

In this chapter, the design and fabrication of the prototype drug delivery device is described and discussed. A porous polysilicon (PPSi) structure is proposed

as the drug reservoir and its fabrication using the stain etching method is described. At present, limited information exists (in the literature) about the stain-etched PPSi structure, especially how the various conditions used for stain etching impact upon the different PPSi structures. In addition, stain-etched PPSi structures have not been evaluated for use as a drug reservoir. Hence, a series of investigations were performed to investigate the stain etching method's suitability to fabricate a possible drug delivery structure.

The study described here is focused towards applying established chemical stain etch conditions and the identification of the resultant morphology of the PPSi structure. The microstructural morphology and surface topography of the prepared samples have been characterised using scanning electron microscopy (SEM) and atomic force microscopy (AFM), respectively.

3.2 Porous Polysilicon by Stain Etching: An Overview

Stain etching is the primary alternative method to the conventional anodic porosification of silicon [241]. In contrast to the anodisation method, where an external bias to form porous silicon (PSi) is used, for stain etching an open-circuit chemical method is utilised with an oxidising agent, a fluoride source for oxide removal and a common diluent. Typical oxidising agents include nitric acid (HNO_3) and sodium nitrate ($NaNO_2$), while hydrofluoric acid (HF) is mainly used to dissolve the oxide formed. The common diluent is de-ionised (DI) water, although acetic acid (CH_3COOH) is sometimes an alternative [242]. The advantages of using the stain etching method include (i) straight-forward implementation, (ii) relatively inexpensive experimental setup for wafer scale processing and (iii) compatibility with main-stream silicon microelectronics fabrication processes. However, most stain-etched porous structures suffer from relatively poor reproducibility and uniformity [180]. The possible maximum thickness of PSi layer obtained by the stain etching process is often thinner than that produced by anodisation due to a 'self-limiting' effect [245, 246], which is a result of simultaneous etching of the top layer of porous film and the formation of the porous structure at the porous-crystalline

interface. These characteristics may be the reasons behind a typically lower intensity in the photoluminescent emission observed in stain-etched films [242, 244].

3.2.1 Principle of Stain Etching

Chemical etching of silicon is essentially an electrochemical process with localised cathode and anode sites [243], albeit in this case, the reaction is started chemically. The dissolution of silicon is believed to consumes holes (h^+) [239, 242, 243] and in a typical electrochemical etching of silicon, the generation of holes is supplied by an external bias, which is sometimes assisted by a strong illumination [227]. For the stain etching method, on the other hand, the key contributor to the injection of holes is the reduction of an oxidising agent at the cathode sites [242, 243]. In a typical stain etching system consisting of HNO_3 (as the oxidising agent) and HF (as the fluoride source), the overall chemical reaction can be written as follows [243]:

$$3\cdot \mathrm{Si} + 4\cdot \mathrm{HNO_3} + 18\cdot \mathrm{HF} \rightarrow 3\cdot \mathrm{H_2SiF_6} + 4\cdot \mathrm{NO} + 8\cdot \mathrm{H_2O} + 3(4-n)\cdot h^+ + 3(4-n)\cdot e^- \tag{3.1}$$

where h^+ and e^- are the exchanged holes and electrons, respectively; and n is the average number of holes required to dissociate one atom of silicon. In principle, this reaction can be analysed by the reactions occurring at both the cathode and anode sites separately.

The localised cathode and anode sites are typically formed randomly during the etching process. The local cathode sites are formed by reaction or attack by the HNO_3 at the surface of the crystalline silicon, especially at the defect sites, such as dislocation or grain boundaries [242]. The HNO_3 reduces to nitric oxide (NO) at these cathode sites via a complex, multi-step reaction and, in the process, holes required for the anodic dissolution of silicon are generated [243]. The typical reaction at these cathode sites can be written as follows:

$$\mathrm{HNO_3} + 3\cdot \mathrm{H^+} \rightarrow \mathrm{NO} + 2\cdot \mathrm{H_2O} + 3\cdot h^+ \tag{3.2}$$

If the injected holes react with silicon, the silicon atoms will be dissolved and thereby switch the original local cathode site into an anode site [242]. Depending on the composition of the etching solution, hence the rate of etching and the current multiplication factor, the average number of holes (n) required to dissociate one atom of silicon can range from 2 to 4 [243]. In general, a dissolution valence of 4 is assumed for HNO_3-rich solutions and hence no excess holes and electrons are produced [243], based on equation 3.1. However, for HF-rich solutions, silicon dissolution could be divalent [222, 225], hence producing excess electrons and holes. The dissolution of silicon is believed to be a two-step process. Firstly, silicon dioxide (SiO_2) is formed as a result of hole injections (equation 3.3). The SiO_2 then reacts with HF to form a water-soluble silicofluoride (H_2SiF_6) complex (equation 3.4). These reactions can be written as follows:

$$\mathrm{Si} + 2 \cdot \mathrm{H_2O} + n \cdot h^+ \rightarrow \mathrm{SiO_2} + 4 \cdot \mathrm{H^+} + \left(4 - n\right) \cdot e^- \tag{3.3}$$

$$\mathrm{SiO_2} + 6 \cdot \mathrm{HF} \rightarrow \mathrm{H_2SiF_6} + 2 \cdot \mathrm{H_2O} \tag{3.4}$$

The residual H^+ at the anode site (equation 3.3) might participate in further reaction with HNO_3 (equation 3.2) and hence repeat the reaction cycle. The constant switching of the reaction (from the cathodic to anodic reaction) thus results in polishing of the silicon by uniformly removing the surface of a silicon substrate [242].

In contrast, during the formation of PSi, the etching of silicon is non-uniform. In this case, the holes from the cathode reaction may not react with the silicon at the original site. Instead, the holes may recombine with the free electrons from the solution before they can react with silicon or may move to another site due to more favourable surroundings [242]. Therefore, the original site remains a cathode while a corresponding site, somewhere else, remains an anode (in order to keep the overall reaction neutral). Over time, this non-uniform, preferential etching produces a rough, porous surface [242]. The rate limiting factor in the stain etching process is believed to be the formation of HNO_2 during the complex reduction of HNO_3 [225, 242]. The reaction cannot occur until a trace of HNO_2 exists and this "wait" time is typically known as the incubation time, t_i.

3.2.2 Stain Etching of Silicon

Fuller and Ditzenberger first reported a "dark stain" surface appearance similar to that observed on anodised silicon, during a chemical etching of silicon in solution containing HF and HNO_3, without applying external bias [223]. Archer [225] and Turner [243] later described chemical stain etching of silicon in greater detail. By using cross-sectional transmission electron microscopy (TEM), Beale and co-workers confirmed that these stain-etched films were indeed porous silicon [248]. They also demonstrated, for the first time, that oxidising agents such as $NaNO_2$ and chromium trioxide (CrO_3) could be used in place of HNO_3.

The earliest studies on the room-temperature photoluminescence (PL) of stain-etched PSi were reported by Fathauer *et al.* [180] and Sarathy *et al.* [181]. In their investigation, Fathauer and co-workers used silicon substrates with various levels of resistivity, doping and crystal orientation and stain etching solutions consisting of $HF:HNO_3:H_2O$ with volume ratios of either 1:5:10 or 4:1:5 [180]. They observed that under white light, these stain-etched PSi films appeared to be coloured (from brown, blue to yellow) and these colours changed with increased etch time. Under ultraviolet irradiation, the samples emitted dull red to bright orange light. Although they have also used $NaNO_2$ in HF and CrO_3 in HF as the stain etching solution, they only observed PL in films stain-etched with $NaNO_2$ in HF.

Concomitantly, Sarathy and co-workers also demonstrated that silicon stain-etched for 5 minutes in a solution containing $HF:HNO_3:CH_3COOH:H_2O$ (with a volume ratio of 1:2:1:4) exhibited a PL spectrum when exposed to a 488 nm laser [181]. They also observed a degradation in the PL intensity as the exposure time was increased. In a separate study, when compared to an anodised PSi sample, they observed an order of magnitude smaller PL intensity with a slight blue shift from PSi stain-etched in 1:3:5 $HF:HNO_3:H_2O$ for 120 s [242]. The stain-etched porous films were also limited in thickness due to the mechanism of chemical etching. The incubation time, t_i, was found to be strongly dependent on the content of HNO_3 in the etching solution.

Steckl and his group later associated the t_i of stain etching to the resistivity, ρ of the substrate [249]. They observed, for p-type boron-doped silicon substrates,

that the t_i increased significantly with greater silicon substrate resistivity; while for phosphorus-doped n-type silicon substrates, increased resistivity resulted in a shorter t_i. By exploiting this phenomenon, they selectively doped an n-type substrate with 30 kV Ga^+ using a focused ion beam (FIB) to achieve, for the first time, a selectively patterned photoluminescence with submicron resolution [249, 250].

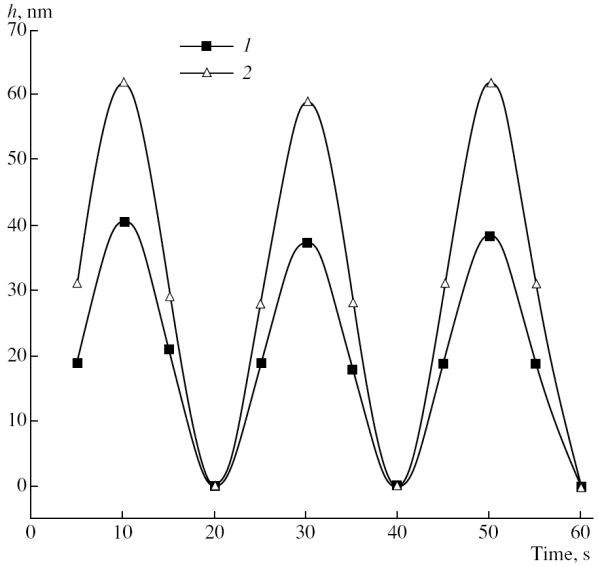

Figure 3.1: Plot of porous layer thickness, h against the etching time in 1:6:5 (*1*, ■) and 1:6:6 (*2*, △) volume ratio of HF:HNO_3:H_2O observed by Starostina *et al.*. The substrate used was <100>, 7.5 Ωcm p-type silicon (reprinted from [246]).

The primary recipe used for the stain etching process mostly consists of HF, HNO_3 and DI water with various volume fractions and composition ratios. Starostina *et al.* investigated the effect of changing these chemical compositions on the morphology of the resultant porous film [246]. In one scenario (type I), they used a higher proportion of HNO_3 than HF and evaluated 10 different volume ratios. The use of DI water was found to be critical in this system as no pores were observed without the addition of DI water. They also found that the thickness of the porous layer varies in an oscillatory fashion, as depicted in Figure 3.1, and the absolute thickness is determined by various factors such as etching time and substrate resistivity. In the other scenario (type II), a higher proportion of HF to HNO_3 is used, and they evaluated 5 different volume ratios. Contrary to the previous studies, they observed that without the addition of DI water, the porous layer formed and the thickness was in fact higher than that formed by type I system. They conclude that

for the type II system, there is a less critical transition between a porous etch and etch polishing and hence a more controllable stain etching is achieved.

Vázsonyi *et al.* also observed a similar limited thickness in stain-etched PSi film [245]. By using gravimetry and spectroscopic ellipsometry, they concluded that the thickness was 'self-limiting' due to simultaneous etching of the top layer of porous film and the formation of the porous structure at the porous-crystalline interface. The stain etching solutions with volume ratios of between 50:1 and 500:1 of HF:HNO_3, were used.

On the other hand, Kelly *et al.* used different stain etching compositions and reported a more reproducible PL (admittedly with a quantum yield ~ ¼ of that observed with anodised porous silicon) [244]. The stain etching systems investigated include those using solutions with various oxidising agents such as nitrosonium tetrafluoroborate ($NOBF_4$), $NaNO_2$, potassium permanganate ($KMnO_4$) and sodium chromate (Na_2CrO_4), with sulphuric acid (H_2SO_4), perchloric acid ($HClO_4$) and DI water as diluents. They proposed that, instead of HNO_2 [243], nitrosodium ions (NO^+) were the active oxidising agents in the reduction of HNO_3 to NO, due to a more positive redox potential of NO^+ which suggests that NO^+ is a better source of injectable holes [244].

Nahidi and Kolasinski later proposed that a large positive redox potential is not the sole deterministic factor in the reliable fabrication of porous silicon [251]. They demonstrated that bubble formation is more deleterious to film homogeneity and can be avoided by using transition metal-containing oxidants such as ferric chloride ($FeCl_3$) and sodium permanganate ($NaMnO_4$). Less bubble formation and more intense PL were also observed when acidified ammonium hydrogen fluoride (NH_4HF_2) was used in place of HF. They also found that, by using an oxidant with a more positive redox potential, a blue shift of the PL occurred.

More recently, González-Díaz and co-workers investigated the effect of temperature on stain etching and reported that, at low temperature (< 10 °C), samples etched for 2 minutes exhibited an anisotropic structure preferentially oriented to Si <100> direction [252]. However, the PL intensity of these samples was relatively low, possibly due to the larger size of porous structure produced.

3.2.3 Porous Polysilicon

Polycrystalline silicon (polysilicon) is an important material both in microelectronics systems and MEMS and its properties have been extensively studied [253, 254]. Polysilicon is the polycrystalline form of silicon which is made up of small single-crystal domains called grains [255]. It can be deposited with various crystallinities and grain sizes using the chemical vapour deposition technology [255]. The as-deposited polysilicon has very high resistivity, but this can be altered by introducing dopants by diffusion or ion implant techniques [255, 256]. On the other hand, polysilicon has been demonstrated to be more chemically reactive than bulk single-crystalline silicon and, like microporous silicon, is bioactive [257]. Hence, it is reasonable to expect that the porous form of polysilicon is also a bioactive material. In fact, porous polysilicon (PPSi) has long been considered as a potential material in MEMS [258]. PPSi has shown significant potential for integration into optoelectronics devices [144], field emission displays [259], as permeable layers for MEMS device packaging [260] and as gas sensors [261, 262].

Despite the vast depository of literature on porous silicon (including stain-etched PSi) and anodised PPSi, the use of stain etching on polysilicon substrates is not widely reported. The earliest report on using stain etching to form a PPSi structure is probably by Jung and co-workers [263]. They demonstrated that epitaxially grown boron-doped amorphous silicon showed visible PL only after annealing at temperature ≥ 725 °C (hence, polycrystalline) and stain-etched in a solution with a ratio of 5:12:32 by volume of $HF:HNO_3:H_2O$. Steckl and his group later demonstrated similar results and showed that, by using a 1:3:5 volume ratio of $HF:HNO_3:H_2O$, phosphorus-doped and undoped polysilicon film on oxidised silicon or quartz could be made porous [182]. In this case, the polysilicon was deposited at 180 mTorr using low pressure chemical vapour deposition (LPCVD) from silane (SiH_4). By incorporating X-ray diffraction (XRD), scanning electron microscopy (SEM) and atomic force microscopy (AFM) studies [264], they observed that the pore sizes and surface morphologies of PPSi film, as depicted in Figure 3.2, varied with the crystallinity of the polysilicon films deposited at different temperatures. They further suggested that, to a certain degree, the presence of surface Si oxyhydrides could be the basis for the observed PL of PPSi films [265].

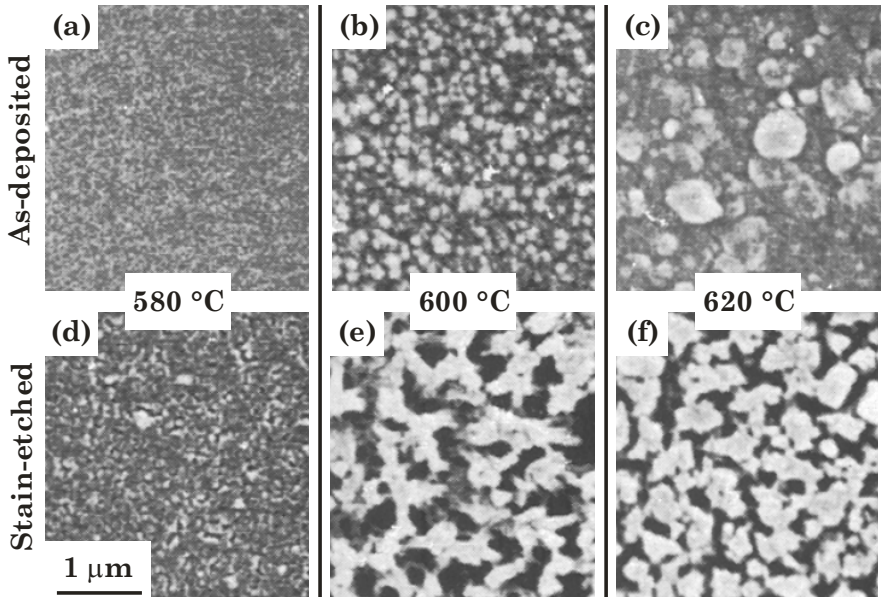

Figure 3.2: Plane-view SEM micrographs of the (a)-(c) as-deposited and (d)-(f) stain-etched polysilicon reported by Steckl *et al*.. The 1 μm thick polysilicon was deposited using LPCVD at various temperatures as indicated. The stain etching was carried out in 1:3:5 volume ratio of HF: HNO_3: H_2O for 2 minutes (reproduced from [264]).

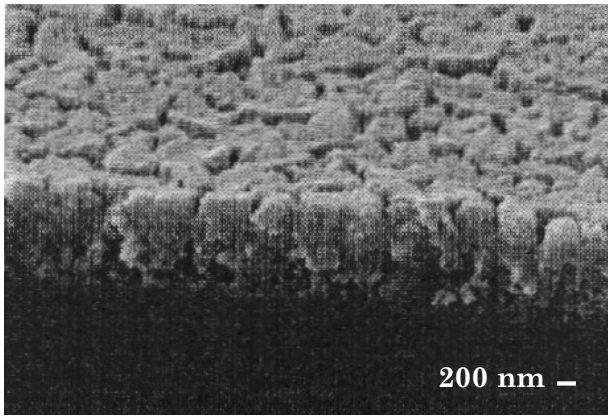

Figure 3.3: Oblique, cross-sectional view SEM micrograph of a PPSi first primed in 1:5:5 HF: HNO_3: H_2O followed by stain etching in 1:3:5 HF: HNO_3: H_2O (reproduced from [188]).

In a separate study, Huang and co-workers incorporated a pre-etching step, by a 1:5:5 volume ratio of HF:HNO_3:H_2O to reduce the incubation time [188]. The stain-etched film, as depicted in Figure 3.3, consists of large granules of size 800 nm to 1000 nm, with gaps or cracks between the granules. They ascribed the formation of these gaps to a faster etch rate due to higher defect densities at these regions. On the other hand, Higa and co-workers used 500:1 volume ratio of HF:HNO_3 to produce PPSi films that exhibit PL peaks ranged between 610 nm and 680 nm, depending on the annealing temperature of the polysilicon [266].

An alternative approach to form PPSi, using a self-aligned oxide mask, has been demonstrated by Han *et al.* [267]. A thicker oxide layer can naturally form, at the polycrystalline grain boundaries, during the thermal oxidation. When the oxide was etched using a short reactive ion etching (RIE), the thicker oxide at the grain boundaries remained and served as a mask. Subsequent RIE of the polysilicon formed the polysilicon islands.

The deposition of polysilicon using LPCVD, within a narrow process window, can spontaneously form pores of 10 nm to 50 nm in diameter [268]. Dougherty *et al.* demonstrated that polysilicon films deposited using LPCVD at 550 mTorr and ~ 600 °C are permeable, suggesting the formation of pores [268, 269]. Permeable polysilicon films were observed at a well-defined process window located at the transition between the tensile, low temperature film growth, and a compressive, high temperature growth regime.

3.2.4 Summary

The stain etching method to produce PSi and PPSi structures has the advantage of straight-forward implementation, relatively inexpensive experimental setups for wafer scale processing and compatibility with main-stream silicon microelectronics fabrication processes. However, it is generally accepted that most stain-etched porous structures suffer from relatively poor fabrication reproducibility and non-uniformity, possibly due to the uncontrolled differences in incubation time and the random sites of pore initiation and pore growth [225, 242, 249]. The possible thickness of PSi layers, obtained by stain etching methods, is usually thinner than that produced by anodisation due to the self-limiting process [245, 246] and this could explain the typically lower intensity in the photoluminescent emission observed in stain-etched films compared to anodised porous film [242, 244].

A summary of various different stain etching conditions, including the chemical composition and etch time, in producing PSi and PPSi, and the microstructural and photoluminescent properties of the resultant PSi and PPSi structures, is presented in Table 3.1. As summarised therein, the combination of HF, HNO_3 and DI water, with a typical volume ratio of 1:3:5, is the most widely used chemical system for the stain etching process [182, 188, 242]. The resultant PSi and

First Author (Year, Reference)	Substrate Material	Stain Etching Conditions	Characterisations	
			Microstructural	PL
Fathauer (1992, [180])	p-type and n-type with various resistivity in both <100> and <111> Si	1:5:10 or 4:1:5 HF:HNO_3:H_2O; $NaNO_2$:HF; CrO_3:HF; typical 30 s to 10 min	(SEM, TEM, XPS) Non-planar, "web-like" surface; ~ 0.5 μm thick; amorphous near surface	Peaks in 700 nm range
Sarathy (1992, [181])	Si substrates (type and resistivity not reported)	1:2:1:4 HF:HNO_3:CH_3COOH:H_2O; 5 min	(AFM) 40 nm to 60 nm feature size; (0.8 – 1.0) μm thick	Peaks centred at ~ 650 nm
Shih (1992, [242])	p-type ((0.02 – 24) Ωcm) and n-type ((0.1 – 10) Ωcm) Si	1:3:5 HF:HNO_3:H_2O, 120 s	(SEM) p-type: Rough and pitted (thousands of Å); n-type: irregular cracks; (100 – 1000) nm thick	Peaks around 630 nm
Jung (1992, [263])	p-type annealed and un-annealed amorphous Si on Si	5:12:32 HF:HNO_3:H_2O	(TEM, TED) Amorphous-like, no evidence of micro-crystallite	Peaks centred at ~ 640 nm to 680 nm
Steckl (1993, [182])	n-type, 400 nm thick, polysilicon on oxidised Si, ~20 Ω/sq	1:3:5 HF:HNO_3:H_2O, 30 to 120 s	(SEM) Grainy; doped: ~ (0.2 – 0.4) μm; undoped: ~ (0.1 – 0.2) μm; (AFM) surface roughness 18.0 nm,	Peaks centred at 640 nm to 645 nm
Higa (1994, [266])	Evaporated boron-doped polysilicon, 1 μm thick	500:1 HF:HNO_3, 1 min	(FEGSEM, TEM) ~ 5 nm nano-crystallites; (500 – 700) nm thick,	Peaks centred at 610 nm to 680 nm
Huang (1997, [188])	p-type, 1 μm thick polysilicon on Si; 10^{15} cm^{-3} doping	1:3:5 HF:HNO_3:H_2O with pre-etching in 1:5:5 volume ratio	(SEM, TEM, XRD) Large granules (800 – 1000) nm with gaps in between; amorphous-like; faster etching at <111>	Peaks at 720 nm
Starostina (2002, [246])	p-type ((0.01, 7.5, 12 and 1000) Ωcm), <100> and high resistivity <111> doped to n^+-type (0.003 Ωcm) Si	Type I (1:20:0, 1:15:0, 1:6:2, 1:6:3, 1:6:5, 1:6:6, 1.2:6:15, 1.3:6:15, 1.3:6:25, 1:7:20) and Type II (1500:1:0, 1200:1:0, 900:1:0, 250:1:0 and 4:1:5) HF:HNO_3:H_2O	(TEM, profilometer, SIMS) Oscillating thicknesses; Type 1: 20 nm to 250 nm; Type 2: 150 nm to 630 nm	Not reported

Table 3.1: Summary of selected stain-etching conditions used in the formation of porous silicon (PSi) and porous polysilicon (PPSi) discussed in §3.2. The microstructural characteristic and photoluminescent (PL) property of the resultant PSi and PPSi are included for comparison.

PPSi structure after stain etching in 1:3:5 volume ratio of HF:HNO_3:H_2O were reported to be either rough and pitted [242] or grainy [182] and granular-like with cracks [188], with typical PL peaks centred at 630 nm to 720 nm. This system is used as the starting point for the investigation here and the development of a stain etching process to form a PPSi structure within the prototype drug delivery device.

3.3 Design of a Porous Polysilicon Drug Delivery Device

The implantable drug delivery microdevices, reported so far, are equipped with one or more micromachined physical containers as drug reservoirs, which are usually capped with biocompatible membranes [125, 130]. A major concern of such a design is the potential for dose-dumping upon device failure, especially the accidental rupture of the membrane. To address this concern, it is proposed that a porous structure, such PSi, is instead used as the drug reservoir. PSi is biocompatible and can be made bioinert, bioactive or biodegradable by manipulating its microstructural properties, such as porosity and pore morphology [60, 61]. The porous structure is ideal for entrapping therapeutic agents by the capillary effect. The biodegradable PSi can be readily and safely dissolved into the human body [62], bringing along the therapeutic agents; while bioinert PSi can rely on the desorption or diffusion of drugs into the human body. These forms of passive release offer a uniform sustainable drug delivery.

Here, a prototype drug delivery device based upon the concept of integrating a porous structure as a drug reservoir is proposed. The initial design of the prototype device, as depicted in Figure 3.4, and the fabrication process (discussed in §3.3.2) have been conceptualised by C. Kaminski as an exchange student project [247]. In the design, electro-thermal actuation is envisaged as a mechanism for active control in the release of the therapeutic agents; a pair of electrodes is to be integrated into a porous drug reservoir. The nanopores are envisaged to be filled with liquid soluble therapeutic agents, which are introduced and incorporated by the capillary effect. By applying a current across the resistive porous drug reservoir, via the pair of electrodes, the entrapped drug could be released by Joule heating. With an

integrated microelectronics system, a pulsatile release profile would be possible using a pre-programmed microcontroller or a telemetry circuitry, which is ideal for the therapeutic control of critical conditions. Alternatively, drugs could be released passively, either by desorption or diffusion, and this could be used where a more sustainable release profile is desired.

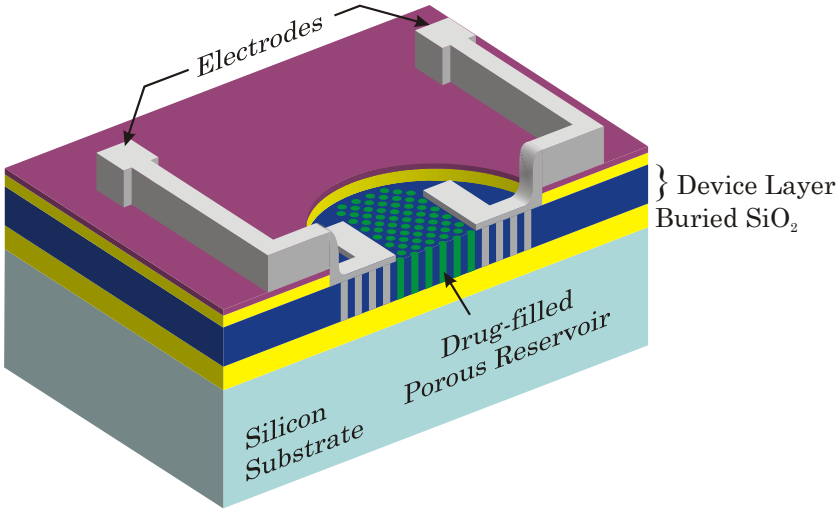

Figure 3.4: Oblique, cross-sectional view conceptual illustration of the envisaged prototype drug delivery device (not to scale; refer to Figure 3.5 for further fabrication details and colour scheme of materials used).

3.3.1 Design Considerations and Challenges

In order to realise a device, such as the one envisaged in Figure 3.4, a few design issues and requirements have to be considered. These design considerations are highlighted as follows:

(I) A good electrical isolation to the pair of electrodes is required to ensure that all the supplied current is used for heating the porous drug reservoir;

(II) A good thermal insulation is required so that the Joule heating generated is not unnecessarily dissipated to the external environment;

(III) A good contact between the pair of electrodes and the pores is essential to ensure efficient current conduction;

(IV) A porous structure with good electrical conductivity is essential to ensure current conduction between the pair of electrodes. A porous structure with suitable microstructural characteristics (pore size, porosity and thickness) is also desirable for ease of drug loading;

These challenges, to some extent, are inter-related and hence a number of compromises are inevitable. It is, however, apparent that the silicon substrate will only be used as the handle wafer and a dedicated device area is certainly needed to ensure good electrical isolation and thermal insulation. Commonly, this is achieved by using a thick layer of dielectric material, such as silicon dioxide (SiO_2) to separate the device layer from the bulk silicon. The silicon-on-insulator (SOI) technology is considered to be the most straight-forward to implement, as it essentially consists of two silicon layers sandwiching a dielectric (typically SiO_2) layer. However, commercially fabricated SOI wafers are generally more costly; while ex-stock SOI wafers may not meet the required thickness and resistivity of the silicon device layer (of the SOI wafers). The device layer will mainly contain the porous drug reservoir and hence has to have a suitably low resistivity to address issue (IV), described earlier. Moreover, as the electrodes need to be in good contact with the porous structure (issue (III)), a porous thickness feasible for the fabrication of the electrodes has to be considered.

Therefore, polysilicon is used as the material for the device layer for a number of reasons. Firstly, it can be practically deposited on almost any substrate to a reasonable thickness (up to 10 μm [270]). Its resistivity can be modified using ion implantation or diffusion to a desirable level, hence it is an attractive proposition to address issue (IV). Polysilicon has also been demonstrated to be bioactive [257], hence the drug reservoir made of PPSi is expected to be at least, biocompatible. By depositing a layer of polysilicon on a thick SiO_2 layer (buried SiO_2), an electrical and thermal isolation analogous to the SOI technology can be realised.

Next, a device area has to be considered to define the porous drug reservoir. This, however, is related to how the PPSi is to be made. In this case, the anodisation method for the formation of PPSi is less appealing as the fabrication process would be complicated with the need for extra electrical contacts. In fact, the contacts would have to be fabricated on either the polysilicon device layer or connected to the bulk

silicon (for back contact) outside the device area. Hence, the alternative stain etching process is preferred here due to its simple and cost effective fabrication setup, which is vital when fabricating a prototype device. In addition, since polysilicon can be deposited with various crystallinities and grain sizes, preferential etching at the grain boundaries, observed in the stain etching [242, 271], could be used to advantage. The resistivity of the polysilicon could also be modified to favour the stain etching process. A photolithographically patterned masking material, such as silicon nitride (Si_3N_4), which is resistant to the stain etching solutions, can then be used to define a region as the porous drug reservoir.

For the electrodes, aluminium is proposed as the best material. Compared to other conductive materials, such as gold and copper, aluminium is relatively inexpensive, it is easier to deposit a sufficient thickness using the evaporation method and normally it does not require a metallic interlayer (such as chromium or titanium) to promote adhesion to the sample surface. However, to fully meet the requirement (III), further development may be necessary to ensure that the evaporated aluminium is able to impregnate the formed PPSi structure.

Since the formation of the porous drug reservoir must be done before the fabrication of the electrodes, a compatible fabrication process has to be developed. The lift-off method is hence proposed. Lift-off is a process where a target (usually metal, and in this case aluminium) thin film is patterned by removal of a sacrificial material (typically photoresist) underneath, hence lifting away the target film at the unwanted areas [272]. In contrast, a conventional wet etch process requires a selective chemical etchant to etch the metal film and this could leave undesirable inorganic residues within the fabricated PPSi structure.

The electrodes must also be electrically isolated from the device layer (issue (I)). This could be achieved by using standard dielectric materials, such as the Si_3N_4 and SiO_2. In fact, both materials are proposed to be used to also provide a masking material, as discussed previously, to define a device area for the porous drug reservoir.

The conceptualised device has a total size of 12 mm x 12 mm, with a 6 mm diameter circular region which defines the PPSi drug reservoir. The buried SiO_2 is

proposed to be 600 nm thick, which should be sufficient to isolate, electrically and thermally, the device layer from the bulk silicon substrate. The proposed polysilicon device layer is 1 μm thick, with four different resistivity levels to facilitate the investigation of suitable stain etching conditions. Although a thicker polysilicon layer (hence yielding a thicker PPSi structure) may be advantageous for drug loading, because of the "self-limiting" effect of the stain etching process, a porous thickness formed in this way has been typically limited to less than 1 μm thick [228]. In addition, the deposition of aluminium of > 1 μm thick is technically challenging using the proposed evaporation method. Hence, a polysilicon layer of 1 μm thick is deemed a good compromise. The Si_3N_4 and the SiO_2 layer are proposed to be 160 nm and 300 nm thick, respectively, and to be patterned by photolithography and RIE. The aluminium is proposed to be 1 μm (similar to the thickness of polysilicon device layer), but the achievement of a good step coverage, at the boundary of the PPSi drug reservoir, has to be verified to ensure good conductivity. A fabrication process to realise the proposed prototype device is discussed next.

3.3.2 Proposed Fabrication Process

The design of the fabrication process has taken into consideration the four requirements (I to IV) discussed in §3.3.1. A number of electrode designs have also been considered [247] and translated into mask layouts (mask *KB35M*, see Appendix B.1.1 and B.1.2). The proposed fabrication process has been divided into 3 main stages and its major steps are schematically depicted in Figure 3.5. The 3 main stages of the fabrication are:

Stage 1: Fabrication of the device area with a multilayer structure (steps (a) to (h) in Figure 3.5).

Stage 2: Formation of a PPSi layer using the stain etching method (step (i) in Figure 3.5).

Stage 3: Fabrication of electrodes using the lift-off method (steps (j) to (k) in Figure 3.5).

Stage 1: Fabrication of Device Area

a) Grow SiO_2 by wet oxidation

b) Deposit polysilicon by LPCVD

c) Dope polysilicon by ion implantation

d) Deposit SiO_2 by LTO, then high temperature drive-in

e) Deposit Si_3N_4 by LPCVD

f) Spin and pattern photoresist by photolithography (*KB35M-AA*)

g) Etch Si_3N_4 and SiO_2 by RIE

h) Strip photoresist by plasma ashing and FNA

Figure 3.5: Schematic illustration of the fabrication process of the porous polysilicon drug delivery device (not to scale; see next page for continued process steps and colour scheme of materials used).

Stage 2: Formation of PPSi Layer

i) Stain etching

Stage 3: Fabrication of Electrodes

j) Spin and pattern bi-layer photoresist by photolithography (*KB35M-M1*)

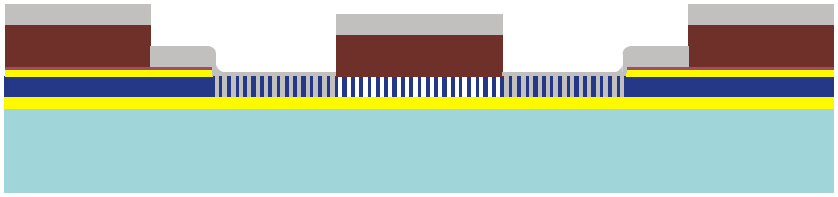

k) Deposit aluminium by evaporation

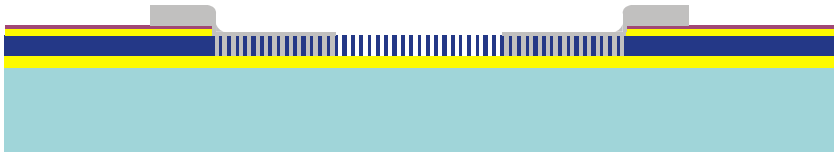

l) Lift-off aluminium by stripping photoresist

Notes:

- Silicon Substrate
- Silicon Nitride, Si_3N_4
- Silicon Dioxide, SiO_2
- Photoresist
- Undoped Polysilicon
- Porous Polysilicon
- Doped Polysilicon
- Aluminium

Figure 3.5: Schematic illustration of the fabrication process of the porous polysilicon drug delivery device (not to scale).

Stage 1: Fabrication of the Device Area

The first fabrication stage is to define a device area with the necessary electrical isolation and the masking layers for subsequent processes. The resistivity of the polysilicon device layer is also processed using ion implantation to achieve the desired resistivity levels. The resultant structure is expected to have a 6 mm diameter circular region with an exposed polysilicon layer, while being isolated from the bulk silicon substrate by the buried SiO_2, as conceptually depicted in Figure 3.6. The starting material consists of both p- and n-type 100 mm diameter silicon wafers. As illustrated in Figure 3.5, the major fabrication steps for Stage 1 are:

Step (a) The wafers are first cleaned using a standard two-stage RCA[19] silicon cleaning process [273]. A wet thermal oxidation is then carried out at 1100 °C to grow a layer of 600 nm thick SiO_2. Apart from electrically and thermally isolating the device layers from the bulk silicon substrate, it also minimises the dopant diffusion from the polysilicon device layer to the silicon substrate during, and post, ion implantation [274]; hence improving the doping profile of the polysilicon.

Step (b) A layer of 1 μm thick polysilicon is deposited by thermal decomposition of silane (SiH_4) at 610 °C using the LPCVD method.

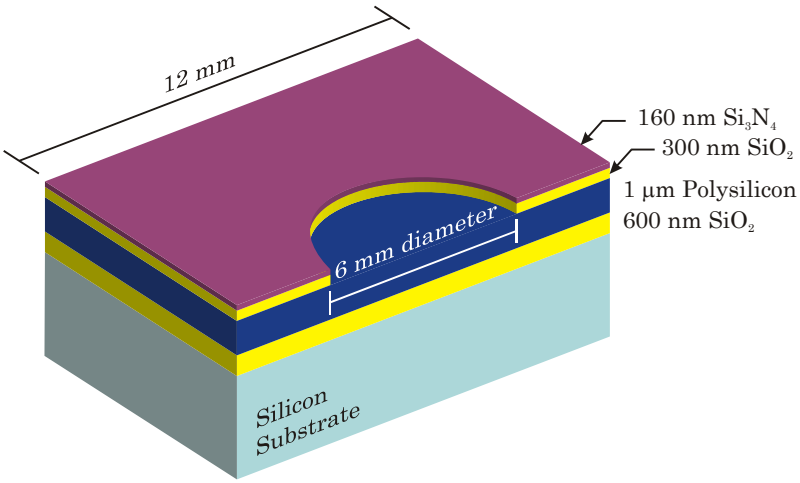

Figure 3.6: Oblique, cross-sectional view, schematic illustration of the prototype device after the first stage of fabrication (not to scale).

[19] The RCA clean was first developed by Werner Kern at the Radio Corporation of America (RCA), hence the name. It consists of first stage clean with a 1:1:5 volume ratio of NH_4OH: H_2O_2: H_2O followed by a second stage clean in a 1:1:6 volume ratio of HCl: H_2O_2: H_2O. In both stages, the cleaning is carried out at a temperature of between 75 °C and 85 °C, for 10 min to 20 min.

Step (c) The polysilicon layer is doped with either boron (for p-type) or phosphorus (for n-type) using ion implantation with four different implantation parameters (dose and energy), as summarised in Table 3.2, to achieve different resistivity levels. The effect of these ion implantations on the resistivity of the polysilicon layer is further discussed in §3.4.1.

Wafer Number	**Doping Level**	**Expected Sheet Resistance, R_{s_exp} (Ω/sq) [247]**	**Ion Implantation Parameters**	
			Dose (ion/cm^{-2})	**Energy (keV)**
W1 to *W4*, *#c13p*	p-type, medium doping	40	Boron, 5 x 10^{15}	80
W5 to *W8*, *#c14p*	p-type, high doping	1	Boron, 1 x 10^{16}	80
W9 to *W12*, *#c15p*	p-type, low doping	100	Boron, 5 x 10^{14}	50
W13 to *W16*, *#c4n*	n-type, low doping	85	Phosphorus, 1.8 x 10^{12}	100

Table 3.2: Summary of the dose and energy used in the ion implantation process. *Wx* denotes the wafer number and wafers *#c13p*, *#c14p*, *#c15p* and *#c4n* are the four check wafers used for the measurement of sheet resistance. The R_{s_exp} are calculated based on a process simulation detailed in [247].

Step (d) A layer of SiO_2 with a nominal thickness of 300 nm is then deposited on the wafers by low temperature oxidation (LTO) at 400 °C using SiH_4 and O_2 gases. This SiO_2 layer firstly protects the polysilicon during the subsequent high temperature drive-in process; and secondly serves as an adhesion and a stress relief layer for the subsequent Si_3N_4 deposition. Next, the drive-in, or annealing, process is carried out at 1150 °C under a nitrogen atmosphere for 200 minutes. This process activates and distributes the ion implanted boron or phosphorus dopants so that the polysilicon lattice could be re-crystallined after the anticipated damage from the implantation process and thus produces a homogenous doping profile [275].

Step (e) A layer of 160 nm thick Si_3N_4 is deposited by LPCVD at 740 °C using dichlorosilane ($SiCl_2H_2$) and ammonia (NH_3) gases. The as-deposited Si_3N_4 layer exhibits a tensile stress which is compensated by the underlying SiO_2 layer.

Step (f) A layer of Shipley SPRT-510 photoresist (positive) is spin-coated on the wafer at 6000 rpm to achieve a nominal thickness of 1.1 μm. The photoresist is then exposed with the first mask (mask *KB35M-AA*, see Appendix B.1.1) and developed.

Subsequently, the photoresist is hard baked for 1 hour at 140 °C in an oven to improve its robustness to sustain the RIE process.

Step (g) A mixture of argon (Ar) and trichloromethane (CHF_3) is used for the RIE process. For etching the Si_3N_4 layer, the flow rate of the Ar / CHF_3 gas mixture is set at 6 sccm / 3 sccm; while to etch the SiO_2 layer, the flow rate of both Ar and CHF_3 gases is set to 25 sccm each. A pressure of 25 mTorr and a radio frequency (RF) power of 160 W are used for the RIE of the Si_3N_4 layer; while the pressure and RF power used for RIE of SiO_2 layer are 40 mTorr and 200 W, respectively.

Step (h) The photoresist is stripped using O_2 plasma ashing and cleaned in fuming nitric acid (FNA).

Stage 2: Formation of a PPSi Layer

The wafers are then stain-etched to form the PPSi layer within the exposed polysilicon region, as masked by the patterned SiO_2-Si_3N_4 layers. Based on previous work [247, 276] and from literature recipes (see §3.2, [182, 188, 242]), a volume ratio of 1:3:5 of HF:HNO_3:H_2O, with an etching time ranging from 10 s to 60 s, was proposed for the initial investigation of the stain etching process. The lower percentage of HF in the stain etching solution is preferred over other systems [246, 266], in order to minimise the undercut caused by HF to the SiO_2 masking layer. The etching conditions are fine-tuned in order to take into account the different resistivity of the wafers and the incubation time. The major step in Stage 2 fabrication, as illustrated in Figure 3.5, includes:

Step (i) PPSi layer is formed using the stain etching.

Stage 3: Fabrication of electrodes

Lastly, the electrodes are fabricated onto the wafers using the lift-off method with a bi-layer photoresist (MicroChem's polymethylglutarimide (PMGI) and Shipley S1813 photoresist) [272]. The S1813 photoresist (positive) is used as the patterning photoresist which would be photolithographically defined. The PMGI photoresist (positive) is used to provide extra undercut so that the bi-layer photoresist could be

feasibly stripped during the last lift-off step. As illustrated in Figure 3.5, the major steps for Stage 3 fabrication are:

Step (j) The PMGI is first spin-coated at 4000 rpm for 30 s to achieve a nominal thickness of 1 μm. The PMGI is then soft baked before being flood-exposed with deep ultraviolet (UV) light. The S1813 photoresist is then spin-coated at 5500 rpm for 30 s and exposed using the second mask (mask *KB35M-M1*, see Appendix B.1.2). The bi-layer photoresist is then developed and hard baked at 95 °C for 30 minutes.

Step (k) A quick dip into 20:1 BHF is carried out to remove the native oxide and a blanket of 1 μm thick aluminium is then evaporated onto the wafers.

Step (l) The bi-layer photoresist is removed in *N*-methylpyrrolidone (NMP) to realise the electrode patterns.

3.4 Fabrication of the Device Area (Stage 1)

The proposed fabrication has been carried out using the batch number K2714s (process listing detailed in Appendix A.1) as detailed in [247, 276]. The Stage 1 fabrication to realise the device area was carried out at the cleanroom facility at the then Southampton University Microelectronics Centre (SUMC) (later known as Innos Ltd. (Innos)). All of the processes in Stage 1 fabrication were processed at the wafer level, mostly performed by the technical staff of SUMC / Innos. Some results and issues faced during the fabrication are discussed here in two parts.

3.4.1 Results and Discussions: Part 1 (Steps (a) to (e))

Steps (a) to (e) (Figure 3.5) of the Stage 1 fabrication were carried out to create a suitably doped device layer with a multilayer structure which aims to provide an adequate electrical isolation and a masking region for the stain etching process. The parameters used in the fabrication are detailed in [247, 276]. The thickness of each of the layers was measured post fabrication using a tabletop small spot spectroscopic reflectometer (Nanometrics NanoSpec) and results are summarised in Table 3.3.

Process	Material	Thickness (nm)	
		Specified	**Measured**
Step (a) Wet Oxidation	SiO_2	600 ± 20	595.5 ± 1.1
Step (b) LPCVD Polysilicon	Polysilicon	1000 ± 25	1049.2 ± 1.0
Step (d) LTO	SiO_2	300 ± 30	289.6 ± 21.8
Step (e) LPCVD Si_3N_4	Si_3N_4	160 ± 20	159.6 ± 1.9

Table 3.3: Summary of the layer thickness measured after each process steps (a) to (e) (refer to Figure 3.5 for the complete fabrication flow).

As summarised in Table 3.3, apart from the thickness of the LPCVD polysilicon, the measured thicknesses of the buried SiO_2 (Step (a)), LTO SiO_2 (Step (d)) and the LPCVD Si_3N_4 (Step (e)) are within the specified range. This is acceptable as it is expected that the thickness of the polysilicon device layer will be reduced in the subsequent fabrication processes. In particular, there is a tendency to over-etch the SiO_2 layer above the polysilicon layer during the RIE process (Step (g)) to ensure full removal of the SiO_2.

The as-deposited polysilicon typically has a very high resistivity and this could be altered by a process known as doping, whereby suitable impurities are introduced into the substrate thus changing its physical properties [275]. This is typically done using the ion implantation process, in which the ions of the desired dopant are produced and accelerated to a high energy to finally impinge onto the target substrate. The implantation dose (or concentration of ions) and the implantation energy, among other parameters, influence the amount, depth and profile of the dopant introduced into the substrate.

Four different sets of implantation parameters within the operational range of the ion implanter, as summarised in Table 3.2, were proposed to modify the resistivity of the polysilicon device layer. In order to evaluate the altered resistivity caused by the ion implantation (Step (c)), the SiO_2 layer on the four check wafers (*#c13p*, *#c14p*, *#c15p* and *#c4n*, which were processed concurrently with the device wafers from the start of the fabrication), were stripped in 7:1 buffered HF (BHF) after the drive-in process (Step (d)). The sheet resistance, R_s, of the annealed, doped polysilicon was then measured [247] using an automated four-point probe station (QuadPro Resistivity System) and results are tabulated in Table 3.4. The four sets of ion implantation parameters from Table 3.2 and the expected sheet resistances,

R_{s_exp}, (calculated based on a process simulation in [247]) are repeated in Table 3.4 for easier reference. The R_s of the n-type check wafers, *#c4n*, was beyond the measurable range of the probe station, and was assumed to be 10000 Ω/sq. The actual resistivity of the device wafers was then inferred from these measurements.

The percentage difference (% difference) was calculated with respect to the measured sheet resistance, R_{s_mea}, as follows:

$$\frac{\left|R_{s\_mea} - R_{s\_sim}\right|}{R_{s\_mea}} \times 100\,\% \tag{3.5}$$

where R_{s_sim} is the simulated sheet resistance. When the R_{s_mea} values were compared to the simulated values of R_{s_exp}, as depicted in Table 3.4, a significant deviation between R_{s_mea} and R_{s_exp} , in fact more than 70 %, was observed for all but check wafer *#c13p*. These deviations were ascribed to either a simulation error (as in check wafer *#c4n*) or fabrication-related issues (as in check wafer *#c15p*) [247]. As briefly discussed in §3.2.2, the resistivity of the substrate is one of the factors that influences the characteristic of the porous structure obtained by the stain etching process. Hence, to validate the experimental results, a revised process simulation was carried out.

Wafer	**Ion Implantation Parameters**	**Measured Sheet Resistance, R_{s_mea} (Ω/sq)**	**Simulated Sheet Resistance, R_{s_sim} (Ω/sq)**			
			R_{s_exp} by [247]	**% Difference**	**This work, R_{s_rev}**	**% Difference**
#c13p	Boron, 5 x 10^{15} cm^{-2}, 80 keV	32.54 ± 0.19	40	22.93	23.60	27.47
#c14p	Boron, 1 x 10^{16} cm^{-2}, 80 keV	28.67 ± 0.59	1	96.51	12.04	58.00
#c15p	Boron, 5 x 10^{14} cm^{-2}, 50 keV	338.94 ± 4.95	100	70.50	175.29	48.28
#c4n	Phosphorus, 1.8 x 10^{12} cm^{-2}, 80 keV	>> 1000*	85	99.15	2911.6	70.88

Table 3.4: Comparison of simulated and measured sheet resistance with respect to four different ion implantation parameters (* assumed to be 10000 Ω/sq for the calculation of % difference).

3.4.1.1 Process Simulation

A revised process simulation was performed using the same two-dimensional, physically-based, numerical process simulation tool, *Athena* (Silvaco Data Systems Inc.[20]), used in [247]. The ion implantation was simulated using the Secondary Ion Mass Spectrometry (SIMS)-Verified Dual Pearson (SVDP) models, instead of the Gaussian distribution used in [247]. The SVDP models are based on the empirical data extracted from implantation experiments conducted by the University of Texas at Austin [277]. In addition, the R_{s_sim} was extracted directly from the simulated device structure by using the built-in extraction tool, which estimates R_{s_sim} based on the following integral [278]:

$$R_{s\_sim} = \int_{x\_left}^{x\_right} \frac{dx}{q \cdot (\mu_n \cdot n + \mu_p \cdot p)} \tag{3.6}$$

where *x_right* and *x_left* are determined by the semiconductor material boundaries (here, the thickness of polysilicon layer), q is the magnitude of electron charge, μ_n and μ_p are the mobility of electron and hole, respectively, and n and p are the concentration of electrons and holes, respectively. A number of assumptions were made during the simulation. Importantly, the deposited polysilicon was assumed to be 1 μm thick, the tilt or angle of ion implantation was assumed to be zero (since the polysilicon was modelled as amorphous) while the damage induced by the ion implantation process was not modelled. In addition, parameters used in the processes from steps (a) to (e), depicted in Figure 3.5, were considered in the simulation. An example simulation input file is included in Appendix C.

Compared to the symmetric parabolic shape of an ideal Gaussian distribution, the doping profile after the ion implantation process (marked by △), simulated using the SVDP models, has a slight skew and an exponential tail, as depicted in Figure 3.7. The dopants, after the drive-in process, are observed to be well-distributed within the polysilicon layer, as depicted by a flat doping profile (marked by ×) in Figure 3.7.

[20] Silvaco Data Systems Inc., Santa Clara, USA. http://www.silvaco.com/ (*last accessed Jul. 2009*).

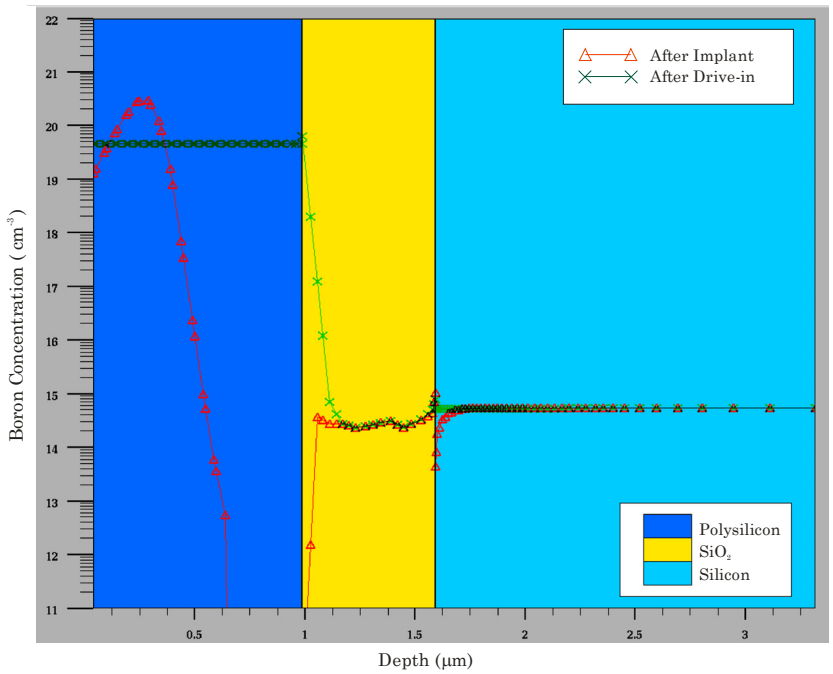

Figure 3.7: Plot of the simulated boron concentration (in log. scale) along the depth of the device structure, before (△) and after (×) the drive-in process (Step (d)). Here, the boron implantation was modelled with a dose of 5 x 10^{15} cm^{-2} and an energy of 80 keV.

The difference between the R_{s_sim} values extracted from this work (denoted as R_{s_rev} for clarity) and the R_{s_mea} values was found to be less than 70 %, as tabulated in Table 3.4. Overall, the R_{s_rev} for each of the check wafers was observed to be lower than the R_{s_mea}. Hence, it can be said that the simulation over-estimated the impact of ion implantation on the shift in resistivity of the polysilicon layer. The two simulations showing the greatest difference between R_{s_rev} and R_{s_mea}, are for check wafers *#c14p* (58.00 %) and *#c4n* (70.88 %) and these can be justified by the limitation of the SVDP model, which has an experimentally verified dose range of 1 x 10^{13} cm^{-2} to 8 x 10^{15} cm^{-2} [277]. Beyond this range, extrapolation was used by the simulator and that could explain the result.

Essentially, compared to the R_{s_exp}, the revised simulation (of R_{s_rev}) provides a better estimation of the sheet resistance. It is also clear that the selection of ion implantation dose and energy did not yield the variation in resistivity as initially intended. By both measurement and simulation, as summarised in Table 3.4, the R_s of the high (*#c14p*) and medium (*#c13p*) dose boron-doped polysilicon device layers were found to be very similar. Hence, effectively, only two ranges of resistivity of p-type have been created. This does not affect the fabrication of the final prototype

device, but it does have an implication on the possible stain etching processes available for development and initial investigation.

3.4.2 Results and Discussions: Part 2 (Steps (f) to (h))

The fabricated multilayer structure was then patterned by photolithography (Step (f)) and RIE (Step (g)) to define the region for the drug reservoir. However, the photolithography was not optimised. In particular, some defects such as pinholes and cracking of photoresist due to particulate contaminations were introduced during the photoresist patterning using the first mask (*KB35M-AA*). The photolithography used here provides a mask to define the circular region (6 mm diameter) where drugs for delivery are to be contained. The masked area would eventually provide the surface for the contact pads for the electrodes.

Unfortunately, these lithography defects were overlooked and, as a result, the defects were transferred over to the SiO_2-Si_3N_4 layers by the RIE process (Step (g)) [276]. These defects affect the integrity of the SiO_2-Si_3N_4 layers at the periphery of the drug delivery reservoir where the contact pads are contacting the electrodes. All the exposed polysilicon areas would also be made porous during the subsequent stain etching process. This fabrication error meant that significant levels of wafer inspection were needed prior to the fabrication stages required for the electrodes.

3.4.2.1 Photolithography and RIE Rework

Therefore, in order to mitigate the problem, the SiO_2-Si_3N_4 layers were removed and re-fabricated. The Si_3N_4 layer was first stripped in phosphoric acid, set at 70 °C for over an hour; the SiO_2 layer was then etched using 7:1 BHF. The SiO_2-Si_3N_4 layers were re-deposited using the methods discussed previously (LTO and LPCVD, respectively). The photolithography rework was then carried out with two attempts before achieving a more satisfactory outcome. The first attempt of rework used a similar photolithography protocol but, instead of the typical hard contact, a soft contact mode was used when aligning the substrate to the mask. The soft contact mode applies minimal pressure to bring the substrate in contact with the mask, hence minimising the damage to the photoresist due to contamination from the mask

and *vice versa*. This attempt yielded an improved photolithography quality, but small defects, such as those depicted in Figure 3.8, were still present.

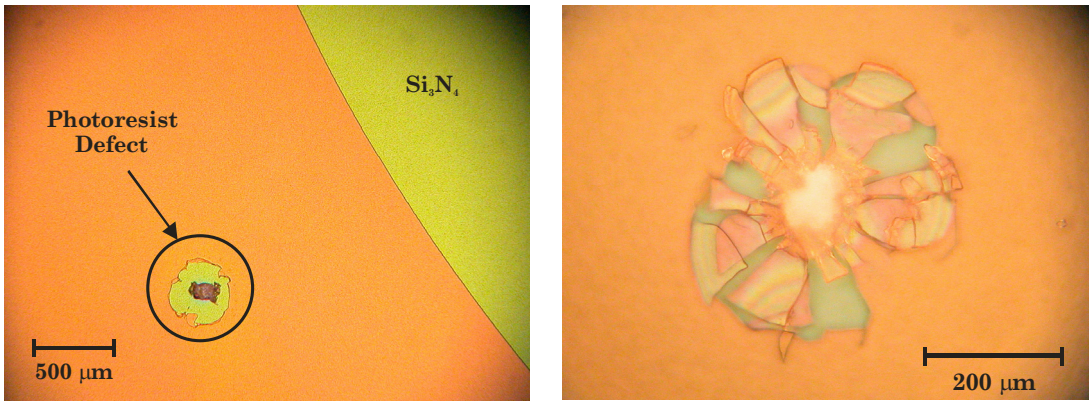

(a) (b)

Figure 3.8: Optical microscope images of photoresist defects showing (a) broken and (b) cracked photoresist due to particulate contamination.

The contamination was probably caused by one or all of the three possible sources: the wafer, the photoresist and the mask. Hence in the second attempt of the photolithography rework, the mask and the wafers were thoroughly cleaned using standard cleaning processes (FNA for wafers followed by solvent using acetone and isopropanol (IPA) for both the wafers and the mask). A fresh and thicker Shipley SPRT-518 photoresist, which provides a nominal thickness of 2.2 μm, was used. The thicker photoresist is more robust and hence is less susceptible to breakage or cracking. The final photolithography rework was considerably better with significantly fewer defects observable across the batch.

The RIE was then carried out to etch the SiO_2-Si_3N_4 layers using the same parameters as previously discussed (Step (g)). The patterned SiO_2-Si_3N_4 layers exhibit a "double-tone" pattern, as depicted in Figure 3.9, due to the patterns left by the initial RIE process. This is understandable as the initial RIE process to etch the SiO_2 layer was longer than necessary to ensure that all the SiO_2 has been completely removed. Hence, a thin layer of polysilicon would also have been etched during the process. This marginal thickness variation may have some effects on the stain etching process, as depicted in Figure 3.9 (b), but the likely influence was not comprehensively investigated.

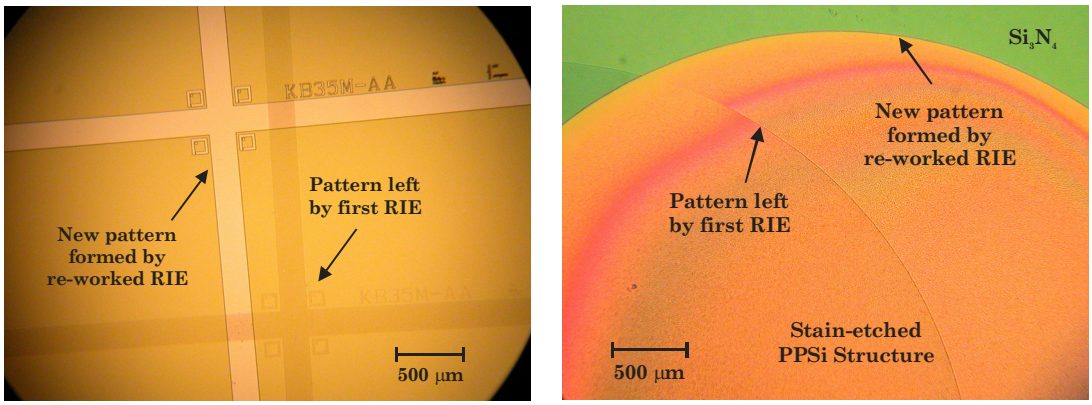

Figure 3.9: Optical microscope images showing the overlapped patterns due to the photolithography and RIE rework after (a) the RIE of Si_3N_4-SiO_2 layers and (b) a stain etching process.

The photoresist on the wafers was only removed (Step (h)) prior to the stain etching process (Stage 2 Fabrication). A typical structure of the device, after the Stage 1 fabrication, is depicted in Figure 3.10. The FEGSEM shows the exposed polysilicon after the patterning and RIE of SiO_2-Si_3N_4 layers. The surface of the polysilicon appears to be rather rough, as expected, due to its polycrystalline grain boundary. This consequently results in an uneven, wavy-like surface of the subsequently deposited SiO_2 and Si_3N_4 layers.

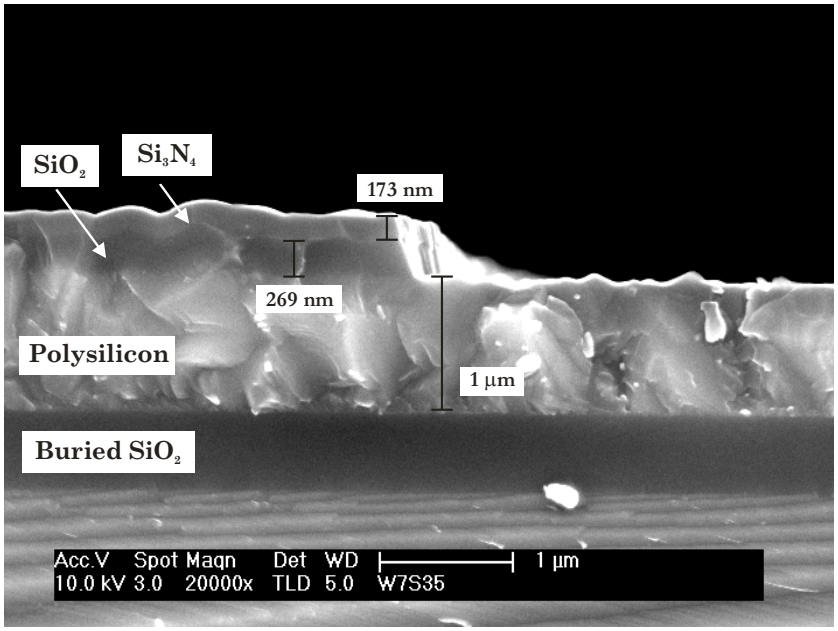

Figure 3.10: Cross-sectional view FEGSEM micrograph showing a typical multilayer structure after the completion of Stage 1 fabrication (up to Step (h) of Figure 3.5).

3.5 Formation of the PPSi Layer by the Stain Etching Method (Stage 2)

Prior to the batch process of the wafers to form the PPSi structure (Stage 2 fabrication), a series of investigations was carried out to evaluate and develop a stain etching process suitable to yield a PPSi structure as a porous drug reservoir. The first phases of the investigation of the stain etching process, which are detailed in [247, 276] and briefly discussed here, were conducted at the SUMC / Innos. However, subsequent work on stain etching was carried out at the cleanroom facility at the University of Manchester after the loss of the facility at SUMC / Innos in the fire (Oct. 2005). The development work on the stain etching process was mostly carried out at the chip level.

3.5.1 Early Investigation of Stain Etching Process

In the early phase of the investigation of the stain etching process, both silicon and polysilicon substrates were used to evaluate the feasibility of the stain etching process [247, 276]. The use of a silicon substrate provides a straightforward way to evaluate the stain etching process with minimal prior fabrication. The silicon substrates used were from p-type and n-type wafers with a resistivity of 85 Ωcm and 39 Ωcm, respectively. A mixture of either 4:1:5 or 1:4:5 volume ratio of $HF:HNO_3:H_2O$, with an etching time between 5 minutes and 45 minutes, was used during the experiment. It has been observed that etching times of at least 20 minutes are required to produce a porous structure with the desired porosity and pore density. Based on these findings, further investigations of the stain etching process on polysilicon substrates (sawn from check wafers *#c14p*, *#c15p* and *#c4n* with R_{s_mea} as detailed in Table 3.4) were carried out with modified volume ratios (1:4:5, 2:5:5 and 1:4:2) of $HF:HNO_3:H_2O$ to adjust for the difference in resistivity between the silicon and polysilicon substrates. The volume ratio of 2:5:5 of $HF:HNO_3:H_2O$ was suggested to be more suitable for the fabrication of the PPSi structure [247].

However, subsequent investigation suggested that the stain etching time of 20 minutes was excessive for polysilicon. In fact, when wafer 6 (*W6*, $R_s \approx (28.67 \pm 0.59)$ Ω/sq) was stain-etched in 1:4:4 volume ratio of HF:HNO_3:H_2O for 17 minutes, the polysilicon film, the buried SiO_2 and some of the bulk silicon substrate (~ 30 μm) were removed [276]. This, consequently, prompted a re-examination into the etching time and the composition of etching solutions.

3.5.2 The Stain Etching Process: Setup and Procedures

The re-examination of the stain etching process was firstly carried at the SUMC / Innos with help from a MSc student, S. Mohmad [276], and subsequently continued at the cleanroom facility at the University of Manchester. Individual chips (samples) of polysilicon substrates with the sheet resistance, $R_s \approx (28.67 \pm 0.59)$ Ω/sq from wafers 5 (*W5*) and 7 (*W7*) of the batch K2714s, were used in this experiment. *W5* was diced using an automated wafer dicing machine; while *W7* was scribed and cleaved manually. These samples were still coated with the post-RIE photolithographically patterned photoresist of Step (g) (in Figure 3.5). To remove this photoresist (Step (h)), some of the samples were then ashed using the TePla System 300 Ash Barrel (30 minutes of standard recipe); while others were treated using a RIE system (Plasma Tech RIE80), with an O_2 flow rate of 50 sccm, at a pressure of 5 mTorr and an RF power of 150 W, for 10 minutes. Subsequently, a wet chemical etching using FNA was carried out to completely remove the photoresist. Typical etching times for FNA are up to 30 minutes and the samples were then rinsed with copious amount of DI water.

The typical chemical composition used for the stain etch is a mixture of 48 % to 49% concentrated HF, 68 % to 70% concentrated HNO_3 and DI water. The acids used were either of electronics (MOS) or AnalaR grade. A volume ratio of 1:3:5 of HF:HNO_3:H_2O was used as the starting point for the process optimisation, based upon the earlier studies [276] and literature studies (refer to §3.2). For most experiments, the etching solution was freshly prepared by mixing, for instance, 15 mL of HNO_3 followed by 5 mL of HF into 25 mL of DI water, in a HF-resistant beaker. The mixture was left "to settle" for at least one hour prior to the stain etching process. The etching solution was re-used during the session, but discarded

at the end. No more than 6 samples were evaluated in a single experimental run. Typically, a sample was immersed into the etching solution and the timer was started simultaneously. After a preset time (typically, less than 1 minute) the sample was taken out and immediately rinsed with copious amount of DI water. For some experiments, other stain etching volume ratios, including using an additional pre-etch step (with 1:5:5 volume ratio of $HF:HNO_3:H_2O$ to reduce the incubation time [188]), have also been evaluated. Most of the experiments were carried out at room temperature under ambient light conditions. Table 3.5 summarises some of the samples discussed here and their respective stain etching conditions. The samples were identified by a simple notation *WxSxx*, where *Wx* denotes the wafer number and *Sxx* denotes the sample number based on its position in the wafer [276].

Sample	**Pre-processing**	**Stain Etching Conditions**
W5S01	Photoresist stripped in TePla Ash Barrel.	1:5:5 (15 s) then 1:3:5 (15 s) of $HF:HNO_3:H_2O$
W5S05	Photoresist stripped in TePla Ash Barrel. Cleaned with acetone (5 min) in ultrasonic bath, rinsed with IPA then in DI water (5 min). Dip in 48 % HF for 5 s and rinsed with copious amount of DI water.	1:5:5 (10 s) then 1:3:5 (10 s) of $HF:HNO_3:H_2O$
W5S14	Photoresist stripped in TePla Ash Barrel. Cleaned with acetone (5 min) in ultrasonic bath, rinsed with IPA then in DI water (5 min).	1:5:5 (10 s) then 1:3:5 (15 s) of $HF:HNO_3:H_2O$
W5S28 and *W5S38*	Photoresist stripped in TePla Ash Barrel. Cleaned with FNA (10 min) and rinsed in DI water in rinse tank (5 min) and super-Q tank (3 min).	1:3:5 (25 s) of $HF:HNO_3:H_2O$
W7S15	Photoresist stripped in RIE80. Cleaned with FNA (5 min) then rinsed in DI water (5 min).	1.3:6:15 (5 min) of $HF:HNO_3:H_2O$
W7S27	Photoresist stripped and cleaned in FNA (5 min) then rinsed in DI water (10 min).	1:3:5 (35 s) of $HF:HNO_3:H_2O$
W7S28	Photoresist stripped in RIE80. Cleaned with FNA (20 min) then rinsed in DI water (10 min).	1:5:5 (15 s) then 1:3:5 (15 s) of $HF:HNO_3:H_2O$
W7S35	Photoresist stripped in RIE80. Cleaned with FNA (5 min) then rinsed in DI water (5 min).	1:5:5 (15 s) then 1:3:5 (15 s) of $HF:HNO_3:H_2O$
W7S38	Photoresist stripped and cleaned in FNA (5 min) then rinsed in DI water (10 min).	500:1 (30 s) of $HF:HNO_3$

Table 3.5: Summary of the pre-processing steps and the stain etching parameters used in the experiment to investigate the etching time and composition of the etching solution. All the samples used here have an $R_s \approx (28.67 \pm 0.59)$ Ω/sq as measured by using check wafer #*c14p*.

3.5.2.1 Investigation of the Effect of Substrate Resistivity

The porous structure and the incubation time during the porosification of silicon either by anodisation or chemical dissolution is believed to be influenced by many factors, including the type of silicon substrate and its resistivity [249]. However, limited literature data exists on how the resistivity of polysilicon substrates would influence the stain etching and yield different porous structures. Hence, a separate experiment was later carried out at the Optoelectronics Research Centre (ORC) temporary cleanroom (the Dairybox), at the University of Southampton, to investigate the effect of substrate resistivity on the stain etching process.

Eight polysilicon samples (*W8S11*, *W8S12*, *W3S11*, *W3S12*, *W9S11*, *W9S12*, *W15S04* and *W15S05*), which have been doped with 4 different ion implantation parameters (resulting in different resistivity levels), were used for this experiment. The substrate type and the sheet resistance (as measured using the check wafers) are tabulated in Table 3.6. These samples were first ashed, to strip the photoresist, using an O_2 RIE system (Oxford Instruments Plasmalab® 80 Plus) with an O_2 flow rate of 10 sccm, a pressure of 50 mTorr and an RF power of 100 W for 10 minutes. A 10-minute FNA clean was then carried out immediately prior to the stain etching.

<table>
<tr><th>Sample</th><th>Type</th><th>Sheet Resistance (Ω/sq)</th><th>Etching time (s)</th></tr>
<tr><td>W8S11</td><td rowspan="6">p-type</td><td rowspan="2">28.67 ± 0.59</td><td>t_i + 40</td></tr>
<tr><td>W8S12</td><td rowspan="6">t_i + 30</td></tr>
<tr><td>W3S11</td><td rowspan="2">32.54 ± 0.19</td></tr>
<tr><td>W3S12</td></tr>
<tr><td>W9S11</td><td rowspan="2">338.94 ± 4.95</td></tr>
<tr><td>W9S12</td></tr>
<tr><td>W15S04</td><td rowspan="2">n-type</td><td rowspan="2">>> 1000</td></tr>
<tr><td>W15S05</td></tr>
</table>

Table 3.6: The substrate type and the sheet resistance (as measured using the check wafers) of samples used to investigate the effect of substrate resistivity on the stain etching. All the samples were processed and stain-etched in 1:3:5 volume ratio of $HF:HNO_3:H_2O$, as detailed in the text. The t_i is the incubation time observed in the experiment.

The stain etch solution with a volume ratio of 1:3:5 of $HF:HNO_3:H_2O$ was prepared one day in advance. For each sample, about 10 mL of etching solution was used and disposed of after each use. The incubation time, t_i was measured from the time the sample was immersed into the etching solution, to the time when the first

sign of etching could be physically observed. The indicator for etching taking place was either the formation of bubbles or a change of colour on the sample surface. All samples were stain-etched for 30 s after the onset of etching, except for sample *W8S11* which was etched for 40 s. The entire experiment was carried out at room temperature under ambient light conditions.

3.5.3 Results and Discussions

A range of samples were stain-etched with a variety of different etching conditions. The stain-etched samples were evaluated by visual inspection and by using the optical microscope. Some of the samples were characterised using the SEM and AFM.

During the stain etching process, there is a period, known as the incubation time, t_i, between immersion of the sample into the stain etching solution and the onset of the stain etching. Bubble formation was normally observed after the incubation time, and this was conveniently used as an indication of "productive" stain etching. Bubbles that formed and were trapped onto the surface of the samples were believed to be one of the sources of non-uniformity of the stain etching across the surface [180]. In addition, a change in the appearance on the surface of the samples could also be observed, as a function of time due to the thin-film interference effect [279]. Not all the stain-etched samples yielded bubbles during the etching process, but most of the samples exhibited a change of colour or appearance on the surface after the stain etching.

In general, the surface of the stain-etched samples varied in colour, with some samples appearing pink to dark brown (under room light) to the naked eye, while the others appeared light green to pale blue in colour. Examples of these surface colour variations are depicted by the bright field optical microscopy images in Figure 3.11, which were acquired using a 2-mega pixels colour digital camera (Nikon Digital Sight, DS-2Mv) fitted to an upright microscope (Nikon Eclipse LV100 with a 12 V, 50 W halogen lamp). It is also common to observe spots or stains on the surface of most of the samples, which is very likely due to the trapping of bubbles which may enhance localised etching. The variation in surface appearance, which implies a deviation of porous structure and thickness, in the first instant, is a direct

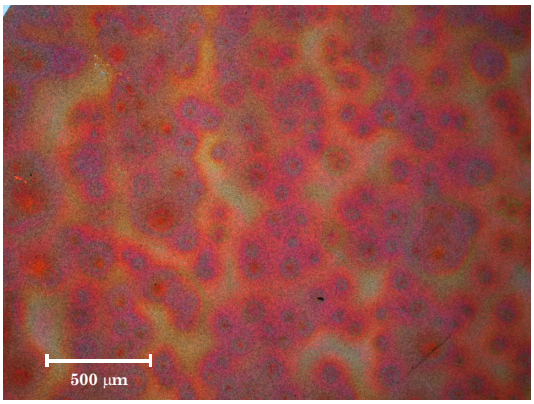

(a) *W5S01*; stain-etched in a 1:5:5 (15 s) then a 1:3:5 (15 s) volume ratio of HF:HNO_3:H_2O

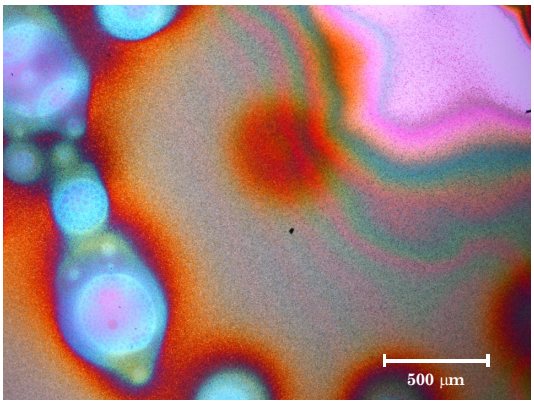

(d) *W7S15*; stain-etched in a 1.3:6:15 (5 min) volume ratio of HF:HNO_3:H_2O

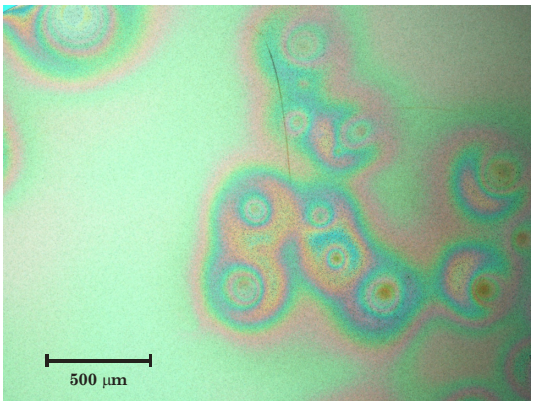

(b) *W5S14*; stain-etched in a 1:5:5 (10 s) then a 1:3:5 (15 s) volume ratio of HF:HNO_3:H_2O

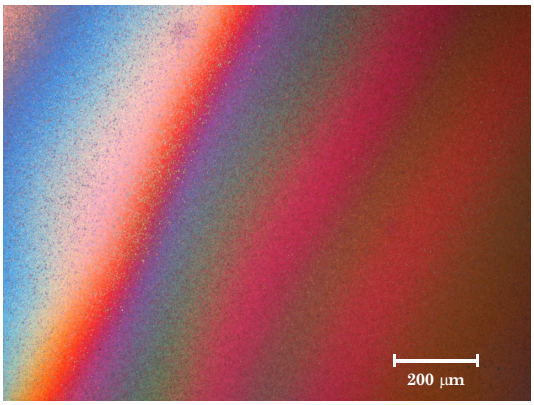

(e) *W7S28*; stain-etched in a 1:5:5 (15 s) then a 1:3:5 (15 s) volume ratio of HF:HNO_3:H_2O

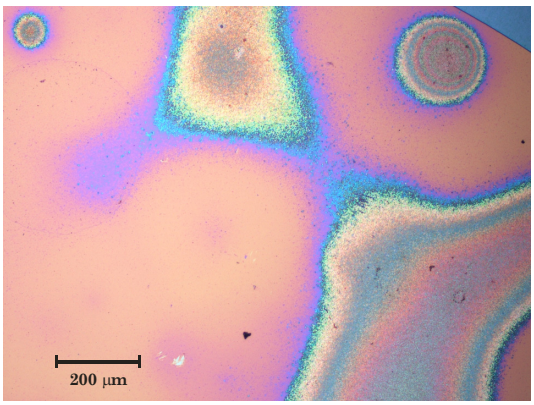

(c) *W5S28*; stain-etched in a 1:3:5 (25 s) volume ratio of HF:HNO_3:H_2O

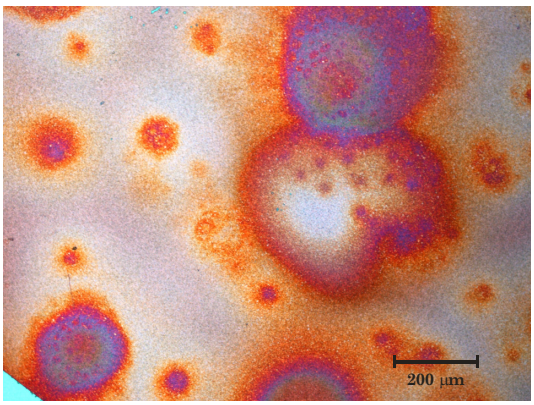

(f) *W5S38*; stain-etched in a 1:3:5 (25 s) volume ratio of HF:HNO_3:H_2O

Figure 3.11: Plan-view, bright field optical microscopy images showing the surface appearance of selected stain-etched samples ($R_s \approx (28.67 \pm 0.59)$ Ω/sq). The stain etching conditions and pre-processing treatments are detailed in Table 3.5.

outcome of the different etching parameters used on the samples. On a closer observation, however, the variation also occurs in two situations: (i) on samples with "identical" etching parameters, as depicted in samples *W5S28* and *W5S38* (Figure 3.11 (c) and (f), respectively, both with $R_s \approx (28.67 \pm 0.59)$ Ω/sq); and (ii) on the individual sample itself, as depicted in samples such as *W7S15* (Figure 3.11 (d)) and *W7S28* (Figure 3.11 (e)). Variation of these surface appearances, to some extent substantiates the irreproducibility and non-uniformity associated to stain etching prepared samples often reported in the literature [180, 225, 242, 249]. The subsequent sections thus discuss the use of SEM and AFM to better understand the microstructure of the prepared PPSi samples.

3.5.3.1 Scanning Electron Microscopy

Scanning electron microscopy (SEM) can be used to investigate the structural morphology and material properties of a sample. By using the secondary electron (SE) imaging, the SEM is capable of producing high resolution images with three-dimensional appearances which are useful for the understanding of the surface structure of a sample. When coupled with backscattering electrons (BSE) and X-ray emission, an image contrast due to the variation in atomic mass number provides an indication of the elemental composition of the sample [280].

In principle, the SEM produces images by detecting the signals from the interaction of the sample's surface with a high energy beam of electrons focused onto the surface of the sample. Typically, a tungsten filament or a lanthanum hexaboride (LaB_6) cathode is used as an electron source where the electrons are thermionically emitted and then accelerated. Alternatively, electrons can also be emitted via a field emission gun (FEG). The FEGSEM micrographs discussed here are obtained from FEI/Philips XL30 or FEI/Philips Sirion FEGSEM at the School of Material, University of Manchester; while the SEM micrographs are obtained from the LEO (now Carl Zeiss) 1455VP SEM at the NanoMaterial Rapid Prototyping Facility, University of Southampton.

Figure 3.12 depicts the cross-sectional FEGSEM micrograph of a typical porous polysilicon sample stain-etched in a system consisting of a 1:3:5 volume ratio of $HF:HNO_3:H_2O$. The sample used for this SEM, *W7S35* ($R_s \approx (28.67 \pm 0.59)$ Ω/sq)

was first stain-etched in a 1:5:5 volume ratio of $HF:HNO_3:H_2O$ solution for 15 s, followed by another stain etch in a typical 1:3:5 volume ratio solution for an additional 15 s (see Table 3.5 for details). In both stages, the sample was raised about one third off the surface of the stain etch solution, hence it maintained a region of un-etched surface. This way, the effect of stain etching could be unambiguously examined by comparing the two regions. The cross-sectional FEGSEM micrographs were obtained 9 days after the stain etching process. Compared to the un-etched region (depicted in Figure 3.10), the stain-etched area of sample *W7S35* is distinctly different. The SiO_2 and Si_3N_4 layers could still be observed, but the majority of the polysilicon has been etched away. The undercut at the SiO_2 and Si_3N_4 masking layers is measured to be ~ 390 nm, with an etch depth of around 605 nm. In this case, the stain etching is believed to have consumed more than half the polysilicon due to chemical dissolution and the etching is observed to be isotropic with a ratio of about 2:1 etch depth versus lateral etch. Some of the SiO_2 has also been etched, as is visible from the slight undercut under the Si_3N_4 layer, but the stain etching solution is clearly selective.

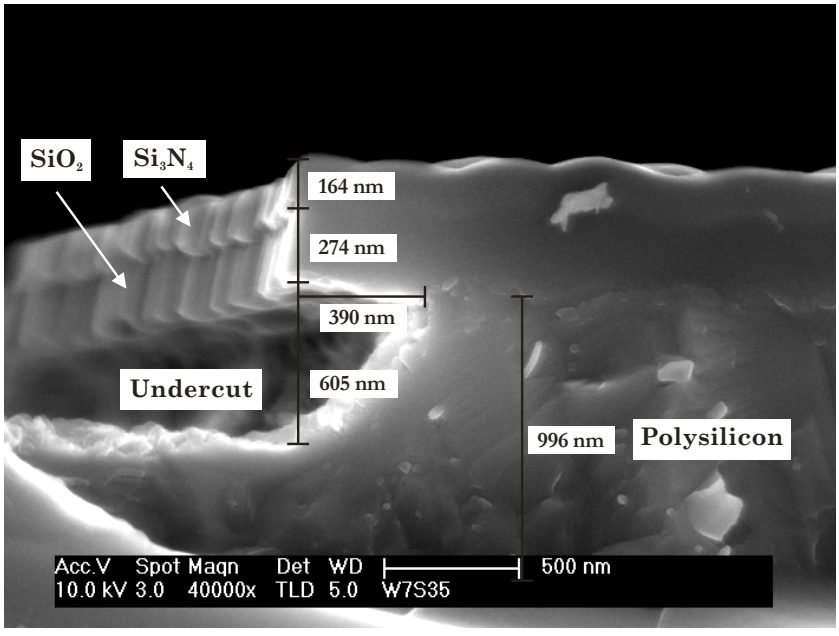

Figure 3.12: Cross-sectional view FEGSEM micrograph showing the undercut caused by the stain etching process on sample *W7S35* ($R_s \approx (28.67 \pm 0.59)$ Ω/sq). The stain etching parameters are detailed in Table 3.5.

The surface of the stain-etched polysilicon of sample *W7S35* is rather rough and granular-like, with irregularly shaped, random etch pits, as depicted in Figure 3.13. The rough surface appearance is in agreement with some of the AFM images (discussed in §3.5.3.4, see Figure 3.23 and related text) on similar stain-etched polysilicon samples of the same sheet resistance. The top layer, which is believed to be the PPSi layer, is measured to be ~ 100 nm thick. When examined with a higher magnification, as depicted in the inset of Figure 3.13, the porous structure could be loosely categorised as interconnected, with some isolated pores. The size of the pores is estimated to be around 70 nm thick and 20 nm to 30 nm in width.

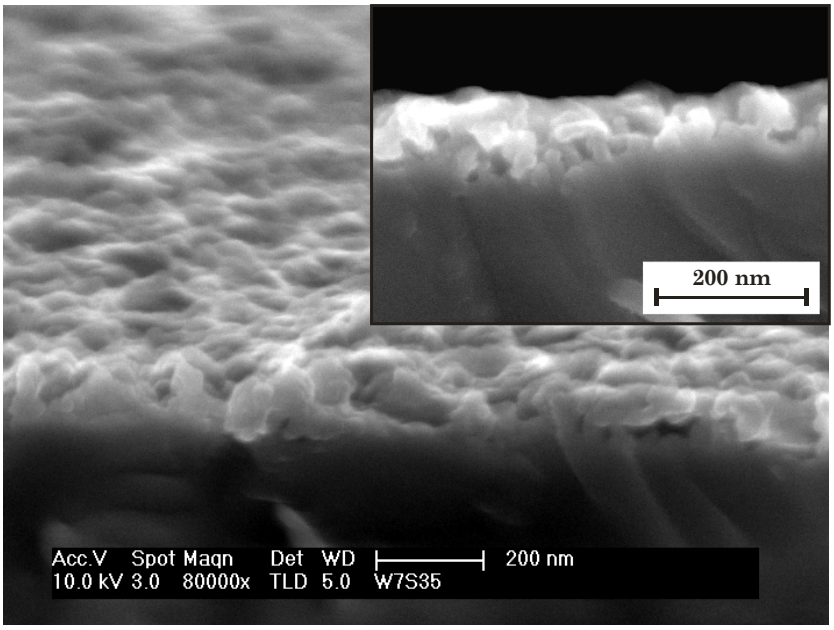

Figure 3.13:Cross-sectional view FEGSEM micrograph showing the top layer of sample *W7S35* after the stain etching. The inset shows a different area of the sample imaged with higher magnification.

Figure 3.14 depicts a FEGSEM micrograph of the cross-section of sample *W7S27* ($R_s \approx (28.67 \pm 0.59)$ Ω/sq), imaged one week after it was stain-etched in a 1:3:5 volume ratio of HF:HNO_3:H_2O solution for 35 s. In order to slow down the natural oxidation and aging process, the sample was stored in a high vacuum chamber and kept at ~ 8.7 x 10^{-7} mbar until the SEM session. The secondary electron image shows a rough surface with some shallow pits, similar to that observed on sample *W7S35* (as depicted in Figure 3.13), albeit with a thicker polysilicon layer that remained after the stain etching process. The PPSi layer appeared to be more

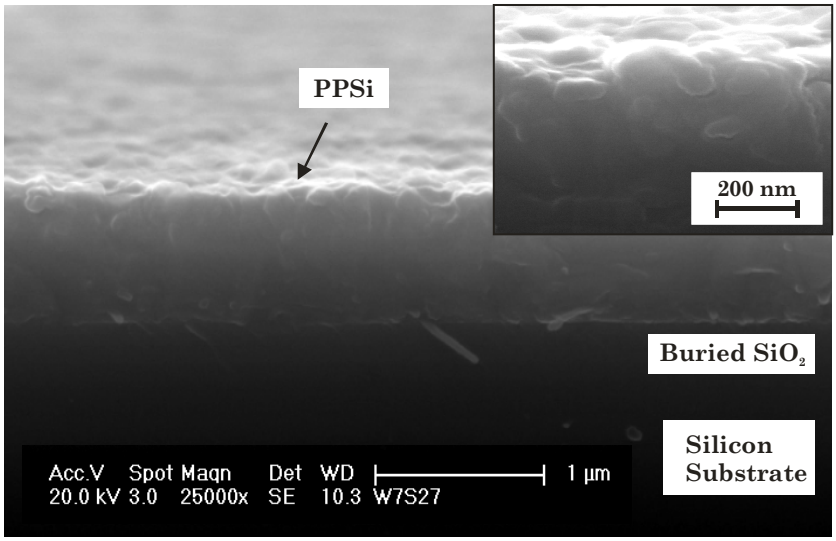

Figure 3.14: Cross-sectional view secondary electron FEGSEM micrograph of sample *W7S27* ($R_s \approx$ (28.67 ± 0.59) Ω/sq) stain-etched in a 1:3:5 volume ratio of HF:HNO_3:H_2O for 35 s. The inset shows the same area at higher magnification

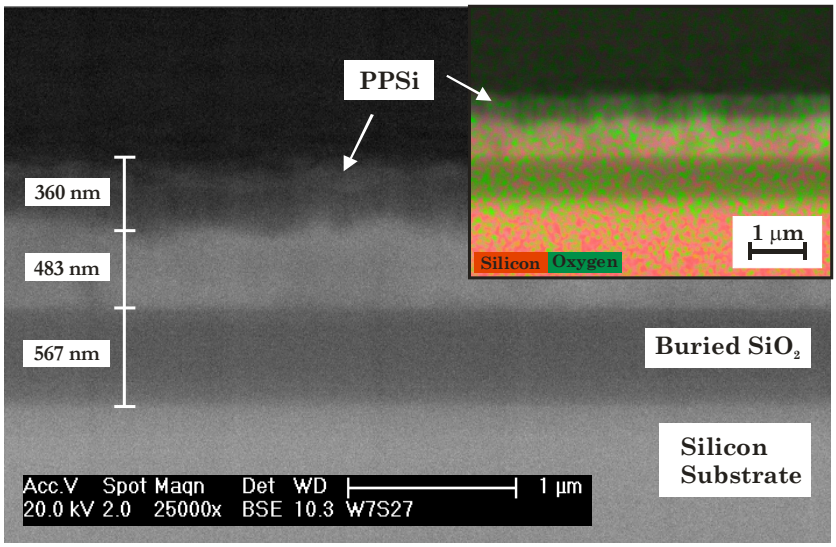

Figure 3.15: Cross-sectional view FEGSEM micrograph of sample *W7S27*, at the same area as in Figure 3.14, imaged by detecting the BSE, clearly showing a good contrast between the PPSi and polysilicon layers. The inset shows the EDX map of the sample with elements of silicon (red) and oxygen (green) highlighted.

uniform in thickness but the pore structure is not clearly visible even when imaged at high magnification (100,000 x).

However, when the sample *W7S27* was subsequently imaged using the BSE detector, a layer of dark contrast of thickness ~ 360 nm on top of the polysilicon layer, as depicted in Figure 3.15, could be observed. The layer, which is believed to be the PPSi structure, is clearly of a different elementary composition than the bulk polysilicon. When examined with the SEM-equipped energy-dispersive X-ray (EDX) map, a more concentrated oxygen component could be observed in the top layer of the polysilicon, as depicted in the inset of Figure 3.15. Since the sample was stored in high vacuum almost immediately after the stain etching, the thick layer of SiO_2 could not be ascribed to the formation of native oxide on the polysilicon layer. In fact, it is well-established that fresh PSi structure naturally oxidises when exposed to air [281]. In addition, stain-etched PSi and PSi that has been cleaned in DI water have been demonstrated to produce higher initial oxidation levels [282]. Hence, it is likely that the SiO_2 layer observed was formed as a result of natural oxidation of the PPSi structure. This provides a good evidence of the existence of the PPSi structure albeit not readily visible in the physical form (by SE imaging). An EDX spectrum would have provided both qualitative and quantitative elemental analysis with characteristic peaks and corresponding intensities (count) to better confirm the existence of the PPSi structure.

3.5.3.2 Stain Etching using Different Volume Ratios

PPSi structures have also been observed when a different chemical composition was used for the stain etching process. For instance, when the sample *W7S15* (see Figure 3.11 (d) for optical microscope image and Table 3.5 for full etching conditions) was stain-etched in a 1.3:6:15 volume ratio solution of $HF:HNO_3:H_2O$, a PPSi structure readily visible under SEM, as depicted in Figure 3.16, was produced. The sample was stain-etched for 5 minutes, but the formation of bubbles was only observed 4 minutes after the immersion of the sample into the etching solution. The PPSi is measured to be around 250 nm thick, with a remaining un-etched polysilicon layer of 565 nm thickness. The pores appear to be branched and roughly aligned to the source of the holes injection point. Due to the limitation of the SEM machine (with respect to obtaining a better resolution image), the pore size is estimated to be

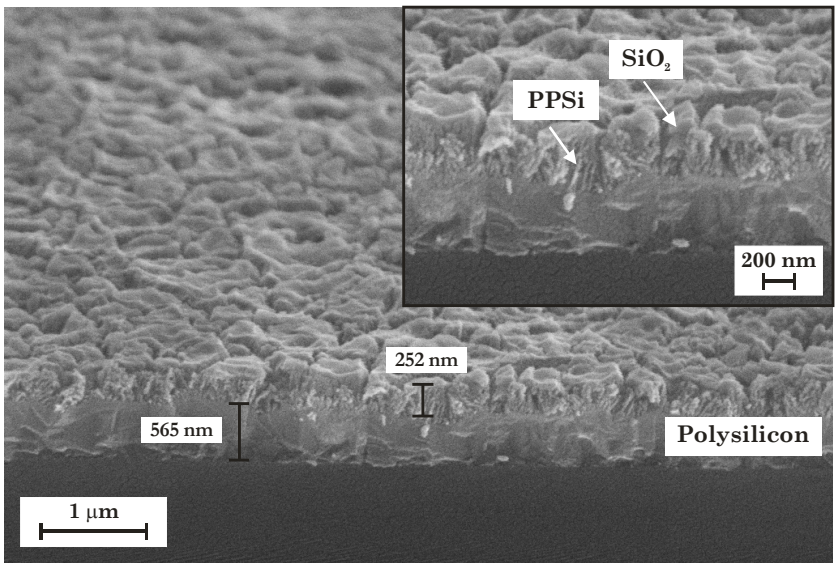

Figure 3.16: Oblique view SEM micrograph showing the PPSi structure formed by stain etching of sample *W7S15*($R_s \approx (28.67 \pm 0.59)$ Ω/sq), using a 1.3:6:15 volume ratio of HF:HNO_3:H_2O for 5 minutes. The inset shows the same area at higher magnification.

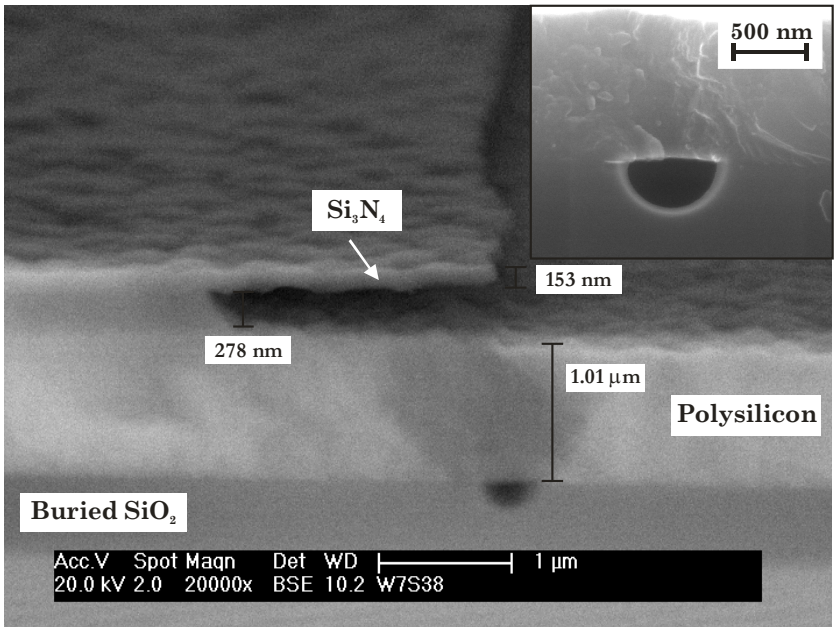

Figure 3.17: Cross-sectional view BSE, FEGSEM micrograph showing the etching of buried SiO_2 of sample *W7S38* ($R_s \approx (28.67 \pm 0.59)$ Ω/sq) stain-etched in a 500:1 volume ratio of HF:HNO_3 for 30 s. The inset shows the magnified view of the hole etched in the buried SiO_2 imaged by SE.

between 30 nm and 50 nm. A layer of capping material, thought to be SiO_2, can also be observed and is believed to be formed as a result of long oxidation in an ambient environment, as the SEM was taken almost 1 ½ years after the stain etching process.

In a slightly different system, where a significantly higher proportion of HF is used [246, 266], a PPSi structure, as depicted in Figure 3.17, could be observed. The sample *W7S38* ($R_s \approx (28.67 \pm 0.59)$ Ω/sq) was stain-etched in a 500:1 volume ratio of HF:HNO_3 for 30 s (see Table 3.5 for full etching conditions). A significant etching of the masking SiO_2 layer, which created an undercut of ~ 2 μm at the Si_3N_4 layer, could be observed. Interestingly, the polysilicon thickness remained at ~ 1 μm and yet, some of the buried SiO_2 layer has been attacked by the stain etching solution, as clearly depicted in the inset of Figure 3.17. This finding is unique and is likely to have been caused by the stain etching solution permeating the polysilicon layer. Hence, the polysilicon is very likely to be porous, at least in the region where the hole has been created. The PPSi structure formed here is believed to be in micropore regime, as deduced by the AFM analysis (discussed in §3.5.3.4, see Figure 3.22 and related text).

3.5.3.3 Investigation of the Effect of Substrate Resistivity

In the experiment to investigate the effect of different polysilicon resistivity (product of R_s and film thickness) levels on the stain etching process, the incubation time, t_i of each sample during the process was monitored (as described in §3.5.2.1) as one of the parameters for analysis. The t_i was believed to be the period required for the accumulation of sufficient HNO_2 and the initiation of preferential etching [242]. It has been demonstrated to be a function of the type and resistivity of the substrate. In fact, it was reported that, when silicon substrates were stain-etched in a 1:3:5 volume ratio of HF:HNO_3:H_2O, an increased resistivity of the p-type silicon substrates resulted in an extended incubation time; while for the n-type silicon substrates, a reduced incubation time was observed with an increased resistivity [249].

In this experiment, the t_i, as tabulated in Table 3.7, was observed to be more than 75 s for all the 8 samples evaluated. In fact, a t_i of > 100 s was observed for

samples with R_s ≈ (28.67 ± 0.59) Ω/sq. This is inconsistent with previous observations, where "productive" etching was observed within a total etching time (inclusive of t_i) of less than 60 s on samples (with R_s ≈ (28.67 ± 0.59) Ω/sq)) stain-etched in a 1:3:5 volume ratio of HF:HNO_3:H_2O (see Table 3.5 for example samples and [276]). It is believed that the fresh etching solution used in this experiment could have extended the t_i; in previous experiment, the stain etching solution was re-used, and hence accumulation of HNO_2 could have primed the etching process.

Sample	Type	Sheet Resistance (Ω/sq)	Incubation time, t_i (s)	Averaged t_i (s)
W8S11	p-type	28.67 ± 0.59	105	107 ± 2.8
W8S12			109	
W3S11		32.54 ± 0.19	105	97 ± 11.3
W3S12			89	
W9S11		338.94 ± 4.95	189	165.5 ± 33.2
W9S12			142	
W15S04	n-type	>> 1000	85	80 ± 7.1
W15S05			75	

Table 3.7: Measured incubation time during stain etching of samples with various levels of sheet resistance (refer to Table 3.6). These samples have been stain-etched in a 1:3:5 volume ratio of HF:HNO_3:H_2O. The detailed sample preparations are described in the §3.5.2.1.

In general, the t_i was found to be dependent on the type and the resistivity of the substrate. For the 8 samples evaluated, it was observed that the phosphorus-doped n-type samples, despite having the highest R_s (>> 1000 Ω/sq), required the shortest t_i, of 80 s ± 7.1 s, to initiate a "productive" stain etching process. The conjecture that a reduced t_i correlates to an increased resistivity in n-type substrates (as proposed by [249]), however, could not be verified since only one resistivity of the n-type substrate was available for evaluation.

For the four p-type samples (*W8S11*, *W8S12*, *W3S11* and *W3S12*) with the lowest two R_s ((28.67 ± 0.59) Ω/sq and (32.54 ± 0.19) Ω/sq), the t_i was very similar (between 105 s and 109 s), except for one sample (*W3S12*) which has a shorter t_i of 89 s. Samples *W9S11* and *W9S12* with higher R_s (32.54 ± 0.19) Ω/sq exhibited a longer incubation time; this dependency of t_i on R_s is similar to the findings by [249]. However, with the distribution of only 6 data points (from the 6 p-type samples evaluated), it is insufficient to produce a statistical correlation to establish if the t_i is indeed linearly related to the resistivity of the substrate.

Four of the 8 polysilicon samples (*W8S11*, *W3S11*, *W9S11* and *W15S04*) were then examined using the SEM to establish the effect of different substrate resistivity on the morphology of the porous structure. The p-type sample with low boron doping (*W9S11*, $R_s \approx (338.94 \pm 4.95)$ Ω/sq) and the n-type sample (*W15S04*, $R_s >> 1000$ Ω/sq) both exhibit similar irregular hillocks with cracking, as depicted in Figure 3.18 and Figure 3.19, respectively. These PPSi structures appear to be similar to those previously reported [188, 283], and has been ascribed to lateral strain induced during the porosification process [283]. The lateral strain is believed to result from the disturbed lattice forces in the silicon crystal as the silicon near the surface region is removed. This causes the formed columnar porous structures to collapse in order to compensate the differential strain, hence forming the hillocks. The effect is believed to be more severe in polysilicon due to preferential etching at the grain boundaries, resulting in cracking in the PPSi and this propagating to the underlying polysilicon layer. In fact, since a similar observation was observed in both p- and n-type samples, as depicted in Figure 3.18 and Figure 3.19, respectively, this cracking phenomenon appears to be independent of the type of the substrate.

Characteristically rough surfaces with shallow pits, as discussed previously on samples *W7S35* and *W7S27* (both with $R_s \approx (28.67 \pm 0.59)$ Ω/sq) have also been observed on the highly-doped p-type samples (*W8S11* and *W3S11*, with $R_s \approx (28.67 \pm 0.59)$ Ω/sq and (32.54 ± 0.19) Ω/sq, respectively). However, when the top surface of sample *W8S11* was examined by SEM, some tiny circular pits, in the range of 40 nm to 50 nm in diameter, resembling pores could be observed at certain areas of the sample; while a crack-like structure, as depicted in the inset of Figure 3.20, could be observed in other areas. This distinctive variation in morphology, observed on sample *W8S11*, is a further evidence of the non-uniform etching of the stain etching process. The tiny pits appear mostly near the grain boundaries of the polysilicon, suggesting that the preferential etching has just started and the porosification rate could be very slow. However, at other areas of the sample, the favourable local environment, perhaps as a result of trapped bubbles, increased the porosification process, hence resulting in the cracking phenomenon, discussed previously.

In addition, in this experiment, the stain-etching process did not appear to etch the stain-etched PPSi layer; the final thickness of the PPSi layer (~ 700 nm to 1 μm for *W9S11* and *W15S04*) plus the remaining polysilicon layer was ~ 1 μm for the

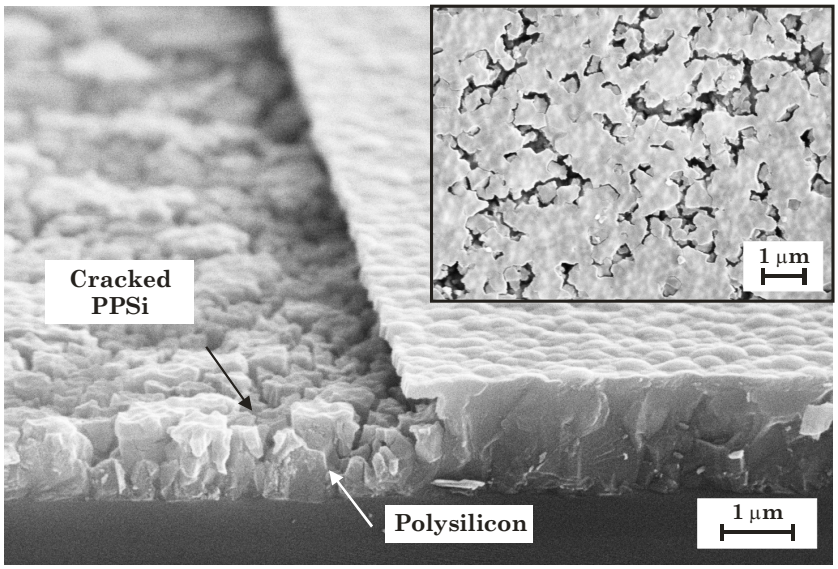

Figure 3.18: Oblique cross-sectional view SEM micrograph showing the crack-like porous structure on the low boron doping p-type sample *W9S11* ($R_s \approx (338.94 \pm 4.95)$ Ω/sq; stain-etched in a 1:3:5 volume ratio of HF:HNO_3:H_2O for (189 + 30) s). The inset shows the plane-view SEM micrograph of the sample imaged at a different area.

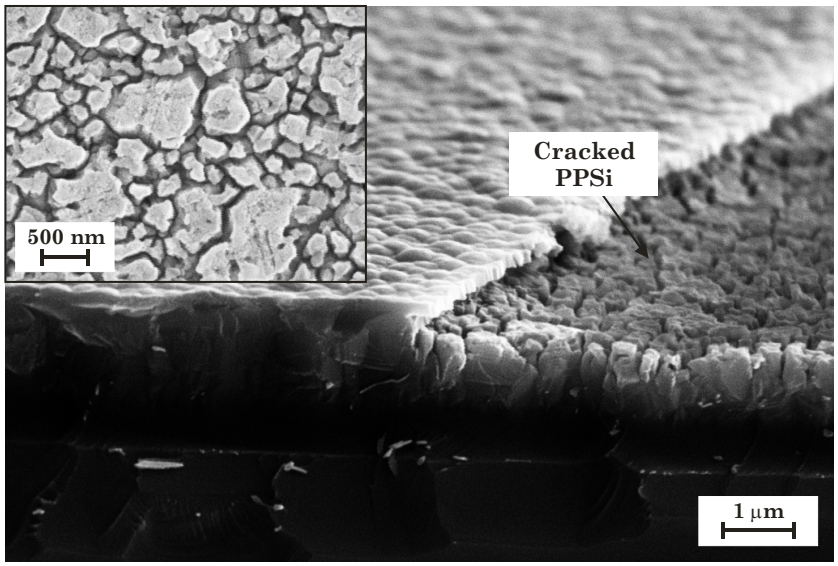

Figure 3.19: Oblique cross-sectional view SEM micrograph showing the crack-like porous structure on the n-type sample *W15S04* ($R_s >> 1000$ Ω/sq; stain-etched in a 1:3:5 volume ratio of HF:HNO_3:H_2O for (85 + 30) s). The inset shows the plane-view SEM micrograph of the sample imaged at a different area.

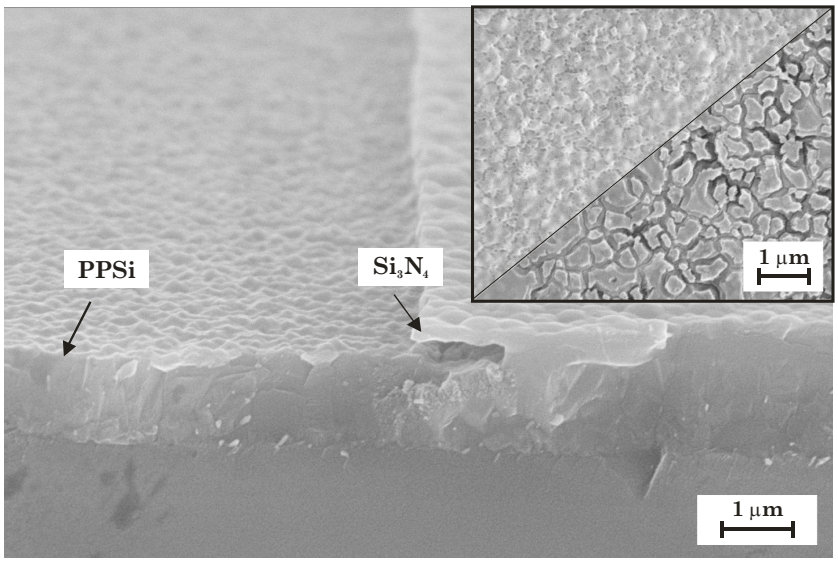

Figure 3.20: Oblique cross-sectional view SEM micrograph showing the porous structure on the highly-doped p-type sample *W8S11* ($R_s \approx (28.67 \pm 0.59)$ Ω/sq; stain-etched in a 1:3:5 volume ratio of $HF:HNO_3:H_2O$ for (105 + 40) s). The inset shows the plane-view SEM micrograph of the sample at two different areas with distinctly different morphology.

four samples (*W8S11*, *W3S11*, *W9S11* and *W15S04*) observed. This is different from the behaviour of the stain etching process discussed previously (in the experiment to re-examine the stain etching process), whereby the remaining (PPSi and polysilicon) structure is significantly less than 1 μm (such as that of samples *W7S35* and *W7S27*, as depicted in Figure 3.12 and Figure 3.15, respectively). It is proposed that the stain etching process used in this experiment was more effective, as preferential etching to create random pores was faster than the etch polishing that removes the polysilicon uniformly. The factor that contributes to this phenomenon is postulated to be the fresh solution used during each etching, which inevitably also results in a more extended incubation time.

3.5.3.4 Atomic Force Microscopy

In order to better understand the surface topography and the 3-dimensional structure of the PPSi sample, the AFM is used. The AFM is one of the scanning probe microscopy (SPM) methods, first developed in 1986 by Binnig and co-workers [284]. Instead of using an electron or light source, like in a SEM or optical microscopy, SPM uses a probe or a tip to investigate the sample by sensing the tunneling current (as in the Scanning Tunneling Microscope (STM)), the deflection of

the probe (as in AFM) or the evanescent wave of the scattered light (as in Near-field Scanning Optical Microscope (NSOM)) [285].

A typical AFM system primarily consists of a cantilever with a sharp tip, a laser system and a position-sensitive photodetector (PSPD) [285]. The sharp tip, often less than 10 nm in diameter at the apex, is located at the free end of the cantilever. The tip can either make soft physical contact with the sample (as in the contact mode), be vibrating near (tens to hundreds of Å) the surface of a sample (as in the non-contact mode) or be vibrating while intermittently in soft contact with the sample (as in the tapping mode). When a sample is scanned under the tip, forces between the tip and the surface of the sample cause the cantilever to either bend or deflect. The movement of the cantilever is measured by the laser and the PSPD and the data is corrected to provide a map of the surface topography.

The contact AFM could operate in one of two modes – constant height or constant force mode [285]. In the constant height mode, the height of the scanner is fixed during the scan; hence the deflection of the cantilever can be used directly to evaluate the surface topography. This mode is more often used for taking atomic resolution images of samples with atomically flat surfaces. In contrast, with the constant force mode, the deflection of the cantilever is fixed. The feedback circuit then moves the scanner up and down during scanning, hence generating the topographic data. This is the preferred mode as the force exerted onto the sample is kept constant and can be well controlled.

The AFM images presented in the following discussion have been obtained using the Omicron NanoTechnology Scanning Probe Microscope at Prof. B. Hamilton's group at the University of Manchester. The Omicron SPM, which is normally maintained at pressures around 10^{-10} mbar, is an ultra high vacuum (UHV) multi-mode SPM capable of carrying out contact and non-contact AFM, and also scanning tunnelling microscopy and spectroscopy. The acquired raw AFM data was typically processed using a SPM image processing software (SPIP™, Image Metrology) to correct for plane distortions. To improve the colour contrast, a typical cut-off of 1.5 standard deviation (or 5 % to 91 % of the full colour map) was used so that only the features of interest are clearly revealed. All of the samples analysed

using the AFM were from the experiment to re-examine the stain etching parameters and the details of the samples are summarised in Table 3.5.

Figure 3.21 depicts 3-dimensional representations of the AFM topography of the polysilicon surface of sample *W7S38* prior to and after the stain etching process. The AFM was carried out in air using a diamond-coated, doped Si conductive tip (radius of curvature ~ 175 nm) operating in the constant force contact mode. The sample was cleaned in acetone for 5 minutes prior to the AFM measurement. The surface of the polysilicon prior to the stain etching process (Figure 3.21 (a)) was observed to be granular and similar to the rough surface observed using SEM (as depicted in Figure 3.10) and that reported in the literature [264]. The root mean square (RMS) roughness (of the AFM image in Figure 3.21 (a)) was measured to be 19.4 nm. The granules or hillocks, which average between 300 nm and 500 nm in width, are believed to be the grains of the polysilicon.

After a stain etch in a 500:1 volume ratio solution of HF:HNO_3 for 30 s, the sample *W7S38* (see Figure 3.17 for SEM micrograph and Table 3.5 for processing details of this sample) shows a similar rough structure (with RMS roughness of 19.1 nm). However, some smaller granule-like features in between the larger hillocks, as depicted in the 3-dimensional AFM representation in Figure 3.21 (b), can be observed. When a reduced area of 2 μm by 2 μm was scanned, as depicted in Figure 3.22, the higher resolution AFM revealed that these smaller features are indeed on the surface of the hillocks or the polysilicon grains. These fine features could be a collection of a wide range of pore sizes at the surface, which have been imaged as a continuous curve due to tip convolution; the tip could have completely missed or underestimated the depth of very narrow features [286]. This potentially justifies the postulation of the existence of microporous structure in PPSi which could not be readily examined using SEM (in Figure 3.17).

A typical AFM image of a PPSi structure stain-etched with the standard etching system of HF:HNO_3:H_2O is depicted in Figure 3.23. The sample *W5S05* (see Table 3.5 for detailed pre- stain etch treatment) was first pre-etched in a 1:5:5 volume ratio of HF:HNO_3:H_2O for 10 s, followed by a stain etch in a 1:3:5 volume ratio of HF:HNO_3:H_2O for another 10 s. Immediately after that, the sample was put

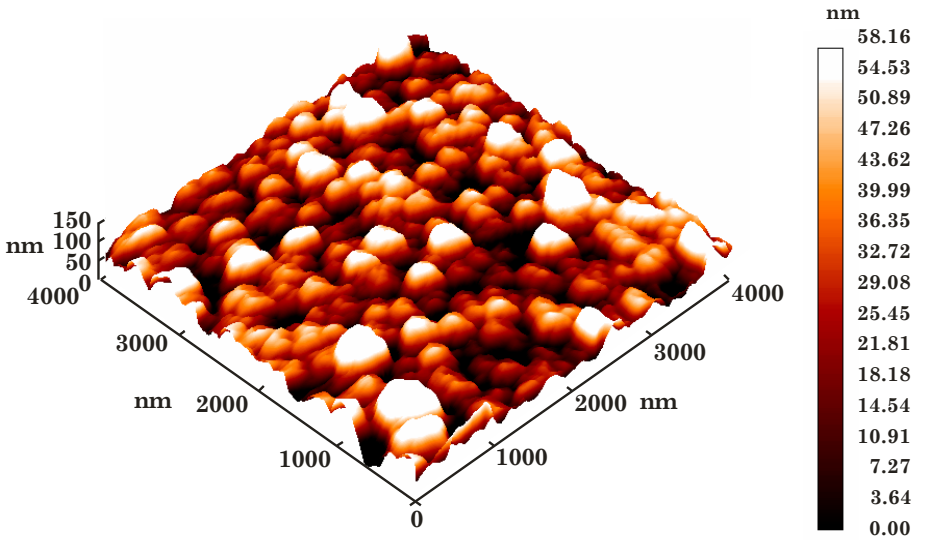

(a) prior to stain etching

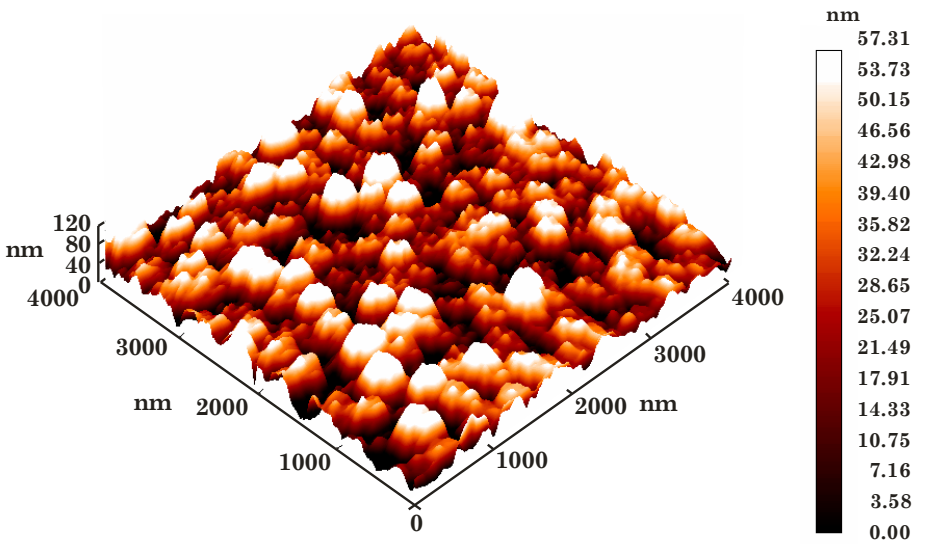

(b) after stain etching

Figure 3.21: 3D AFM image (4 µm x 4 µm) of sample *W7S38* ($R_s \approx (28.67 \pm 0.59)$ Ω/sq) (a) prior to and (b) after a stain etch in a 500:1 volume ratio of HF:HNO_3 for 30 s.

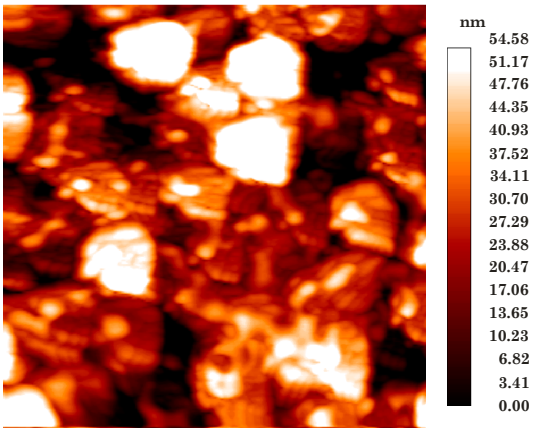

Figure 3.22: 2D AFM topography image (2 µm x 2 µm) of sample *W7S38* ($R_s \approx (28.67 \pm 0.59)$ Ω/sq) about centre of the area scanned in Figure 3.21 (b).

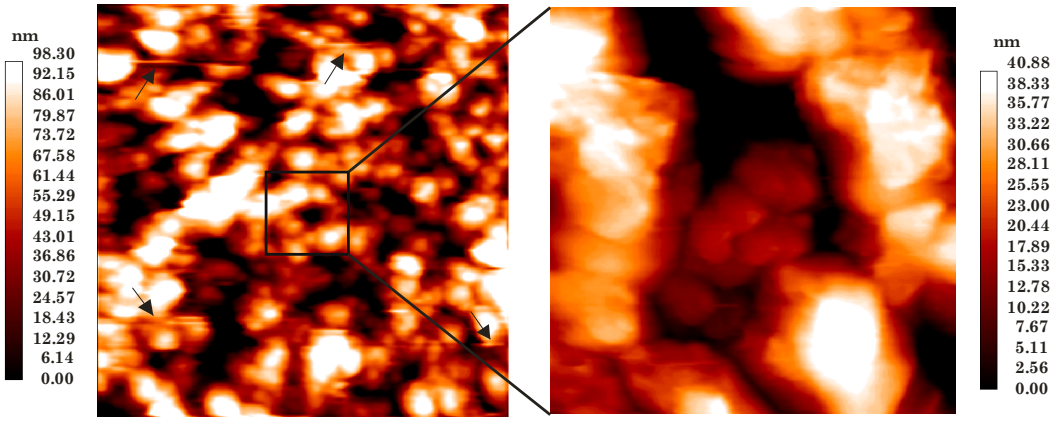

Figure 3.23: 2D AFM image with an area of (a) 2.5 µm x 2.5 µm and (b) 0.5 µm x 0.5 µm of sample *W5S05* ($R_s \approx (28.67 \pm 0.59)$ Ω/sq) after a pre-etch in a 1:5:5 volume ratio of HF:HNO_3:H_2O for 10 s, followed by a stain etch in a 1:3:5 volume ratio of HF:HNO_3:H_2O for 10 s. The arrows indicate the present of streaking artefacts.

into the vacuum at the load-lock of the Omicron SPM to minimise the build-up of native oxide. The AFM was carried out in UHV using a platinum-iridium (Pt-Ir) coated Si tip (radius of curvature ~ 25 nm) operating in the constant force contact mode. As depicted in Figure 3.23, the PPSi structure of stain-etched sample *W5S05* exhibits similar granular features (such as those depicted in Figure 3.22), but with greater height variation (~ 98 nm as compared to ~ 55 nm depicted in Figure 3.22) across the scanned area. The granules or hillocks are also observed to be smaller in size (between 100 nm and 200 nm). Some random etch pits with irregular shape, which may indicate the present of pores, could be observed. However, a subsequent AFM scan with a reduced area of 500 nm by 500 nm (about the centre of the area depicted in Figure 3.23 (a)) reveals additional granular-like features on the etch pit,

suggesting no existence of apparent pores (within the resolution limit of the AFM system). During the AFM measurements of sample *W5S05*, streaking in the acquired AFM images could be observed even after a few scans of the same area. This could be due to the present of loose debris on the sample surface which interacts strongly with the tip.

3.5.4 Summary

The implication of stain etching parameters (etching time and chemical composition) on the formation of PPSi has been investigated. Variations in the surface appearance of the stain-etched samples, as depicted in Figure 3.11, which implies a divergence of porous structure and thickness, could be observed by the naked eye and with an optical microscope. These variations appeared locally on a sample (for instance, sample *W7S28*; stain-etched in a 1:5:5 (15 s) followed by a 1:3:5 (15 s) volume ratio of $HF:HNO_3:H_2O$) and across samples processed in identical etching times and chemical composition (for instance, samples *W5S28* and *W5S38*, both with $R_s \approx (28.67 \pm 0.59)$ Ω/sq and stain-etched in a 1:3:5 volume ratio of $HF:HNO_3:H_2O$ for 25 s). These observations, to some extent substantiate the irreproducibility and non-uniformity associated with porous structure formed by using stain etching, often reported in the literature [180, 225, 242, 249].

In general, most samples prepared by the stain etching method do not produce a PPSi film with a distinct pore morphology or clear microstructural characteristics observable using the SEM and the AFM. In fact, most of the PPSi structures observed under SEM and AFM often show a rough surface with shallow pits or a cracked structure, as summarised in Table 3.8. The rough surface exhibited by most samples (such as *W7S35* and *W5S05*, see Table 3.8 for details) may be an indication of a chemical polishing instead of a "productive" porosification of polysilicon; the random, preferential etching of the polysilicon may have been suppressed by the uniform chemical etching. In contrast, the cracked-like PPSi structure (as observed on samples *W9S11* and *W15S04*, see Table 3.8 for details) is believed to result from the intense preferential etching, especially at the grain boundaries of the polysilicon layer.

Sample	Doping of Polysilicon	Sheet Resistance (Ω/sq)	Stain Etching Conditions	Characterisations	Comments
W7S35	Boron, p-type	28.67 ± 0.59	1:5:5 (15 s) then 1:3:5 (15 s) volume ratio of $HF:HNO_3:H_2O$	FEGSEM (Figure 3.12 and Figure 3.13)	Rough surface with 20 nm to 30 nm interconnected pores; thin (~ 70 nm) PPSi layer; huge undercut suggesting vigorous etching
W7S27	Boron, p-type	28.67 ± 0.59	1:3:5 (35 s) volume ratio of $HF:HNO_3:H_2O$	FEGSEM (Figure 3.13); BSE and EDX map (Figure 3.15)	Similar to *W7S35*; BSE and EDX map suggest existence of PPSi of ~ 360 nm thick
W7S15	Boron, p-type	28.67 ± 0.59	1.3:6:15 (5 min) volume ratio of $HF:HNO_3:H_2O$	SEM (Figure 3.16)	Best PPSi observed, 30 nm to 50 nm branched pores, ~ 250 nm thick PPSi layer
W7S38	Boron, p-type	28.67 ± 0.59	500:1 (30 s) volume ratio of $HF:HNO_3$	FEGSEM and BSE (Figure 3.17); AFM (Figure 3.21 and Figure 3.22)	Rough surface; PPSi possibly exists shown by etched buried SiO_2
W9S11	Boron, p-type	338.94 ± 4.9	1:3:5 (189 s + 30 s) volume ratio of $HF:HNO_3:H_2O$	SEM (Figure 3.18)	Crack-like PPSi structure similar to that reported [188, 283], ~ 800 nm to 1 μm thick
W15S04	Phosphorus, n-type	>> 1000	1:3:5 (85 s + 30 s) volume ratio of $HF:HNO_3:H_2O$	SEM (Figure 3.19)	Similar to *W9S11*, ~ 700 nm to 1 μm thick
W8S11	Boron, p-type	28.67 ± 0.59	1:3:5 (105 s + 40 s) volume ratio of $HF:HNO_3:H_2O$	SEM (Figure 3.20)	Rough surface with tiny circular pits (40 nm to 50 nm in width) at some areas; crack-like PPSi structure in other areas
W5S05	Boron, p-type	28.67 ± 0.59	1:5:5 (15 s) then 1:3:5 (15 s) volume ratio of $HF:HNO_3:H_2O$	AFM (Figure 3.23)	Granular-like topography with hillocks between 100 nm and 200 nm in width

Table 3.8: Summary of selected samples discussed in this section, with their corresponding sheet resistance, stain etching conditions and characterisation methods. The order of the samples in the table follows the order as they first appeared in the text.

Nevertheless, there are indications of pore formation, such as the finding of EDX analysis (sample *W7S27*, see Figure 3.15) and the observation of etching of buried SiO_2 (sample *W7S38*, see Figure 3.17). It is proposed that the PPSi structures formed in these two samples (*W7S27* and *W7S38*) are in the micropore size regime (< 2 nm), where the imaging of this kind of porous structure using SEM is more challenging due to the resolution limit of most of the SEM.

Based on the samples evaluated thus far (summarised in Table 3.8), the stain etching using a volume ratio of 1.3:6:15 of $HF:HNO_3:H_2O$ appears to produce the best PPSi structure which could be suitably used as drug reservoir. The sample (*W7S15* with $R_s \approx (28.67 \pm 0.59)$ Ω/sq) etched for 5 minutes (presumably inclusive of 4 minutes incubation time) using this volume ratio produced pores visible under SEM, as depicted in Figure 3.16, with a size in the range of 30 nm to 50 nm and a thickness of ~ 250 nm.

In the experiment to investigate the effect of substrate resistivity on the stain etching process, the incubation time, t_i, was found to increase with higher substrate resistivity in p-type samples. The substrate resistivity, however, did not seem to influence the resultant PPSi structure, as generally, similar PPSi structures (with cracking) can be observed in both p-type (such as *W9S11*, $R_s \approx (338.94 \pm 4.95)$ Ω/sq, as depicted in Figure 3.18) and n-type (such as sample *W15S04*, $R_s >> 1000$ Ω/sq, as depicted in Figure 3.19) samples after a stain etch in a 1:3:5 volume ratio of $HF:HNO_3:H_2O$ for 30 s past the t_i.

3.6 The Fabrication of Electrodes (Stage 3)

The development work, to fabricate the electrodes required for the drug delivery device (Stage 3 fabrication), was carried out in the cleanroom facility at the University of Manchester, concurrent to the work on the stain etching process described in §3.5. The aim is to establish a feasible revised lift-off process; this was due to the change of cleanroom facility which necessitated a modification to the proposed bi-layer photoresist (of PMGI and S1813 in Step (j)) in the lift-off process.

In this work, a single layer lift-off process was used instead. In order to ensure a good lift-off with a single layer process, the photoresist should be at least twice the thickness of the deposited metal film to be lifted-off. Since the aluminium electrodes are proposed to be 1 μm thick, the positive Shipley S1828 photoresist, which has a nominal thickness of 2.8 μm, was used. In addition, in order to improve the success of lift-off, an undercut can be formed by surface modification of the S1828 such that the top surface of the photoresist is hardened and hence dissolved in the photoresist developer at a slower rate than the bulk of the photoresist. Typically, this is achieved by soaking the photoresist coated wafer in toluene or chlorobenzene either before or after the UV exposure step [287].

3.6.1 Revised Lift-off Process: Setup and Procedures

Due to the restriction of wafer size (device wafers are 4 inch in diameter but most machines at the University of Manchester only capable of handling 3 inch wafers), individual chips or samples were used for the development work. A new 3" emulsion mask (see Appendix B.1.3 for mask layout) with the pattern of electrodes was designed and fabricated to comply with the mask aligner (Karl Suss MJB-3). The p-type polysilicon samples used for this work were manually scribed and cleaved from wafers 7 (*W7*, $R_s \approx (28.67 \pm 0.59)$ Ω/sq) and wafer 10 (*W10*, $R_s \approx (338.94 \pm 4.95)$ Ω/sq) of the batch K2714s.

The samples were first pre-treated to remove the photoresist (as detailed in §3.5.2) and stain-etched in a 1:3:5 volume ratio of HF:HNO_3:H_2O to form the PPSi structure; Table 3.9 summarises the detailed process parameters. Immediately after the stain etching process, the samples were dehydrated in an oven at 110 °C for at least 30 minutes. The S1828 photoresist was then spin-coated on the stain-etched sample at 4000 rpm for 40 s to 60 s. Next, the samples were pre-baked in an oven for 25 minutes at 90 °C. The samples were then cooled to room temperature before being immersed in chlorobenzene for 4 minutes to 6 minutes. Once gently blown dry using a nitrogen gun, the samples were exposed using the mask aligner with either a simple stripe pattern (2 mm wide stripe from an existing mask) or a four-square (1 mm by 1 mm) electrode pattern (from the 3 inch emulsion mask), as depicted in Figure 3.24. The exposure wavelength was 365 nm and exposure time ranged from

90 s to 100 s with a power density of 18 $mW \cdot cm^{-2}$. Finally, the sample was developed in a diluted 1:1 volume ratio of Shipley MICROPOSIT® developer: DI water, for 1 minute to 2 minutes. The samples were then immediately rinsed with copious amount of DI water to stop the developer from further etching the patterned photoresist.

Sample	Sheet Resistance (Ω/sq)	Pre-processing	Stain Etching Conditions
W7S14	28.67 ± 0.59	Photoresist stripped in RIE80. Cleaned with FNA (5 min) then rinsed in DI water (10 min).	1:3:5 (30 s) volume ratio of $HF:HNO_3:H_2O$
W7S25	28.67 ± 0.59	Photoresist stripped in FNA (5 min) then rinsed in DI water (10 min).	1:3:5 (30 s) volume ratio of $HF:HNO_3:H_2O$
W7S26	28.67 ± 0.59	Photoresist stripped in FNA (5 min) then rinsed in DI water (10 min).	1:3:5 (40 s) volume ratio of $HF:HNO_3:H_2O$
W10S40	338.94 ± 4.95	Photoresist stripped in RIE80. Cleaned with FNA (5 min) then rinsed in DI water (10 min).	1:3:5 (60 s) volume ratio of $HF:HNO_3:H_2O$

Table 3.9: Summary of the pre-processing and stain etching parameters used by the samples discussed in this section. All samples are boron-doped p-type polysilicon substrates.

Process		Samples			
		W7S14	*W7S25*	*W7S26*	*W10S40*
i)	Dehydration bake	110 °C in oven, 30 minutes			
ii)	Spin coat S1828 photoresist at 4000 rpm	60 s	60 s	60 s	40 s
iii)	Pre-bake	90 °C in oven, 25 minutes			
iv)	Chlorobenzene soak	5 minutes	5 minutes	5 minutes	4 minutes
v)	UV expose with mask	100 s	90 s	90 s	100 s
vi)	Develop in 1:1 Microposit developer: DI water	120 s	60 s	60 s	120 s
vii)	Attach to carrier using S1813 photoresist	110 °C in oven, 30 minutes			-
viii)	Aluminium evaporation	~ 1.2 μm	~ 1.4 μm	~ 1.4 μm	-
ix)	Lift-off of aluminium in acetone	Short (~ 30 s) ultrasonication	Extended (few minutes) ultrasonication and mechanical scrubbing		-

Table 3.10: Summary of the steps involved in the revised lift-off process and the relevant parameters used for selected samples. All samples have been pre-treated and stain-etched as detailed in Table 3.9.

The photoresist patterned samples were then attached to a carrier (a microscope glass slide or a cut wafer piece) using the Shipley S1813 positive photoresist. The carrier and the attached samples were then post-baked in an oven at 110 °C for 30 minutes, prior to the deposition of aluminium. Instead of using an e-beam evaporation, the aluminium was deposited using a modified thermal evaporator with aluminium pellets (99.999 % purity, Goodfellow Cambridge Ltd., UK) that are manually delivered using a custom-made feeding system [288] (see Chapter 4, §4.3.1 for more details). Here, aluminium of thickness between 1.2 μm and 1.4 μm was deposited. Finally, to realise the aluminium electrodes, the samples were immersed in acetone (sometimes with ultrasonication) to dissolve the photoresist and, hence, achieve lift-off and removal of the aluminium at the unwanted areas. The exact process parameters of selected samples, used during the lift-off process, are summarised in Table 3.10.

3.6.2 Fabrication Results and Issues

Figure 3.24 depicts the digital photographs (captured using Canon IXUS 55, 5 megapixels) of samples *W10S40* and *W7S26* (see Table 3.9 and Table 3.10 for details of samples and processing conditions) after the photolithography patterning of the S1828 photoresist. The thickness of the S1828 was measured using a stylus profilometer (Talystep 1, Rank Taylor Hobson) and was found to range from 2.8 μm to 2.9 μm. Some photoresist defects, such as pinholes and particulate contamination, could be observed but this was not critical. In most cases, the chip-level alignment marks (120 μm by 120 μm, at the four corners of the chip) were not properly developed due to an edge bead effect, which is particularly severe in photolithography with small samples. The problem is not critical, as this is the last photolithography step of the fabrication process. The edge bead problem is typically overcome by using commercially available edge bead remover solvent (such as Microposit EBR-10A) or by additional exposures of the edge (prior to pattern exposure) using a suitable mask.

After the aluminium deposition, the samples were immersed in acetone to remove the photoresist for the lift-off of the aluminium film. Samples with a simple two contact pads pattern (such as sample *W7S14*, as depicted in Figure 3.25 (a))

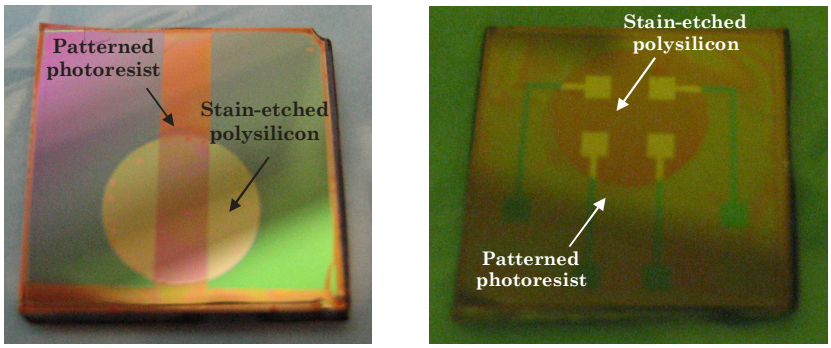

(a) *W10S40* (b) *W7S25*

Figure 3.24: Digital photographs of samples (a) *W10S40* and (b) *W7S25* patterned with photoresist S1828, ready for aluminium evaporation to realise (a) a simple two contact pads as electrodes and (b) a four-square (1 mm by 1 mm) electrode pattern. Both the samples have been processed up to step (vi) as detailed in Table 3.10.

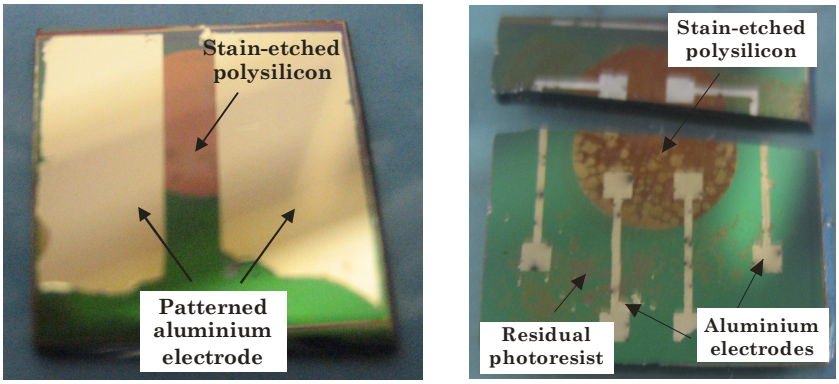

(a) *W7S14* (b) *W7S26*

Figure 3.25: Digital photographs of aluminium patterned samples after lift-off process: (a) *W7S14* with a simple two contact pads pattern; and (b) *W7S26* with a four-square (1 mm by 1 mm) electrode pattern.

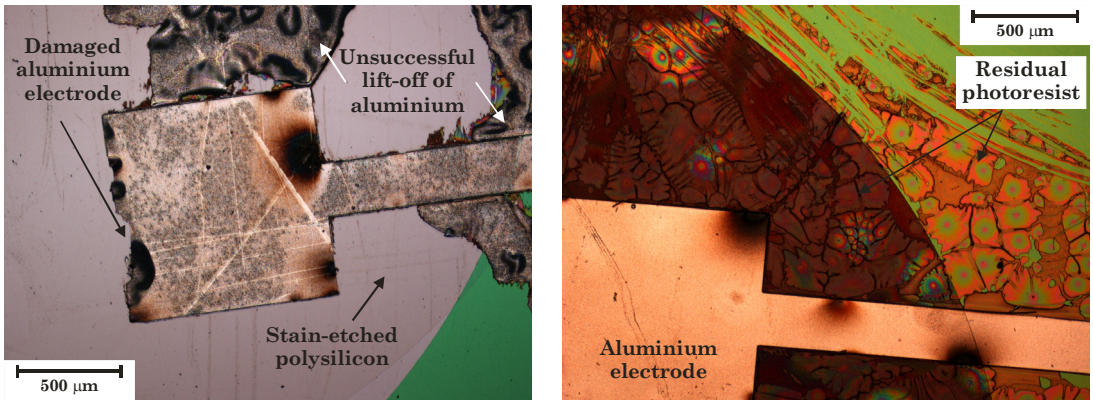

(a) *W7S25* (b) *W7S26*

Figure 3.26: Optical microscope images showing samples (a) *W7S25*; and (b) *W7S26* after the lift-off process. Aluminium electrode was partially damaged in (a) with some "left-over" aluminium due to unsuccessful lift-off. In (b), residual photoresist can be observed even after ultrasonication and mechanical scrubbing.

were found to easily achieve a successful lift-off. The S1828 dissolved in acetone after a quick (~30 s) ultrasonication. The aluminium electrode at one edge of the pads was found to have peeled off from the surface during the process, as depicted in Figure 3.25 (a), possibly due to poor adhesion to the Si_3N_4 surface of the aluminium film.

In contrast, samples with the actual electrode pattern (such as sample *W7S26*, as depicted in Figure 3.25 (b)) showed a less successful lift-off process even after mechanically scrubbing (using a cotton bud) the surface of the samples during the ultrasonication in acetone. This is believed to be mainly due to the S1828 photoresist becoming hardened as a result of overheating during the aluminium evaporation. The "burnt" S1828 showed severe cracking and was very difficult to remove as it adheres well to the surface of the samples (see example depicted in Figure 3.26 (b)). Due to excessive scrubbing, scratch marks were observed on many regions of these samples (such as samples *W7S25* and *W7S26*) and some regions of the electrodes were found to be damaged (see example depicted in Figure 3.26 (a)). In both samples (*W7S25* and *W7S26*), the aluminium electrode was observed to exhibit black-rusty-like (possibly oxidised) patches, at some arbitrary regions, likely to be due to high temperature treatment during the evaporation process.

The development of the lift-off process described here provides a number of useful observations. Firstly, the conditions necessary for the aluminium evaporation are critical, most importantly over-heating must be avoided. Photoresist which has been exposed to high temperature is difficult to remove in the subsequent lift-off process (Step (j)) and hence damaged electrodes can result. Secondly, the thickness of the photoresist and accessibility to the sacrificial photoresist layer via an undercut both influence the success of the single-layer lift-off process. A thicker photoresist and a greater undercut improve the success of the lift-off. Finally, the aluminium layer adheres mostly on the sample without the need for a quick dip in BHF to remove the native oxide.

There are several issues that have not been extensively assessed in this development work. Firstly, the level of residual photoresist, which may have been trapped in the porous structure after a successful lift-off step, has not been fully investigated. The PPSi structure should retain its porosity and be free of photoresist at the end of the lift-off step, to allow for the loading of the therapeutic agents.

Secondly, the level of impregnation of aluminium into the pores has not been extensively studied. It is desirable that the evaporated aluminium infiltrates well into the porous structure to make a good electrical contact (to fulfil design requirement (III)). These issues, however, can be better examined when a suitable PPSi structure has been fabricated.

3.7 Conclusion

This chapter describes the design and the fabrication of a porous polysilicon (PPSi) based drug delivery device, with an emphasis on the development of a stain etching process to form a suitable PPSi structure for incorporation as a drug reservoir.

During the Stage 1 fabrication of the device, the ion implantation process (Step (c)) effectively yielded only two different resistivity levels of boron-doped p-type polysilicon layers. The sheet resistance of the high boron doping (dose of 1 x 10^{16} cm^{-2} at 80 keV) and medium boron doping (dose of 5 x 10^{15} cm^{-2} at 80 keV) p-type polysilicon layers were found to be very similar (measured to be (28.67 ± 0.59) Ω/sq and (32.54 ± 0.19) Ω/sq, respectively) and were confirmed by a process simulation detailed in §3.4.1.1.

The investigation of the stain etching process to form the PPSi structure (Stage 2) resulted in mixed conclusions. Based on the evidence obtained by SEM and AFM, the stain etching on sample *W7S15* (with $R_s \approx$ (28.67 ± 0.59) Ω/sq) using a 1.3:6:15 volume ratio of HF:HNO_3:H_2O appears to produce the best PPSi structure, which may be suitable as a drug reservoir. By stain etching in the mentioned system for 5 minutes, branched pores in the range of 30 nm to 50 nm in width, and a thickness of ~ 250 nm have been produced (see Figure 3.16).

However, in general, most samples prepared by the stain etching process, do not produce a PPSi film with a distinct pore morphology or microstructural characteristics observable using SEM and AFM. Most of the PPSi structures observed under SEM have hillocks, cracked or rough surfaces, as summarised in Table 3.8. There are indications of pore formation, such as the findings of EDX

analysis (sample *W7S27*, see Figure 3.15) and the observation of etching of buried SiO_2 (sample *W7S38*, see Figure 3.17), but these observations alone could not quantitatively characterise the physical properties (in particular, the pore width, inter-pore spacing and porous thickness) of the formed PPSi structure.

The development work on a revised lift-off process to fabricate the electrodes (Stage 3) is preliminary and is greatly dependent on the outcome of the formation of PPSi in Stage 2 fabrication. Some potential fabrication issues and challenges were identified. The evaporation of the 1 μm thick aluminium must be carefully carried out to avoid over-heating of the photoresist and substrate. Photoresist that was exposed to a high temperature was found to be difficult to remove in the subsequent lift-off step, which can result in damaged electrodes (as depicted in Figure 3.26). The revised lift-off process used a single layer of S1828 positive photoresist, with a chlorobenzene soak of 5 minutes to surface modify the S1828 to achieve an undercut for successful lift-off. An exposure time of 90 s (with a power density of 18.3 mW/cm^2) and a development time of 60 s were found to be sufficient to pattern the S1828. Further work is still needed to investigate the level of residual photoresist after the lift-off process. The impregnation of aluminium into the porous structure needs to be investigated to ensure a good electrical contact.

The lack of success in obtaining well-characterised PPSi structures formed by the stain etching processes tested, increases the reliability issues in the entire fabrication of the drug delivery device. This also casts doubt as to whether a PPSi structure formed in this way would be suitable as the reservoir of the drug delivery device. The size of the pores created thus far was estimated to be in the micro- to mesopore size regimes. Typical sizes of proteins and peptides are often in the size regime of 5 nm to 20 nm [61, 228]. Hence, a microporous structure (< 2 nm in width) may be too small to entrap proteins and peptides; while protein loading into the mesoporous structure (2 nm to 50 nm in width) may be very challenging. The random pore structure and the self-limiting thickness of PPSi structure formed by stain etching further increased the need to investigate alternative, novel methods, such as those discussed in Chapter 4 and Chapter 5, to fabricate a more orderly and reproducible porous structure, in the size range of 50 nm to 100 nm.

Chapter 4

The Fabrication of Porous Polysilicon using a Porous Anodic Alumina Template

4.1 Introduction

Conventionally, ordered porous silicon (PSi) structures have been fabricated by the electrochemical etching of a silicon substrate that is pre-patterned with ordered starting pits. These predefined pits are created firstly by the fabrication of a patterned masking layer, and then the creation of pits by anisotropic etching into silicon using an alkaline-based etchant such as potassium hydroxide [165, 166, 289, 290]. The diameter of the pores and the interpore distance is usually restricted in size (typically > 1 μm with contact optical lithography). This size restriction is due to the limitation of the optical lithography process, which is typically used to define a masking layer for the creation of the initial pits. The achievable pore structure, such as the pore diameter, pore depth, type and size distribution, is also restricted by the electrochemical etching process. The type of silicon (either p-type or n-type), its resistivity and orientation and anodisation conditions, such as current density, electrolyte compositions, etching time and temperature, all play a significant role in the pore geometry obtained by anodisation. Thus far, the smallest straight cylindrical ordered PSi structure realised is of the order of 0.2 μm in diameter [165, 167].

Alternatively, next-generation lithography technologies [42], such as extreme ultraviolet, electron beam (e-beam), X-ray and scanning probe lithography techniques, can be used to produce patterns with nanoscale features. However, these techniques, in general, are costly and relatively slow for creating large pattern areas. On the other hand, lithography methods, which are dependent on self-organisation, such as anodic alumina [291-293] or self-assembly of nanospheres [294, 295], have been used as a cost effective alternative to nanoscale patterning. In particular, porous anodic alumina (PAA), which is formed during the electrochemical etching (anodisation) of aluminium, has recently been demonstrated to provide a high aspect ratio, ordered, porous structure [296]. Primarily, PAA film has been used as templates in the fabrication of metal nanowires [291, 297-299] and carbon nanotubes [291, 300].

In this chapter, an attempt to fabricate a porous polysilicon (PPSi) structure with pore sizes in the 50 nm range, using a PAA film as a masking template, is described. Thick aluminium film (> 7 μm) was deposited on a polysilicon substrate, which was initially designed for the fabrication of a PPSi structure using the stain etching method (see Chapter 3). Therefore, a number of modifications were made to allow for the fabrication of the PAA template. A reactive ion etching (RIE) process was subsequently used to transfer the pattern of the PAA template onto the polysilicon layer.

4.2 Porous Anodic Alumina (PAA): An Overview

Depending on the pH of the electrolyte, two types of aluminium oxide (Al_2O_3) can be formed during the anodisation process of aluminium. A thin, uniform, nonporous oxide layer (commonly known as the barrier-type alumina) is typically formed when a near neutral electrolyte (pH 5 to 7) is used [293]. In contrast, when an acidic electrolyte (such as sulphuric, oxalic and phosphoric acid) is used, a thick porous oxide layer (or porous anodic alumina, PAA) is formed as a result of partial dissolution of the oxide layer in the strong acidic environments [293]. Under optimum anodisation conditions, the porous-type alumina self-organises into a hexagonally ordered structure, and the pores fabricated in this way are typically

straight and cylindrical in shape. These pores have diameters ranging from 20 nm to 200 nm and depths of up to a few microns. The spacing between adjacent pores (or the interpore distant) is well-established to be linearly related to the applied anodic voltage with a proportionality constant, ζ_{int}, of ~ 2.5 nm·V^{-1} [301]. The pore diameter is determined by the applied voltage and the concentration and temperature of the electrolyte. In addition, the pore diameter can be adjusted by a post-anodisation process. It is the consensus that an ideal, naturally occurring pore has a diameter primarily affected by the applied voltage with a proportionality constant, ζ_p, of ~ 1.29 nm·V^{-1} [302, 303]. The pore depth of the PAA is directly proportional to the anodising time. The ability to effectively control these geometrical structures of PAA thus provides an attractive proposition to using the PAA as a template for the fabrication of nanostructures and nanomaterials [291-293].

4.2.1 Fabrication Approaches

A typical fabrication of PAA film includes pre-treatment of the aluminium surface, the anodisation and a post-anodisation treatment step. The pre-treatment process, which includes annealing, degreasing and polishing of the aluminium surface, is essential to provide a highly smooth surface that is required for a self-organised anodisation process [304]. Annealing of the aluminium film or substrate is typically performed between 400 °C and 500 °C, in an Ar or N_2 atmosphere, for half an hour to 6 hours. The annealing process re-crystallises the aluminium grains of deposited aluminium [305], and reduces stresses and increases the grain size of the bulk aluminium substrate [304]. The degreasing step is typically carried out using solvents such as acetone and ethanol. The essential step of the pre-treatment process is the polishing step, which can be achieved by means of mechanical [306] or electrochemical polishing. The electrochemical polishing, using either a mixture of phosphoric acid (H_3PO_4), and sulphuric acid (H_2SO_4) [304, 307] or a mixture of perchloric acid ($HClO_4$) and ethanol [308-310], with a typical voltage of < 30 V, is more commonly used.

The anodisation of aluminium to form a self-organised PAA with long-range ordered structure, is known to occur within a relatively narrow range of fabrication conditions [293, 308]. The most critical parameter is the applied voltage, which is

specific to the type of electrolyte used for the anodisation. The three most investigated and commonly used conditions include using:

i) sulphuric acid (H_2SO_4) at 25 V [311-315];

ii) oxalic acid ($H_2C_2O_4$) at 40 V [296, 300, 302, 304, 307, 310, 316];

iii) phosphoric acid (H_3PO_4) at 195 V [314, 317-319].

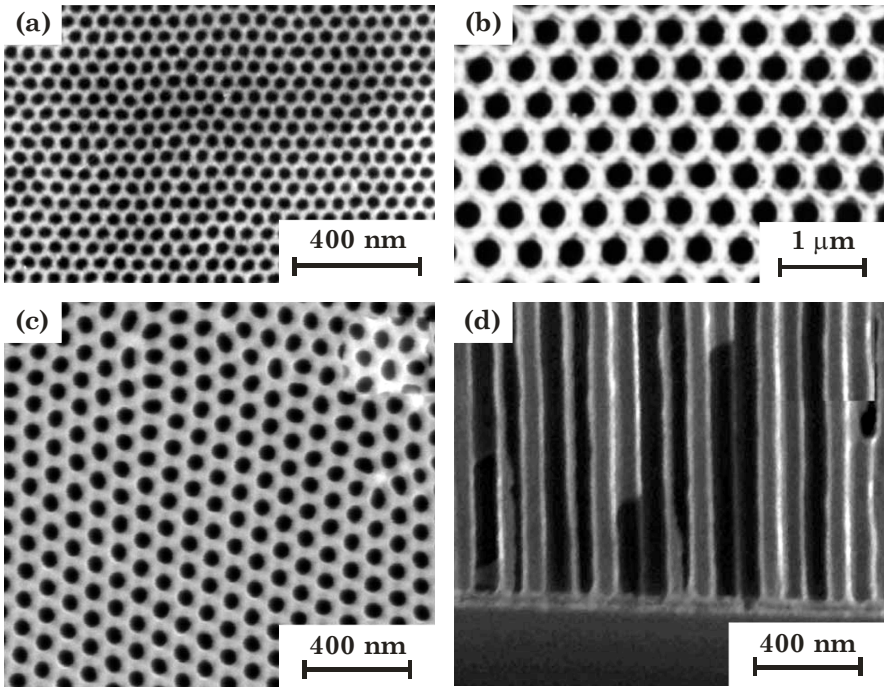

Figure 4.1: (a) – (c) Plane-view and (d) cross-sectional view SEM micrographs of various PAA structures fabricated by anodisation in (a) 0.5 M H_2SO_4 at 25 V for 750 minutes at 10 °C (reprinted from [315]); (b) 10 wt% H_3PO_4 at 195 V for 240 minutes (reprinted from [317]); (c) and (d) 0.3 M $H_2C_2O_4$ at 40 V for several hours at 10 °C using a 2-step anodisation process (reprinted from[310]).

Example PAA structures fabricated using these three conditions are depicted in Figure 4.1. The voltages used in these cases typically result in low current density and hence a slow growth rate of PAA (2 $\mu m \cdot h^{-1}$ to 6 $\mu m \cdot h^{-1}$) [320]; this is commonly known as the mild anodisation. Recently an anodisation technique, using voltages higher than the conventional ones, which results in high current density with a 2 500- to 3 500-fold increase in oxide growth rate, has been successfully developed [320-322]; this is known as the hard (or high-field) anodisation. The PAA structure fabricated using the hard anodisation process exhibits a non-conventional self-

ordering regime with a lower ζ_{int} of ~ 2.0 $nm \cdot V^{-1}$ (ζ_{int} for mild anodisation is ~ 2.5 $nm \cdot V^{-1}$) [320].

In order to improve the process, a two-step anodisation process was first demonstrated by Masuda and Satoh in 1996 [316]. The process significantly reduces the total anodisation time that is required to achieve a long-range ordering of the self-organised PAA; a typical one-step anodisation process needs a long period (of a few days) to achieve similar ordering [296]. In the two-step anodisation process, following an initial anodisation process (at the pre-selected electrolyte-voltage condition), the formed quasi-ordered PAA is removed using a mixture of H_3PO_4 and chromic acid (H_2CrO_4) at a temperature between 60 °C and 80 °C. The removal of the PAA forms a textured pattern of shallow concave features on the surface of the aluminium, which now becomes a template for pore initiation sites during the subsequent anodisation. The second anodisation is typically carried out using the same parameters as in the first anodisation, but with a much shorter anodisation time. The anodising and removing of PAA can be repeated for a three-step [309] or multistep [300, 308] anodisation process; generally, the uniformity of pore size increases with an increasing number of anodisation-removal cycles. The idea of pre-texturing the polished aluminium surface to form an ideally ordered PAA in a large area, has also been extended by direct indentation using scanning probe microscopy [323], focused-ion beam methods [324] and nanoimprint lithography [325-328].

A post-anodisation treatment step is primarily used to obtain a PAA template suitable for the subsequent fabrication of nanostructures and nanomaterials. The post-anodisation process includes removal of the aluminium base, pore widening and barrier layer removal. The removal of the un-oxidised aluminium base is mainly applicable to the PAA formed using an aluminium substrate (such as a foil, sheet, plate or disc) and is typically performed using wet chemical etching of aluminium in a saturated mercuric chloride ($HgCl_2$) solution [296, 304, 316]. The barrier layer of the PAA formed by the anodisation process can be removed by chemical etching of the oxide, typically using a solution of H_3PO_4; this opens the base of the pores and as a result, through-pores are created. The barrier layer removal process, when performed over a longer time, can simultaneously enlarge the pore diameter [316, 318, 329].

4.2.2 Anodisation of Aluminium-on-Silicon

Much of the effort in the fabrication and characterisation of PAA has been focused on using high purity aluminium substrates. Recently, greater attention has been focused on the fabrication of PAA films using aluminium deposited on top of different substrates, such as silicon [302, 305, 330-332] and glass [333-335]. This approach of forming a PAA template has numerous advantages – the substrates can be patterned into nanoholes or nanodots [331, 332] by subsequent post-anodisation processes. In addition, nanomaterials can be grown or deposited [291, 298, 310] with ease using various established methods previously developed for silicon substrates. In particular, PSi structures have been fabricated by RIE [302, 328] and electrochemical etching [330] using PAA templates as masks.

A typical anodisation process of aluminium-on-silicon has the current-time characteristic as depicted in Figure 4.2. Briefly, the current density rises sharply during the first few ms due to a spontaneous localised anodisation of the aluminium thus starting the formation of a thin oxide (Al_2O_3) barrier layer. After reaching its maximum, the current density drops sharply as the oxide barrier layer grows in thickness and spreads onto the entire surface of the aluminium that is exposed to the electrolyte. The current density then rises slightly due to a field-enhanced partial dissolution of the formed oxide barrier layer, at the interface between the barrier layer and the electrolyte [336]; a pore nucleation process is believed to have taken place [337]. A competing oxidation (of aluminium) and dissolution (of Al_2O_3) occurs as a result of anodisation across the entire exposed surface. As the growth and dissolution of Al_2O_3 reaches equilibrium, the current density remains more or less constant. During this constant-current stage, the formation and self-organisation of PAA take place (up until point *A* in Figure 4.2); this is a common behaviour in anodisation of both high purity aluminium substrate [309, 336, 337] and aluminium deposited on a silicon substrate [331, 332, 338].

A rapid decrease in current density (point *B* in Figure 4.2) is then observed, as the aluminium film is consumed gradually and converted into a transparent PAA film, which could be verified by a visible change in colour of the Al_2O_3 / Al / Si structure [331]. When the aluminium film is completely exhausted, the current density reaches a minimum value (point *C* in Figure 4.2) and it is believed that

silicon dioxide is formed at the interface of the barrier layer and the silicon substrate [339, 340]. The barrier layer, at this stage, is typically found to be inverted and arched, as depicted in Figure 4.3, and voids are formed at the interface between the barrier layer and the silicon substrate [302, 305, 333]. Further anodisation results in a sharp increase in the current density (point *D* in Figure 4.2), suggesting the localised anodisation of the underlying silicon. A partial detachment of the barrier layer of the PAA film from the silicon substrate accompanied by gas evolution may occur at this stage [331]. The subsequent broad peak (point *E* in Figure 4.2) indicates that the anodisation of the silicon substrate has been extended to the entire area of the sample and the PAA film will eventually detach from the substrate by extensive gas evolution [340].

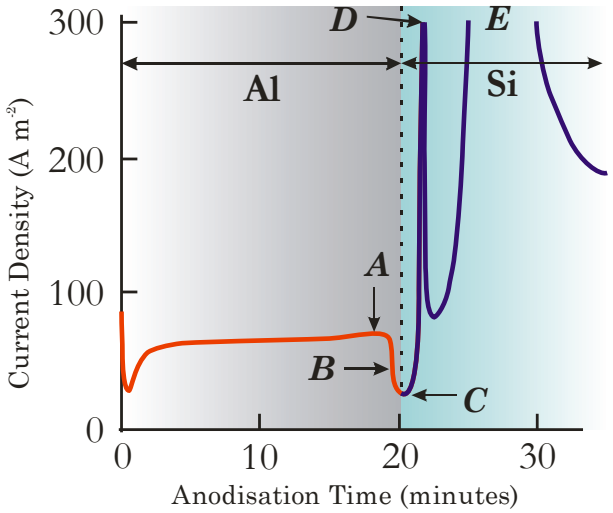

Figure 4.2: A representative current-time curve during anodisation of an aluminium film sputtered on top of a silicon substrate. The anodisation was carried out in 0.3 M oxalic acid at 20 °C at a constant voltage of 40 V (adapted from [332]).

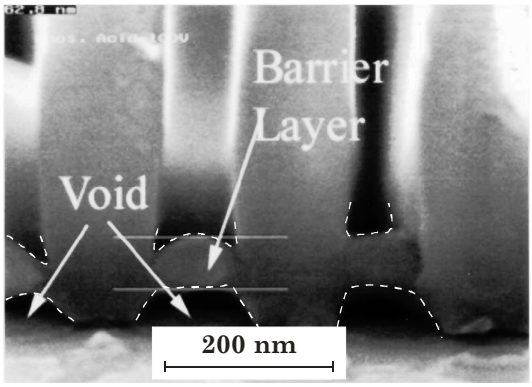

Figure 4.3: Cross-sectional view SEM micrograph of the inverted, arched barrier layers (outlined with dotted lines) typically formed when the aluminium is almost exhausted, during the anodisation of aluminium-on-silicon (reprinted from [302]).

4.3 Fabrication of a PAA Template on a Polysilicon Substrate

The use of a PAA template for the fabrication of a PPSi structure was proposed and subsequently investigated using a check wafer (*#c13p*, p-type, sheet resistance of (32.54 ± 0.19) Ω/sq) from batch K2714s (which was previously developed for the investigation of stain etching method to produce a PPSi structure (see Chapter 3)). The check wafer was used for the measurement of the sheet resistance (as discussed in Chapter 3, §3.4.1), and was processed in the same way as the device wafers, up to Step (d) of Figure 3.6. The use of a check wafer simplifies the modifications required for the fabrication of the PAA template. These modifications include:

i) depositing a thick layer of aluminium on top of the polysilicon layer (Step (a) of Figure 4.4);

ii) dicing the wafer into chips of 10 mm x 10 mm (Step (b) of Figure 4.4);

iii) making an electrical connection, between the bulk silicon substrate and the polysilicon layer (Step (b) and (c) of Figure 4.4);

The fabrication of the PAA template was primarily carried out at Prof. B. Hamilton's group, at the University of Manchester, using a fabrication method developed by Mazhar E. Nasir [288], which includes a low temperature electrochemical polishing step (Step (d) of Figure 4.4) and a multistep anodisation process (Step (e) of Figure 4.4) using oxalic acid-based electrolyte. The pattern on the PAA template can then be transferred to the polysilicon layer, for instance, by using a RIE process (Step (f) of Figure 4.4), to realise a PPSi structure.

Check wafer *#c13p* after stripping the SiO_2 by 7:1 buffered HF
for the measurement of sheet resistance (see Chapter 3, section 3.4.1)

a) Deposit thick (> 4 μm) layer of aluminium by evaporation via a shadow mask and then anneal at 450 °C

b) Deposit Au by evaporation and then dice into chips

c) Deposit Au by evaporation to bridge contact to front-side

d) Low temperature electro-polishing of aluminium

e) Multistep anodisation and barrier removal

Figure 4.4: Schematic illustration of the proposed fabrication of the PPSi structure using a PAA template (not to scale; see next page for continued process steps and colour scheme of materials used).

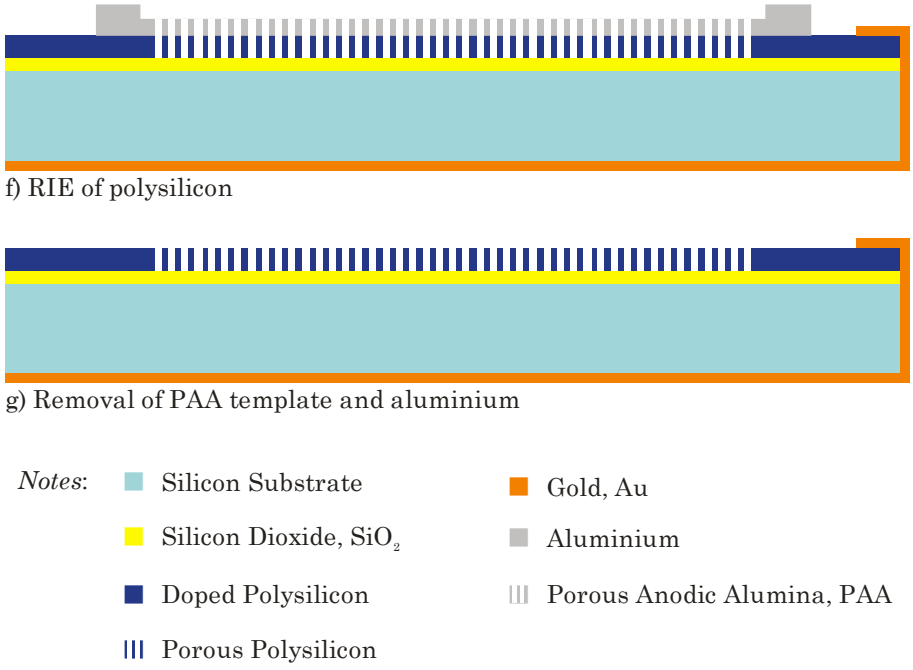

Figure 4.4: Schematic illustration of the proposed fabrication of the PPSi structure using a PAA template (not to scale).

4.3.1 Aluminium Deposition and Electrical Contact

The check wafer *#c13p* was first cleaned using plasma, solvent and chemical approaches. A RIE (Plasma Technology RIE80) using O_2 gas, with a flow rate of 50 sccm, was first performed at a pressure of 60 mTorr and a radio frequency (RF) power of 150 W. The RIE was performed for 10 minutes. Next, a solvent clean using trichloroethylene (TCE), followed by acetone, methanol and de-ionised (DI) water, for 10 minutes each in an ultrasonic bath, was carried out. The wafer was then sawn into a square piece of 75 mm x 75 mm and then thoroughly degreased with a similar solvent cleaning process. A Piranha clean with 2:1 volume ratio of 95 % concentrated H_2SO_4: 30 % weight in volume (w/v) hydrogen peroxide, was performed to remove any organic residues off the substrate. The wafer was finally cleaned with 10:1 volume ratio of DI water: 48 % hydrofluoric acid (HF) to remove the native oxide prior to the evaporation process.

A thermal evaporation of aluminium (Step (a) of Figure 4.4) was carried out using a modified resistive thermal evaporator (BOC Edwards) [288]. High purity aluminium pellets (99.999 % purity, Goodfellow Cambridge Ltd. UK) were used as the source and were delivered using a custom-made, movable, solenoid-controlled

feeding system, as depicted in Figure 4.5. This allows multiple evaporations without the need to break the vacuum system to provide the aluminium source; hence a thick layer of aluminium (potentially up to 10 μm) can be deposited. A shadow mask, made of stainless steel, with a 7 x 7 array of 8 mm diameter circular holes, was used to pattern the wafer. Each cycle of evaporation was performed at a base pressure of < 4 x 10^{-6} mbar; only one aluminium pellet was used per cycle. A total of 27 aluminium pellets were used in the evaporation process, resulting in an aluminium thickness of ~ 7.04 μm, as recorded by a quartz crystal film thickness monitor interfaced to a desktop computer via National Instruments™ (NI) LabVIEW™ software.

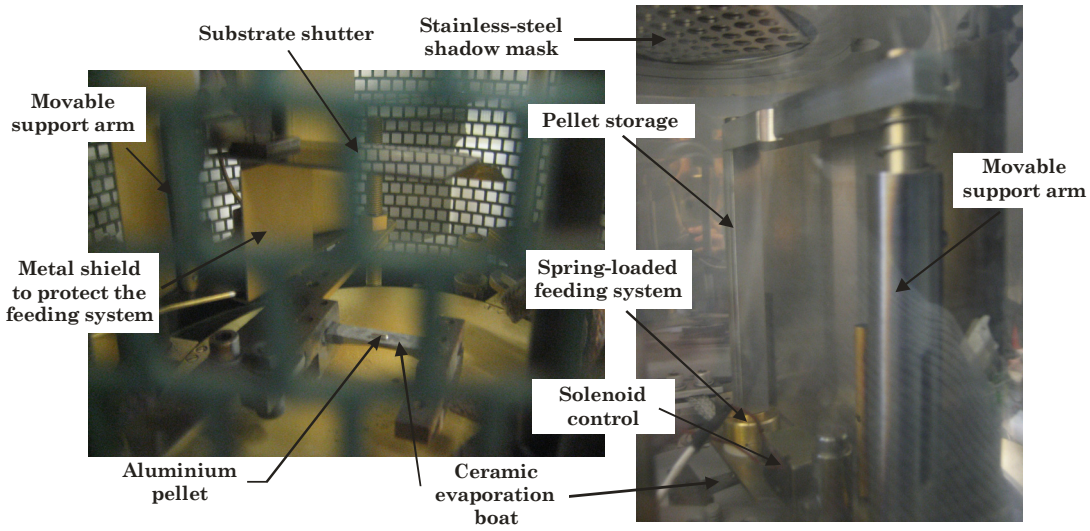

Figure 4.5: Digital photographs of the custom-made feeding system in the modified thermal evaporator, with the feeding system (a) in the standby position, after an aluminium pellet was dropped on a ceramic evaporation boat; and (b) in the feeding position, ready for dropping the aluminium pellets.

The surface of the as-deposited aluminium varied in appearance, from dull, milky white colour to metallic silver colour, as conceptually depicted in Figure 4.6, which suggests non-uniformity in the aluminium thickness. This is possibly a result of a secondary evaporation masked by a mechanical, substrate shutter, which was used to protect the wafer from excessive heat radiation, at the beginning and near the end of each evaporation cycle. This non-uniformity in thickness proved to be problematic to subsequent processes, as discussed in the following sections. The lack of a mirror-like surface finish also suggests a grainy surface roughness.

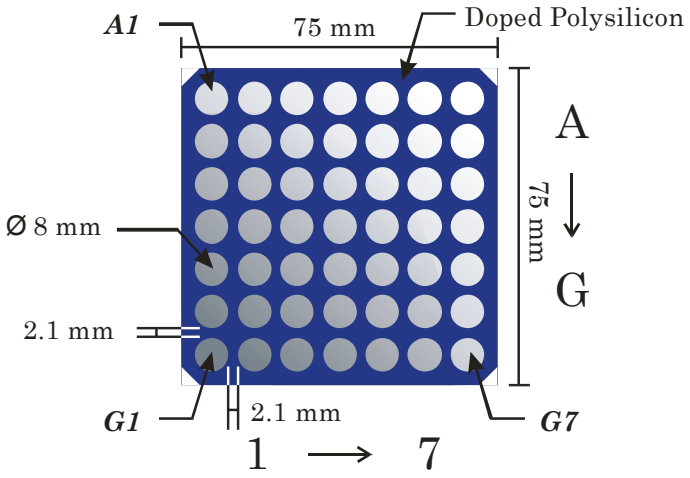

Figure 4.6: Illustration of the colour variation across the wafer indicating the non-uniformity in thickness of the evaporated aluminium. The colour scheme used is not truely representative of the colour observed and is simply for illustration purposes only.

The wafer was subsequently annealed at 450 °C for 45 minutes, in a nitrogen atmosphere, to re-crystallise the aluminium grains [305]. However, as a typical result of the annealing, hillocks were observed when the wafer was inspected with a microscope, and this was confirmed by SEM micrographs, as depicted in Figure 4.7. The size (longest length) of the hillocks varies from as large as a few microns, to as small as ~ 0.5 μm. The average size of the hillocks was estimated to be ~ 1.4 μm, based on the SEM micrograph inset in Figure 4.7.

The annealed wafer was then spin-coated with a layer of Shipley S1813 photoresist on the front-side and hard-baked at 110 °C for at least 1 hour. The wafer was then cleaned with 10:1 DI water: HF prior to a gold evaporation to make the back electrical contact. Gold of ~ 100 nm thick was evaporated at the back-side of the wafer (Step (b) of Figure 4.4) using the same thermal evaporator, with a base pressure of 5 x 10^{-6} mbar. The back-side of the wafer was then spin-coated with another layer of the S1813 photoresist to protect the wafer from silicon particulates during the dicing process. The wafer was diced into 10 mm x 10 mm smaller pieces with the 8 mm diameter aluminium roughly centred on each samples. The samples were labelled as per their grid position (as depicted in Figure 4.6) for easier identification. Side contacts (Step (c) of Figure 4.4) were then made individually on the samples, such that a bridge could be created that extended from the front-side, to the edge-side and to the back-side contact of the sample, as conceptually depicted in Figure 4.8. Electrical connection was then made, at the back-side of each sample,

using a two-part conductive silver epoxy, and cured at 120 °C for at least 30 minutes. The resistance from the wire to the surface of aluminium was measured and found to range from 8 Ω to 75 Ω.

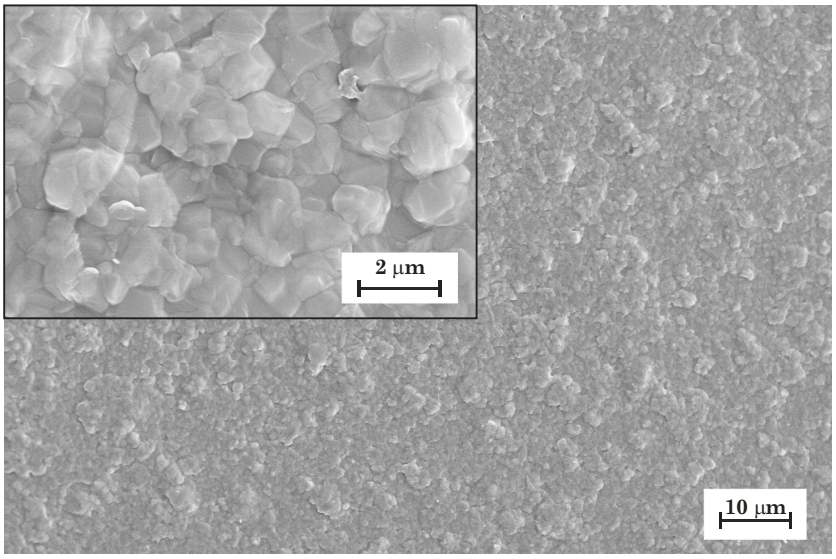

Figure 4.7: Plane-view SEM micrograph showing the surface of the annealed aluminium on sample *D5*. The annealing was performed at 450 °C in a N_2 atmosphere for 45 minutes. The inset shows the magnified view at a different area of the sample.

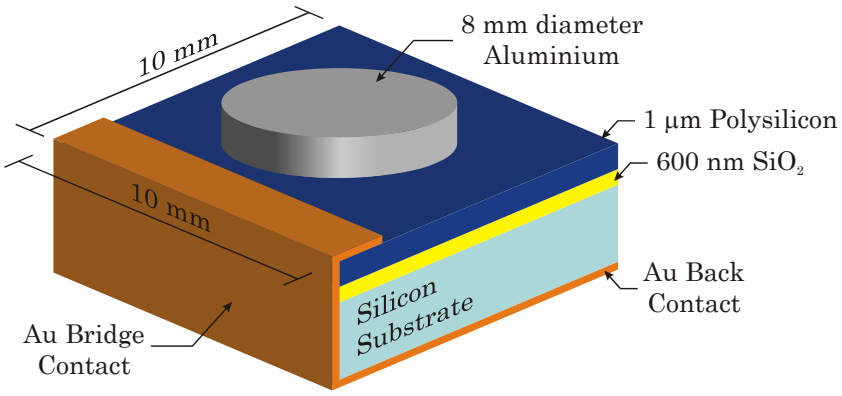

Figure 4.8: Schematic illustration of a sample deposited with aluminium and ready for the fabrication of the PAA template.

4.3.2 Electro-polishing of Aluminium

Individual samples were then electrochemically polished (Step (d) of Figure 4.4) in a custom-made, polytetrafluoroethylene (PTFE) electrochemical etching cell [288], as depicted in Figure 4.9. The electrolyte used in the electro-polishing process consists of 1:2:4 volume ratio of 2-butoxyethanol (> 99 %): 35 percent volume per volume (% v/v) $HClO_4$: ethanol (all reagents are of ACS grade from Sigma-Aldrich Ltd., UK).

Due to the highly flammable and explosive nature of $HClO_4$, the mixture was prepared in an ice bath. The electro-polishing was performed under a controlled low temperature (of below 5 °C), which was achieved by feeding liquid nitrogen to the back-side of the sample, and circulating the liquid nitrogen within the etching cell, as depicted in Figure 4.9. The electrolyte was stirred (~ 40 rpm), using a PTFE stirrer connected to an electric motor (330-799, RS Components Ltd., UK), during the electro-polishing process.

An aluminium counter electrode was used as the cathode, with the sample as the anode, and connected to a constant voltage power supply (Delta Electronika E0300-0.1). The voltage drop across the sample and the counter electrode was measured using a digital multimeter (TTi 1604, Thurlby Thandar Instruments Ltd. UK). The current passing through the sample and the counter electrode was measured using a programmable multimeter (TTi 1705, Thurlby Thandar Instruments Ltd. UK), which also measures the temperature in the etching cell via a thermocouple. The two multimeters were connected to a computer via an RS-232 interface and all the measurements were recorded using NI LabVIEW™ software.

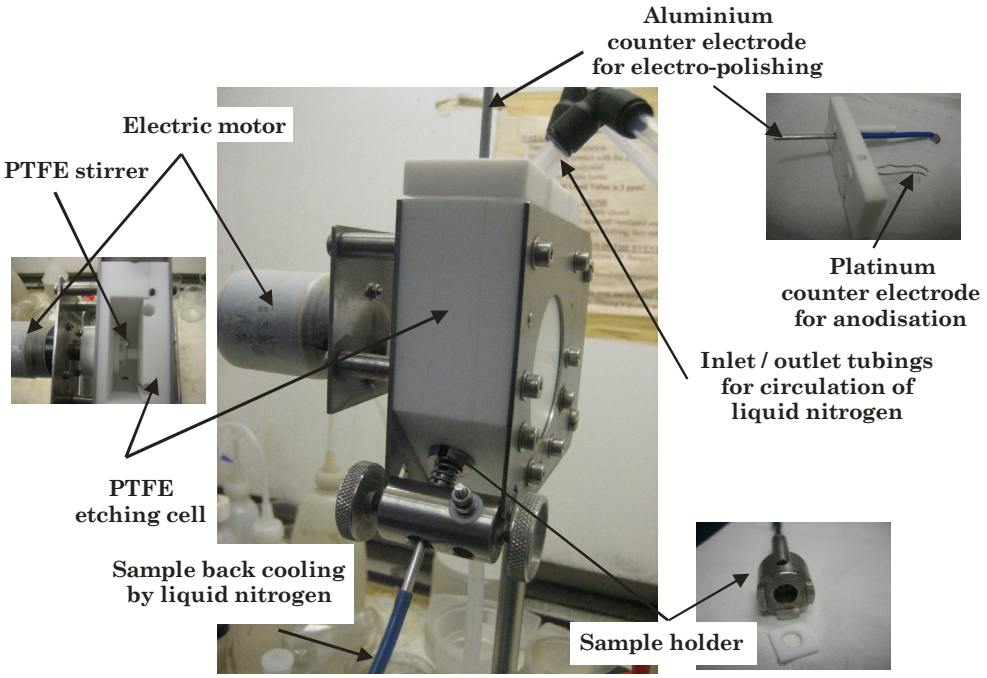

Figure 4.9: Digital photograph of the electrochemical etching cell used in an electro-polishing configuration, which allows for the cooling by liquid nitrogen.

The electro-polishing voltage ranged from 20 V to 30 V and the etching time was between 35 s and 70 s. At 20 V, the maximum electro-polishing time before some of the aluminium was exhausted was found to be between 50 s and 60 s, while samples electro-polished with 25 V and 30 V appeared to be over-polished after 55 s and 45 s, respectively. The rate of electro-polishing was not only influenced by the etching time and the applied voltage, but also dependent on other factors, such as the initial surface roughness of the aluminium, the thickness of the aluminium, the etching temperature, and the stirring of the electrolyte [288]. The electro-polishing process also appears to have a narrow window of optimum conditions.

The surface finish of the electro-polished aluminium depends on the rate of electro-polishing. Some samples exhibited a mirror-like finish when electro-polished at the optimum conditions. These samples, including sample *E5*, which is depicted in Figure 4.10, when observed under the SEM, showed a smooth surface with a significant reduction in aluminium grain sizes. Other samples, although they appeared to have a mirror-like finish, exhibited macroscopic defects, such as etch pits and over-etched spots, which indicated a non-uniform thickness of the aluminium layer.

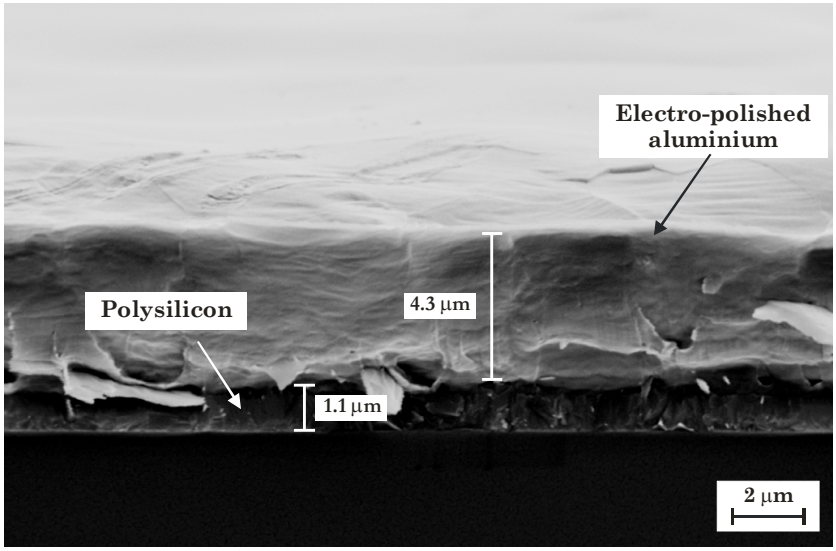

Figure 4.10: Oblique, cross-sectional view SEM micrograph of sample *E5*, which was electro-polished for 45 s at a voltage of 20 V.

4.3.3 Anodisation of Aluminium

Anodisation (Step (e) of Figure 4.4) of the samples was then carried out using the same electrochemical etching setup, at room temperature (varies from 18 °C to 24 °C). A platinum counter electrode was used instead of the aluminium electrode (used in the electro-polishing process). The electrolyte consists of 0.3 M oxalic acid, which was prepared by dissolving 5.4 g anhydrous $H_2C_2O_4$ (> 99.0 %, puriss. p.a. grade) into 200 mL DI water. The typical voltage used for the anodisation process was at 40 V, although anodisation steps using 50 V and 60 V have also been tested on selected samples. The anodisation process ranged from a single step to 5 steps. Between each step, of the multistep anodisation process, the formed PAA was removed in a mixture of 1:1 volume ratio of 45 $g \cdot L^{-1}$ H_2CrO_4 (prepared from chromium (III) oxide, > 98 %): 3.5 % v/v H_3PO_4 (> 85 % in weight, ACS grade) that was heated to 70 °C, typically for 30 minutes (all reagents are from Sigma-Aldrich Ltd., UK). Multiple steps of anodisation were carried out so that a thinner PAA film, with ordered, cylindrical straight pores, could be fabricated. Some of the anodised samples were then immersed in a mixture of DI water and 10 % v/v H_3PO_4 with equal volume, for 1 hour, to remove the barrier layer and enlarge the pore size. Table 4.1 summarises the parameters used in the electro-polishing and anodisation processes, of selected samples discussed in this chapter.

Sample	Electro-polishing	Anodisation	Post-anodisation
E5	20 V, 45 s	-	-
F5	20 V, 55 s	Single step: 40 V, 3600 s	-
F4	20 V, 45 s	1st step: 40 V, 1200 s 2nd step: 40 V, 1200 s 3rd step: 40 V, 3800 s	-
E4	20 V, 45 s	1st step: 40 V, 600 s 2nd step: 40 V, 900 s 3rd step: 40 V, 900 s 4th step: 40 V, 600s	Pore widening and barrier removal, 1 hour
G6	20 V, 35 s	1st step: 40 V, 200 s 2nd step: 40 V, 600 s 3rd step: 40 V, 1800 s 4th step: 40 V, 1200s 5th step: 40 V, 480 s	Pore widening and barrier removal, 1 hour; RIE of polysilicon

Table 4.1: Summary of the parameters used during the electro-polishing and anodisation process, of some of the samples, sorted in the order as they first appeared in the text.

4.3.3.1 Single Step Anodisation

Based on the understanding of the anodisation current curve (see §4.2.2), the anodisation should be stopped just before the point where the current density reaches a minimum value (between point *B* and *C* of Figure 4.2), thus when the barrier layer has been removed, the PAA film will selectively expose the polysilicon layer. In this way, a subsequent RIE of the polysilicon can be carried out to transfer the pattern on the PAA template to the polysilicon layer. In order to predict the stoppage point, a single step anodisation was performed, where current density measurements were taken whilst the entire thickness of the deposited aluminium was consumed and anodised.

To examine the typical anodisation behaviour, sample *F5* was anodised for 1 hour and the current density transient at constant voltage was recorded, and plotted in Figure 4.11. After the initial formation of barrier layer and the initiation of pores, the anodisation process reached equilibrium between oxidisation and dissolution of the formed alumina. However, instead of a constant-current behaviour typically observed in the anodisation of aluminium, the sample *F5* exhibits a gradual decrease in current density. The characteristic sudden drop (point *B* in Figure 4.2), followed by a rapid increase (point *D* in Figure 4.2) in the current density, could not be readily observed; this made the estimation of the stoppage point during the anodisation process difficult. It is suspected that these non-typical behaviours are partly due to a non-uniform thickness of the deposited aluminium (as discussed in §4.3.1) and the resultant etch pits from the electro-polishing process, and partly due to a poor contact between the aluminium film and the polysilicon layer. Thus, a non-uniform etch rate across the surface of a sample is believed to have occurred during the anodisation process and results in different regions of the sample experiencing different stages of the anodisation process. Consequently, the current measurement is less indicative of the different phases of the anodisation process.

The current density during the anodisation of sample *F5*, as depicted in Figure 4.11, eventually reaches a minimum point; it is believed that the aluminium has been completely exhausted at this stage. The SEM micrographs of sample *F5*, as depicted in Figure 4.12, obtained after the anodisation process, confirm that the aluminium has been completely consumed, forming a ~ 7.5 μm thick PAA film. Some

voids within the formed PAA film, as depicted in Figure 4.12 (a), could be observed; these voids are large in size (microns range) and not to be confused with the typical voids resulting from the arching of the barrier layer at the base of the pores (see §4.2.2). The voids were believed to be formed prior to the electro-polishing process and most likely as a result of the annealing process [341, 342], which forms hillocks during the re-crystalline process of the aluminium grains.

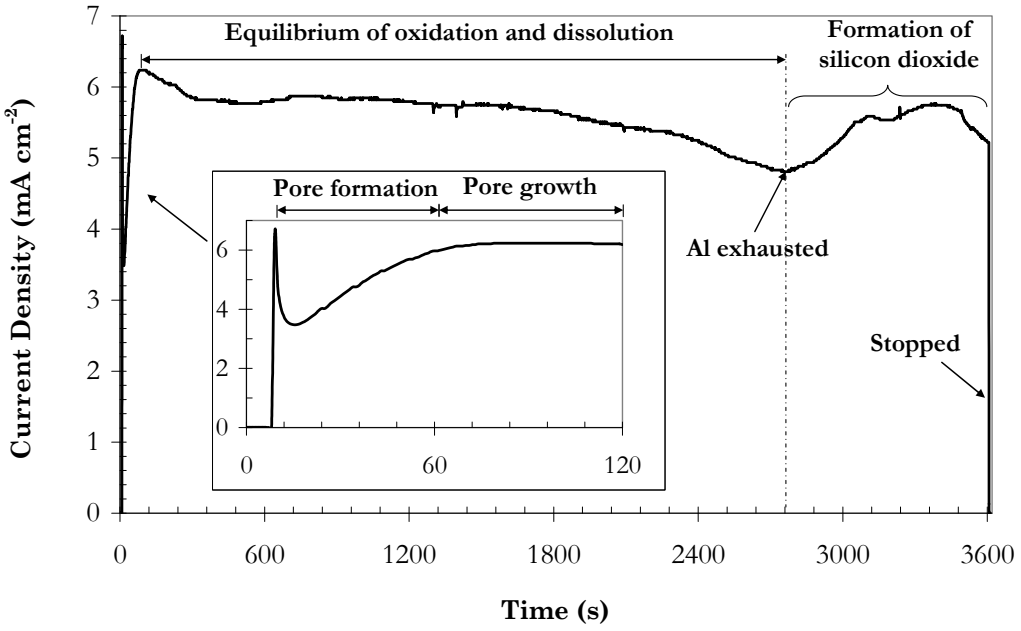

Figure 4.11: Current-time anodisation curve of sample *F5*, which was anodised for 1 hour in 0.3 M oxalic acid with a constant voltage of 40 V, at room temperature (22 °C to 24 °C).

The pores of the formed PAA film were observed to be in a quasi-order, hexagonal arrangement, as depicted in Figure 4.12 (e). The pore diameter is estimated to be 38 nm ± 7 nm, while the interpore distance is ~ 73 nm; both were measured using an edge detection tool of the NI Vision Assistant™ image processing software. These are consistently lower (~ 27 %) than the theoretical values of 100 nm (based on ζ_{int} of 2.5 nm·V^{-1} [301]) and 52 nm (based on ζ_p of 1.29 nm·V^{-1} [302, 303]) for interpore distance and pore diameter, respectively. It is believed that the discrepancy is primarily due to the poor resolution obtained by the SEM, which underestimates the actual pore diameter and interpore distance. In addition, it is observed that the pores are not entirely vertical, as depicted in Figure 4.12 (c), and this could be problematic for the subsequent RIE process. The PAA film is believed to

start to detach from the polysilicon surface, as depicted in Figure 4.12 (d), this is very likely due to the extended etching beyond the stoppage point.

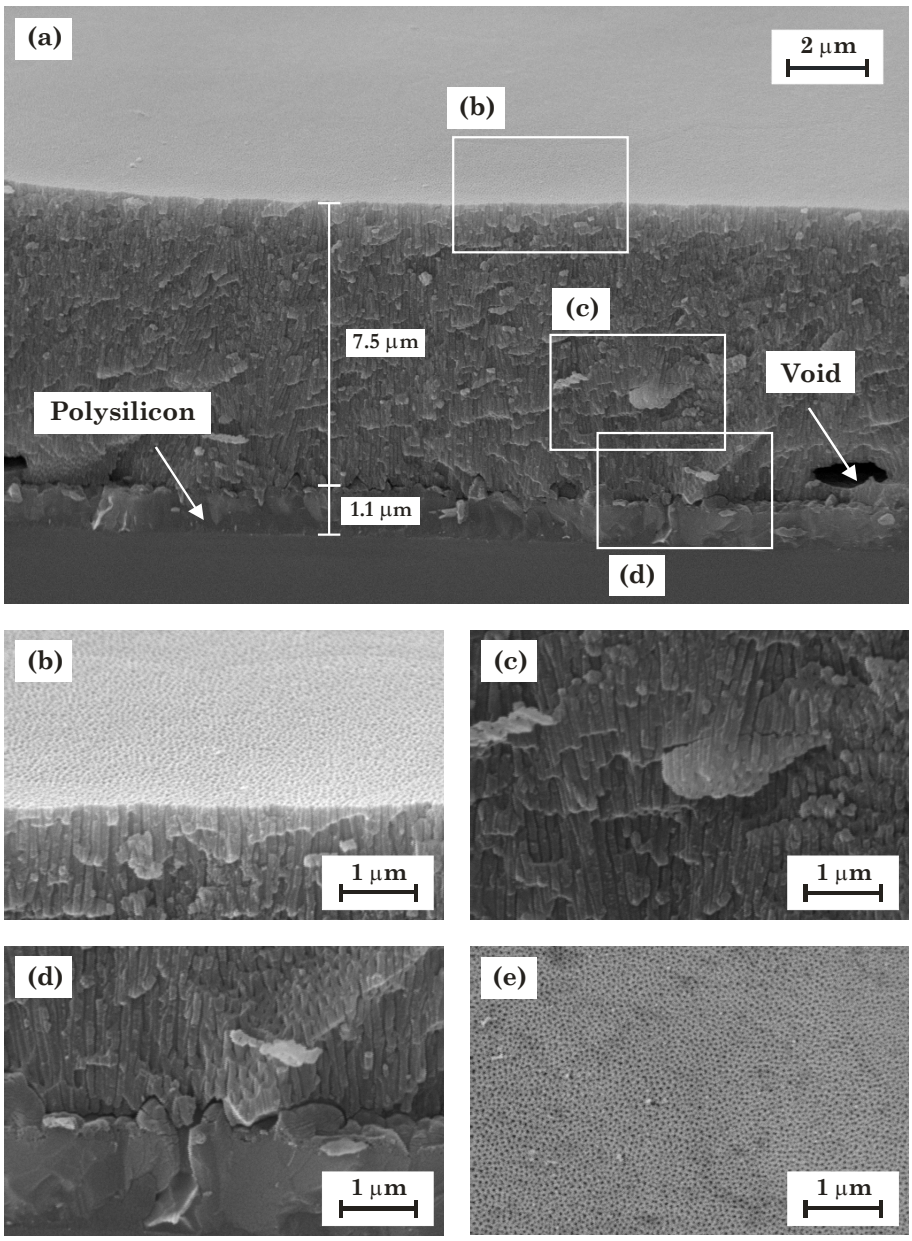

Figure 4.12: SEM micrographs showing (a) an oblique, cross-section view; (b) – (d) magnified view of the corresponding boxed areas in (a); and (e) plane-view of sample *F5*. The single step anodisation was carried out in 0.3 M oxalic acid, at room temperature (22 °C to 24 °C), with a constant voltage of 40 V, for 1 hour.

4.3.3.2 Multistep Anodisation

Multistep anodisation was performed in an attempt to fabricate a highly ordered, thin (< 1 μm) PAA film. Figure 4.13 depicts the cross-sectional view SEM micrograph of sample *F4*, which was anodised at 40 V with a 3-step process (detailed parameters are summarised in Table 4.1). The pore diameter was measured to be 53 nm ± 9 nm, and the interpore distance is ~ 103 nm; both values are close to the theoretical estimation. The depth of the resultant PAA film was ~ 3.7 μm, which is thicker than the desired thickness and hence may not be suitable as a masking template for the RIE of polysilicon. It is observed that a slightly porous layer of ~ 370 nm thick exists in between the polysilicon layer and the PAA template. It is suspected that the layer is a form of aluminosilicate, which is porous in nature. The PAA film is also observed to be detached from the polysilicon layer, suggesting an over-anodised process.

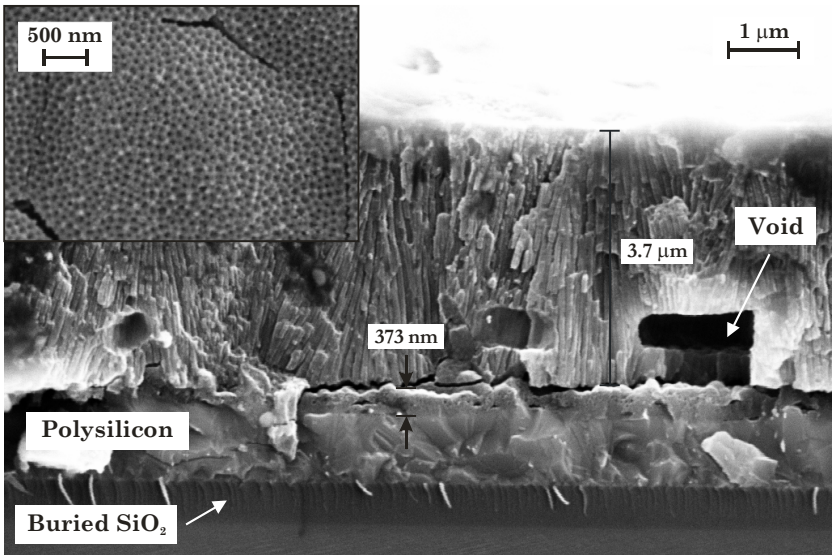

Figure 4.13: Cross-sectional view SEM micrograph of sample *F4* after a 3-step anodisation process, using the process parameters as detailed in Table 4.1. The last step anodisation was performed using 0.3 M oxalic acid, at room temperature (20 °C to 21 °C), with a constant of 40 V, for 3800 s. The inset shows the plane-view SEM micrograph of the same sample.

The problem of non-uniform aluminium thickness is more evident in sample *E4*, which was anodised at 40 V with four, shorter steps of anodisation (anodisation time detailed in Table 4.1). At a region of the sample, the aluminium was completely consumed, as depicted in Figure 4.14 (a), however, relatively thick (~ 920 nm) aluminium was still present at certain parts of the sample, such as the one depicted in Figure 4.14 (b). The current-time anodisation curve of the fourth step process

exhibited typical constant-current behaviour and did not show signs of aluminium being completely consumed.

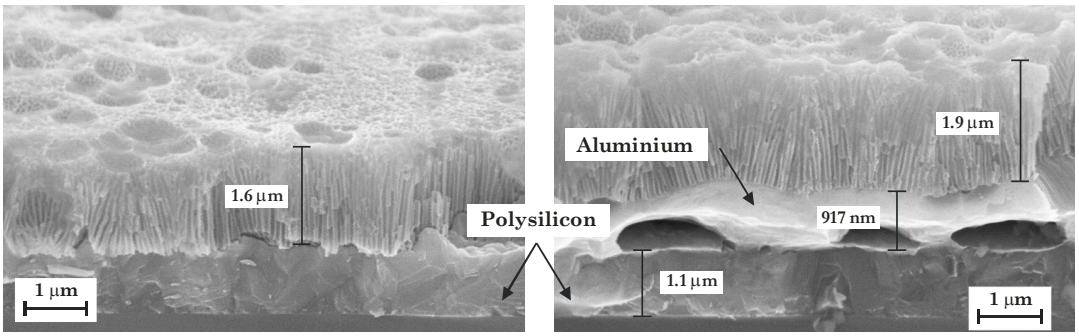

Figure 4.14: Oblique, cross-sectional view SEM micrographs of sample *E4* after the pore widening and barrier removal process. The 4-step anodisation was performed based on the parameters summarised in Table 4.1. In (a), the aluminium was completely consumed by the anodisation process but in (b), ~ 920 nm thick of aluminium layer still remains.

In an attempt to produce a much thinner PAA film, a 5-step anodisation was performed. Figure 4.15 depicts the current-time curve of sample *G6* which was anodised in 5 steps of varying anodisation time, as summarised in Table 4.1. The fourth step anodisation of sample *G6*, which was performed for 20 minutes, exhibited a current density transient consistent with the characteristic behaviour of a typical anodisation process. However, during the last step anodisation, a higher average current density, accompanied with uncharacteristic anodisation behaviour, as depicted in Figure 4.15, was observed. The higher current density suggests that the aluminium film was significantly thinner while the uncharacteristically oscillating current-time behaviour could be explained by the vigorous and aggressive anodisation process due to a non-uniform thickness of the aluminium film; it is believed that the aluminium film at some regions of the sample could have already been completely consumed. The anodisation process could not be predicted and hence was stopped after 8 minutes of anodisation.

Figure 4.16 depicts the cross-sectional SEM micrograph of the anodised sample *G6* after the pore widening process. Instead of film with a uniform thickness, the formed PAA film exhibits a hemispherical structure, with the maximum thickness of ~ 1.1 μm at the centre of the hillock. The pores are observed to be formed at an angle such that each pore is perpendicularly aligned to the curved top surface; a similar structure has been reported on curved aluminium surfaces [343]

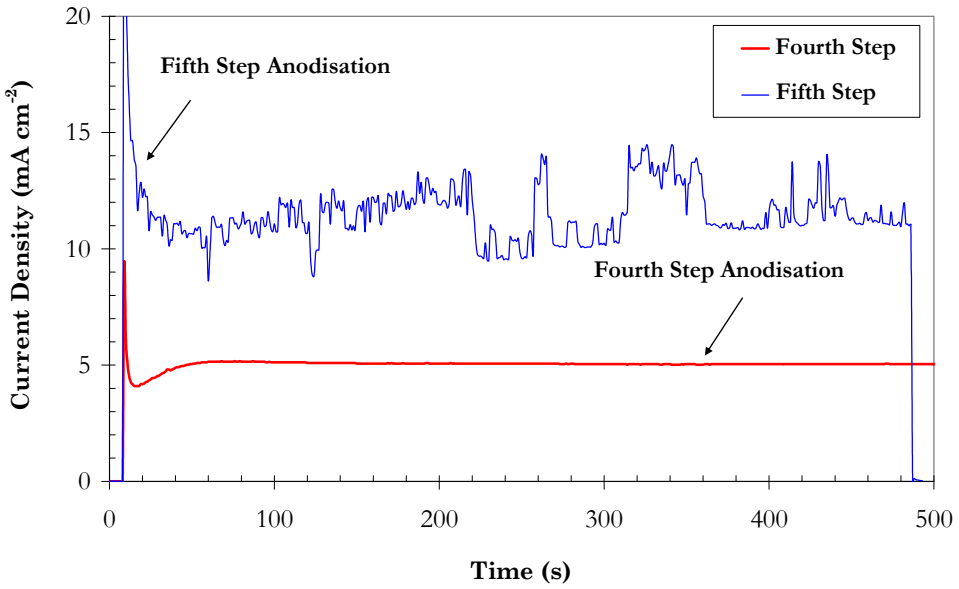

Figure 4.15: Current-time curve during the fourth and fifth step anodisation of sample *G6*. The anodisation was carried out using 0.3 M oxalic acid with a constant voltage of 40 V, at room temperature (18.5 °C to 20.5 °C for the fourth step; 15 °C to 25 °C for the fifth step) for anodisation times of 20 minutes and 8 minutes for the fourth and fifth step, respectively.

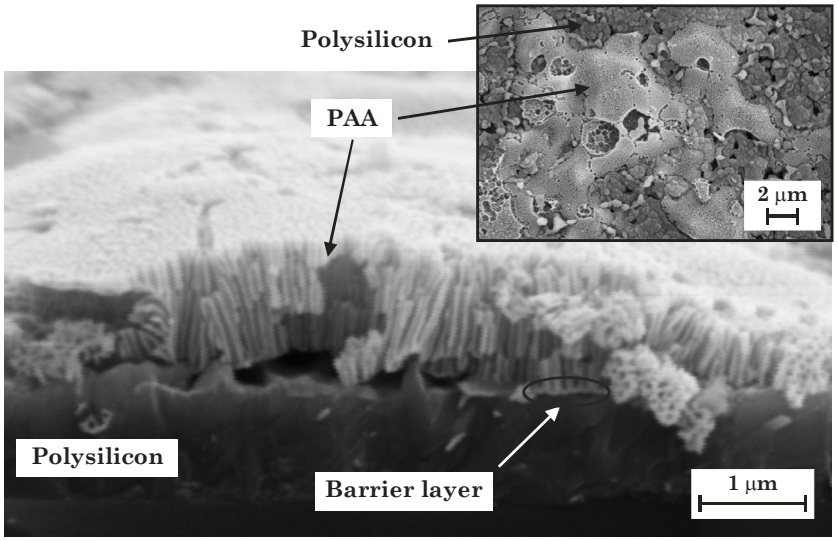

Figure 4.16: Cross-sectional view SEM micrograph of sample *G6* after the pore widening and barrier removal process. The 5-step anodisation was performed based on the parameters summarised in Table 4.1. The inset depicts the plane-view SEM micrograph of the sample at a different area.

and pre-annealed aluminium film on silicon [305]. At some regions of the formed PAA film, the barrier layer and a thin interface between the polysilicon and the PAA film are still present. The plane-view SEM micrograph, as depicted in the inset of Figure 4.16, further demonstrates the non-uniformity of the PAA films. Some PAA films were removed thus exposing the underlying material, possibly the polysilicon.

This could be associated to the non-uniform, aggressive etching during the last step anodisation.

4.3.4 RIE of Polysilicon

The RIE of the polysilicon layer (Step (f) of Figure 4.4), using the PAA template as a mask, was performed using a Plasmalab 80 Plus (Oxford Instruments Ltd. UK) RIE system. A gas flow rate of 10 sccm of sulphur hexafluoride (SF_6), at a pressure of 50 mTorr and an RF power of 100 W, was used in the 2-minute RIE process. The RIE using SF_6 gas alone typically results in isotropic etching of silicon [42]. This is evident on sample *G6*, as depicted in Figure 4.17, which has a thin PAA template formed by a 5-step anodisation process. Some of the PAA structures are believed to have collapsed and removed during the RIE process, resulting in a non-preferential etching of the underlying material (possibly a mixture of polysilicon and barrier oxide layer). The angled pore structure of the PAA film is also believed to inhibit the exposure of SF_6 gas to the polysilicon layer, thus producing a less effective directional etching. The PAA film used in this preliminary investigation was found to be less suitable as a masking template, due to its uneven film thickness, as discussed in previous section. In addition, the RIE process is clearly not optimised for anisotropic etching of the polysilicon; an improved RIE process (with more appropriate parameters) was used later and is discussed in Chapter 5 and 6.

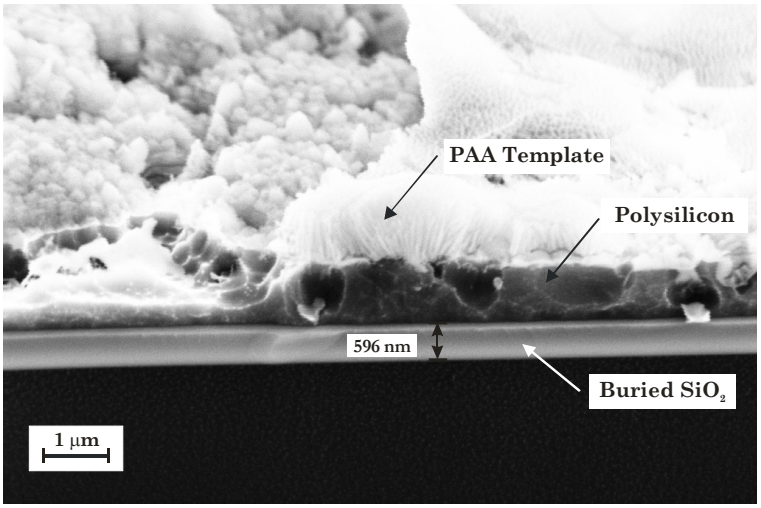

Figure 4.17: Cross-sectional view SEM micrograph of sample *G6* after RIE of the polysilicon layer using a PAA template (depicted in Figure 4.16) as a mask. The RIE process was performed using 10 sccm flow rate of SF_6, at a pressure of 50 mTorr and an RF power of 100 W, for 2 minutes.

4.4 Conclusion

A PAA film was fabricated on top of a polysilicon surface by using electro-polishing and multistep anodisation processes. The electro-polishing process was used to remove the surface roughness of the annealed aluminium layer that is grainy with hillocks of microns in size. Some etch pits were observed after the electro-polishing process, suggesting a non-uniform etching possibly due to a non-uniform thickness in the evaporated aluminium. It is suspected that the substrate shutter of the evaporator may have masked part of the evaporated aluminium source, during the evaporation process, hence resulting in a varied thickness across the wafer.

The anodisation of the aluminium was performed using the one step and multistep process with various etching times. Ideally, the anodisation should be stopped after the entire thickness of aluminium has been consumed, but just before the formed PAA film starting to detach from the substrate surface. This is characteristically manifested in the current density transient curve by a sudden drop, followed by a rapid increase in the current density (see Figure 4.2). However, during the anodisation process, this characteristic behaviour could not be readily observed. Hence, the point when the anodisation needs to be stopped is difficult to predict during the anodisation process. As a result, most of the fabricated PAA films were either already detached from the polysilicon surface (due to over-anodisation) or not fully anodised. It is suspected that these non-typical behaviours are partly due to a non-uniform thickness of the deposited aluminium.

The non-vertical pore structure, observed for some of the fabricated PAA films, is unsuitable as a mask for RIE of the polysilicon layer. An additional problem is the fact that some samples also had detached or non-uniform PAA layers which are not ideal as masking templates for the RIE of the polysilicon layer. Therefore, in Chapter 5, an alternative templating method was developed.

Chapter 5

The Fabrication of Porous Polysilicon using the Nanosphere Lithography Technique

5.1 Introduction

In this chapter a novel approach for the fabrication of porous polysilicon (PPSi) is presented. This approach makes use of the nanosphere lithography (NSL) technique, to fabricate a masking layer suitable for the reactive ion etching (RIE) of the polysilicon. The NSL technique, which utilises the self-assembly of polymer nanospheres, is well-known as an inexpensive and scalable method of producing periodically-ordered patterns. A metal mask consisting of arrays of nanoholes patterns was produced by careful deposition of a monolayer of hexagonally close-packed nanospheres and subsequently reducing the size of the nanospheres. This metal mask was then used in an RIE process to form a quasi-ordered PPSi structure with macropore sizes. Nanospheres with mean diameters of 500 nm and 200 nm were used to demonstrate the feasibility of the proposed technique.

5.2 The NSL Technique: An Overview

The NSL technique was initially demonstrated by Deckman and Dunsmuir [344] and, has recently been extensively studied and improved by the group of Van Duyne[21] [345-351]. The NSL technique exploits the self-assembly of polymer nanospheres (typically polystyrene) and subsequent etching or deposition processes, as depicted in Figure 5.1, to realise various hexagonally ordered nanostructures. The most straight-forward implementation of the NSL technique is to directly use the self-assembled nanospheres as a masking layer (route A of Figure 5.1), and deposit a thin layer of metal film to realise arrays of triangular-shaped nanodots [345, 347, 349, 350, 352]. The size of the nanodots can be reduced by increasing the initial diameter of the nanospheres (route B of Figure 5.1), either by microwave annealing [353] or by thermal annealing near the glass transition temperature of the polymer [354]. The shape of the nanodots can be modified into nano-scale rings and rods [353] by tilting the deposition angle of the metal film. Alternatively, by reducing the initial diameter of the nanospheres using an RIE process (route C of Figure 5.1),

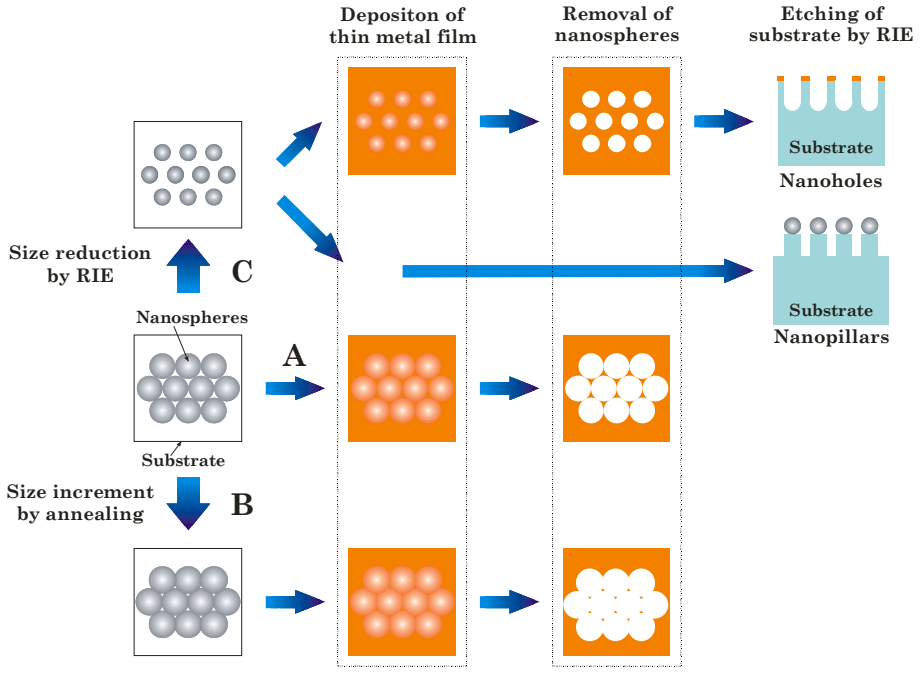

Figure 5.1: Schematic illustration of possible routes (A, B or C) of fabrication, using the NSL technique, to produce various hexagonally ordered nanostructures.

[21] Richard P. Van Duyne, Charles E. and Emma H. Morrison Professor of Chemistry, Northwestern University, Illinois, USA, http://chemgroups.northwestern.edu/vanduyne/ (*last accessed Jul. 2009*).

nanopillars [355-357] or nanoholes [358] can be fabricated from the size-reduced nanosphere template or its inverse pattern created from the deposition of a thin metal film, followed by removal of the nanosphere template. The diameter of the size-reduced nanospheres thus defines the diameter of the nanoholes or the nanopillars.

The NSL technique is an inexpensive, simple to implement and "materials general" nanofabrication technique. It has been demonstrated to provide masking against ion implantation [359] and electrochemical etching [360] for the fabrication of porous silicon, and to serve as the template for the fabrication of nanoholes [358], nanopillars [355-357], nanowires [361, 362] and carbon nanotubes [352, 363]. In the case of macroporous polysilicon, a nanosphere template can be used to define a metal mask to be used during the etching of polysilicon.

5.2.1 Methods of Nanospheres' Self-Assembly

Monodispersed nanospheres can be self-assembled into a monolayer of hexagonally close-packed arrays by a number of approaches. Figure 5.2 illustrates some typical methods, which include drop-coating, dip-coating, spin-coating and self-assembly at an interface.

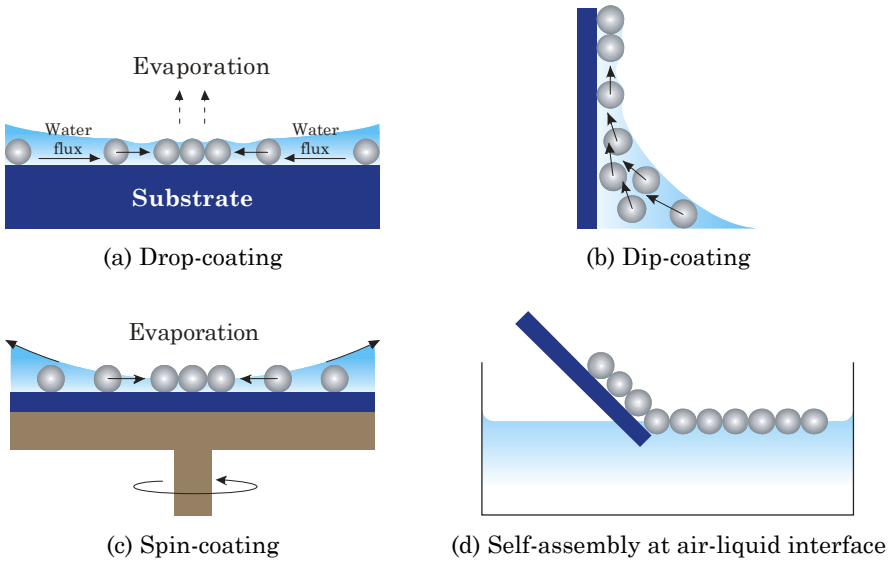

Figure 5.2: Schematic illustration of the typical fabrication methods to produce a self-assembled nanosphere template.

The most straight-forward method to form a self-assembled nanosphere array is to drop-coat the nanosphere suspension onto the surface of a flat substrate; this method has been largely explored by Nagayawa and co-workers [364-368]. Under controlled environmental conditions (temperature and humidity are the key elements), the dispersant solvent (typically water) slowly evaporates and spontaneously starts the self-ordering process when the thickness of the liquid layer of the suspension becomes smaller than the diameter of the nanospheres [364, 365]. A nucleus – an ordered domain of a number of nanospheres – is formed, which subsequently attracts and organises more nanospheres around the nucleus due to attractive capillary forces (see Figure 5.2 (a)). A flat and clean surface is necessary to form a highly ordered array with large domain sizes. The substrate can be tilted to control the solvent evaporation process, hence improving the ordering of the nanospheres [358, 369, 370].

The solvent evaporation rate can also be controlled by using the dip-coating or the vertical deposition method (see Figure 5.2 (b)). In this case, the wettable substrate is placed vertically into a vial containing the nanosphere suspension. The evaporation of the dispersant solvent is achieved at the triple point of the suspension-substrate-air interface, by lateral capillary forces, under a controlled temperature [371, 372] and pressure [373] environment. A stepper motor can be used to provide a controlled evaporation process by slowly (between 0.1 $\mu m \cdot s^{-1}$ and 30 $\mu m \cdot s^{-1}$) lifting up the wettable substrate from the vial [366].

By contrast, the spin-coating method [345, 346, 355, 374] (see Figure 5.2 (c)) accelerates the solvent evaporation process by centrifugal spreading. The substrate surface must be wettable and exhibit an electrostatic repulsion against the nanospheres [294, 295]. The group of Van Duyne improved the wettability of the nanosphere dispersion to the substrate by incorporating the surfactant Triton X-100 into the nanosphere suspension prior to the spin-coating process [345, 346]. The spin speed and the nanosphere concentration are two critical parameters that determine the thickness and the quality of the self-assembled layer [294, 295]. Low spin speeds coupled with high solid concentrations result in multilayer structures with a higher apparent level of defects [294]. The spin-coating method is capable of wafer-scale mass production, as demonstrated by Jiang and McFarland using silica particles dispersed in a photocurable polymer matrix [375]. Well-ordered non-close-packed 3-

dimensional colloidal crystals were formed within minutes, and the thickness was controlled uniformly over a 4-inch wafer.

The drop-coating, dip-coating and spin-coating approaches discussed thus far mainly rely on the capillary force-induced convective solvent evaporation, self-ordering phenomenon. Another way to form an ordered monolayer of nanospheres is by self-assembly at an interface, such as a water-air interface [352, 353, 376-378], an octane-water interface [376] or a hexane-water interface [379]; subsequently, the ordered array can be transferred onto the surface of a substrate by lifting up the monolayer film (see Figure 5.2 (d)) [377, 379] or by controlled evaporation of the underlying liquid [353, 378]. The nanospheres are typically negatively charged as a result of the polymerisation process used in the manufacturing. A mismatch in the dielectric constants can arise if the nanospheres are trapped between a non-polar (such as air or oil) interface, which results in long-range dipolar repulsion [380]. The electrostatic stresses caused by the dipolar field also distort the interface and hence induce capillary forces which attract neighbouring nanospheres to each other [380]. This strong, long-range attractive interaction leads to the formation of an ordered monolayer at the interface [378, 380, 381]. The quality and packing of the array can be controlled by optimising the size, concentration and surface charge density of the nanospheres, and the electrolytic properties of the underlying liquid [294, 295]. Compared to other methods discussed thus far, the interface assembly method is the most suitable to form a uniform monolayer with large area ordering.

5.3 Fabrication of Porous Polysilicon by the NSL Technique

Macroporous (pore width > 50 nm) structures are fabricated in polysilicon substrates using the NSL technique. The schematic flow of the fabrication process is illustrated in Figure 5.3, and described in detail in the following sections. Briefly, the NSL technique is used to create a metal mask (here, chromium (Cr) and gold (Au)) with arrays of holes arranged in a hexagonal pattern. The pattern of holes is then

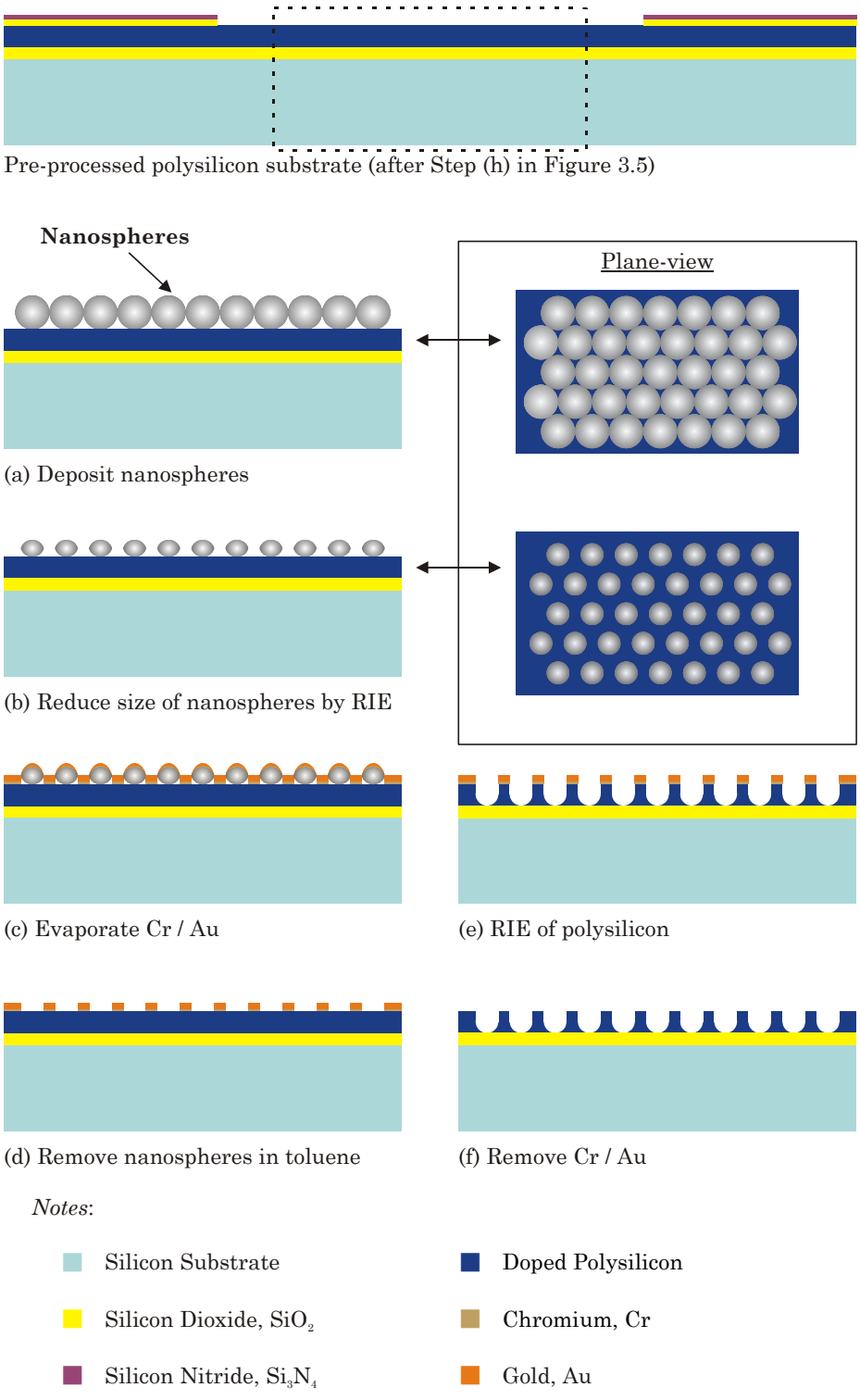

Figure 5.3: Schematic illustration of the fabrication process of the macro-PPSi structure using the NSL technique (not to scale).

transferred to the polysilicon device layer using a fluorine-based RIE process (Step (e) in Figure 5.3), followed by the removal of the metal mask by appropriate etchants, to realise the macro-PPSi (Step (f) in Figure 5.3). To create the patterned metal mask using the NSL technique, nanospheres are first assembled on the polysilicon surface (Step (a) in Figure 5.3) and a subsequent RIE is used to reduce the diameter of the polystyrene nanospheres (Step (b) in Figure 5.3). The metal mask is created by evaporation of thin layers of metal films (here, Cr then Au), over the ordered, size-reduced nanospheres (Step (c) in Figure 5.3). Lift-off of the nanospheres (Step (d) in Figure 5.3) thus provides the metal mask suitable for fabrication of the macro-PPSi.

5.3.1 Substrate Preparation and Treatment

The polysilicon substrates from the wafers of batch K2714s, which was partially used in the investigation of the stain etching method (as discussed in Chapter 3, §3.5), were used here. The wafers (*W10* and *W11*, both with sheet resistance of ~ (338.94 ± 4.95) Ω/sq) were first cut by manual scribing and cleaving. Due to the lack of availability of ashing or RIE systems during the initial development work, the photoresist on the polysilicon substrate samples, mainly from *W10*, was stripped by successively sonicating the samples in acetone, methanol and deionised (DI) water, for 10 minutes to 30 minutes each. In order to maintain the cleanliness and improve the hydrophilicity of the surface, the samples were kept, until used, in specimen bottles containing DI water. These samples were primarily used for the evaluation of NSL using 500 nm spheres.

Samples from *W11* were used for the work using the smaller 200 nm spheres. The photoresist on the samples was "ashed" by using an RIE system (Plasmalab® 80 Plus, Oxford Instruments, UK) with an oxygen (O_2) gas flow rate of 10 sccm, a pressure of 50 mTorr and a radio frequency (RF) power of 100 W, for 10 minutes. After the ashing process, the samples were degreased by sonication in acetone, followed by methanol and DI water, for 10 minutes each. Next, the samples were cleaned using a Piranha solution, which typically consists of a 3:1 volume ratio of 95 % concentrated sulphuric acid (electronic (MOS) grade, Fisher Scientific, UK): 30 % weight in volume (w/v) hydrogen peroxide (general laboratory work (SLR) grade,

Fisher Scientific, UK), to remove any organic and anionic contaminants. This also leaves a more hydrophilic surface on the samples. An O_2 plasma clean, using the same parameters as described above, was then performed to further improve the hydrophilicity of the surface of the samples. Finally, the samples were kept individually, until used, in specimen bottles containing DI water.

5.3.2 Nanosphere Template with 500 nm Spheres

Monodispersed carboxyl polystyrene nanospheres (Polysciences Europe, Germany) with a nominal diameter of 500 nm (coefficient of variance of 3 %, 2.65 weight percent (wt%) aqueous suspension) were used to form the nanosphere template (Step (a) in Figure 5.3). These nanospheres were further diluted with DI water (ELGA® PURELAB Ultra, typical resistivity of 18.2 MΩ·cm, pH of 7.0), into a 1 wt% suspension before use.

A method described by Abdelsalam *et al.* [382] was used to produce the nanosphere template. This method is similar to the dip-coating method (see Figure 5.2 (b)); a physical confinement by two parallel plates, termed "thin layer cell" by Abdelsalam, was used to ensure the formation of monolayer ordered nanosphere arrays, during the vertical deposition process. First, the "thin layer cell" was prepared by sandwiching a thin layer (~ 100 μm thick) of spacer, cut from a single sheet of Parafilm® M (Fisher Scientific, Loughborough, UK), between a pre-treated sample and a glass cover slip ((20 x 20) mm x (0.16 to 0.19) mm thick, MNJ-400-020L, Fisher Scientific UK Ltd., Loughborough, UK). The Parafilm® spacer was cut to form either a trapezoidal or a hexagonal void, as depicted in Figure 5.4 (a). The void was aligned to the 6 mm diameter circular region of the polysilicon device layer. The "thin layer cell" was heated, at 40 °C for about 30 s to enhance the adhesion of the Parafilm® spacer to both the sample and the cover slip, and thus ensuring a proper sealing.

Next, a micropipette was used to dispense the diluted nanosphere suspension at the opening of the patterned void into the "thin layer cell". Extra care was taken during the filling process to avoid the trapping of air bubbles into the cell. Trapped air bubbles were typically removed by gently tapping the sample. The filled sample, such as the one depicted in Figure 5.4 (b), was then held vertically in a sealed

container to control the evaporation of the aqueous solution. The samples typically took 12 to 24 hours to completely dry. Once dried, the "thin layer cell" was heated up to 40 °C to soften the Parafilm®; the glass cover slip and the Parafilm® template were gently peeled off while the Parafilm® was still soft.

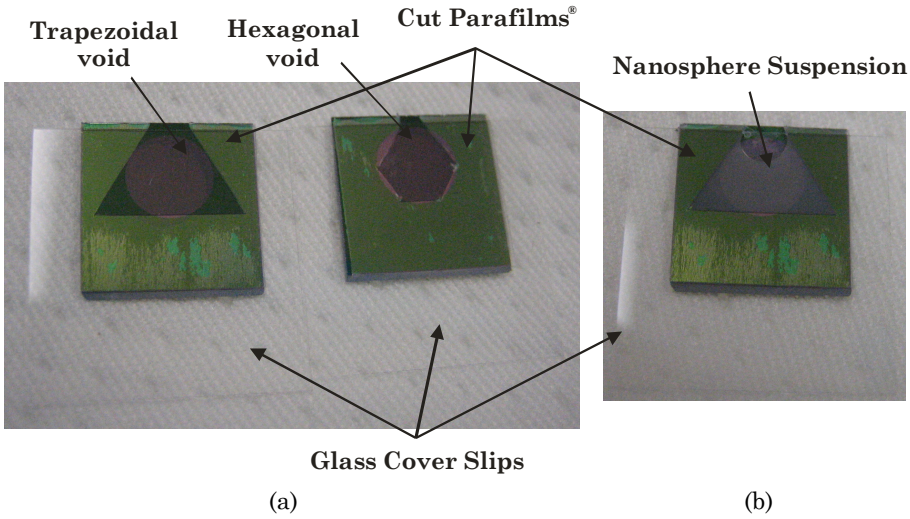

Figure 5.4: Digital photographs of (a) two samples with a trapezoidal void (left) or a hexagonal void (right) cut from a thin layer of Parafilm®; and (b) the sample with trapezoidal void (in (a)) filled with the diluted nanosphere suspension.

5.3.3 Nanosphere Template with 200 nm Spheres

The 200 nm initial-sized nanosphere template was prepared using monodispersed, carboxylate-modified polystyrene (CMPS) nanospheres (Duke Scientifics, (Brookhaven, UK)) with a coefficient of variance of < 5 % and a surface group parking area of 45 Å^2 per carboxyl group. The nanospheres, which were initially suspended into a 4 wt% aqueous solution when purchased, were further diluted with ethanol prior to use.

Prior to a typical deposition process of the nanospheres, a pre-treated and cleaned sample was first coarsely patterned with a layer of thin Parafilm®, as depicted in the inset of Figure 5.5. A square pattern of approximately 6 mm x 6 mm was cut in the Parafilm® layer, so that only the polysilicon device region was exposed and would be deposited with nanospheres. The sample was heated to 40 °C to promote the adhesion of the Parafilm®. For the self-assembly of 200 nm diameter nanospheres, the method described by Weekes *et al.* [378], which relies on the self-

assembly of nanospheres at the water-air interface (see Figure 5.2 (d)), was used. A trough, with an internal dimension of 190 mm x 45 mm and a depth of 10 mm, and two detachable sliders were made using Teflon® for this purpose. The bottom of the trough was covered with black adhesive tape to improve visibility of the monolayer during the deposition process. The trough was first slightly overfilled with DI water. Due to the strong hydrophobicity of Teflon®, it is possible to overfill and retain the DI water within the trough, and hence forming a convex meniscus. Any visible particles or contaminant on the water surface were removed using the sliders. A glass slide of about 100 mm x 40 mm, pre-treated in 1 % w/v of sodium dodecyl sulphate (SDS) was placed at an angle of about 30° at one end of the trough. The patterned sample was then placed onto a sample holder such that the sample surface would be just beneath the water meniscus. Figure 5.5 depicts a sample in the trough ready for the introduction of the nanosphere suspension.

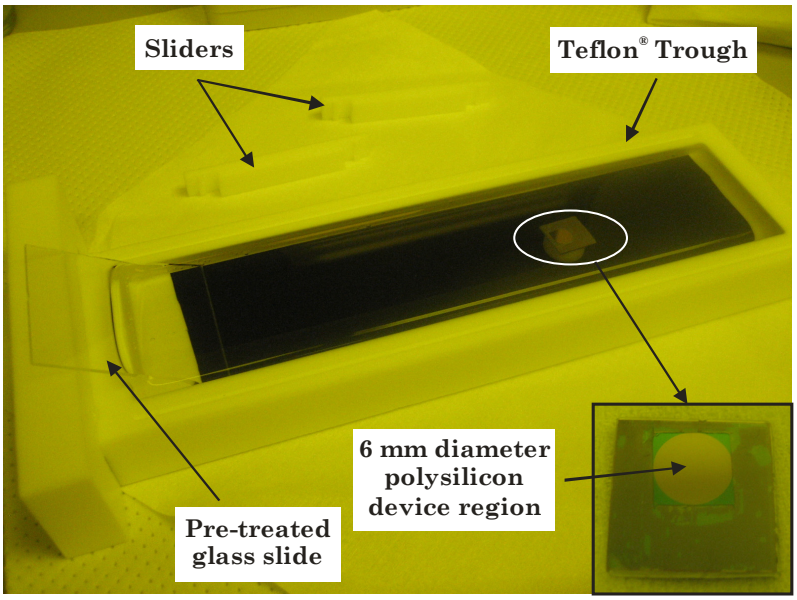

Figure 5.5: Digital photograph of a sample placed in the Teflon® trough, ready for the deposition of nanospheres. The inset shows a digital photograph of the sample patterned with a layer of Parafilm®.

The diluted nanosphere suspension (1:1 mixture of ethanol: 4 wt% CMPS) was slowly dispensed onto the pre-treated glass slide using a micropipette. The nanospheres were allowed to gently float and self-assemble on the water surface. Four 20 μL aliquots of the nanosphere suspension were dispensed, to a total volume of 80 μL, to provide a partially ordered monolayer of nanospheres on the meniscus

surface of the water. The ordering of the self-assembled monolayer (SAM) of nanospheres was further improved by compressing the surface using the two sliders. Figure 5.6 depicts an area of a SAM of nanospheres at the surface of the water. Some water in the trough was then carefully withdrawn therefore transferring the SAM of the nanospheres to the upper surface of the polysilicon substrate in the trough. The sample was then covered and left to dry in the trough with the remaining water, usually overnight. Once dried, the sample was removed from the trough, and the Parafilm® mask was peeled off.

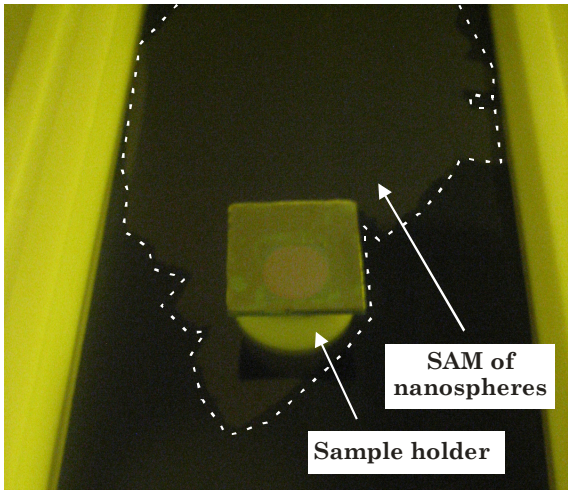

Figure 5.6: Digital photograph of a sample with the self-assembled monolayer (SAM) of nanospheres "floating", at the water-air interface, just above the sample. The dotted white line highlights the boundary of the SAM, for clarity.

5.3.4 Nanosphere Size Reduction

In order to create a template suitable for the formation of macro-PPSi, the nanospheres have to be non-closely packed while still maintaining a hexagonal lattice, as illustrated by the plane-view in Step (b) of Figure 5.3. This is achieved by reducing the diameter of the nanospheres using an RIE process. This way, the initial diameter of the nanospheres defines the spacing of the eventual macro-pores, while the reduced diameter determines the eventual diameter of the pores.

The RIE process was performed in an RIE system (Plasmalab® 80 Plus, Oxford Instruments, UK) using a quartz cover plate. Pure O_2 or a gas mixture of Ar and O_2 was used, with a typical gas flow rate of 5 sccm each, at a pressure between 5

mTorr and 10 mTorr and an RF power of 100 W. It was necessary to first strike the plasma at a slightly higher pressure (typically at 50 mTorr) and later ramp down to the desired RIE pressure. The etching was performed for times between 2 minutes and 5 minutes for nanospheres of 500 nm in diameter, and for times between 60 s and 120 s for 200 nm diameter nanospheres.

5.3.5 Metal Mask

The etched polystyrene nanospheres were covered with a thin layer of chromium (Cr) and gold (Au) to produce a metal mask (Step (c) in Figure 5.3). Evaporation was performed using a BOC Edwards E306A thermal evaporator. The typical mass thickness of the evaporated Cr was 20 nm and the Au was between 100 nm and 120 nm thick for the initial-sized 500 nm diameter nanosphere template, although a mask of only 20 nm Cr was used for the subsequent lift-off process (see §5.4.3). For the nanosphere template with initial diameters of 200 nm, the typical mass thickness of Cr was 5 nm and that of Au was 15 nm, deposited using an electron-beam evaporator (BOC Edwards E500A). The evaporation base pressure was between 1 x 10^{-6} mbar and 5 x 10^{-6} mbar for both cases.

After deposition of the metal layer, lift-off of the nanospheres (Step (d) in Figure 5.3) was achieved by sonicating the substrate in toluene, for approximately 30 minutes to 1 hour, to yield the patterned metal mask.

5.3.6 RIE of Polysilicon

The fabrication of the macro-PPSi by RIE (Step (e) in Figure 5.3) was performed using a Plasmalab® 80 Plus (Oxford Instruments, UK), with a gas mixture of $SF_6/CHF_3/O_2$. This method is commonly known as the "black silicon" method [383]. The typical etching pressure was at 5 mTorr, with an RF power of 100 W, and the etching time ranged from 5 minutes to 10 minutes. After the RIE, the Cr / Au metal mask was removed by sequential exposure of the substrate to gold and chromium etchants (OM Group Ultra Pure Chemicals Ltd., UK) (Step (f) in Figure 5.3), to realise the macro-PPSi structure.

5.4 Results and Discussions

All of the scanning electron microscopy (SEM) micrographs were obtained using the LEO (now Carl Zeiss) 1455VP. Some of the SEM micrographs were image-processed using the National Instruments™ Vision Assistant image processing package to enhance the contrast of the image. Mean diameters of the nanospheres or the pores were measured using an edge detection tool in the Vision Assistant software. Fast Fourier Transforms (FFT) (512 x 512 pixels) of the SEM micrographs were produced using Gwyddion[22] with a 2D FFT tool using Hann windowing.

5.4.1 Nanosphere Template

For the creation of nanosphere templates, polystyrene nanospheres of 500 nm and 200 nm were used. In the case of templates made from 500 nm diameter nanospheres, the majority of the surface of the polysilicon substrates is covered with a monolayer of self assembled polystyrene nanospheres in a hexagonally close-packed structure; other areas consist of either double layers of nanospheres or sparsely-packed nanospheres. In particular, the regions near to the edge of the Parafilm® spacer exhibited multiple growth bands or stripes, as depicted in Figure 5.7, similar to that observed during the growth of colloidal crystals using the vertical deposition method [372]. It is likely that the non-uniform solvent evaporation process, coupled with competing surface tensions from the suspension, resulted in stick-slip motion [372], which alternates the deposition of ordered arrays of nanospheres (the "stick" phase) with no nanosphere deposition (the "slip" phase).

Figure 5.8 depicts the SEM micrograph of the hexagonally close-packed monolayer region of a template formed using the 500 nm diameter polystyrene nanospheres. The nanosphere template typically exhibits polycrystalline domains and natural microscopic defects which are inherent to the NSL technique. These point and line defects, such as those depicted in Figure 5.8, and polycrystalline boundaries are typically due to disordered packing attributed to the polydispersity of

[22] Gwyddion is a scanning probe microscopy (SPM) data visualisation and analysis tool. http://gwyddion.net (*last accessed Jul. 2009*).

the nanospheres, multiple nucleation sites, and uncontrolled solvent evaporation process [350, 384]. The inset of Figure 5.8, which is the digital FFT of the SEM micrograph, demonstrates the effect of defects on the diffraction pattern of the nanosphere arrays. Six first-order Bragg peaks can be observed in the FFT image, which reveals the contributions from the ordering of the hexagonal structure. However, the peaks are not sharp and almost form complete ring patterns at higher orders, which indicates the presence of defects and a lower degree of ordering of the nanospheres.

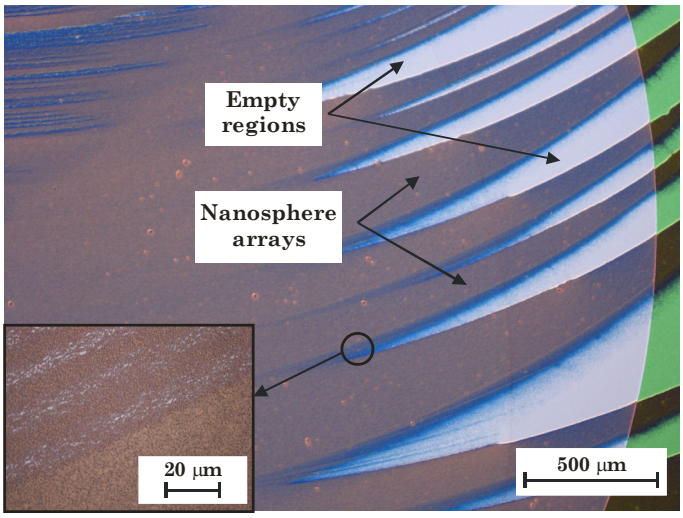

Figure 5.7: Optical microscope image of sample *W10S7* showing the alternating growth bands of nanosphere arrays and empty regions. The inset shows the magnified view of the circled region.

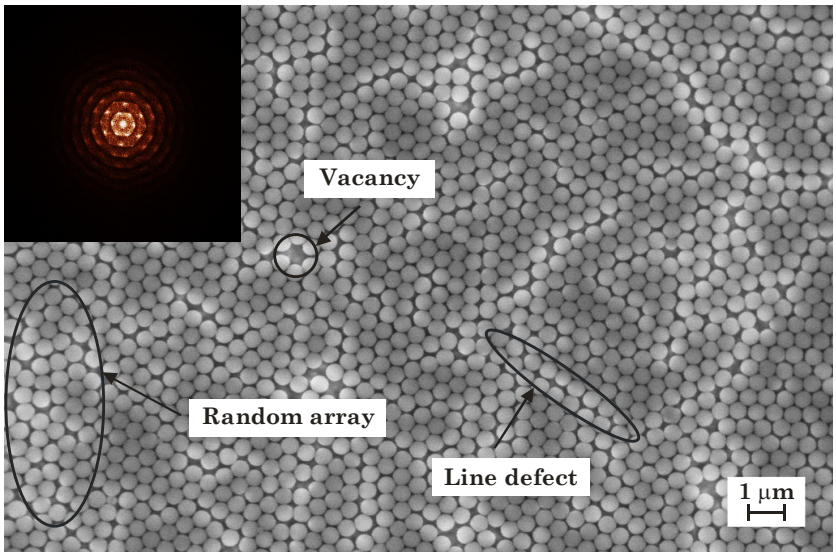

Figure 5.8: Plane-view SEM micrograph of a self-assembled nanosphere template formed by 500 nm diameter polystyrene nanospheres on the polysilicon substrate (sample *W10S1*). The inset shows the digital FFT of the SEM micrograph.

Whilst the assembly method of Abdelsalam *et al.* [382] worked well for the 500 nm sized nanospheres, this method was less successful for the assembly of 200 nm sized nanospheres and thus the method of using a Teflon trough (see §5.3.3) was used. The assembly of the 200 nm nanospheres using the Teflon trough method yielded a higher coverage of the polysilicon substrate in a monolayer (> 98 %) of hexagonally close-packed nanospheres and with fewer overall defects, as depicted in Figure 5.9. The FFT of the SEM micrograph shows distinct, well-defined equidistant first-order peaks, which indicates that the image is constituted from larger single crystalline, hexagonal grains; a negligible amount of defects and polycrystalline domains are present.

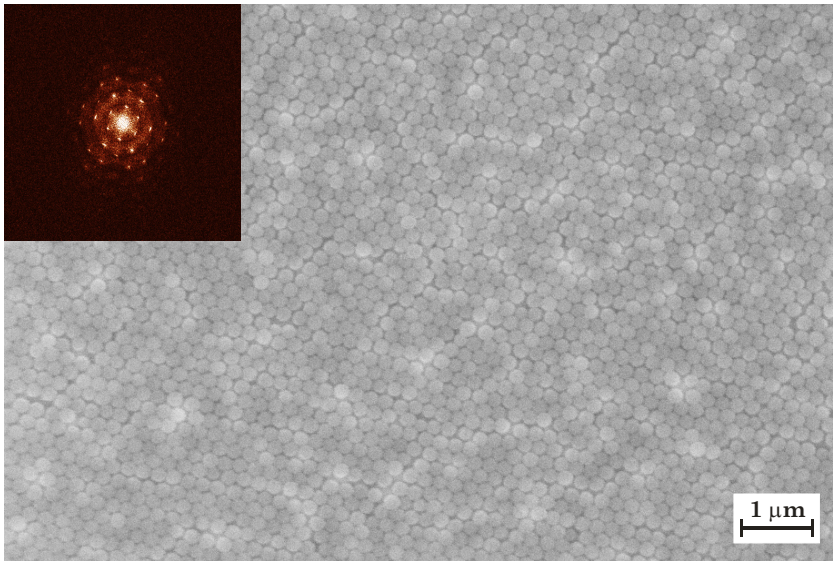

Figure 5.9: Plane-view SEM micrograph of a self-assembled nanosphere template, formed by 200 nm diameter polystyrene nanospheres on a polysilicon substrate (sample *W11S20*). The inset shows the digital FFT of the SEM micrograph.

5.4.2 Nanosphere Size-Reduction

The self-assembled, hexagonally close-packed nanosphere template was etched using an RIE process (Step (b) in Figure 5.3). Theoretically, the diameter of the etched nanospheres determines the eventual diameter of the macropores. In order to better control the size-reduction of the nanospheres, the RIE process must be carefully controlled. Therefore, the size of the resulting nanospheres after the Ar/O_2 RIE was measured as a function of the etch time, and this is plotted in Figure 5.10. Typically, a 2-minute etch at a pressure of 10 mTorr and an RF power of 100 W resulted in a

reduction in the mean diameter, of the 500 nm diameter nanospheres, to 403 nm ± 16 nm (SEM micrograph depicted in Figure 5.11 (a)). A 4-minute RIE reduced the diameter to 284 nm ± 29 nm. As for the 200 nm diameter nanosphere templates, a 60 s and 90 s RIE at a pressure of 5 mTorr, reduced the mean diameter of the nanospheres to 143 nm ± 9 nm (SEM micrograph depicted in Figure 5.11 (b)) and 139 nm ± 14 nm, respectively. As depicted in Figure 5.10, the RIE etching time is found to correlate linearly with the nanosphere diameter, as previously observed by Cheung *et al.* [355]. Based on the linear regression, the etch rates are estimated to be 0.86 nm·s^{-1} and 0.72 nm·s^{-1} for nanospheres with initial sizes of 500 nm and 200 nm, respectively.

After RIE the nanospheres were observed to have a high surface roughness, which has also been reported by other groups [355, 358]. For short etch times, "oblate spheroidal-shaped" nanospheres are formed because the etching occurs preferentially along the top surface of the nanospheres as opposed to the sidewalls. However, for the longer etching times, the polystyrene nanospheres have rather

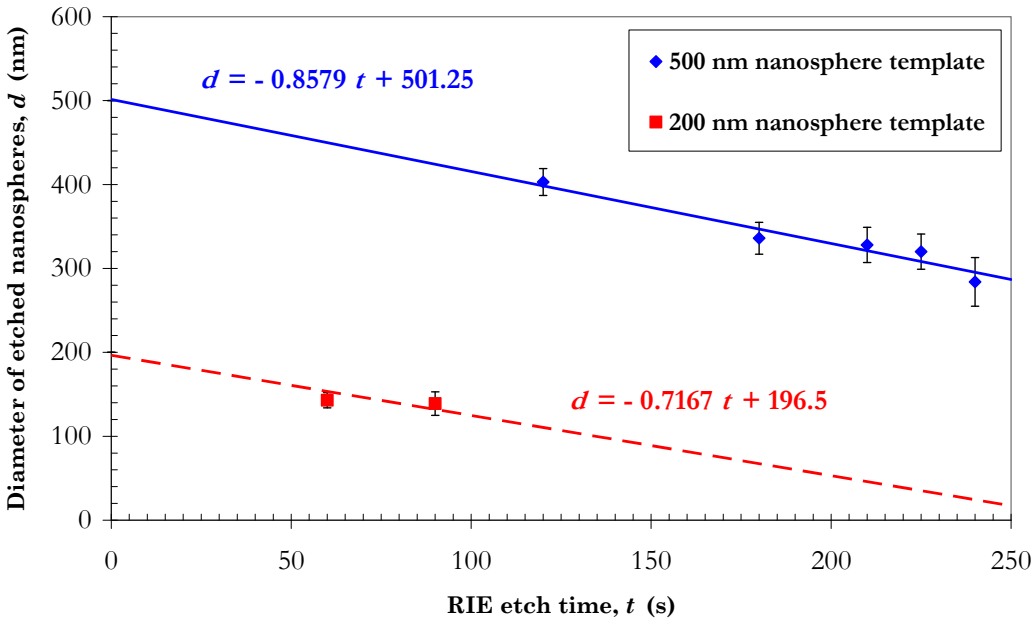

Figure 5.10: Plot of the mean diameter of the nanospheres against the RIE etch time, for nanosphere templates with initial diameter of 500 nm (◆) and 200 nm (■), fitted with linear regression represented by a solid line and a dashed line, respectively. The error bars represent the standard deviations of the detected and measured diameters on the respective SEM micrographs. All the nanosphere templates were processed using Ar/O_2 gas flow of 5 sccm each, with an RF power of 100 W, and at a pressure of 10 mTorr for the 500 nm nanosphere templates and 5 mTorr for the 200 nm nanosphere templates.

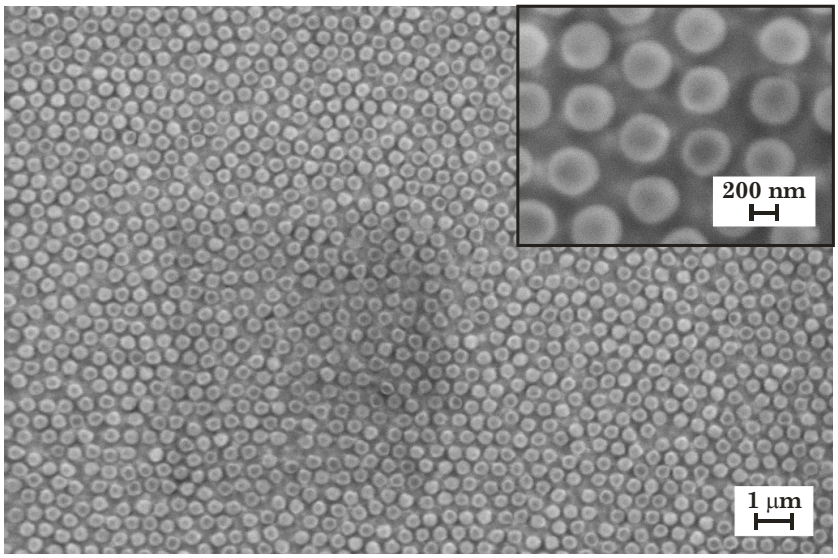

(a) Sample *W10S1*

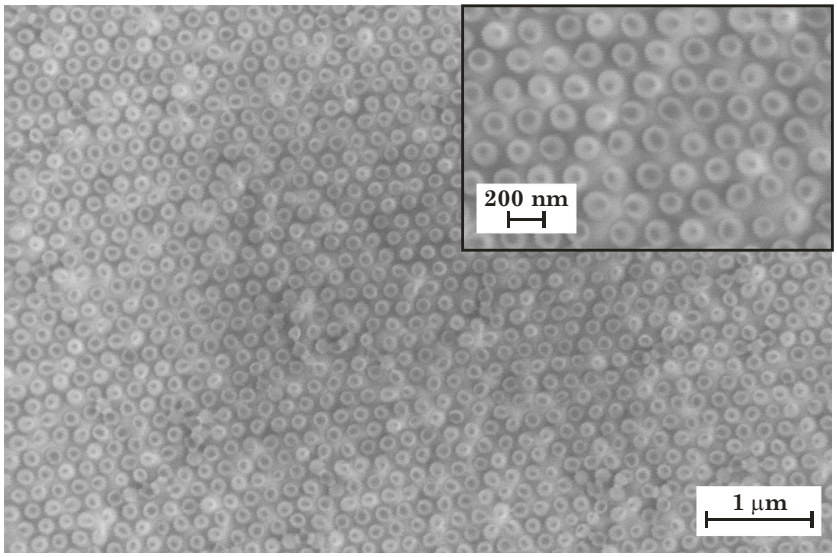

(b) Sample *W11S30*

Figure 5.11: Plane-view SEM micrographs of the size-reduced nanosphere template, after an Ar/O_2 RIE of (a) 2 minutes, at a pressure of 10 mTorr, to achieve a reduction in diameter from 500 nm to 403 nm ± 16 nm; and (b) 1 minute, at a pressure of 5 mTorr, to achieve a reduction in diameter from 200 nm to 143 nm ± 9 nm. The insets in (a) and (b) show the micrographs of the magnified view of the respective sample at a different area.

distorted geometries. This was most obvious for the 500 nm diameter nanospheres, which were etched for times of 3 minutes or longer. For instance, nanospheres etched for 5 minutes (at a pressure of 5 mTorr) are presented in the SEM micrographs depicted in Figure 5.12; it is proposed that the outer shell of the polystyrene nanospheres has swollen and become distorted after exposure to the etching gases for the longer time scales. Therefore, in most cases, the size of the nanospheres was not reduced by more than half the original size during the RIE process.

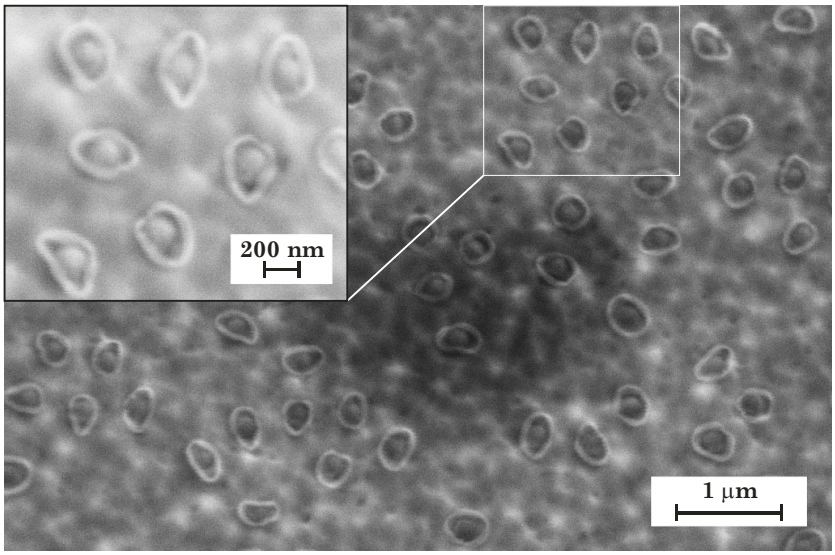

Figure 5.12: Plane-view SEM micrograph of the 500 nm initial-sized nanospheres (sample *W10S26*) after 5 minutes RIE using Ar/O_2 gases, at a pressure of 5 mTorr and an RF power of 100 W. The inset shows the magnified view of the boxed area of the micrograph, showing the swollen outer shell of the polystyrene nanospheres.

5.4.3 Metal Mask

The size-reduced, non-close-packed, hexagonally-ordered nanosphere template was used as a mask for the subsequent metal evaporation and lift-off processes. The size-reduced nanospheres exhibited an oblate spheroidal shape, therefore an evaluation of the optimal thickness of the evaporated metal was required in order to provide a mask that is thin enough to allow successful lift-off of the etched nanospheres, but thick enough to provide sufficient masking for the subsequent RIE of polysilicon. For the 500 nm diameter initial-sized nanosphere template, a thickness of between 100 nm and 120 nm of Au was used, with a 20 nm thick Cr as the adhesion layer. However, during the lift-off process, most of the nanospheres were found to be embedded by the Cr / Au films; some of the nanospheres were eventually removed after the Au film was etched in a gold etchant (1% - 10 % iodine: < 25 % potassium iodide, OM Group Ultra Pure Chemicals Ltd., UK). Therefore, the total thickness of the metal mask was reduced to 20 nm (5 nm of Cr and 15 nm of Au) for the nanosphere templates prepared using the 200 nm diameter nanospheres. An improved lift-off process was observed with this thinner metal masking layer.

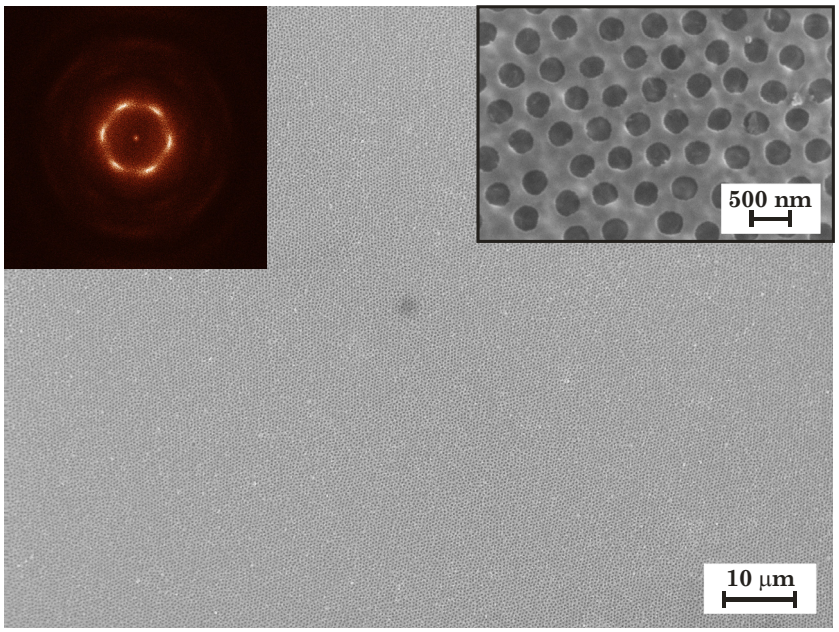

(a) Sample *W10S18*

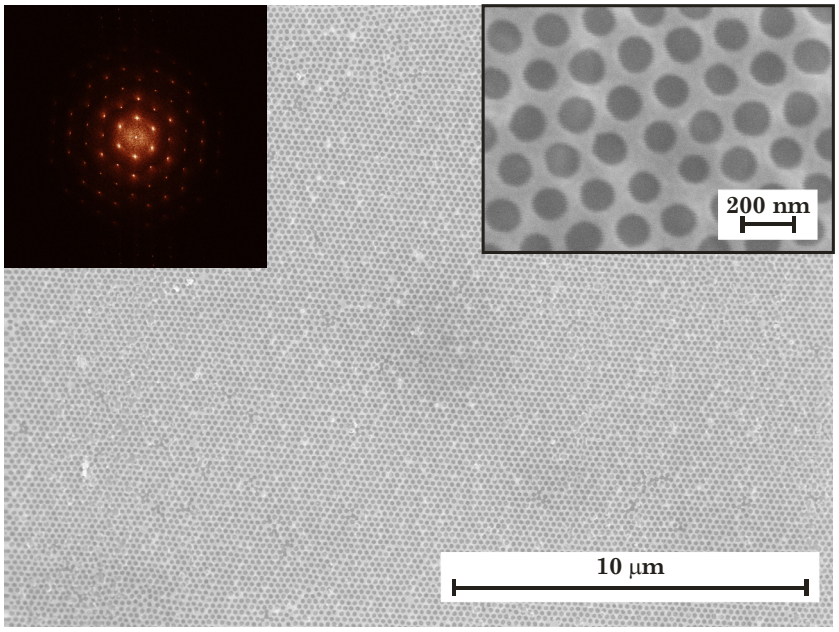

(b) Sample *W10S27*

Figure 5.13: Plane-view SEM micrographs of the metal mask after removal of the size-reduced nanosphere template. (a) the 500 nm diameter nanosphere template (sample *W10S18*) was RIE for 3 minutes using Ar/O_2 gases, at a pressure of 10 mTorr, and then coated with 20 nm thick Cr; (b) the 200 nm diameter nanosphere template (sample *W10S27*) was RIE for 60 s using Ar/O_2 gases, at a pressure of 5 mTorr, and coated with 6.8 nm thick Cr and 14.1 nm thick Au. The insets show the digital FFT diffraction pattern (left) and a magnified view (right) of the SEM micrograph.

Figure 5.13 (a) depicts a high resolution SEM micrograph of an area of 117 μm by 88 μm of sample *W10S18* with the patterned Cr metal mask. The sample was prepared using the self-assembled 500 nm diameter nanospheres, which were then reduced to 336 nm ± 19 nm in diameter by a 3- minute RIE process. The digital FFT of the SEM micrograph, as depicted in the inset of Figure 5.13 (a), demonstrates the preservation of the six-fold hexagonal lattice; the first-order peaks are not sharp, which indicates the presence of defects in the lattice. The mean diameter of the nanoholes in the metal mask was measured to be 337 nm ± 16 nm. Thus, the size of the size-reduced nanospheres was transferred to the metal mask with good accuracy.

The metal mask produced by using the 200 nm initial-sized nanospheres, which were then reduced to 143 nm ± 9 nm in diameter, shows intense, well-defined first-order peaks of the hexagonal diffraction pattern, as depicted by the FFT image of the inset in Figure 5.13 (b). The presence of higher-order peaks demonstrates the high degree, long-range ordering of the hexagonal hole array. The sample *W10S27* was coated with ~ 7 nm thick Cr and 14 nm thick Au. Here, the mean diameter of the nanoholes of the metal mask was measured to be 135 nm ± 10 nm. Thus, the size of the nanoholes, of the metal mask, is ~ 5.6 % smaller than the reduced diameter of the nanospheres, very likely due to a different evaporation condition of the e-beam evaporator used in this case; a thermal evaporator was used for the preparation of the metal mask for the 500 nm initial-sized nanosphere template.

5.4.4 RIE of Polysilicon

The RIE using the "black silicon" method (with appropriate etch conditions as reported by Elwenspoek *et al.* [383]) was used to transfer the pattern of the metal mask to the polysilicon substrate, to form an ordered macro-PPSi structure. Typically, the RIE resulted in a positively tapered etch profile. A number of etch conditions were tested to establish the most effective conditions for transfer of the pattern of holes into the polysilicon substrate with a minimum degree of tapering in the porous structures.

The example, presented in Figure 5.14 was fabricated from self-assembled 500 nm diameter nanospheres. The holes in the metal mask had a diameter of 257 nm ± 20 nm. After 10 minutes of an RIE process, using 15/5/10 sccm flow rate of

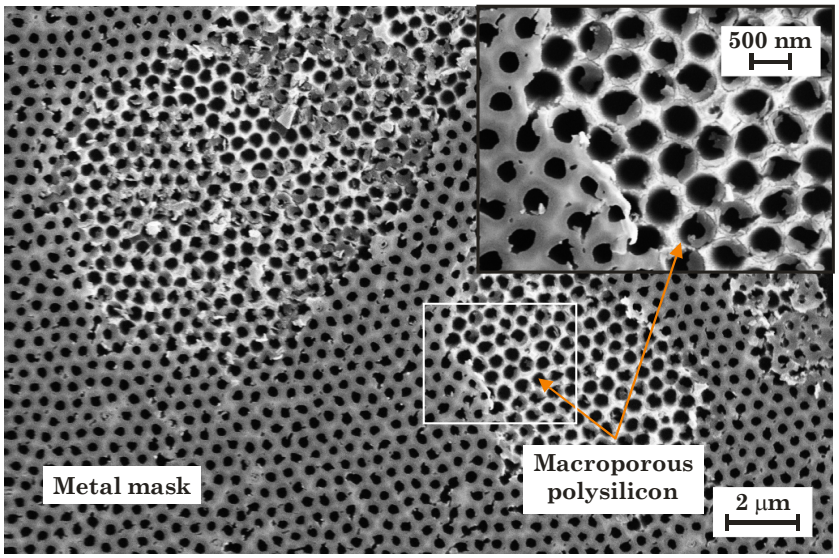

(a)

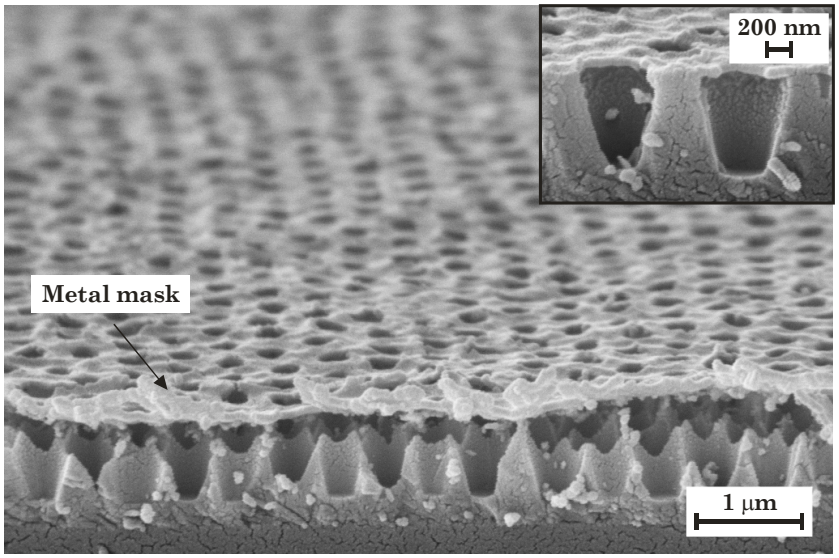

(b)

Figure 5.14: SEM micrographs of the macro-PPSi structure (sample *W10S26*) after 10 minutes RIE of polysilicon, using 15/5/10 sccm of $SF_6/O_2/CHF_3$, at a pressure of 5 mTorr and an RF power of 100 W. (a) the plane-view SEM micrograph shows that some regions of the metal mask were etched by the RIE, thus revealing the macro-PPSi structure (the inset shows magnified view of the boxed area); and (b) the oblique, cross-sectional view SEM micrograph shows the metal mask detached from the porous structure (the inset is a magnified view of pores not within the hexagonal ordered arrays, showing full taper).

$SF_6/O_2/CHF_3$, at a pressure of 5 mTorr and an RF power of 100 W, the polysilicon layer was etched to a depth of 795 nm. The pore diameter of the fabricated macro-PPSi was measured to be 382 nm ± 39 nm after the removal of the metal mask. An undercut of approximately 130 nm, as depicted by the inset of Figure 5.14 (b), is

observed for pores created from spheres in a sparsely-packed arrangement. Due to the undercutting and the tapered etch that results from the etch conditions used, it is clear that there is a limitation to the etch depth before lateral etching at the top surface of the pores would lead to interconnection. This was observed for the area of the sample where the pores in the mask are in the ordered hexagonal array. Figure 5.14 (b) shows a cleaved wafer where the upper surface of the etched polysilicon has pointed 'crown-like' structures, with the point apex at a location where the metal mask width between adjacent pores is greatest. As depicted in Figure 5.14 (a), the regions where the metal mask has been unintentionally removed by the RIE process show that the porous structure is intact. The polysilicon surface and structure show various etch rate under the conditions used, possibly due to the polycrystalline nature of the polysilicon, slight non-uniformities of the original polysilicon surfaces, or poor adhesion of the mask.

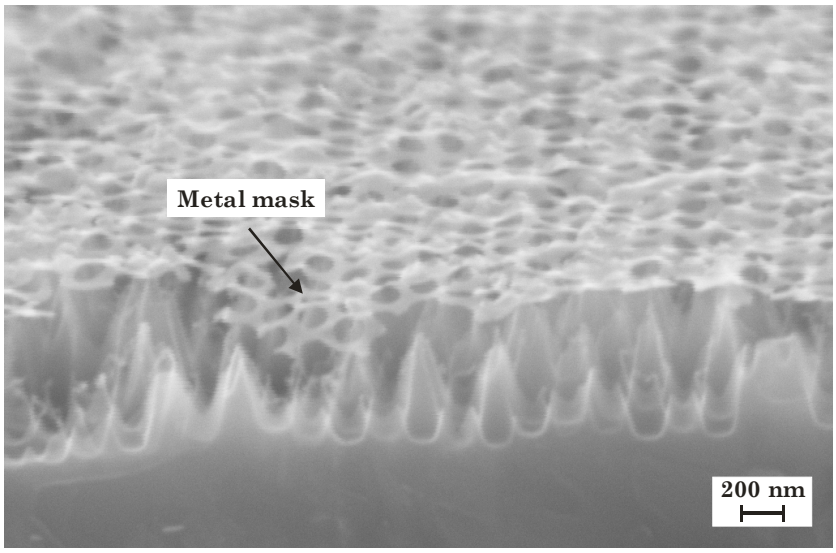

Figure 5.15: Cross-sectional view SEM micrograph of cleaved sample *W11S29* showing the macro-PPSi structure after a 10 minutes RIE of polysilicon using 15/5/10 sccm flow rate of $SF_6/O_2/CHF_3$ at a pressure of 5 mTorr and an RF power of 50 W.

By an 'over-etching' of the samples or the use of non-optimised etch conditions, hexagonally ordered, microneedle-like, spiked triangular pyramids were formed rather than pores. This is a result of the tapered etch profile, which ultimately causes a lateral 'through-etching' between the pores at the upper surface. An example of the spiked structure is depicted in Figure 5.15, where the sample *W11S29* was fabricated from the self-assembled 200 nm diameter nanospheres. A metal mask with holes of 134 nm ± 9 nm in diameter was used. The RIE of the

polysilicon layer was carried out with a reduced power of 50 W. In this sample, the structures were measured to be ~ 500 nm high; ordered spikes are clearly seen below the metal mask.

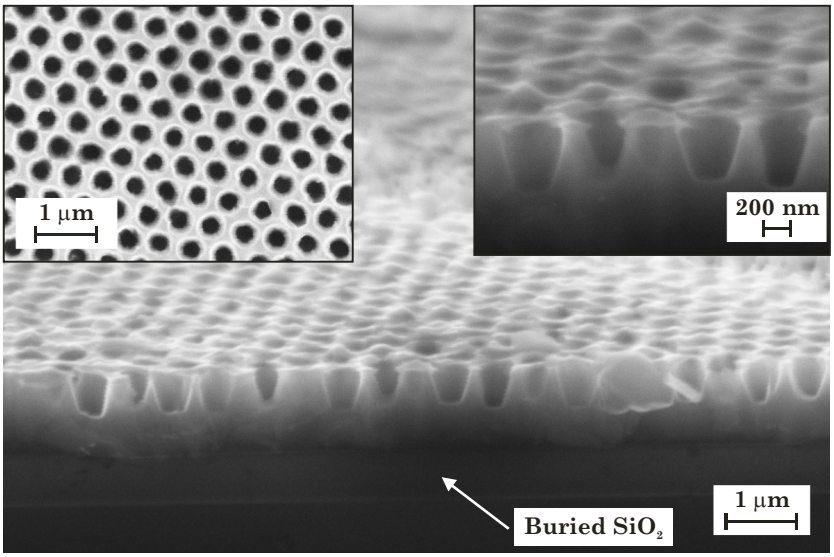

Figure 5.16: Oblique, cross-sectional view SEM micrograph of the macro-PPSi structure of sample *W10S13*, after 5 minutes RIE of polysilicon using 30/10/12 sccm flow rate of $SF_6/O_2/CHF_3$, at a pressure of 5 mTorr and an RF power of 100 W. The inset SEM micrographs show the plane-view (left) and the magnified view (right) of the cleaved edge.

A macro-PPSi structure after the chemical removal of the metal mask is illustrated in Figure 5.16. The sample *W10S13* was fabricated using a metal mask with holes of 279 nm ± 15 nm in diameter. The RIE of polysilicon was performed using a gas flow rate of 30/10/12 sccm of $SF_6/O_2/CHF_3$ and an etch time of 5 minutes. The etch depth of the positively tapered pores was limited to ~ 417 nm and the pore diameter was measured to be 370 nm ± 30 nm. The reduced etch depth ensures that the sample has a smooth upper surface with uniformly sized pores in hexagonally ordered arrays.

5.5 Conclusion

A practical approach for fabricating a PPSi structure using the NSL technique has been described. Nanospheres with mean diameters of 500 nm and 200 nm were used to form metal masks with hexagonally arranged hole-patterns. Macro-PPSi with

tapered pores was fabricated from these metal masks. For example, a macro-PPSi with pore width of 370 nm ± 30 nm and a pore depth of ~ 417 nm (see Figure 5.16) was achieved using the "black silicon" RIE process and a metal mask formed using the 500 nm initial-sized nanospheres. Although the quasi-ordered PPSi exhibited a tapered profile, this is the first demonstration of the fabrication of PPSi with ordered pores of sizes in the macropore range (of ~ 370 nm). PPSi structures fabricated using a metal mask formed using the 200 nm initial-sized nanospheres typically exhibit a microneedle-like, spiked triangular pyramidal shape. This is a result of lateral through-etching between the pores at the upper surface (see Figure 5.15).

In principle, the NSL technique provides an inexpensive and practical approach for pattern generation of hexagonally-arranged holes, with tuneable diameter and spacing (or pitch size) of the holes. The initial size of the nanospheres used in the NSL technique provides the pitch size; while careful control of the RIE process reduces the size of the nanospheres (quasi-linearly, as depicted in Figure 5.10), and hence defines the eventual diameter of the holes. In practise, however, there is a limit to the minimum size that can be achieved. The smaller the size-reduced nanospheres are, the thinner the metal mask has to be to enable the later removal of nanospheres. Additionally, a thin metal mask limits the etch depth of the polysilicon using the RIE process. Therefore, in most cases, the size of the nanospheres was not reduced (by RIE) by more than half the original size. A metal mask with total thickness of 20 nm was found to produce successful lift-off and was also sufficiently robust during the RIE of the polysilicon layer.

Due to the under-cutting and the formation of a tapered etch profile, as a result of using the etch tool, it was necessary to limit the depth by which the samples were etched. Lateral etching between adjacent pores resulted in interconnecting porous structures at the upper surface, or even hexagonally-ordered, spiked triangular pyramid surfaces. It is clear that the fabrication approach could be used for creating macroporous regions in other substrates. With different etching tools, the geometry of the pores could be improved so that the sidewalls would be straight. Hexagonally ordered, uniform, cylindrical macro-PPSi structures could thus be obtained by careful control of the etch conditions.

Chapter 6

The Design and Fabrication of a Porous Silicon Membrane Drug Delivery Device

6.1 Introduction

Novel fabrication techniques, by applying a porous anodic alumina (PAA) template or the nanosphere lithography (NSL) approach, to form a porous polysilicon (PPSi) structure, have been demonstrated and discussed in Chapter 4 and Chapter 5, respectively. Both successful and less successful outcomes were achieved, primarily affected by the physical properties of the polysilicon device layer. However, it is clear that, with the proper tools and optimised processes, there is very good potential for these techniques.

In this chapter, the design and fabrication of a drug delivery device with a silicon substrate, rather than a polysilicon layer, is described. A silicon membrane, with a quasi-ordered porous silicon (PSi) structure as the drug reservoir, was integrated and fabricated using an improved NSL technique. An integrated heater and temperature sensor, instead of a pair of electrodes (as discussed in Chapter 3), was proposed for the electro-thermal actuation of the drug delivery device. The application of a finite element analysis (FEA) modelling approach to investigate the operational range of the heater is also presented.

6.2 Device Design

The PPSi-based drug delivery prototype device, discussed thus far, was found to be non-ideal. Firstly, the polysilicon device layer, used as a material for the fabrication of PPSi, created a number of fabrication issues. Two novel approaches to fabricate the PPSi structure have been described and these include using a PAA template (as discussed in Chapter 4) and the NSL technique (as discussed in Chapter 5). In the case of the PAA template, the non-uniform thickness in the evaporated aluminium caused uncharacteristic anodising behaviours, which resulted in the PAA films to detach from the substrate due to over-etching (see Chapter 4, §4.3.3 for details). This, in addition to the poor contact between the deposited aluminium and the rough polysilicon surface, led to the formation of pores with sloped side walls. As such, these PAA structures are not ideal to be used as a masking template for the subsequent reactive ion etching (RIE) of the polysilicon layer. In the case of the NSL technique, the "black silicon" method used in the RIE of the polysilicon layer formed an undercut beneath the NSL-formed metal mask and thus resulted in a positively tapered, "crown-like" PPSi structure (see Chapter 5, §5.4.4 for details). The depth of the fabricated pores is therefore limited. Secondly, the fabrication of the aluminium electrode, as described in Chapter 3, §3.6, was not feasible. For a good electrical contact, the evaporated aluminium needs to fill the pores in the PPSi structure, which is technically challenging.

Therefore, an improved prototype drug delivery device, using a silicon membrane substrate with an alternative electro-thermal actuation method, is proposed. In this design, as depicted in Figure 6.1, the silicon membrane substrate consists of a nanostructured, quasi-ordered PSi layer, fabricated at the back-side of the membrane, which is used as the drug reservoir. An integrated heater and temperature sensor is incorporated at the front-side of the silicon membrane. By using a resistive heating, it is envisaged that the heating element will provide a rapid increase in temperature, for a short period of time, to the PSi structure, therefore promoting the release of the loaded therapeutic agents from the pores. The temperature sensor can be used to provide feedback of the temperature distribution of the device. When coupled with a closed-loop control circuitry, this enables precise modulation of the temperature for the electro-thermal actuation.

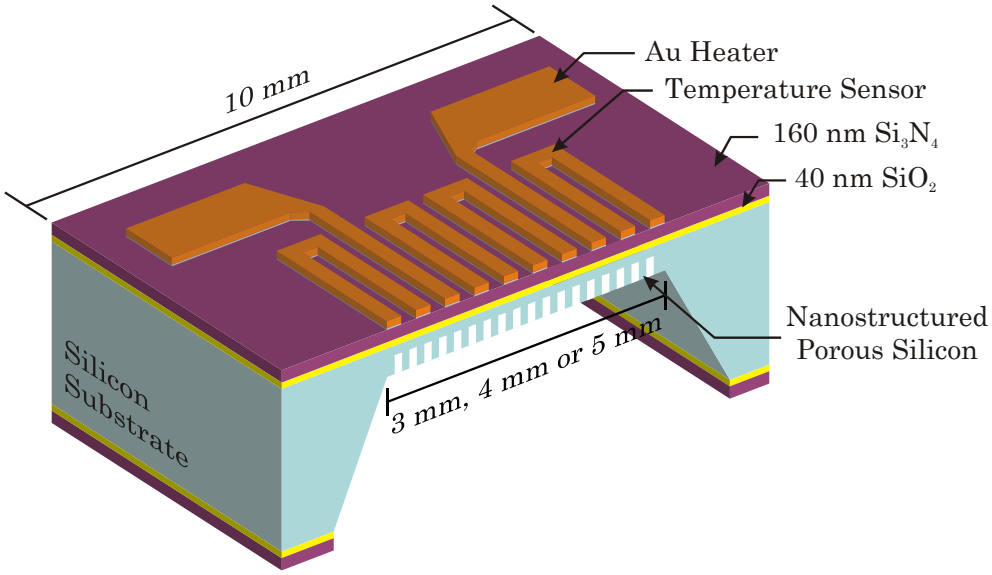

Figure 6.1: Oblique, cross-sectional view, conceptual illustration of the envisaged prototype drug delivery device (not to scale; see Figure 6.8 for further fabrication details and colour scheme of materials used).

6.2.1 Design of the Silicon Membrane

For this revised, second generation prototype drug delivery device, single-crystal silicon is used instead of polysilicon as the substrate. Single-crystal silicon is a popular and well-established substrate for the fabrication of microelectromechanical systems (MEMS) devices. A polished silicon wafer is nearly atomically flat and hence provides a smoother surface than the polysilicon layer. The RIE of silicon has also been more comprehensively investigated than the RIE of polysilicon. Fabrication of a porous structure in single-crystal silicon has been extensively studied (see Chapter 2, §2.3 for a literature review of PSi), and various fabrication approaches, including using PAA templating and the NSL technique have been investigated by both academia and industry.

A thin silicon membrane is preferred over the bulk silicon substrate, for the device area, to ensure a good thermal conductivity and heat transfer from the heating element to the PSi layer. The membrane is proposed to be 50 μm thick, which is a compromise between ease of fabrication, mechanical robustness (for handling) and optimum heat transfer. Three membrane sizes were proposed – 3 mm

x 3 mm, 4 mm x 4 mm and 5 mm x 5 mm and the conceptualised prototype device has an overall dimension of 10 mm x 10 mm.

A wet chemical anisotropic etch is the most straight-forward method to fabricate the proposed membrane structure [42]. Potassium hydroxide (KOH), tetramethyl ammonium hydroxide (TMAH) and ethylenediamine pyrocatechol (EDP) are three common etchants that are capable of anisotropic etching of silicon. These etchants produce characteristic 54.74° inward sloping walls, as depicted in Figure 6.2, on silicon wafers with <100> orientation. To realise the three membrane sizes on a silicon wafer with thickness of 525 μm, the masking materials (typically silicon dioxide (SiO_2) and silicon nitride (Si_3N_4)) would need an opening of either 3.67 mm x 3.67 mm, 4.67 mm x 4.67 mm or 5.67 mm x 5.67 mm. To achieve a membrane thickness of 50 μm, the etch depth is measured intermittently during the etching process. An etch rate can then be estimated, hence providing a total etch time needed to achieve the 50 μm thickness for the silicon membrane. Alternatively, *in-situ* optical monitoring [385, 386] can be used to control the etching; a boron-doped layer can be used as an etch stop; or a silicon-on-insulator (SOI) technology can be used with the insulator layer readily providing the etch stop.

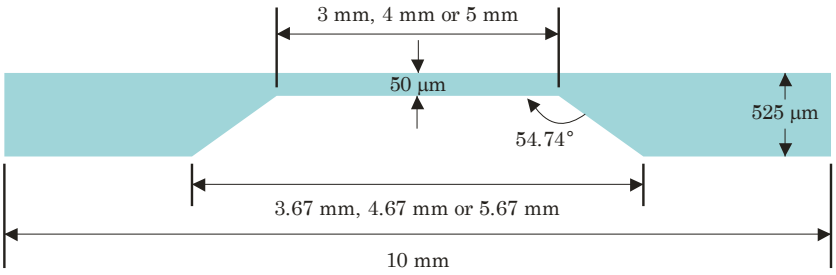

Figure 6.2: Cross-sectional view of the conceptualised, 50 μm thick, silicon membrane.

6.2.2 Nanostructuring of Porous Silicon

The PSi region is designed to have a pore diameter in the range of 50 nm to 100 nm, with an aspect ratio of 10:1 (due to the limitation of dry etching), resulting in a pore depth in the range of 500 nm to 1 μm. The fabrication of the PSi structure was originally proposed to be carried out using RIE with both masking approaches: i) a PAA template (for a smaller pore diameter in the range of 50 nm), as discussed in Chapter 4; and ii) a metal mask formed by NSL technique (for a pore diameter in the

range of 100 nm), as discussed in Chapter 5. However, the approach using the PAA template was later suspended, primarily due to the limited access to the modified thermal evaporator used to deposit a thick layer of aluminium that is necessary for the formation of the PAA template.

The PSi structure could be formed either on the front-side or the back-side of the silicon membrane. However, at the back-side of the silicon membrane, optical lithography is not easy to achieve inside the etched cavity as the sloping wall of the silicon membrane imposes a potential problem in getting a uniform thickness of photoresist. Since a lithographic step is required for the fabrication of the heater and the temperature sensor, it is sensible to fabricate the PSi structure (which does not involve a process using photoresist) in the base of the etched cavity.

6.2.3 Design of the Integrated Heater and Temperature Sensor

Instead of using a pair of electrodes impregnated into the porous structure, as described in Chapter 3, a heating element was proposed for the electro-thermal actuation. The principle is to rapidly heat the PSi structure for a short time to accelerate the dissolution of the PSi and assist desorption of the therapeutic agents into the environment (human body). The generated heat needs to be localised; it should not critically increase the temperature of the surroundings (to prevent thermal shock to the human body), and should not affect the biological activity of the therapeutic agents (such as protein and peptide-based biopharmaceuticals, specifically, bone morphogenetic protein-2 (BMP-2), see Chapter 1, §1.1.1). Hence, two primary design specifications and assumptions for the heater were prescribed:

i) The critical temperature of the surrounding environment to avoid thermal shock was assumed to be 43.5 °C ± 1.5 °C [387]. The heater should not be heated beyond the critical temperature for a long time (not more than 1 s) when it is turned on, and should cool down relatively quickly to below the critical temperature after being turned off;

ii) The temperature limit deemed safe before a significant reduction in biological activity of the therapeutic agents was assumed to be 60 °C ± 10 °C (since

recombinant human BMP-2 showed little reduction in biological activity, after being heat-treated for 8 hours at 70 °C [30]). Therefore, the heating element should be made of material with a high thermal conductivity (hence, a short thermal response time), so that the heat can be generated and transferred before the temperature of the surrounding environment exceeded the critical temperature, as discussed above.

The temperature sensor is essentially a resistance temperature detector, which exploits the predictable change in electrical resistance with changing temperature. Hence the temperature sensor should have a linear, stable and reproducible thermoelectric characteristic. Importantly, the temperature coefficient of resistance (TCR) of the material used to fabricate the thin film temperature sensor should be low, so that the resistance of the material does not change over a long operational time.

The most widely used material for the temperature sensor is platinum and, due to an integrated fabrication process, the heater is commonly made of the same material as the temperature sensor. Platinum has a low TCR value of 0.00373 K^{-1} [388], but the thermal conductivity is only 71.6 $W \cdot m^{-1} \cdot K^{-1}$ [389]. In addition, gold wires (for connection to the external world) do not bond well to a platinum surface; additional fabrication process steps are required to create the bond pads. In contrast, gold has a similar TCR value (0.00372 K^{-1} [388]), but a higher thermal conductivity (317 $W \cdot m^{-1} \cdot K^{-1}$ [389]), and hence a potentially shorter thermal response time. Consequently, gold is preferred over platinum for both the integrated heater and the temperature sensor.

Three designs of the heater and the temperature sensor were proposed: meander, spiral and coil, as depicted in Figure 6.3. The meander design is an implementation of a simple resistor design and serves as the basis for comparison. The spiral design optimises the heater length with area, while the coil design minimises the hot spot typically created by sharp, abrupt corners. The thickness of the gold (Au) heater and temperature sensor was proposed to be 300 nm, with a 10 nm thick layer of titanium (Ti) as the adhesion layer. Table 6.1 summarises the dimensions and expected resistance of the designed heaters and temperature sensors.

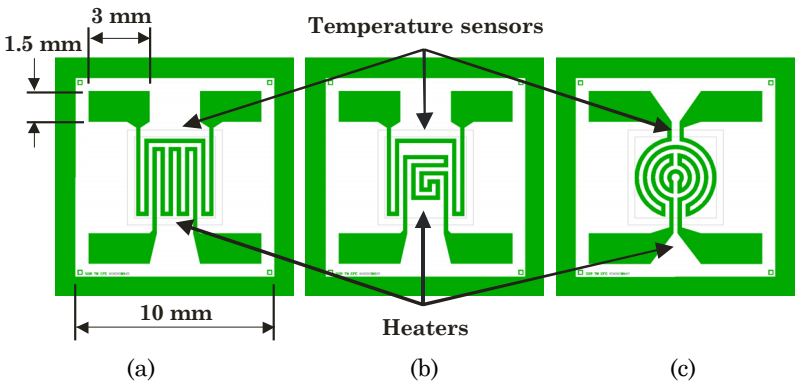

Figure 6.3: Schematic illustration of the heater and the temperature sensor designs: (a) meander; (b) spiral; and (c) coil.

Design	Membrane size (mm)	Track Width (µm)	Heater		Temperature Sensor	
			Track Length (mm)	Track Resistance (Ω)	Track Length (mm)	Track Resistance (Ω)
Meander	3 x 3	150	16.2	7.970	13.8	6.790
	4 x 4	200	21.6		18.4	
	5 x 5	250	27.0		23.0	
Spiral	3 x 3	150	12.0	5.904	13.8	6.790
	4 x 4	200	16.0		18.4	
	5 x 5	250	20.0		23.0	
Coil	3 x 3	150	10.1	4.971	19.4	9.532
	4 x 4	200	14.7	5.418	19.4	7.161
	5 x 5	250	19.4	5.739	19.8	5.858

Table 6.1: The dimensions of the three designed heaters and temperature sensors. The thickness of both the heater and the temperature sensor is 300 nm.

6.2.3.1 Thermal Analysis of the Heater

In order to investigate the temperature distribution resulting from the three heater designs, and thus to estimate the performance and operational range, an electro-thermal analysis using an FEA simulation tool, COMSOL[23], was performed. In addition to the heater material (as discussed previously), other parameters that affect the heat generation by Joule heating are the voltage applied to the heater (actuation voltage) and the time the heater is turned on (heater on-time). Hence, actuation voltages of 1 V to 5 V, with a heater on-time of 0.5 s, were investigated in

[23] COMSOL Ltd., http://www.comsol.com/ (*last accessed Jul. 2009*).

the simulation; heater on-times of 0.1 s and 1.0 s were also used in some simulations. Both steady-state and time-dependent analyses were performed.

The 3D simulation was performed by coupling the electrical heat generation by the Joule heating and the heat transferred to the device due to this heat generation. This multiphysics simulation uses the AC / DC Module in combination with the Heat Transfer Module of COMSOL. In the AC / DC Module, the *Shell, Conductive Media DC* application mode (see Appendix D.1.2 for details) was used to take into account the thickness effect of the heater, without the need to geometrically model the actual dimensions of the heater. The geometrical dimensions of the heater span 4 orders of magnitude (the heater thickness is 300 nm, while the length is in the millimetre range). This makes the simulation practically unfeasible with common desktop computers. The *Shell, Conductive Media DC* application mode eliminates this geometrical constraint by providing a reasonably accurate approximation to the actual solution of the FEA.

The heat generated by the Joule heating is then coupled into the *General Heat Transfer* application mode (see Appendix D.2.1 for details) of the Heat Transfer Module. The *Highly Conductive Layer* feature was enabled, to model the thin conducting layer of the heater, which specifies the generated heat as an inward heat flux at the top surface of the silicon membrane.

The following assumptions were also made in the COMSOL simulation:

i) The heat transfer is assumed to be mainly by conduction, from the heater to the PSi structure (at the back-side of the silicon membrane), and a natural convective heat transfer occurs from the device to the surrounding environment, which is modelled as a fluid with a constant temperature of 37 °C. All the surfaces of the device are thus subjected to a natural convective heat transfer coefficient, h_c, which is assumed to be 200 $W \cdot m^{-2} \cdot K^{-1}$. The value of h_c was assumed based on the typical value of h_c of liquid (between 50 $W \cdot m^{-2} \cdot K^{-1}$ and 1000 $W \cdot m^{-2} \cdot K^{-1}$ [390]) and a proposed equivalent heat transfer coefficient (of between 100 $W \cdot m^{-2} \cdot K^{-1}$ and 300 $W \cdot m^{-2} \cdot K^{-1}$), between a biological tissue and blood, based on a porous media model [391];

ii) The temperature sensor was not included in the model. The heat transferred to the temperature sensor, by convection and radiation from the heater, is hence assumed to be negligible in accordance to assumption (i) above;

iii) The Ti adhesion layer (of 10 nm thick) was not considered in the model, since its resistance (in kΩ range) is much larger than the resistance of the heater and, thus, the effective resistance is dominated by the resistance of the heater;

iv) The insulating Si_3N_4 (160 nm) and SiO_2 (40 nm) layers were not considered in the model. A 2D simulation (see Appendix D.3 for results) demonstrated that the effect of the insulating layers were negligible to the overall heat transfer;

v) The PSi structure was assumed to have the same thermal and electrical properties as the bulk silicon (which is not true since PSi is typically more resistive, both electrically [392] and thermally [393]) due to the thickness factor (as the PSi layer is between 500 nm and 1 μm);

vi) In the model, the silicon substrate has a size of 10 mm x 10 mm x 525 μm. Only the membrane with a size of 4 mm x 4 mm was simulated, with an assumed thickness of 50 μm. The length and width of the heater tracks were simulated using the dimensions of the 4 mm x 4 mm membrane, as described in Table 6.1, with a track thickness of 300 nm.

The Joule heating was simulated as a result of an input voltage, V_{in} to the heater. In the steady-state simulation, V_{in} equates to the actuation voltage, V_{dd}. In the time-dependent simulation V_{in} is defined using a Heaviside function as follows:

$$V_{in} = V_{dd}\left[1 - flc1hs\left(t - t_{ON}, S_{HS}\right)\right] \tag{6.1}$$

where t_{ON} is the heater on-time and S_{HS} is the slope of the Heaviside function, $flc1hs$, to model the transient switching off of the heater. Only the heater was involved in this part of the simulation, with the electrical conductivity as the only governing material property. The electrical conductivity of the heater, σ_{Heater} was modelled using a temperature-dependent equation:

$$\sigma_{Heater} = \frac{1}{\rho_0\left[1 + \alpha\left(T - T_0\right)\right]} \tag{6.2}$$

where ρ_0 is the resistivity at a reference temperature, T_0, and α is the TCR value of the material. For this, the electrical properties of gold, as summarised in Table 6.2, were used.

Parameter	Value	Unit	Reference
Reference Resistivity, ρ_0	2.2×10^{-8}	Ω·m	[389]
Reference Temperature, T_0	293.15	K	[389]
Temperature Coefficient of Resistance, α	0.00372	K^{-1}	[388]

Table 6.2: The electrical properties of gold used in the settings of the *Shell, Conductive Media DC* application mode.

Properties	Gold	Silicon
Specific heat capacity, C ($J \cdot kg^{-1} \cdot K^{-1}$)	129	703
Thermal conductivity, k ($W \cdot m^{-1} \cdot K^{-1}$)	317	163
Density, ρ ($kg \cdot m^{-3}$)	19300	2330

Table 6.3: The thermal properties of gold and silicon used in the settings of the *General Heat Transfer* application mode. All the properties were obtained from the *Materials Libraries* of COMSOL.

In the heat transfer analysis, both the silicon membrane and the gold heater were included in the simulation. The thermal properties of both silicon and gold, as presented in Table 6.3, were used in the simulation. The time-dependent simulation was performed with an initial temperature of 37 °C, as described in assumption (i) (page 169).

As predicted, the steady-state temperature of the device (at the centre of the membrane), as summarised in Table 6.4 and depicted in Figure 6.4, increases proportionally with an increase in the actuation voltage. In fact, the behaviour of steady-state temperature with respect to the actuation voltage can be best described by a 4^{th} order polynomial, as depicted in Figure 6.4. Among the three heater designs, the coil heater (design (c) in Figure 6.3), having the shortest heater track length (hence, the least resistive), produces the greatest temperature rise per length.

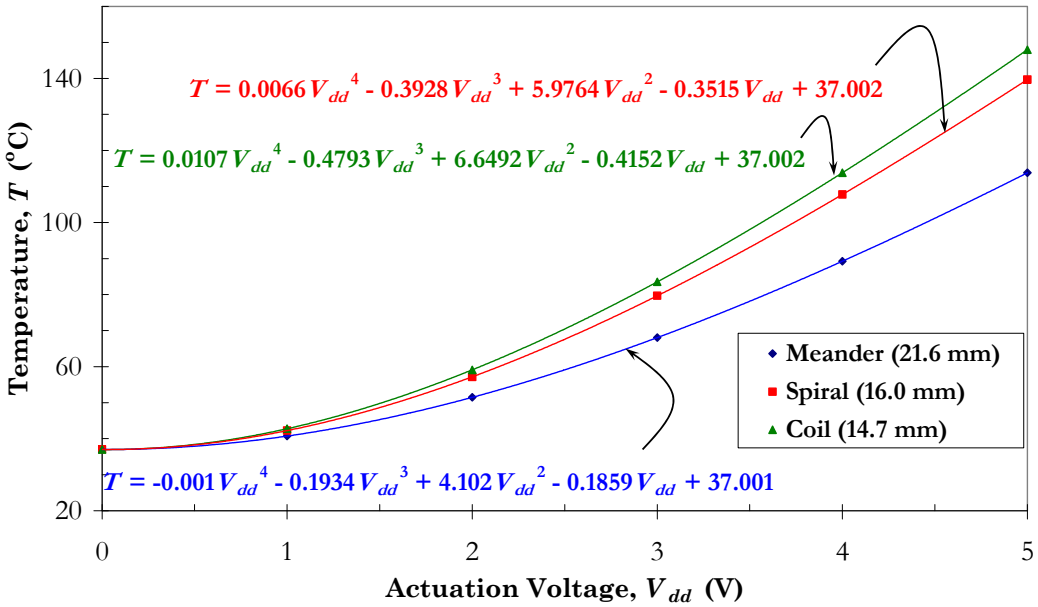

Figure 6.4: Simulated steady-state temperature, at the centre of the membrane, with respect to the actuation voltages of 1 V to 5 V for the meander (◆), spiral (■) and coil (▲) heaters. The solid lines represent the least square fit with a 4th order polynomial described by the expressions.

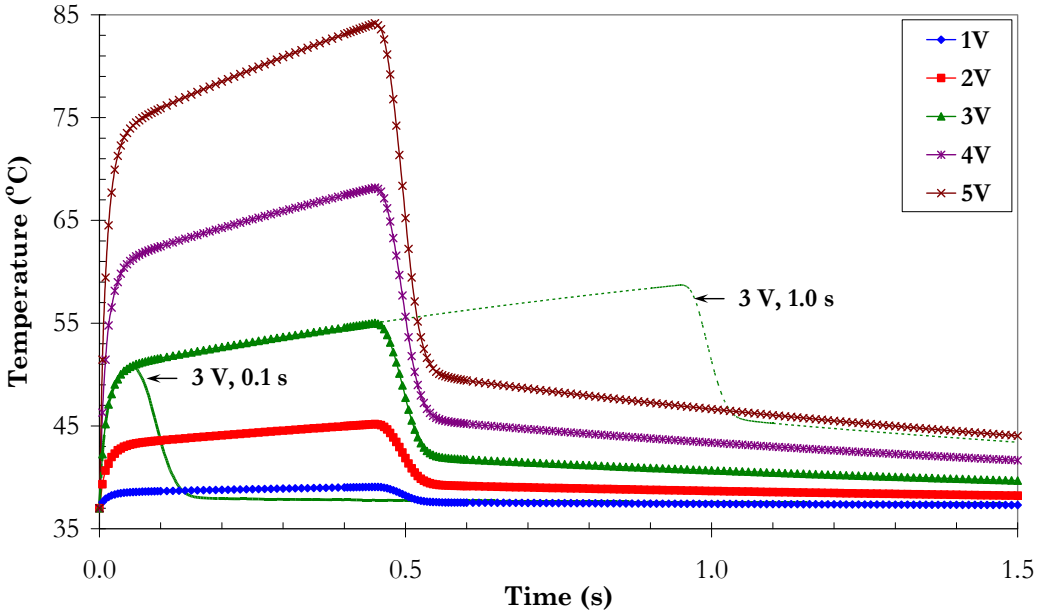

Figure 6.5: Simulated transient plot of temperature over time, at the centre of the membrane of the meander heater, after applying actuation voltages of 1 V to 5 V, for 0.5 s. The bold and dashed lines are the temperature curves with heater on-times of 0.1 s and 1.0 s, respectively, actuated with a voltage of 3 V.

Figure 6.5 depicts a time-dependent simulation in which a meander heater was investigated. Voltages from 1 V to 5 V and a heater on-time of 0.5 s were considered. The peak temperature at the centre of the membrane is shown to be directly proportional to the actuation voltage, as was expected. In addition, the peak temperature is also found to be directly proportional to the heater on-time, as depicted by the bold and dashed lines in Figure 6.5, for heater on-times of 0.1 s and 1.0 s, respectively, with an actuation voltage of 3 V. These findings suggest that an optimum operational range of the heater can be found by careful selection of the actuation voltage and the heater on-time.

The time-dependent simulations of different heater designs yield similar findings by the steady-state simulation: the coil heater produces the largest temperature rise. In fact, as depicted in Figure 6.6, apart from the high peak temperature (66.0 °C at a time of 0.45 s), the coil heater also cools down more rapidly (to 44.2 °C at time 0.55 s, or ~ 21.8 °C in 0.1 s, compared to 19.4 °C and 13.0 °C in 0.1 s, for the spiral and the meander heater, respectively).

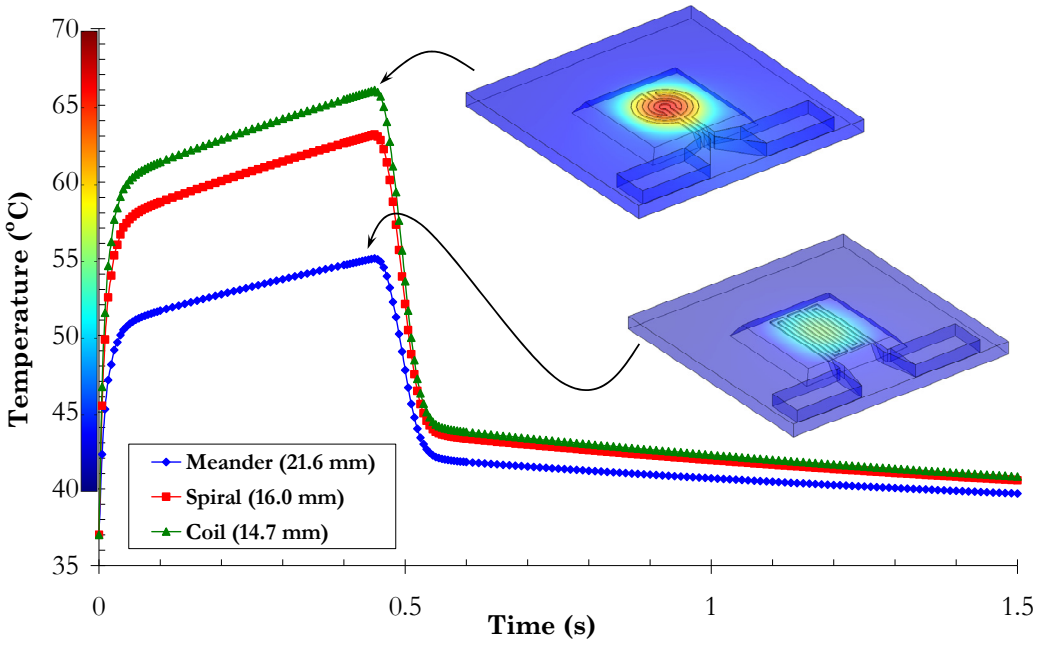

Figure 6.6: Simulated transient plot of temperature over time, at the centre of the membrane, after applying 3 V of actuation voltage, for 0.5 s, for the meander (◆), spiral (■) and coil (▲) heaters. The insets show the temperature distribution, for graphical comparison, of the coil heater and the meander heater, at time = 0.45 s.

Table 6.4 summarises both the findings of the steady-state and the time-dependent simulations for the three heater designs, with actuation voltages of 1 V to 5 V and a heater on-time of 0.5 s. For the meander heater, an actuation voltage of 3 V is sufficient to provide the heat to increase the temperature from 37 °C to ~ 55 °C, in 0.5 s; this is within the design requirement of the heater's temperature limit of 60 °C ± 10 °C and a heater on-time limit of 1 s. Moreover, the temperature reduced to ~ 40 °C, 1 s after the meander heater was turned off; this is below the critical temperature of 43.5 °C. Hence, an actuation voltage of 3 V with a heater on-time of 0.5 s will be used for the meander heater (highlighted in pink in Table 6.4) for the initial testing of the heater's performance (discussed in §6.4.3). The actuation voltage of 3 V can also be used for the spiral and the coil heaters, but the heater on-time needs to be reduced to 0.1 s (highlighted in yellow in Table 6.4).

Design	**Actuation voltage (V)**	**Temperature (°C)**		
		Steady-state	**Time-Dependent**	
			Peak	**After 1.5 s**
Meander	1	40.73	39.07	37.31
	2	51.46	45.18	38.22
	3	**68.07**	**55.02**	**39.69**
	4	89.24	68.18	41.66
	5	113.81	84.17	44.04
Spiral	1	42.25	40.04	37.42
	2	57.15	48.92	38.62
	3	79.69	63.09	40.56
	3 V, 0.1 s	**-**	**57.58**	**37.54**
	4	107.76	81.68	43.08
	5	139.69	103.88	46.09
Coil	1	42.78	40.41	37.45
	2	59.08	50.30	38.74
	3	83.55	65.99	40.81
	3 V, 0.1 s	**-**	**60.13**	**37.58**
	4	113.79	86.41	43.48
	5	147.96	110.61	46.65

Table 6.4: The simulated steady-state and time-dependent temperature of the meander, spiral and coil heater, with actuation voltages of 1 V to 5 V. The time-dependent simulation was performed with a heater on-time of 0.5 s, except for the rows highlighted in yellow, which were simulated with an actuation voltage of 3 V and a heater on-time of 0.1 s. The bold parameters represent the proposed operational parameters for the respective heater designs.

6.3 Device Fabrication

The integration of the fabrication process has taken into consideration the design constraints and requirements discussed in §6.2. The fabrication process is thus divided into 3 main stages, and the major steps are schematically depicted in Figure 6.8. The 3 main stages of the fabrication are:

Stage 1: Fabrication of the silicon membrane (steps (a) to (j) in Figure 6.8).

Stage 2: Formation of PSi structure using the NSL technique (step (k) in Figure 6.8).

Stage 3: Fabrication of the integrated heater and temperature sensor using the lift-off method (steps (l) to (n) in Figure 6.8).

6.3.1 Fabrication of the Silicon Membrane (Stage 1)

The fabrication of the silicon membrane was performed by the technical staff of the Nanofabrication Laboratory, Chalmers University of Technology, Sweden. The main aim of this fabrication was to realise a 50 μm thick silicon membrane, as depicted in Figure 6.7, with the proposed square membrane sizes of 9 mm^2, 16 mm^2 and 25 mm^2. All of the processes in Stage 1 fabrication were processed at the wafer level. The detailed listing of the fabrication process is in Appendix A.2.

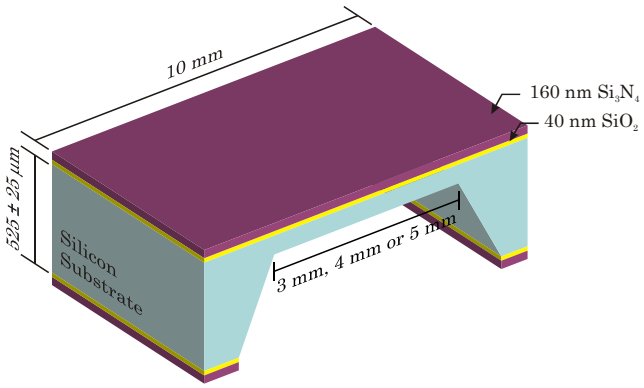

Figure 6.7: Oblique, cross-sectional view, schematic illustration of the silicon membrane after the Stage 1 fabrication (not to scale; refer to Figure 6.8 for colour scheme of materials).

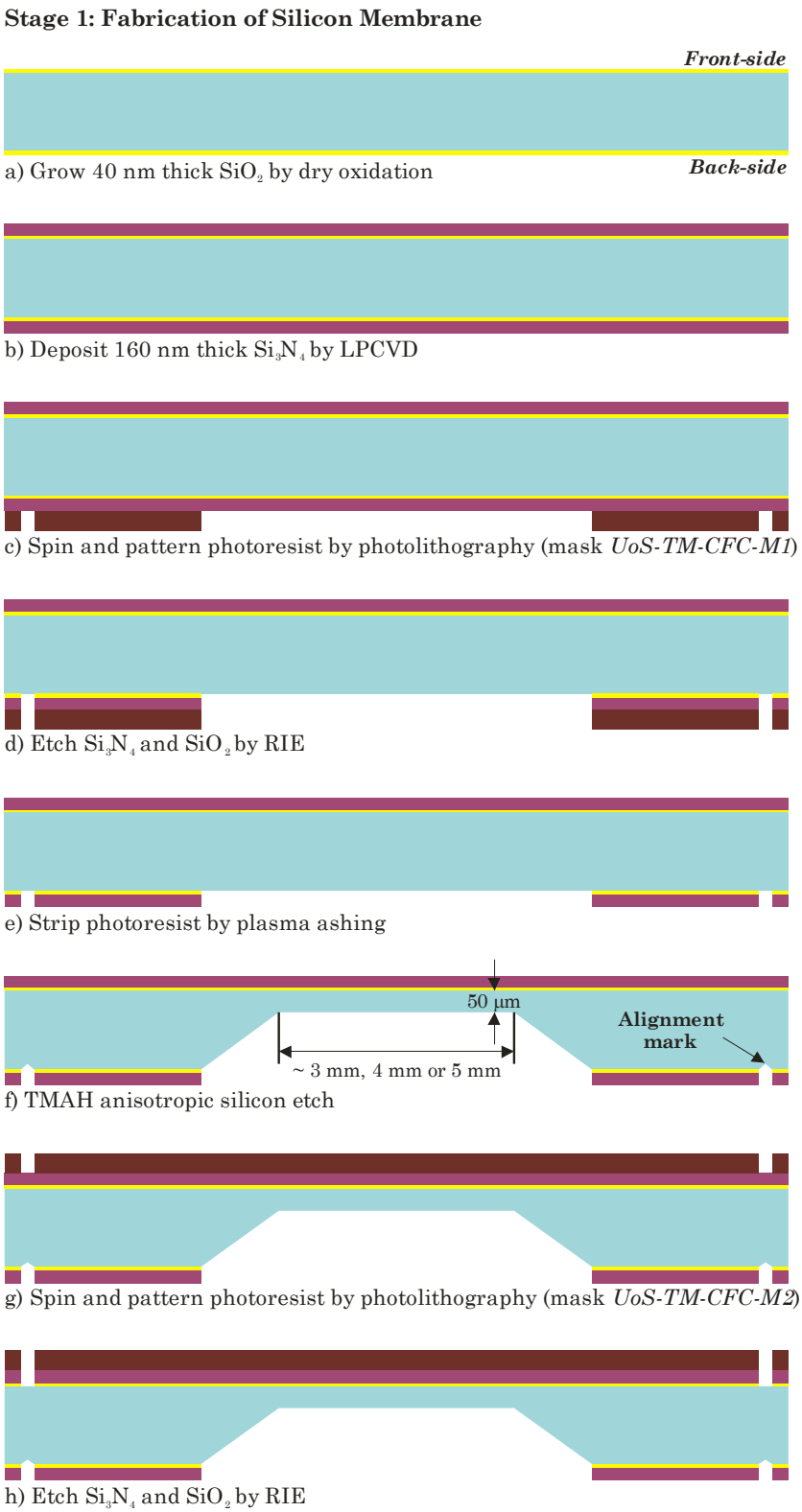

Figure 6.8: Schematic illustration of the fabrication process of the PSi membrane drug delivery device (not to scale; see next page for continued process steps and colour scheme of materials used).

i) Strip photoresist by plasma ashing

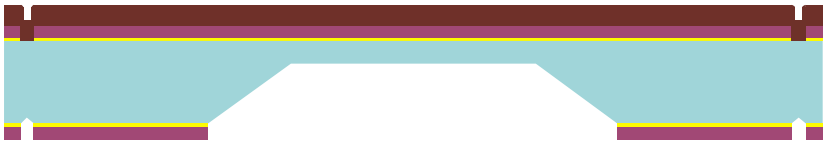

j) Spin coat photoresist for protection and then dice into chips

Stage 2: Nanostructuring of PSi Structure

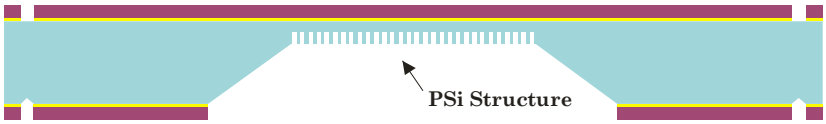

k) Formation of PSi by NSL technique (see section 6.3.2 for detailed steps)

Stage 3: Fabrication of Heater and Temperature Sensor

l) Spin and pattern photoresist by photolithography (mask *UoS-TM-CFC-M4*)

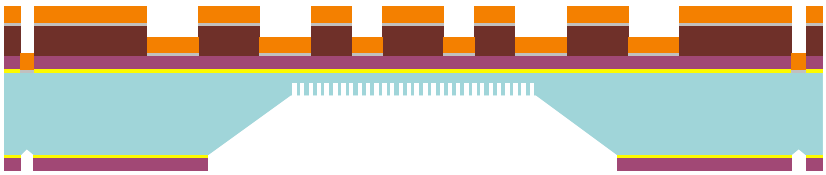

m) Deposit Ti/Au (10 nm / 300 nm) by evaporation

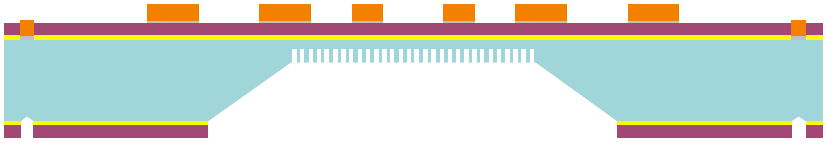

n) Lift-off Ti/Au by stripping photoresist

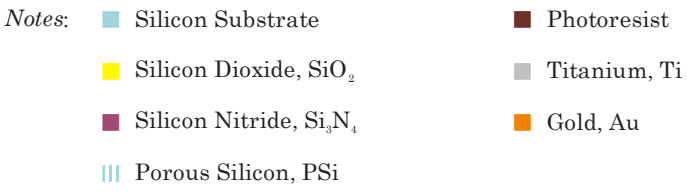

Figure 6.8: Schematic illustration of the fabrication process of the PSi membrane drug delivery device (not to scale).

The starting material consisted of twelve 150 mm diameter, 525 μm ± 25 μm thick, double-side polished, silicon wafers with <100> crystal orientation. Six of the twelve wafers were of boron-doped p-type (1 – 10 Ω·cm, labelled *P01* to *P06*); while the other six were of phosphorus-doped n-type (1 – 10 Ω·cm, labelled *N07* to *N12*) wafers. The major steps involved in the fabrication of the silicon membrane, as illustrated in Figure 6.8, include:

Step (a) The wafers are first cleaned using a standard two-stage RCA silicon cleaning process [273]. A dry oxidation is then carried out at 950 °C to grow a layer of 40 nm ± 5 nm thick silicon dioxide (SiO_2); this serves as a stress relief and an adhesion layer for the subsequently deposited silicon nitride (Si_3N_4) layer.

Step (b) A layer of 160 nm ± 20 nm thick Si_3N_4 is deposited by LPCVD at 770 °C, at a pressure of 200 mTorr, using dichlorosilane ($SiCl_2H_2$) and ammonia (NH_3) gases. The SiO_2-Si_3N_4 bi-layer serves as a masking layer for the subsequent tetramethyl-ammonium hydroxide (TMAH) deep anisotropic etch of silicon (Step (f)) to create the membrane. Furthermore, the front-side SiO_2-Si_3N_4 bi-layer provides electrical isolation between the heater and temperature sensor.

Step (c) The back-side of the wafers is then spin-coated with a layer of Clariant AZ1512HS positive photoresist, at 4000 rpm to achieve a nominal thickness of 1.2 μm. The photoresist is then exposed with the first mask (mask *UoS-TM-CFC-M1*, see Appendix B.2.1) and developed. Subsequently, the photoresist is hard baked for 30 minutes at 120 °C in an oven to improve its robustness to sustain the subsequent RIE processes.

Step (d) A mixture of tetrafluoromethane (CF_4) and oxygen (O_2) gases is used for the RIE process of the SiO_2-Si_3N_4 bi-layer. In both processes, the flow rate of the CF_4/ O_2 gas mixture is set at 30 sccm / 3 sccm, while the RIE pressure and the radio frequency (RF) power are set at 100 mTorr and 100 W, respectively.

Step (e) Following the RIE process in Step (d), the photoresist is stripped, within the same chamber, using a 40 sccm flow of O_2 gas with an RF power of 250 W.

Step (f) The exposed silicon is then deep-etched anisotropically using a 25 wt% TMAH solution maintained at 80 °C in a circulating bath.

Step (g) A layer of AZ1512HS photoresist is then spin-coated at 4000 rpm onto the front-side of the wafers. The photoresist is then exposed with the second mask (mask *UoS-TM-CFC-M2*, see Appendix B.2.2), and developed and hard baked for 30 minutes at 120 °C in an oven. The patterned photoresist defines the chip level alignment marks (used in Stage 3 fabrication) and the dicing tracks (for Step (i)).

Step (h) RIE using CF_4 and O_2 gases, with process parameters similar to that of Step (d), is then carried out to etch the front-side SiO_2-Si_3N_4 bi-layer.

Step (i) The photoresist is then stripped, with the same process parameters detailed in Step (e).

Step (j) A layer of AZ1512HS photoresist is then spin-coated on the front-side of the wafers, to protect the wafers from the contamination of the silicon dust typically produced during the wafer dicing process. The wafers are subsequently diced into chips for the following, Stage 2 and Stage 3 fabrication processes, which were carried out in-house (the Optoelectronics Research Centre (ORC) temporary cleanroom and the NanoMaterial Rapid Prototyping Facility) at the University of Southampton.

6.3.1.1 Fabrication Results and Issues

During the fabrication of the silicon membrane, all but one wafer (wafer *P03*) were damaged due to an accidental handling error. Wafer *P03* was processed as a development wafer, ahead of the other wafers, and hence avoided the incident. A second batch of wafers was later processed and, for clarity, these wafers are identified with a prefix "*b2*".

The membrane thickness was measured using a stylus surface profiler (KLA-Tencor P-16), to be about 70 μm for wafer *P03*, after etching in TMAH solution for 19 hours 26 minutes. The overall etch rate, based on an estimated etch depth of 478 μm, was calculated to be 0.41 $\mu m \cdot min^{-1}$. Based on these measurements, the TMAH etching during the second batch fabrication was carried out with a longer etch time

of 23 hours 42 minutes; this produced membranes with a thickness of 46.6 µm ± 0.5 µm (measured on sample *b2P02S38*) and an etch rate of ~ 0.35 µm·min^{-1}. The selectivity of <111> over <100> crystal orientation of silicon, was estimated to be between 1:10 and 1:35. Hence, the lateral etch (or mask undercut) was estimated to be between 14 µm and 49 µm for an etch depth of ~ 490 µm. This undercut, in certain cases, was severe enough to destroy some of the features on the wafer, such as the chip level alignment marks, as depicted in Figure 6.9 (b). Undercutting, due to failure of the Si_3N_4-SiO_2 masking layers, was also observed and this produced undesirable features, as depicted in Figure 6.9 (c).

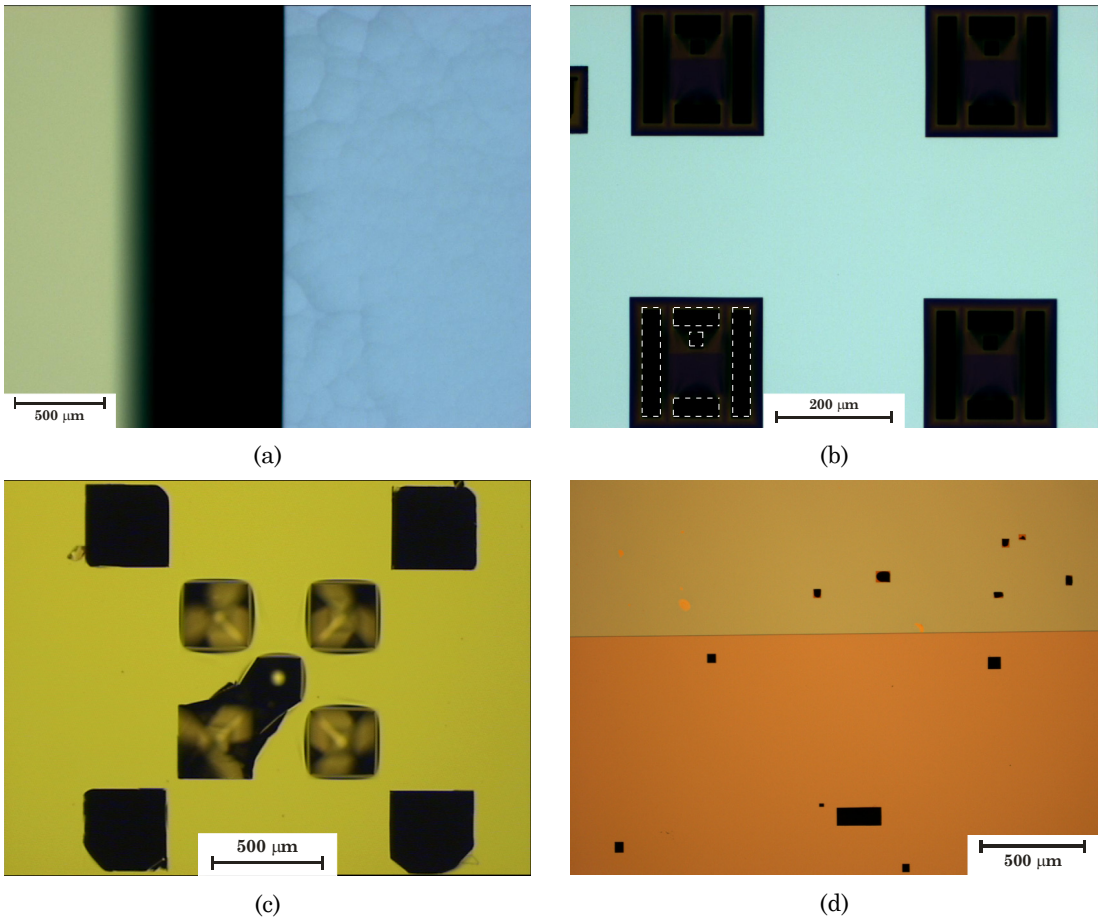

Figure 6.9: Bright field, microscope images showing (a) the bottom trench or surface of the membrane; (b-c) undercut and lateral etch at the (b) chip level (the dashed line outlines the intended features) and (c) wafer level alignment marks; and (d) pinholes on the front-side of the membrane after the TMAH etch.

During the initial fabrication process, the vacuum chuck often failed to hold the TMAH-etched wafers during the spin-coating of photoresist (Step (g) of Figure 6.8). The loss of vacuum was suspected to be due to cracked membranes and pinholes, such as those depicted in Figure 6.9 (d), produced by the TMAH etching. Hence, during the second batch fabrication, the wafers were mechanically clamped to the chuck during the spin-coating process. In addition, Step (i) in Figure 6.8 was omitted so that the photoresist could be re-used to protect the wafer during the dicing process (Step (j)). Photoresist drops were applied manually to protect the areas where the wafers were exposed (after the RIE process (Step (h) in Figure 6.8)), hence eliminating the need to deposit the photoresist by the spin-coating process.

6.3.2 Fabrication of the PSi Structure using the NSL Technique (Stage 2)

In the second stage of the fabrication process individual silicon membrane chips (samples) from the diced wafers are processed to form the PSi structure (Step (k) in Figure 6.8). The nanosphere lithography (NSL) technique, as detailed in Chapter 5, is used to fabricate a template made of a thin layer of metal film (here, chromium (Cr)) with holes arranged in a quasi-ordered, hexagonal lattice. By using an RIE, the pattern of holes is transferred into the silicon membrane, hence producing a quasi-ordered PSi structure. Figure 6.10 illustrates the detailed steps of the NSL technique used in the fabrication of the PSi structure.

Selected samples from the diced wafers *P03*, *b2P01*, *b2P02*, *b2P06* and *b2N07*, were primarily used for the fabrication of the PSi structures. These samples were coated with a layer of photoresist to protect the wafer in the dicing step (Step (j) in Figure 6.8). The samples were cleaned in acetone and then rinsed in isopropanol (IPA) to remove the photoresist. The samples were further treated in a Piranha solution, which typically consisted of a 3:1 volume ratio of 95 % concentrated sulphuric acid (electronic (MOS) grade, Fisher Scientific, UK): 30 % weight in volume (w/v) hydrogen peroxide (general laboratory work (SLR) grade, Fisher Scientific, UK). The Piranha solution removes organic and anionic contaminants and leaves a more hydrophilic surface, which is essential for the nanosphere deposition. The samples were typically cleaned in the Piranha solution for 30 minutes, rinsed

with copious amount of DI water and individually kept, until used, in specimen bottles containing DI water.

The NSL technique, as illustrated in Figure 6.10, was used to form the PSi structure at the back-side of the silicon membrane samples. Monodisperse, carboxylate-modified polystyrene nanospheres (Duke Scientifics (Brookhaven, UK)) with a nominal diameter of 200 nm, a coefficient of variance < 5 % and a surface group parking area of 45 $Å^2$ per carboxyl group, were used. The nanospheres (suspended into a 4 weight percent (wt%) aqueous solution, as purchased) were further diluted, into a 1 wt% suspension (2:1:1 volume ratio of ethanol: DI water: 4 wt% nanosphere suspension) prior to use. The nanosphere suspension was deposited (Step (k-1) in Figure 6.10) onto the samples, using the method described in Chapter 5, §5.3.3, to provide self-assembled monolayer of hexagonally close-packed nanospheres.

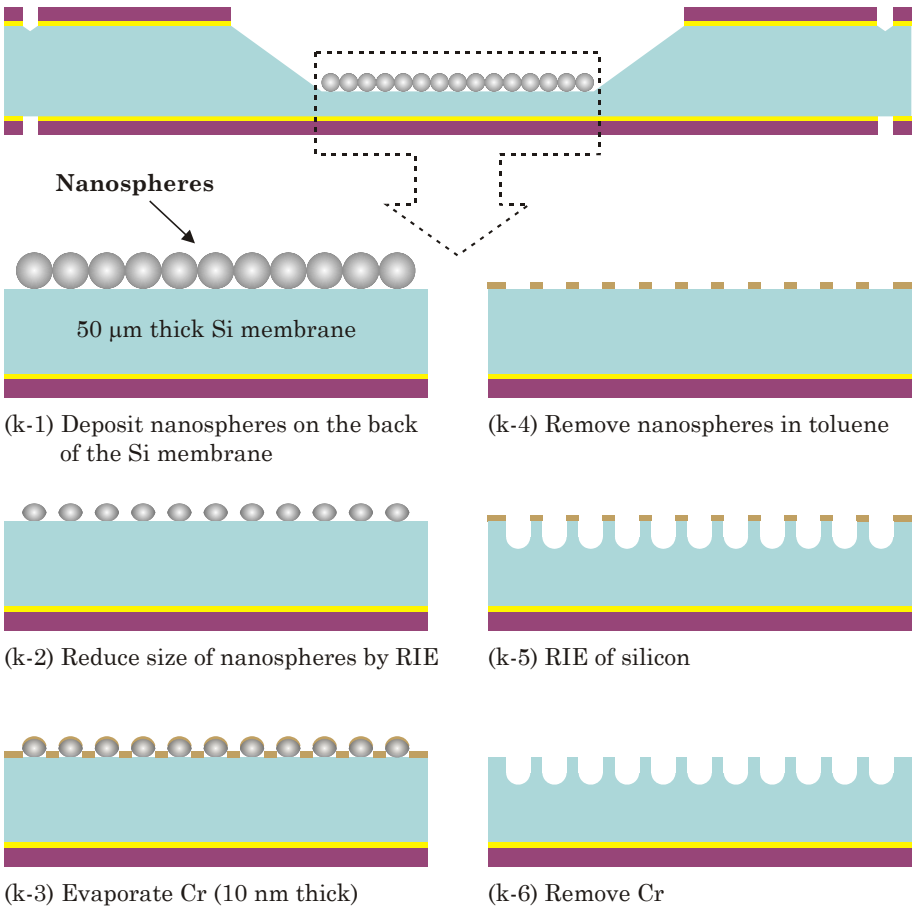

Figure 6.10: Schematic illustration of the fabrication process of the PSi structure using the NSL technique (not to scale; see Figure 6.15 for colour scheme of materials used).

In general, the nanospheres deposited on the silicon membrane substrates exhibited better ordering with less significant defects compared to on the polysilicon substrates, as depicted by the SEM micrograph (obtained from LEO 1455VP) in Figure 6.11. The inset fast Fourier transform (FFT) of the digital diffraction pattern of the SEM micrograph demonstrates the well-defined maxima and confirms the good hexagonally close-packed ordering. Minor defects, such as line dislocations, point vacancies and stacking of second-layer nanospheres, which are intrinsic to the nanospheres' deposition method, could still be observed.

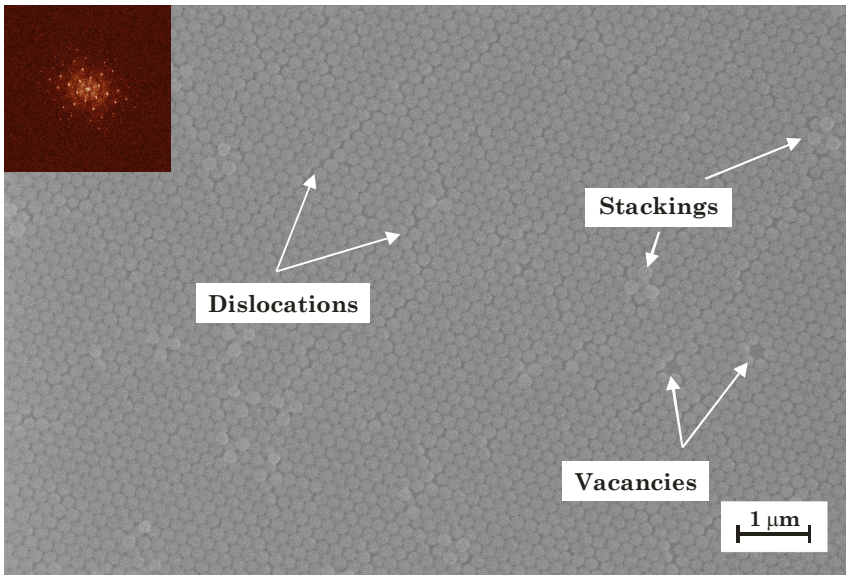

Figure 6.11: Plane-view SEM micrograph showing a self-assembled monolayer, hexagonally close-packed nanospheres (on sample *b2N07S33*), with defects such as line dislocations, stacking of nanospheres and vacancies. The inset depicts the FFT diffraction pattern of the SEM micrograph.

The size of the nanospheres was reduced (Step (k-2) in Figure 6.10) by an RIE process using an Oxford Instruments Plasmalab® 80 Plus plasma etcher. This produces a non-close-packed nanosphere template, with the reduced diameter of the nanospheres defines the diameter of the pores of the eventual PSi structure. Instead of using the Ar/O_2 gas mixture, as detailed in Chapter 5, §5.3.4, an O_2 gas with a gas flow rate of 5 sccm, with a higher pressure of 10 mTorr and an RF power of 100 W, was used. This change of RIE parameters was necessary due to a significantly reduced DC bias (near zero), sometimes with flickering plasma, observed during the RIE process when the Ar/O_2 gas mixture with the previous parameters was used. It is suspected that the reduced DC bias may have been caused by the prior deposition of polymer (from processes that use tri-fluoromethane (CHF_3)) onto the electrode.

The influence of the RIE etch time on the reduction of the diameter of the nanospheres, for the revised RIE parameters, was evaluated for etch times of 40 s to 70 s, and the results are depicted in Figure 6.12. The mean diameter of the size-reduced nanospheres was measured using the National Instruments™ (NI) Vision Assistant image processing package. Plane-view SEM micrographs of selected samples after the RIE process, with the same magnification (of 30 000 times), were first digitally enhanced. The boundaries of the nanospheres were detected and the bounded areas were measured, to deduce the diameter of the nanospheres. Assuming a linear regression, the etch rate was estimated to be ~ 1.9 $nm \cdot s^{-1}$, which yields a theoretical reduced diameter of 88 nm for a typical etch time of 60 s. In principle, by the careful control of the RIE etch time, the diameter of the nanospheres can be arbitrarily reduced to achieve a required size. However, the reduction in the diameter of the nanospheres affects the success of the subsequent lift-off of the nanospheres and the metal over them (Step (k-4) in Figure 6.10). Hence, in practice, there is a limit of a reasonable size that can be reduced. For this reason, the RIE etch time of most of the samples was set to 60 s, which yielded an average reduced diameter of 86 nm ± 3 nm.

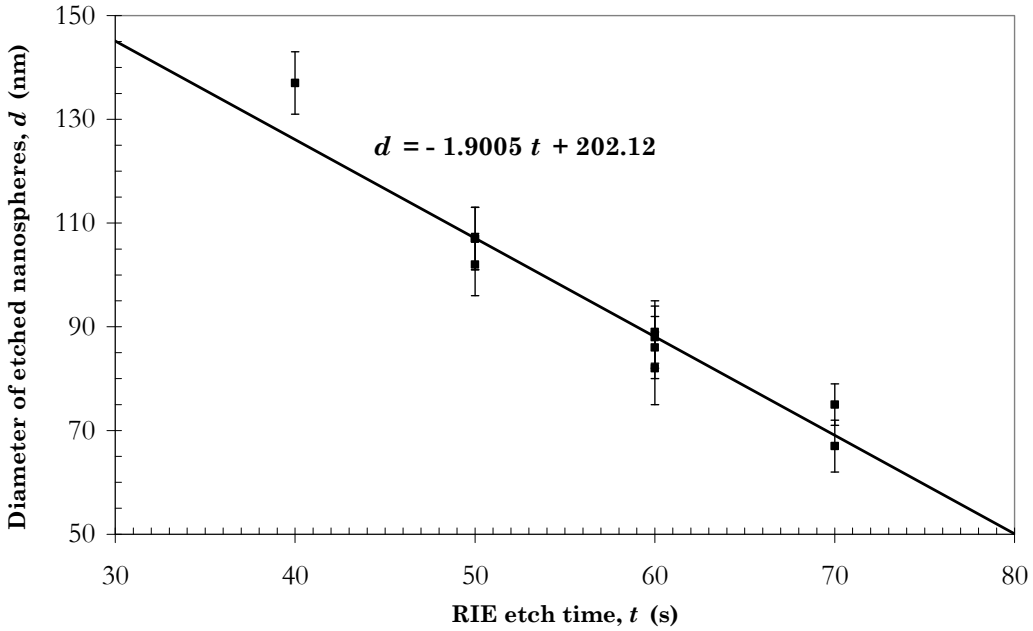

Figure 6.12: Plot of the mean diameter of the nanospheres after the RIE process, against the RIE time. The solid line represents the least squares experimental fit as described by the expression. The error bars represent the standard deviations of the total detectable diameters on a SEM micrograph.

A layer of Cr with a nominal thickness of 10 nm was then deposited (Step (k-3) in Figure 6.10) using an e-beam evaporator (BOC Edwards Auto E500). The typical evaporation base pressure was between 1 x 10^{-6} mbar and 5 x 10^{-6} mbar. The nanospheres were removed (Step (k-4) in Figure 6.10) by ultrasonication in toluene for 30 s to 60 s. The space left by the nanospheres thus formed holes, arranged in a non-close-packed hexagonal lattice, in the Cr layer, as depicted in Figure 6.13, which now serves as the template for the subsequent RIE of silicon to form the eventual PSi structure.

The removal of nanospheres is a critical process, as the nanospheres that remained on the sample, as depicted in Figure 6.13, would act as a mask to prevent the formation of the pore in the silicon by the subsequent RIE of the silicon. However, a prolonged exposure to ultrasonication (of more than 120 s, for instance) to remove the nanospheres, has been demonstrated to crack the silicon membrane. Use of other solvents, such as tetrahydrofuran (THF), dichloromethane (DCM) and dimethylformamide (DMF), did not show any significant improvement. Hence, to achieve the best possible result, the compromises made include limiting i) the RIE etch time (to reduce the size of the nanospheres) to 60 s; ii) the thickness of Cr to 10 nm; and iii) the ultrasonication time (to remove the nanospheres) to a maximum of 60 s.

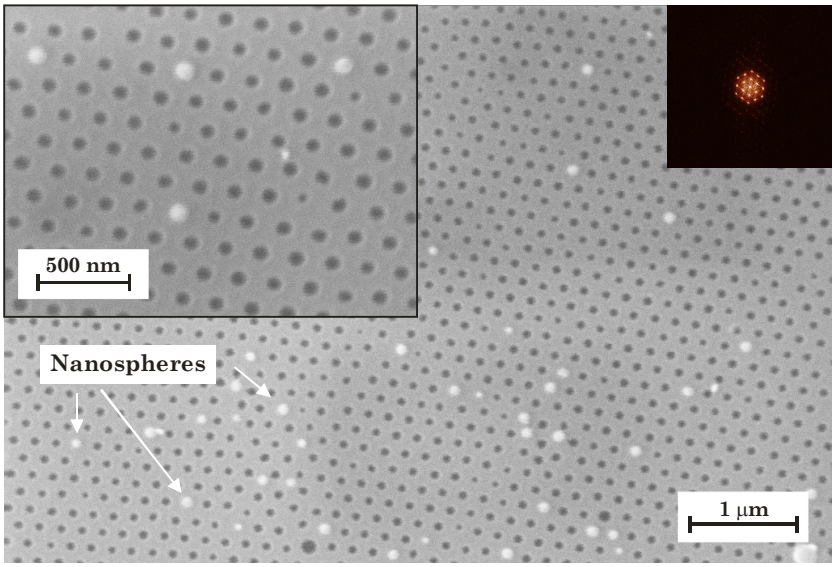

Figure 6.13: Plane-view SEM micrograph showing the Cr template (sample *b2N07S53*), with holes of 80 nm ± 5 nm in diameter, after most of the nanospheres were removed. The insets show (right) the FFT diffraction pattern of the SEM micrograph and (left) the magnified view of the same sample at a different area.

The RIE of silicon using the "black silicon" method, as described in Chapter 5, §5.3.6, was used to transfer the patterns on the Cr layer into the silicon membrane. A typical RIE process to etch the silicon uses a gas mixture of sulphur hexafluoride (SF_6), CHF_3 and O_2 gases, with a gas flow rate of 15 sccm, 10 sccm and 5 sccm, respectively. The pressure was typically set at 5 mTorr with an RF power of 50 W. After etching for 10 minutes, a tapered profile, such as the one depicted in Figure 6.14, was observed. Here, the pointed, "crown-like" PSi structure was believed to be formed as a result of the severe undercut of the Cr layer. In fact, at an etch depth of ~ 290 nm, as depicted in Figure 6.14, the width of the pore opening was more than 200 nm; this suggests that an over-etching, which resulted in a lateral through-etch, has occurred. The Cr layer has been, very likely, completely etched. The pore (or more precisely, spiked triangular pyramid) diameter was measured to be 150 nm ± 6 nm (based on the plane-view SEM micrograph in the inset of Figure 6.14), considerably enlarged from the initial, 134 nm ± 4 nm in diameter of the nanoholes in the Cr layer.

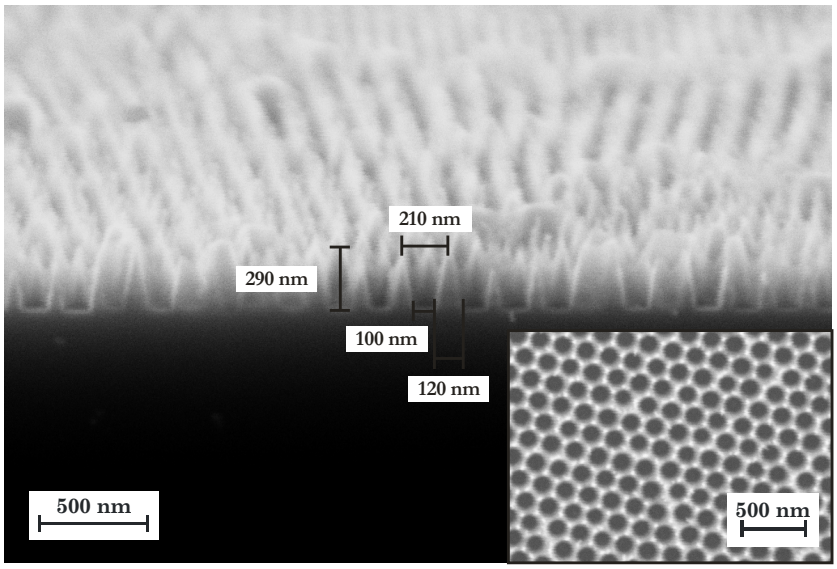

Figure 6.14: Oblique, cross-sectional view SEM micrograph showing the cleaved edge of the sample *P03S50* after an RIE in $SF_6/O_2/CHF_3$ gases for 10 minutes (gas flow rate of 15/5/10 sccm, respectively, and a pressure of 5 mTorr with an RF power of 50 W). The inset shows the plane-view SEM micrograph of the sample at a different area.

6.3.2.1 Improved Silicon RIE using STS LPX Pegasus

The RIE conditions of the "black silicon" method result in undercutting, both on the silicon membrane and polysilicon samples. Initially, it had been thought that the substrate could be the root of the problem. In fact, after these studies it was decided that the "black silicon" method is unsuitable for the fabrication of the desired PSi structure. The use of conventional fluorine-based RIE processes to produce silicon structures with a high aspect ratio and a good profile control (vertical, smooth sidewall and critical dimensions in the sub-micrometer scale) is a technical challenge [394-396]. Instead, modern dry etching technologies, such as deep-RIE (DRIE) using the "Bosch process" [95], inductively coupled plasma (ICP) etching [397], chlorine-based ICP [398] and cryogenic RIE [399], have been more widely used to fabricate high aspect ratio silicon structures. Among these technologies, the Bosch-based DRIE process, which is a sequential, cyclic ICP-RIE process consisting of alternating steps of etching (using SF_6 gas) and passivation (using octafluorocyclobutane (C_4F_8) gas) processes [400], has been an increasingly important tool in MEMS fabrication. This is primarily due to its anisotropic silicon etch with high etch rate, which is capable of realising silicon structures with an aspect ratio of up to thirty [401, 402].

Here, the process was performed in a Surface Technology Systems[24] (STS) LPX Pegasus system, which uses the Advanced Silicon Etch (ASE®) technology based on the Bosch process. The NSL technique was modified to incorporate a SiO_2 hard mask to serve as the masking layer, for the transfer of the hole pattern into the silicon. This is necessary due to a compatibility issue; the NSL-patterned Cr layer previously used in the RIE of silicon could not be used in the STS LPX Pegasus system. The SiO_2 hard mask was patterned using the Cr layer, which was fabricated in the same way as discussed previously. The modified NSL technique is detailed in Figure 6.15.

In brief, after cleaning the samples in the Piranha solution (as described previously), a layer of SiO_2 was deposited onto the back of the silicon membrane

[24] Surface Technology Systems Plc., Newport, UK. http://www.stsystems.com/ (*last accessed Jul. 2009*).

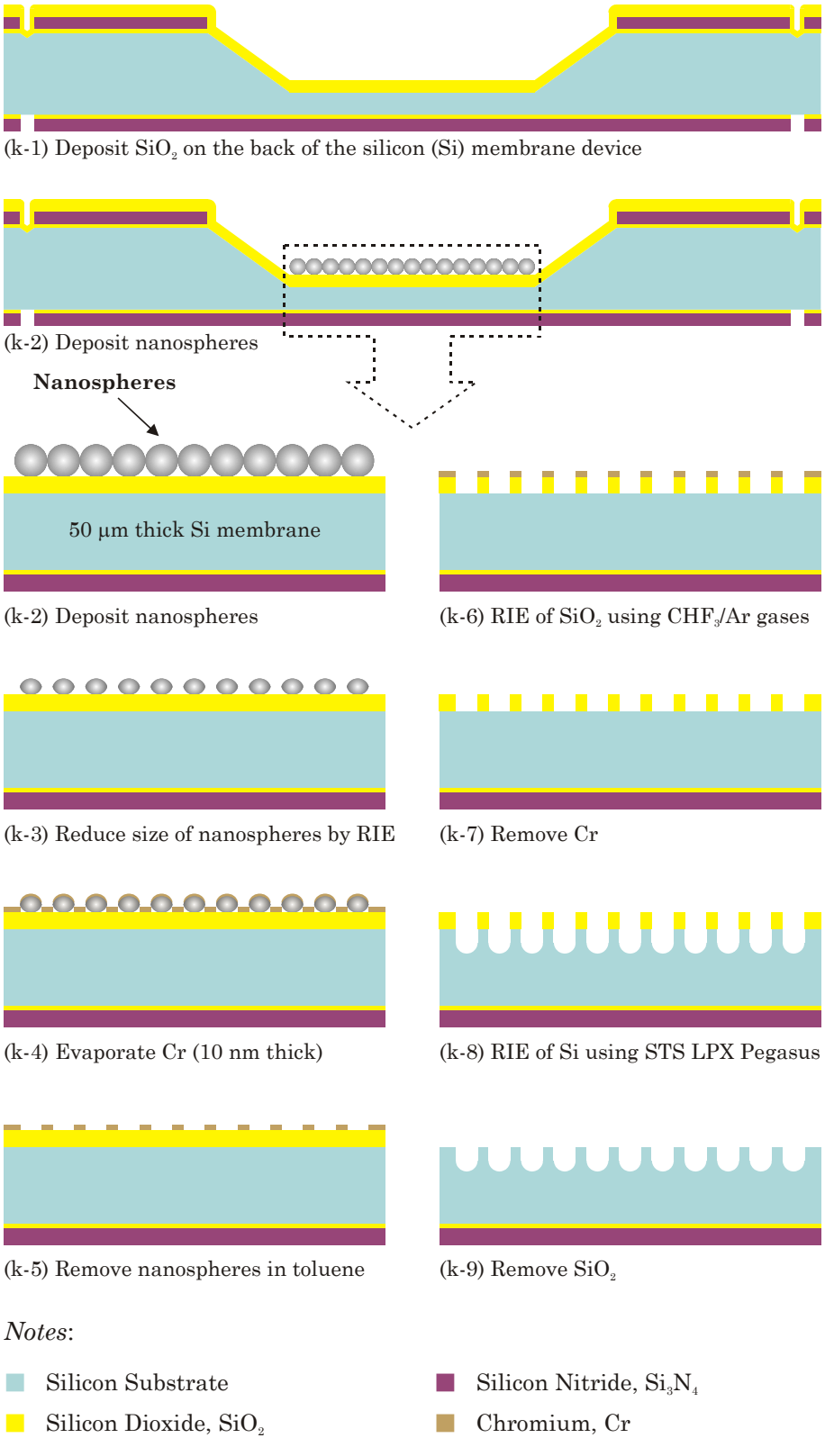

Figure 6.15: Schematic illustration of the fabrication process of the PSi structure using a modified NSL technique with improved RIE of silicon (not to scale).

(Step (k-1) in Figure 6.15), by either sputtering (Kurt J. Lesker Sputter system) or e-beam evaporation (BOC Edwards Auto E500), to achieve nominal thicknesses between 150 nm and 200 nm. The SiO_2 coated samples were then cleaned in the Piranha solution and individually kept, until used, in specimen bottles containing DI water.

The typical NSL process steps were then performed, as described previously. These include the deposition of nanospheres onto the back of samples (Step (k-2) in Figure 6.15), size reduction of the nanosphere template using the RIE process (Step (k-3) in Figure 6.15), Cr deposition by the e-beam evaporation (Step (k-4) in Figure 6.15), and nanospheres' removal in toluene with ultrasonication (Step (k-5) in Figure 6.15). The pattern on the Cr layer was then transferred onto the SiO_2 hard mask by an RIE process (Step (k-6) in Figure 6.15), which utilised a gas mixture of CHF_3 and Ar (with a flow rate of 25 sccm each) at a pressure of 40 mTorr and an RF power of 200 W. The typical RIE etching of SiO_2 was 10 minutes. The Cr layer was then removed in a Cr etchant (OM Group Ultra Pure Chemicals Ltd., UK) (Step (k-7) in Figure 6.15), which consists of acetic acid and ceric ammonium nitrate.

The samples with a metal-free, SiO_2 hard mask were then etched in the STS LPX Pegasus system (Step (k-8) in Figure 6.15). Most Bosch-based DRIE processes only produce good results for structures with critical dimensions in the micrometers scale. However, high aspect ratio structures in deeply sub-micrometer range (< 100 nm), with a smooth (no scalloping) sidewall profile often requires considerable modifications to the conventional Bosch process [394, 395]. Hence, to realise the PSi structure with the desired pore diameter (in the range of 100 nm) with a good critical dimension control and a smooth sidewall profile, the low frequency (LF) process was exploited. Instead of operating at the widely used 13.56 MHz high frequency, the LF process utilises a power supply operating at 380 kHz to drive the platen. The LF process has been specifically developed to prevent the notching effect, which has been observed to frequently occur in etching of SOI wafers [403]. Here, the LF process has been applied to provide a controlled etch of tight critical dimensions with a virtually smooth sidewall profile by scarifying the high etch rate of a typical Bosch process. To slightly improve the etch rate, the parameter ramping feature of the ASE® technology [404] was used. The base recipe for the RIE process was modified from [394], and is detailed in Table 6.5. Typically, to maintain the macro-loading,

two samples were attached to a 6 inch carrier wafer during each run. The micro-loading, however, varied due to the nature of defects inherent in the NSL technique. The total process time was limited to 10 minutes, which amounts to 120 cycles of etching and passivation process steps.

Parameters	Etch Cycle	Passivation Cycle
Cycle time	2 s	3 s
Gas flow rate	SF_6 – 50 sccm O_2 – 5 sccm	C_4F_8 – 80 sccm
Pressure	13 mTorr, ramped to 18 mTorr	18 mTorr, ramped to 23 mTorr
LF Platen Power	11 W, ramped to 16 W	0 W
Coil Power	350 W	350 W

Table 6.5: The parameters developed for etching of silicon with feature sizes in 100 nm range, to realise the PSi structure using a STS LPX Pegasus system.

The development of optimised process parameters was not performed due to inconsistent micro-loading and varied aspect ratios as a result of the intrinsic defects introduced by the nanosphere deposition method. The varied micro-loading and aspect ratios effectively result in a differential etch rate (also known as RIE-lag effect) by which isolated pores etch faster than pores in a dense array, while pores with smaller diameter tend to etch more slowly than relatively larger pores. SEM micrographs in Figure 6.16 depict such an effect, as clearly shown by the different etch depths. In fact, the sample *b2N07S53* revealed two nanostructures – nanopillars and nanopores. It is believed that the nanopillars resulted from a double-layer stacking of nanospheres during the deposition process. After the size-reduction process, the bottom layer of nanospheres retained its initial size, as the spheres were masked by the nanospheres on the top layer. Hence, instead of hole patterns, three-pronged patterns (from the interstitial spaces between the nanospheres) were formed after the deposition of the Cr that was followed by the subsequent removal of nanospheres. The larger exposed area of the three-pronged nanopillar array (as opposed to the array of nanopores), as depicted by the plane-view SEM of the inset of Figure 6.16, hence resulted in faster etch rate. A more typical PSi structure, with the SiO_2 hard mask, after the RIE of silicon using the STS LPX Pegasus, is depicted in Figure 6.17. The PSi structure of sample *b2P06S62* exhibited a mean pore diameter of 105 nm ± 5 nm, while the pore depth was estimated to be 335 nm ± 28 nm. The SiO_2 hard mask was observed to be intact, suggesting a good selectivity of SiO_2 to silicon, although the precise figure was not investigated. Overall, pore diameters of

between ~ 75 nm and ~ 120 nm have been observed on various samples, while the etch depth, for a process time of 10 minutes, was observed to range from ~ 330 nm to ~ 500 nm (see Appendix E for more SEM micrographs of various fabricated PSi structures).

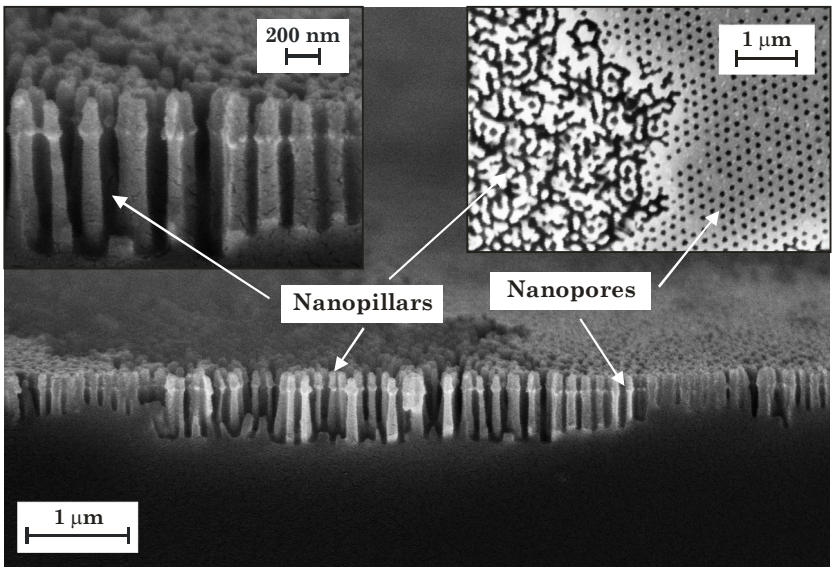

Figure 6.16: Oblique, cross-sectional view SEM micrograph showing the cleaved edge of the sample *b2N07S53*, highlighting the RIE-lag effect. The insets show the plane-view (right) and a magnified cross-sectional view (left) of the sample. The mean diameter of the pores is 85 nm ± 8 nm.

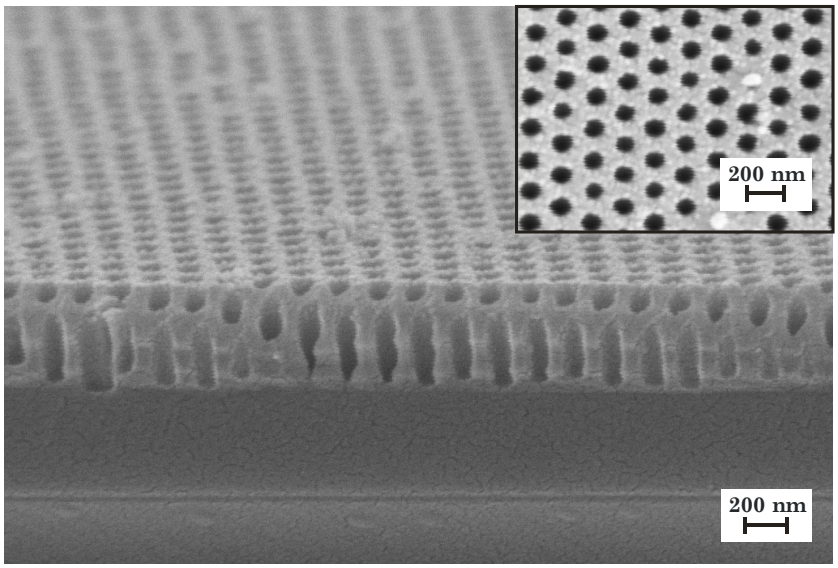

Figure 6.17: Oblique, cross-sectional view SEM micrograph showing the cleaved edge of sample *b2P06S62* after the RIE of silicon using STS LPX Pegasus. The mean diameter of the pores was calculated to be 105 nm ± 5 nm, with a pore depth estimated to be 335 nm ± 28 nm. The inset shows the plane-view SEM micrograph of the sample at a different area.

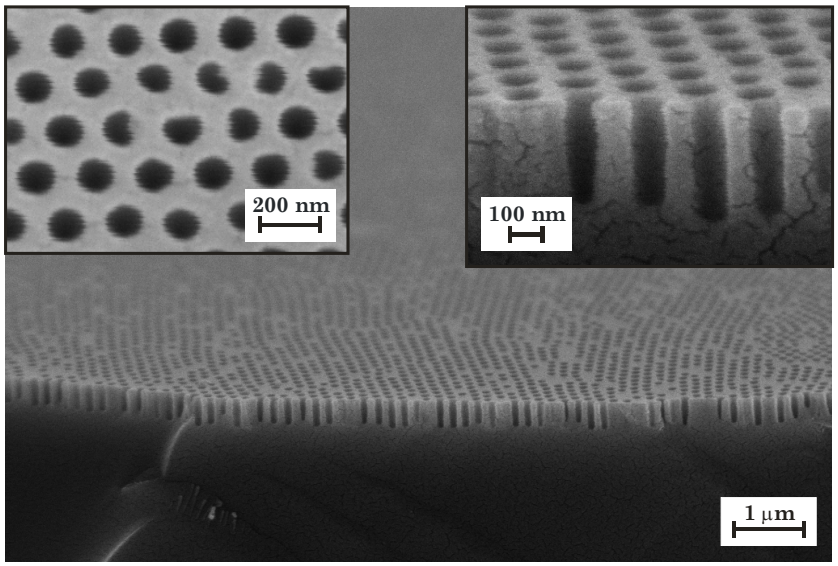

Figure 6.18: Oblique, cross-sectional view SEM micrograph showing the cleaved edge of the PSi structure, of sample *b2N07S72*, after the removal of the SiO_2 hard mask. The pore diameter was estimated to be 118 nm ± 7 nm; while the pore depth was estimated to be 334 nm ± 21 nm. The insets show the magnified, cross-sectional view (right) and the plane-view (left) of the same sample at a different area.

Finally, the SiO_2 hard mask was removed using a buffered oxide etchant (Lodyne SiO_2 Etchant 7:1, OM Group Ultra Pure Chemicals Ltd., UK) to realise the PSi structure (Step (k-9) in Figure 6.15). Figure 6.18 depicts an example PSi structure, with quasi-ordered, cylindrical pores, after the removal of the SiO_2 hard mask. The pores (of sample *b2N07S72*) exhibited a relatively smooth and vertical sidewall. The mean pore diameter was calculated to be 118 nm ± 7 nm, with a pore size distribution (PSD) as depicted in Figure 6.19. The pore depth was estimated to be 334 nm ± 21 nm. The theoretical porosity, P_{theory} for pores in a hexagonal arrangement, was estimated to be 31.5 %, based on:

$$p_{theory} = \frac{\pi \times d_p^{\,2}}{2\sqrt{3} \times d_{\text{int}}^{\,2}} \tag{6.3}$$

where d_p is the mean pore diameter and d_{int} is the interpore distance or the pitch size. The porosity derived from the plane-view SEM micrograph, used in the measurement of mean pore diameter and PSD, was found to be 27.4 %, which is in good agreement with the theoretical value.

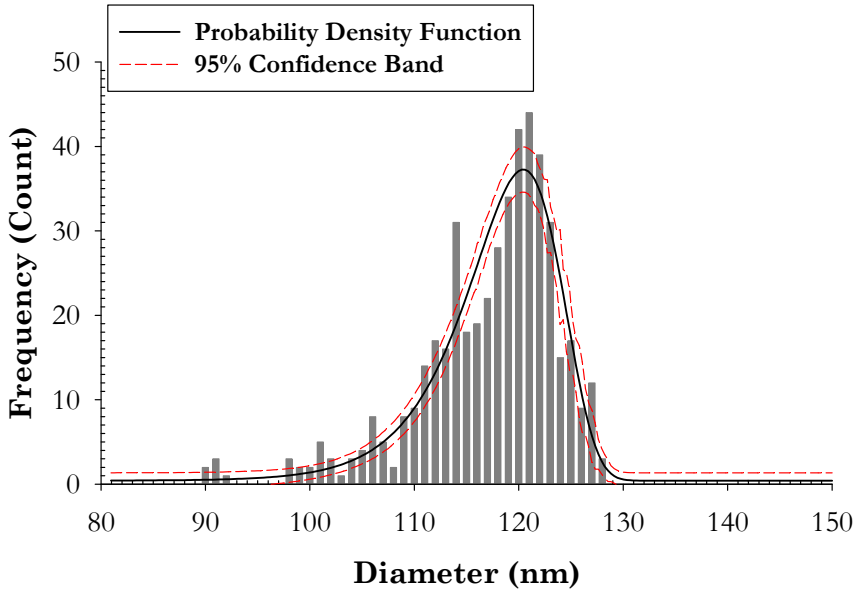

Figure 6.19: The pore diameter distribution plot of sample *b2N07S72*, as estimated from a plane-view SEM micrograph (partly shown as inset (left) of Figure 6.18; 30, 000 times magnification). The solid line represents a statistical fit with Weibull distribution[25]; while the dashed red lines represent the upper and lower bound of the 95 % confidence of the fit.

6.3.3 Fabrication of the Integrated Heater and Temperature Sensor (Stage 3)

The Stage 3 fabrication aims to create a patterned heater and a temperature sensor on the front-side of the silicon membrane devices, using the lift-off method described in Chapter 3, §3.6. Briefly, as illustrated in Figure 6.8, a typical process of the Stage 3 fabrication includes the following steps:

Step (l) The positive tone, Shipley MICROPOSIT® S1828 photoresist is first spin-coated and exposed using a mask (mask *UoS-TM-CFC-M4*, see Appendix B.2.4). The S1828 photoresist is then surface modified by immersing the samples into toluene before being developed. Toluene was preferred over the previously used chlorobenzene, due to its reduced environmental hazard.

Step (m) An adhesion layer of Ti with a nominal thickness of 10 nm is deposited by e-beam evaporation, followed by a layer of Au with a nominal thickness of 300 nm.

[25] Fitted using a non-linear regression tool of a graphing software, SigmaPlot (Systat Software Inc., http://www.sigmaplot.com (*last accessed Jul. 2009*)).

Step (n) Finally, the S1828 photoresist is removed in a photoresist removal to realise the patterns of the heater and the temperature sensor.

The silicon membrane devices with a PSi structure fabricated on the back-side were primarily used in the fabrication of the heater and the temperature sensor. Some non-processed silicon membrane samples ("dummy samples"), mainly from wafers *P03*, *b2P02* and *b2N07*, were also used to determine the exposure and development time. The samples were first cleaned using solvents (acetone and IPA), followed by a short, 1 minute RIE using O_2 gas (with a gas flow rate of 10 sccm, at a pressure of 50 mTorr and an RF power of 100 W). Some of the samples (mainly from wafer *b2N07*), which had the SiO_2 hard mask removed, were further cleaned in fuming nitric acid (FNA) for 30 minutes before being sputter-deposited (Kurt J. Lesker Sputter system) with a nominal 200 nm thick SiO_2 on the front-side of the samples, to serve as electrical insulation for the heater and temperature sensor. The samples were cleaned in a Piranha solution after the sputtering process.

All the samples were then dehydrated in an oven (ED 23 Benchtop Oven, Binder UK) at 120 °C for at least 30 minutes. The samples were then attached to glass cover slips (22 mm x 22 mm, 0.13 mm to 0.16 mm thick, Menzel-Gläser) using the Shipley MICROPOSIT® S1813 photoresist. This is to assist the spin-coating process, as the samples could not be held firmly by the vacuum due to a cavity forming the membrane at the back of the samples. The Shipley MICROPOSIT® S1828 photoresist (Rohm and Haas Ltd., UK) was then spin-coated onto the samples using a programmable photoresist spincoater (SCS G3P-8 Spincoat, Specialty Coating Systems (SCS) Coating Centre, UK). A typical program includes the following steps: i) spin at 500 rpm for 5 s to spread the photoresist; ii) ramp to 3000 rpm for 50 s for a uniform coating; iii) ramp to 5000 rpm for 10 s to expel the extra photoresist from the edges and for evaporation of residual solvent from the photoresist; and iv) reduce to 500 rpm for 5 s to settle the photoresist. The thicknesses of the S1828 photoresist, achieved using the described spin cycles, were between 3.7 μm and 4.2 μm, as measured using the KLA-Tencor P-16 stylus surface profiler.

Next, the samples were pre-baked in an oven for 30 minutes to 45 minutes at 90 °C. Once cooled to room temperature, a sample was placed on a Pyrex® (Corning

7740, 100 mm diameter, 500 μm thick) handler wafer, which was overlaid on an one-to-one scale mask layout. This way, the sample could be approximately aligned to the desired heater and temperature sensor pattern; while the precise alignment was performed using the mask aligner (MA-6, Suss MicroTec Ltd. UK). Using the mask *UoS-TM-CFC-M4* (see Appendix B.2.4), the typical exposure time was 20 s, with an exposure wavelength of 365 nm and a power density of 18 $mW \cdot cm^{-2}$.

The exposed samples were then immersed into toluene for 1 minute. Once gently blown dry using a nitrogen gun, the samples were dried on a hotplate (EMS 1000-1, Electronic Micro System Ltd. UK), at 90 °C, for 15 s. Finally, the sample was developed in a metal-ion-free developer, Shipley MICROPOSIT® MF®-319 (Rohm and Haas Ltd., UK), for between 90 s and 120 s. The samples were then immediately rinsed with a copious amount of DI water to stop the developer from further etching the patterned photoresist.

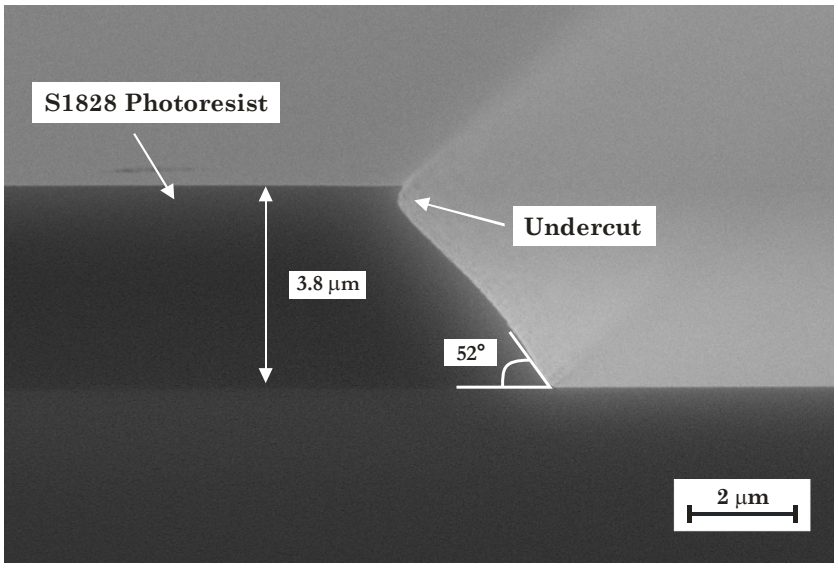

Figure 6.20: Oblique, cross-sectional view SEM micrograph showing the cleaved edge of the photoresist S1828 with a shallow undercut (dummy sample *b2N02sxA*).

A typical developed S1828 photoresist exhibits a positive taper profile, as depicted in Figure 6.20, with a sidewall slope between 40° and 60°. A sidewall profile less than 90° (resulting in an overcut) is characteristic of positive tone photoresists [42]. However, in this case, the slope of the taper was exacerbated, probably due to the un-optimised exposure time and exposure depth used in the process. In particular, it is suspected that the depth of focus of the UV lamp was thought to be

near to the surface of the photoresist, very likely due to a wider than expected gap between the mask and the sample. This is possible since some dummy samples were placed around the Pyrex® handler wafer to accommodate the wedge error compensation feature of the MA-6 mask aligner; this could have, inadvertently, increased the mask-to-sample gap.

The undercut achieved using the described method is shallow, as depicted in Figure 6.20, but is sufficient to provide a successful lift-off, as demonstrated later. The mask-to-sample misalignment, in general, is acceptable and estimated to be between 10 μm and 20 μm (in both x- and y-direction). Figure 6.21 depicts an example of a typical misalignment and the edge bead effect which renders the exposed pattern, under-developed, due to a thicker photoresist near the edge.

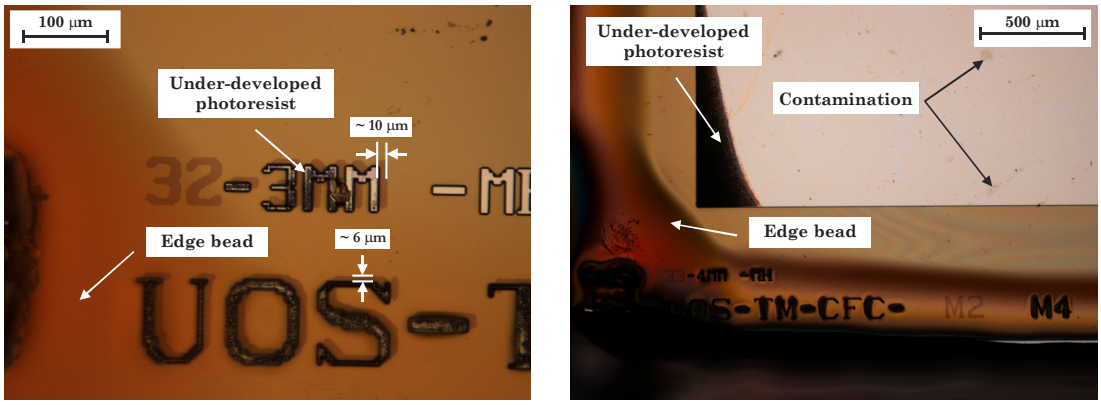

(a) (b)

Figure 6.21: Optical microscope images of (a) sample *b2P06S32*, showing the extent of the mask misalignment; and (b) sample *b2P06S33*, highlighting the edge bead effect.

The samples with patterned photoresist were then blanket deposited, using the e-beam evaporation (BOC Edwards Auto E500), with a nominal 300 nm thick Au (99.99 % pure, G4-5005-M, Testbourne Ltd., UK) and a Ti (99.995 % pure, T8-5003-M, Testbourne Ltd., UK) of 10 nm thick as the adhesion layer. The evaporation was carried out without rotating the sample holder to prevent the evaporated metal from coating the sidewall of the photoresist. Finally, the photoresist was removed, at 120 °C, using the Shipley SVC-175 (Chestech Ltd., UK) photoresist removal, for 30 minutes to 60 minutes.

Despite the shallow undercut created on the S1828 photoresist, the unwanted sections of the metal films were successfully lifted-off on almost all of the samples.

Figure 6.22 depicts the three designs of the heater and the temperature sensor, after undergoing the lift-off step. On closer examination using the optical microscope, however, the edges of the lifted-off heater and the temperature sensor were observed to peel off in places, as depicted in Figure 6.23 (b). SEM micrographs, such as the one depicted in Figure 6.24, later revealed that the edges were actually curved, following the positive taper profile of the photoresist. It is thought that the curved edges should have a negligible effect in terms of performance and functionality of the heater and the temperature sensor, but the full extents of the consequences were not investigated. An optimised photolithography process, to yield an undercut profile of the photoresist, should eradicate the problem. Some contamination and photoresist residue, as depicted in Figure 6.25, was also observed and believed to be related to the edge bead effect, as briefly discussed in Chapter 3, §3.6.2.

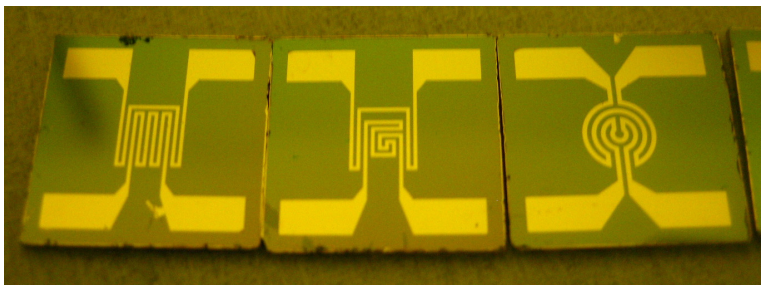

Figure 6.22: Digital photograph of three samples with different heater and temperature sensor designs fabricated using the lift-off method. From left to right: meander, spiral and coil configurations of 3 mm x 3 mm size.

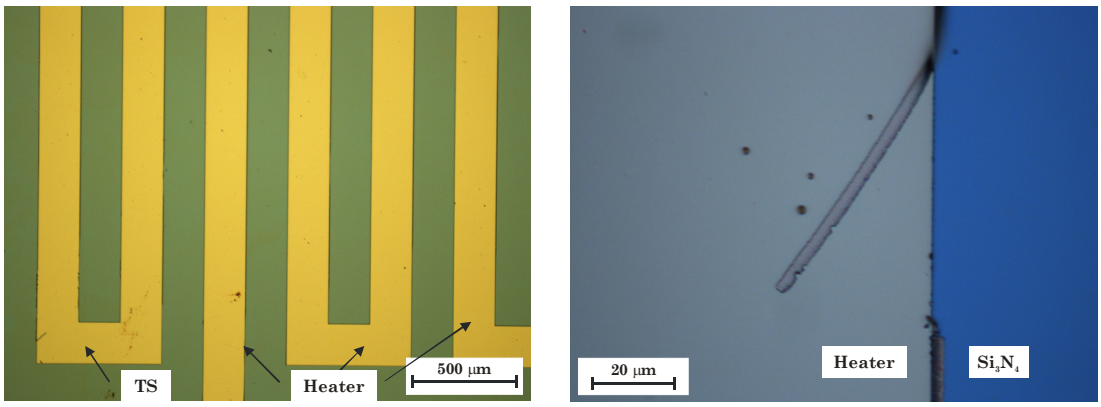

(a) (b)

Figure 6.23: Optical microscope images of (a) low (5 x) and (b) high (100 x) magnifications of samples *b2P02S51* (total Ti and Au thickness of 443.4 nm ± 5.2 nm) with the heater and the temperature sensor (TS) fabricated using the lift-off method. In (b), the edge of one of the heater tracks is shown to have peeled off.

The total thickness of the evaporated Ti and Au, on average, is between 1.25 and 1.5 times thicker than the desired total thickness (10 nm of Ti and 300 nm of Au). The thicker metal layers inadvertently result in reduced resistance of the heater and the temperature sensor. Due to the directional evaporation, the thickness of the deposited metal was not uniform. The thickness uniformity[26] ranges between 2.5 % and 6.5 %; while the single run, sample-to-sample uniformity was measured to be ~ 15 %.

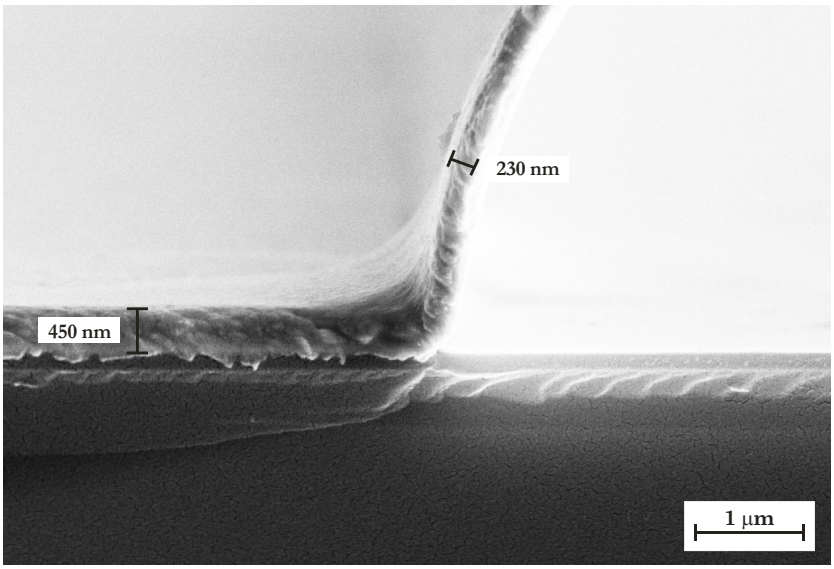

Figure 6.24: Oblique, cross-sectional view SEM micrograph showing the curved edge of the Ti / Au metal track (of sample *b2P02S43* with total Ti and Au thickness of 414.9 nm ± 5.6 nm).

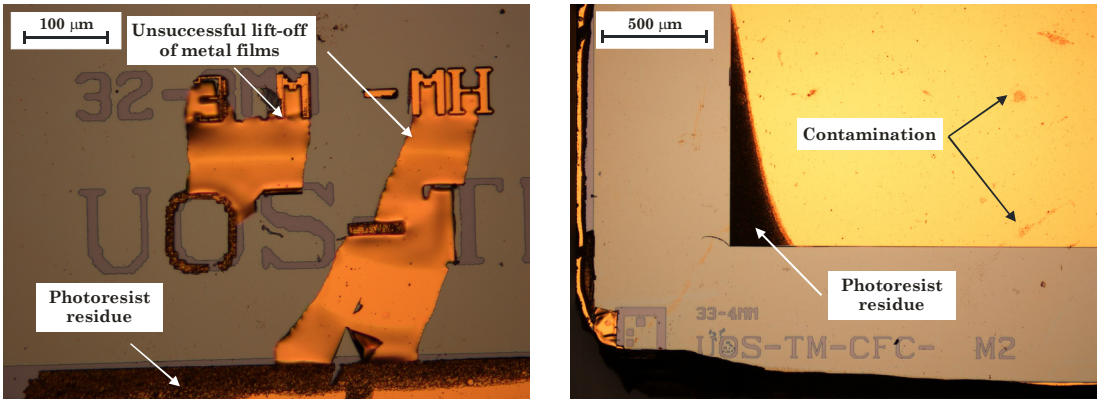

(a) (b)

Figure 6.25: Optical microscope images, of the same regions depicted in Figure 6.21, after the lift-off step. (a) Sample *b2P06S32* (total Ti and Au thickness of 460.6 nm ± 4.8 nm), showing regions of unsuccessful lift-off. (b) Sample *b2P06S33* (total Ti and Au thickness of 409.9 nm ± 9.6 nm), showing the photoresist residue due to under-development caused by edge bead effect.

[26] Based on: 100 % x (maximum thickness – minimum thickness) / average thickness.

6.4 Tests of Integrated Heater and Temperature Sensor

The fabricated heater and the temperature sensor need to be characterised and calibrated for proper operation. Fundamentally, the temperature sensor is a resistance temperature detector whose electrical resistance changes as a result of a varying temperature, as briefly discussed in §6.2.3. It is thus imperative that this relative change of the resistance (or the temperature coefficient of resistance (TCR)) is characterised for the fabricated devices, to ensure proper functionality of the temperature sensor. In addition, the measurement of the TCR of the heating element will also provide useful information for the operation of the heater. Therefore, the resistance of both the heater and the temperature sensor were measured as a function of increasing temperature, and the TCR values were extracted from the measured resistance-temperature curves.

For the proof-of-concept experiments, a simple open-loop driver circuit, which is based on a preset voltage and current value to actuate the heating element, is preferred over the more complex, closed-loop feedback-controlled circuit. Based on the measurement of the TCR, an actuation voltage and current value can be selected to achieve a temperature rise, to the first approximation, in the PSi structure. Thus, a test was performed to calibrate this driver circuit and examine the operational behaviour of the heater, in comparison with the results obtained in the simulation (as discussed in §6.2.3.1).

6.4.1 Experimental Apparatus and Procedures

To determine the TCR values of the heater and the temperature sensor, two PSi membrane devices (*P03S72* and *b2P02S51*) with an integrated heater and temperature sensor in the meander configuration (see Figure 6.3 for the designs of the heater and the temperature sensor) were used. The sample *b2P02S51* was subsequently used to determine the functionality of the heater. The sample *P03S72* has a 3 mm x 3 mm nominal membrane size, while the sample *b2P02S51* has a membrane size of 4 mm x 4 mm. Both samples were bonded to contact connectors

using a two part silver-filled conductive epoxy (Aremco-Bond™ 556), cured at room temperature for over 24 hours. A tiny amount of cyanoacrylate Superglue (159-3963, RS Components Ltd., UK) was also applied to the back of each connector to provide structural bonding. The connectors were then attached to connecting wires using soldering, as depicted in Figure 6.26. Finally, the heater, temperature sensor and the connectors were then coated with nail vanish (Boots, UK) to provide electrical isolation.

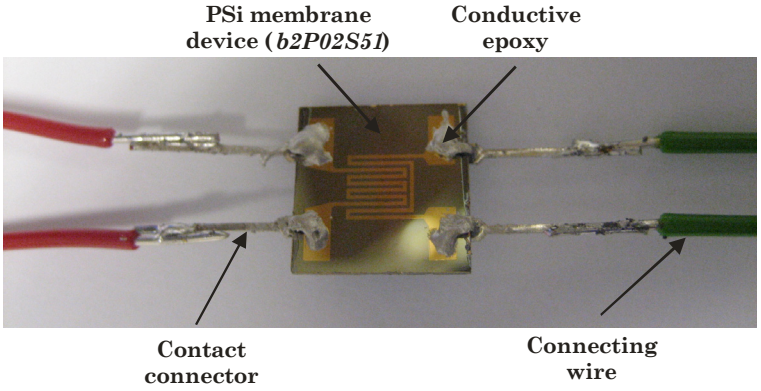

Figure 6.26: Digital photograph of sample *b2P02S51*, which was epoxy-bonded to connectors for external circuitry.

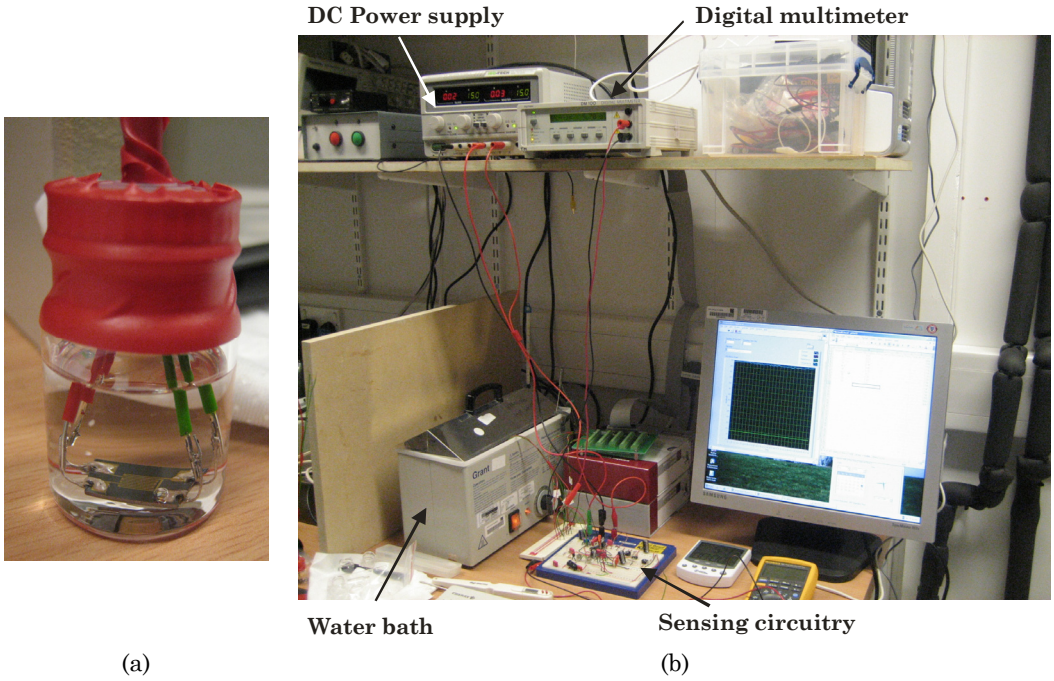

Figure 6.27: Digital photograph of (a) sample *b2P02S51* immersed in a glass specimen bottle filled with ~ 5 mL of DI water; and (b) the experimental setup.

6.4.1.1 Measurement of Temperature-Dependent Resistance

In order to obtain the most relevant information, the measurement was carried out in a similar way to that devised for the protein release experiment (see Chapter 7). Here, the device under test was immersed into a glass specimen bottle containing DI water (typically 5 mL), as depicted in Figure 6.27 (a). To increase the temperature, the bottle was placed in a water bath (JB1, Grant Instruments Ltd., UK), which can be controlled up to 100 °C. A type K thermocouple (SC-TT-K-30-36, Omega Engineering Ltd., UK) was placed near the sample, to monitor the temperature of the DI water, in the specimen bottle. The thermocouple was connected to a handheld temperature / humidity meter (Omegaette® HH314, Omega Engineering Ltd., UK) and the measurement was recorded in the internal memory of the meter.

To measure the temperature-dependent resistance of the temperature sensor, a small excitation current is needed to drive the temperature sensor, while the resulting voltage needs to be monitored to obtain the resistance (by Ohm's Law). Hence, a sensing circuit, as schematically depicted in Figure 6.28, was constructed. The sensing circuit consists of a simple constant current source (CCS) and a voltage amplifier [405]. The CCS was tuned to output a constant current of (1.0 ± 0.05) mA, which is believed to be small enough to prevent self-heating of the temperature sensor. The change in the voltage across the temperature sensor was then amplified by an operational amplifier configured in the non-inverting mode. A positive and a negative voltage regulator (LM7815 and LM7915, respectively) were used to regulate the voltage supply to the sensing circuit. The sensing circuitry was monitored by a NI LabVIEW™ program via a NI Data Acquisition (DAQ) Card (NI PCI-6014) using the 68-pin terminal block (NI CB-68LP). The NI-DAQ™mx module, which greatly simplifies the programming of the software, was used in developing the LabVIEW™-based monitoring system.

The change in resistance of the heating element was measured concurrently using a digital multimeter (DM100, Digimess). Figure 6.27 (b) depicts the overall experimental setup for the measurement of temperature-dependent resistance. The measurements were performed for a range of temperatures from room temperature (~ 20 °C) to ~ 100 °C, with an interval of around 5 °C. For each measurement, a

period of 5 minutes wait time was used to ensure the temperature in the specimen bottle reached thermal equilibrium.

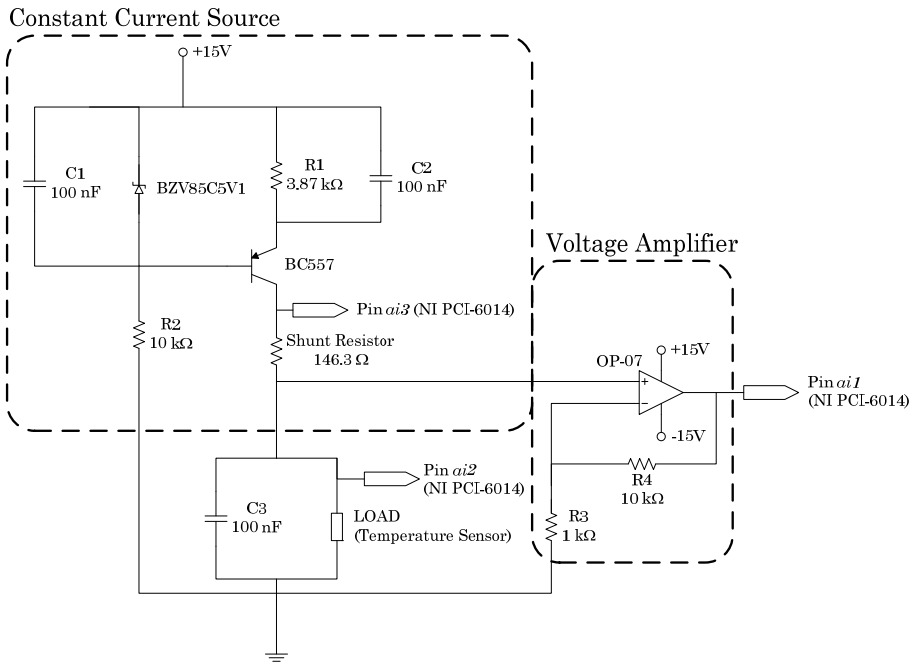

Figure 6.28: Schematic diagram of the sensing circuit. The regulated +15V and -15V supplies were connected (not shown in the schematic) to LM7815 and LM7915, respectively.

6.4.1.2 Heater Functionality Test

To test the functionality of the heater, a simple voltage controlled current source [115], as depicted in Figure 6.29, was constructed to drive the heater. A separate DAQ card (NI USB-6009) was used to provide a signal to enable and disable the driver circuit, hence turning on and off the heater. A separate power supply (HY3003-2, Digimess) was used to power the driver circuit, which is used to turn the heater on at different actuation voltages of about 3 V to 5 V. These correspond to current values of between ~ 0.35 A and ~ 0.56 A, which pass through the heater and result in Joule heating. The temperature rise was then detected using the temperature sensor and measured using the sensing circuit, as described previously. Similarly, the driver circuit was controlled and monitored by the NI LabVIEW™ program, based on the NI-DAQ™mx module.

During the experiment, sample *b2P02S51* was immersed into a glass specimen bottle containing DI water (typically 5 mL), as described previously. The

bottle was then placed into the water bath, which was maintained at 37 °C. Both the sensing and the driver circuits were started with the driver circuit programmed to actuate the heater at predetermined periods between 0.1 s and 1 s. When the temperature in the bottle reached a thermal equilibrium (at 37 °C), the heater was turned on with actuation voltages between 3 V and 5 V. The temperature rise of the sample was monitored and recorded by the temperature sensor, and the temperature change of the DI water was recorded using the SC-TT-K-30-36 thermocouple attached to the Omegaette® HH314 handheld temperature / humidity meter.

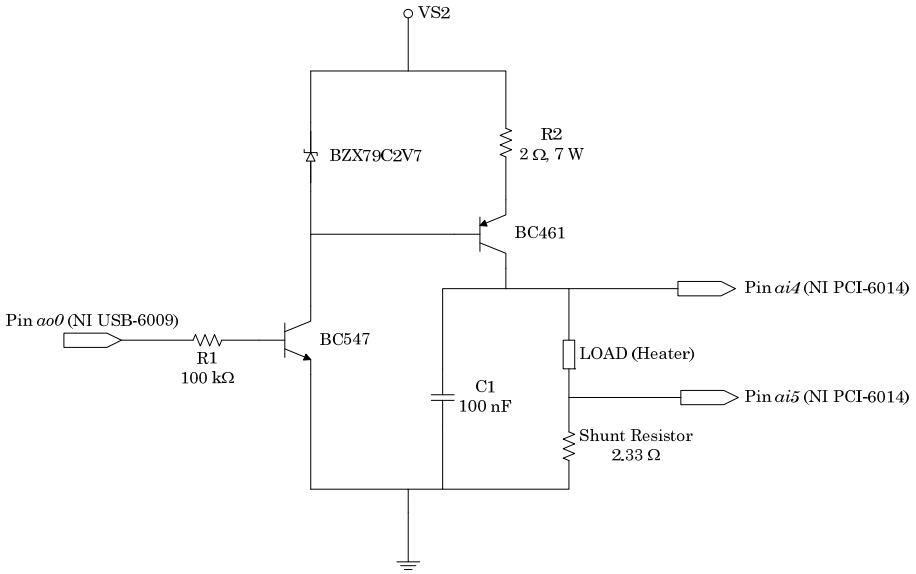

Figure 6.29: Schematic diagram of the heater driver circuit.

6.4.2 Resistance-Temperature Curves and TCR Values

The measured resistance of the temperature sensor and the heater were plotted against the temperature, as depicted in Figure 6.30 and Figure 6.31 for sample *P03S72* and *b2P02S51*, respectively. From the plots the measured data could be fitted with a linear approximation. The TCR, α, could then be approximated by the equation:

$$R = \alpha R_0 (T - T_0) + R_0 \tag{6.4}$$

where R_0 is the initial resistance at temperature T_0. The y-intercept of the linear fit can be approximated to be R_0 (by assuming T_0 of 0 °C), and α can be obtained by dividing the slope of the linear fit by the y-intercept. Table 6.6 summarises the calculated α for both samples, *P03S72* and *b2P02S51*. Overall, the TCR values were calculated to be ~ 16 % to ~ 25 % smaller than the theoretical TCR of bulk gold (3.72 x 10^{-3} K^{-1} [388]). This is expected as the TCR of a metallic thin film, firmly attached to a substrate, is typically lower than its bulk TCR value, primarily due to a thermal mismatch between the film and its substrate [406]. The stray resistance from the contact connectors, the conducting epoxy and the connecting wires, could have also contributed to the discrepancies.

Ideally, the TCR values of the temperature sensor and the heater should be similar, as both should have the same thicknesses of materials (Ti / Au). In addition, the TCR should be independent of the geometry factor (apart from the thickness effect); hence, the sample *P03S72* should have similar TCR values to the sample *b2P02S51*. However, from Table 6.6, it is found that the TCR values for the heater (2.776 x 10^{-3} K^{-1} and 3.003 x 10^{-3} K^{-1}) are smaller than the TCR values for the temperature sensor (3.097 x 10^{-3} K^{-1} and 3.117 x 10^{-3} K^{-1}), for both the samples. It is also observed that the temperature sensor of both samples exhibited more consistent TCR values as compared to the heaters. Hence, it is believed that these errors could be attributed to the technique used to measure the resistance. The resistance of the heater was measured using a direct, two-probe connection to a DMM; this introduces an error to the resistance measurement due to the voltage drop across the probe resistance which adds to the measured voltage. In contrast, the resistance of the temperature sensor was measured using a four-probe technique (one pair for current excitation and one pair for voltage sensing), hence minimising the error contributed by the probes.

Sample	**Temperature Coefficient of Resistance, α (x 10^{-3} K^{-1})**	
	Temperature sensor (% error)	**Heater (% error)**
P03S72	3.097 (16.7 %)	2.776 (25.4 %)
b2P02S51	3.117 (16.2 %)	3.003 (19.3 %)

Table 6.6: The calculated temperature coefficient of resistance of the temperature sensor and heater of samples *P03S72* and *b2P02S51*, based on the measured data plotted in Figure 6.30 and Figure 6.31, respectively. The % error was calculated based on a theoretical value of 3.72 x 10^{-3} K^{-1}, used in the simulation.

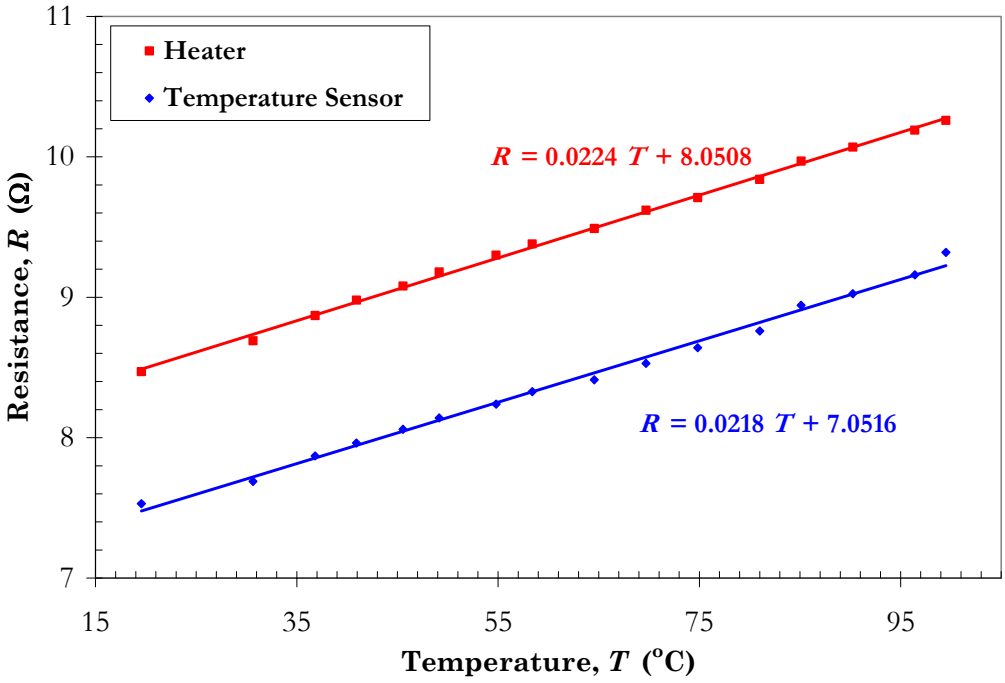

Figure 6.30: Plot of resistance against temperature for sample *P03S72*. The solid lines represent the experimental fits based on linear approximations (shown as equations on the plot).

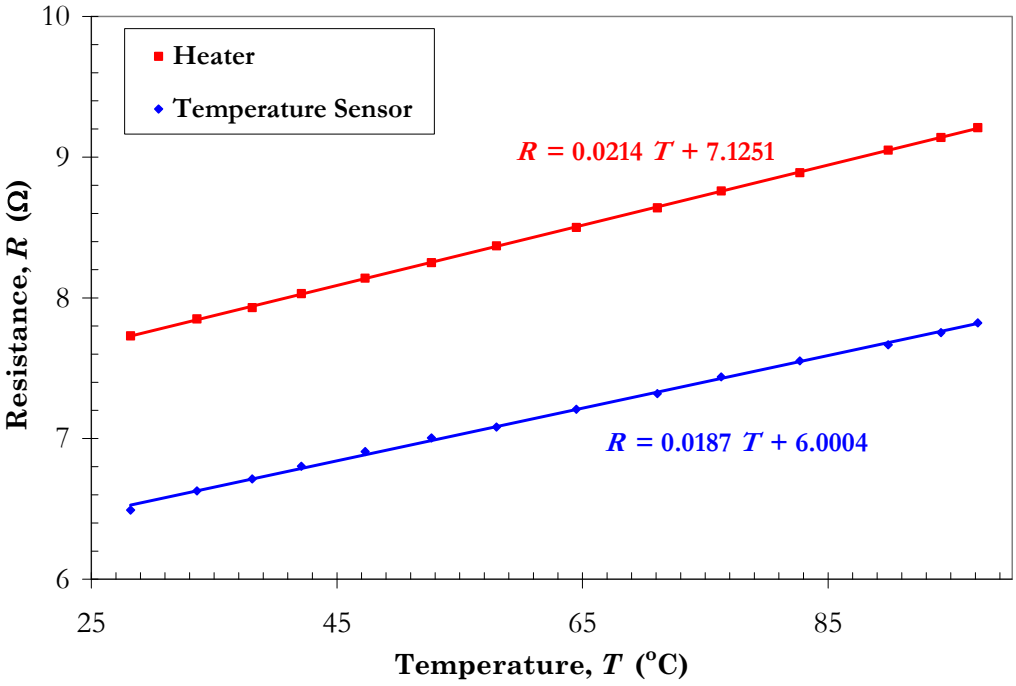

Figure 6.31: Plot of resistance against temperature for sample *b2P02S51*. The solid lines represent the experimental fits based on linear approximations (shown as equations on the plot).

6.4.3 Heater Performance

The functionality and performance of the heater were evaluated for actuation voltages of 3 V, 4 V and 5 V, with heater on-times of 0.1 s, 0.5 s and 1.0 s. The results are summarised in Table 6.7. Overall, the peak temperature during the on-time of the heater for sample *b2P02S51* was measured to exceed the simulated peak temperature of the meander heater (see Figure 6.5 and Table 6.4). It is believed that the higher deposited thickness (hence, reduced resistance) of the metal layers (as discussed in §6.3.3) and the smaller than expected TCR value (as discussed in §6.4.2) are the two major factors that contributed to the discrepancy.

Actuation Voltage (V)	Peak Temperature (°C)			Average Power Consumption (W)
	0.1 s	0.5 s	1.0 s	
3	62.65	64.86	69.34	1.03
4	71.21	78.98	85.27	1.80
5	-	-	97.22	2.82

Table 6.7: The measured peak temperature for actuation voltages of 3 V to 5 V, with heater on-time of 0.1 s, 0.5 s and 1.0 s. The average power consumed, P during the heater on-time was calculated based on the measured voltage, V, and current, I, across the heater ($P = V \times I$).

Figure 6.32 depicts a plot of temperature, as measured by the temperature sensor and the thermocouple, over time, for an actuation voltage of 3 V, with a heater on-time of 0.5 s. The temperature of the device, as measured by the temperature sensor, reached a steady state almost instantaneously after the heater was turned on. The mean temperature, averaged over the heater on-time, was found to be 62.7 °C ± 1.2 °C. The temperature of the DI water, as measured by the thermocouple, barely changed over the duration of the experiment (60 s). Although both the measured peak temperature and the mean temperature were beyond the simulated value, these are still within the limit of the critical temperature (of 60 °C ± 10 °C) assumed in the design specification (as described in §6.2.3). Hence, a rapid local heating, with minimal heat dissipation to the surrounding (DI water), was achieved.

A revised simulation (for a heater on-time of 0.5 s), which uses a heater thickness of 443 nm, a TCR value of 3.00×10^{-3} K^{-1} and a natural convective heat transfer coefficient, h_c of 200, shows a good agreement with the measured peak temperature, as depicted in Figure 6.33. The measured data was smoothed using

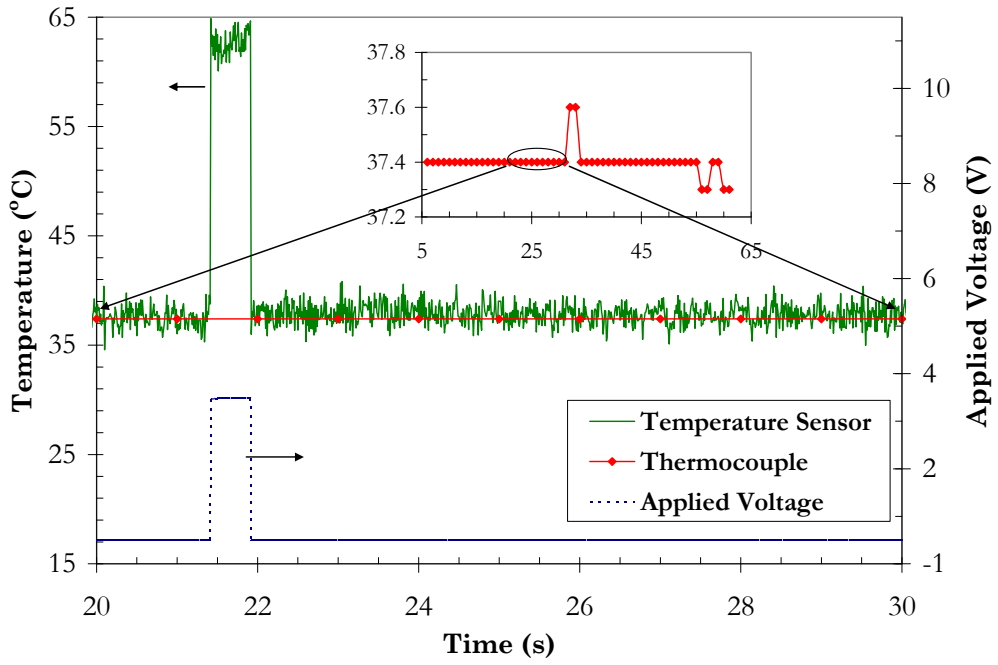

Figure 6.32: Plot of the actuation voltage (- - -) and the temperature, of the temperature sensor (—) and the thermocouple (◆), over time, of sample *b2P02S51*. The sample was actuated using 3 V input voltage for 0.5 s. The inset shows the temperature variation of the thermocouple over the duration of the experiment (60 s).

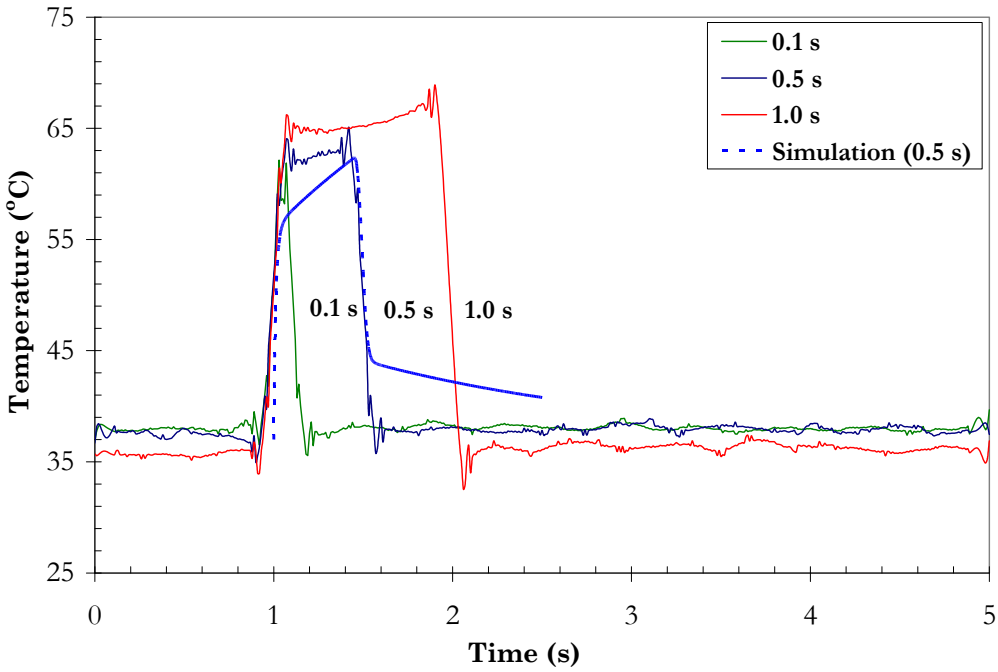

Figure 6.33: Plot of the temperature over time for an actuation voltage of 3 V, for heater on-time of 0.1 s, 0.5 s and 1.0 s. The dashed blue line represents a revised simulation using COMSOL, with an actuation voltage of 3 V and a heater on-time of 0.5 s, using a heater thickness of 443 nm, a TCR value of 3.00×10^{-3} K^{-1} and a natural convective heat transfer coefficient, h_c of 200.

an adaptive smoothing method[27]. The mean temperature was observed to increase, as summarised in Table 6.7. The simulated temperature reached ~ 40 °C after the heater was turned off; this is well above the ~ 37 °C measured. It is suspected that the value of h_c used in the simulation may not be accurate. In fact, different values of h_c used in the simulation resulted in different heat transfer rates to the surroundings, and hence affected the maximum transient temperature (see Appendix D.4 for detailed results). Therefore, it may be necessary to empirically determine the value of h_c in order to validate the simulation.

6.5 Conclusion

The successful design and fabrication of an improved drug delivery prototype device, based on a silicon membrane substrate, was described. The silicon membrane, fabricated using an anisotropic wet chemical etching process, exhibited an average thickness of 46.6 μm ± 0.5 μm. A modified NSL technique, with an improved RIE of silicon using a STS LPX Pegasus system (see Figure 6.15 for detailed process steps) was used to realise a quasi-ordered, cylindrical PSi structure, at the back-side of the silicon membrane, to be used as the drug reservoir. Nanospheres with a mean diameter of 200 nm were used, thus resulting in the interpore distance of ~ 200 nm of the eventual PSi structure. An optimised O_2 RIE etch time of 60 s was primarily used to reduce the size of the nanospheres. With a typical O_2 gas flow rate of 5 sccm, a pressure of 10 mTorr and an RF power of 100 W, the nanospheres were reduced to a diameter of 86 nm ± 3 nm on average, which is in good agreement with the theoretical value of 88 nm (based on an etch rate of 1.9 $nm \cdot s^{-1}$). To improve the success of the removal of nanospheres, a 10 nm thick Cr layer and an ultrasonication time of < 60 s, were used.

By exploiting the LF process and the parameter ramping feature of the STS LPX Pegasus system, the fabricated PSi structures exhibited mean pore diameters between ~ 75 nm and ~ 120 nm, with pore depths in the range of ~ 330 nm to 500 nm. The theoretical porosity was thus calculated to be between 12.8 % and 32.6 %.

[27] Implemented using a Microsoft® Office Excel© macro *ELSauto* of MacroBundle, developed by R. de Levie. http://www.bowdoin.edu/~rdelevie/excellaneous (*last accessed Jul. 2009*).

The aspect ratio was found to be 5:1, at best; however, the parameters used in the STS LPX Pegasus system, as detailed in Table 6.5, could be optimised to achieve higher aspect ratios. This novel nanofabrication technique is versatile and various other nanostructures, such as nanopillars (see Appendix E, §E.6) and nanowires (see Appendix E, §E.7), have been successfully fabricated. It is a "materials general" technique and has been successfully demonstrated on both p-type and n-type silicon substrates (both substrates with resistivity of 1 – 10 Ω·cm); ordered PSi with cylindrical pores in 100 nm diameter range has been difficult to achieve using conventional electrochemical etching method. One limitation of this technique would be the possible non-uniformity in the pore diameter and the pore depth due to inconsistent micro-loading and varied aspect ratios as a result of the intrinsic defects introduced by the nanosphere deposition method.

An integrated heater and temperature sensor, fabricated at the front-side of the silicon membrane, is envisaged to provide the electro-thermal actuation by rapidly heating the PSi structure, for a short time, to assist the desorption of the therapeutic agents into the environment (human body). Three configurations of the heater and temperature sensor were designed, as depicted in Figure 6.3, each with different sizes to accommodate the three sizes of the membrane. The heater and the temperature sensor were fabricated using the lift-off method described by Steps (l) to (n) in Figure 6.8. The total thickness of the evaporated Ti and Au was found to be on average 1.25 to 1.5 times thicker than the desired total thickness (10 nm of Ti and 300 nm of Au). The uniformity of the thickness varied between 2.5 % and 6.5 % due to the directional evaporation. This resulted in a reduced resistance of the heater and the temperature sensor, and a ~ 16 % to 25 % (detailed in Table 6.6) reduction in TCR values (as compared to the bulk TCR value). Consequently, by using an actuation voltage of 3 V and a heater on-time of 0.5 s, the meander heater exhibited a peak temperature of 64.86 °C, which is well beyond the simulated value of 55.02 °C (see §6.2.3.1 for details). A revised simulation using the measured thickness of 443 nm and a calculated TCR value of 3.00 x 10^{-3} K^{-1} (of sample *b2P02S51*), however, demonstrated a good agreement with the experimental result. Hence it is verified, both by experiment and simulation, that the actuation voltage of 3 V and a heater on-time of 0.5 s is sufficient to provide a rapid local heating (up to 60 °C ± 10 °C) with minimal heat dissipation to the surrounding environment.

Chapter 7

Protein Loading and Passive Release using a Porous Silicon Membrane Drug Delivery Device

7.1 Introduction

To date, the release of a drug using a porous silicon (PSi) structure has been demonstrated from PSi particles [54, 55], PSi powder [215] or PSi pieces [216] (see Chapter 2, §2.3.2 for a literature review); however, there are limited reported studies on using a PSi structure that is integrated on a microdevice, for the delivery of drugs. In this chapter, a "proof-of-concept" investigation of drug loading and release, using the drug delivery device fabricated as described in Chapter 6, is presented. The microdevice incorporates a nanostructured PSi on a thin membrane (as the drug reservoir) and an integrated heater and temperature sensor (for a controlled, active release using electro-thermal actuation).

In this study, an attempt to achieve the loading and the passive release (without using the electro-thermal actuation) of a model protein, using the fabricated PSi membrane prototype device, is demonstrated. Fluorescently labelled model protein, Papain (see §7.2.1 for more details) which has a similar molecular weight to the protein of interest (bone morphogenetic protein 2) was loaded into the PSi membrane device. Fluorescence microscopy and scanning electron microscopy (SEM)

were used to investigate the efficacy of the loading strategy. The protein was then released from the PSi membrane, *in vitro*, at different temperature conditions. The concentrations of the fluorescently-labelled Papain released were evaluated at single time points and interpolated from a plot of fluorescence emission as a function of a series of standards.

7.1.1 Methods of Drug Loading into Porous Silicon

The loading of model proteins or drugs into PSi structures can be performed using one of the three commonly used approaches: i) by covalent attachment [55], ii) by physical trapping [55] and iii) by spontaneous adsorption [54, 55]. Covalent attachment of drug molecules, to the inner pore walls of the PSi structure, is the most robust approach for attaching the drug payload to the porous matrix; the release of the drug payload can only be achieved by breaking the covalent bonds or by the degradation of the porous matrix [55]. However, this approach adds a level of complication for the fabricated PSi membrane device due to a need to chemically functionalise inside the pores without trapping secondary reaction products. The physical trapping approach requires the drug molecules to be trapped into the pores first. The oxidation process, used in the physical trapping approach, merely shrinks the pores and thus "locks" the drug molecules in place [55].

A more straight-forward and hence commonly used method is the spontaneous adsorption of the drug molecules into a porous matrix [54, 55]. This can be achieved by a simple immersion of the porous matrix (typically in powder or particulate form) into a dissolved drug solution. Loading of model drugs, including ibuprofen and gentamicin, and human serum albumin, have been demonstrated in mesoporous silica, such as SBA-15 powder [407, 408] and MCM-41 particles [409, 410], and PSi layers [411] and PSi particles [70, 71]. This method may require a controlled, but thorough, washing step to remove the fractions of drugs from the surface. Alternatively, a precise amount of the drug solution can be introduced into the porous structure by impregnation [54]. The drug solution is then allowed to infuse, via capillary action, into the pores; this is also known as the incipient wetness method [54]. PSi layers [216, 412] have been loaded with model protein or fluorescent dye this way. Both the immersion and impregnation techniques can be typically performed at room temperature and at favourable chemical (such as pH

level) environments. The surface of the PSi structure can be also be chemically modified [211, 212] to enhance the adsorption of the drug molecules [54]. A suitable drying method is also important and methods, such as freeze drying [215], vacuum drying [69, 216, 408] or thermal drying [70, 409], have been used.

7.2 Protein Labelling

For selective optical detection and quantitative analysis, proteins are typically fluorescently labelled. The conjugation of the fluorescent probes to proteins is achieved by the formation of a covalent bond with the amine residues on the side chains of the proteins [413].

In practice, the labelling reaction is also determined by a number of factors, including the pH value of the buffer solution, the concentration of the protein, the temperature of the reaction mixture and the time of reaction [413, 414]. Most protein labelling protocols are thus designed to provide reproducibility with an optimum molar reaction ratio, *MR* (or simply, the number of moles of labelling reagent to be reacted to one mole of protein), which can be described by the following:

$$MR = \frac{MW_P}{MW_F} \times \frac{C_F \cdot V_F}{C_P \cdot V_P} \tag{7.1}$$

where *MW*, *C* and *V* represent the molecular weight (in Dalton), concentration (in $mg \cdot mL^{-1}$) and volume (in mL), respectively, of the fluorophore and protein, as denoted by the subscript of *F* and *P*, respectively. A favourable *MR* can better control the extent of conjugation and hence ensure optimum labelling yield. Over-labelling of protein may result in loss of protein activity and specificity, aggregation and precipitation and quenching of fluorophores [413]; while, in contrast, too few labels results in weak fluorescent signals, and thus the protein is difficult to detect.

7.2.1 Model Protein: Papain

The integrated drug delivery device is intended for the use of a sustained and controlled release of osteoinductive growth factors, specifically, bone morphogenetic protein 2 (BMP-2), to promote bone regeneration and repair (see Chapter 1, §1.1.1 for more details). For the PSi membrane prototype device, as a proof of concept, a model protein was used which has similar molecular weight to BMP-2. BMP-2 has a molecular weight of about 26 000 Dalton [27], with dimensions of 7 nm x 3.5 nm x 3 nm [28].

A few model proteins were considered, but Papain, which is a cysteine protease typically used in the enzymatic synthesis of amino acids and peptides, appeared to be the best candidate. Papain is a single chain polypeptide with 212 residues [415] folded into two distinct parts which are separated by a cleft [416]. It has a molecular weight of 23 406 Dalton [415] and an approximate dimensions of 4.8 nm x 3.6 nm x 3.6 nm [416]; both the molecular weight and dimension are similar to the BMP-2. In its native form (without activator), Papain exhibits low activity and is remarkably stable at high temperatures [416], hence making it suitable for this study. Papain is also readily soluble in water, which makes it more straight-forward to work with. In addition, it is inexpensive, compared to BMP-2, and hence is available in a larger quantity for experimental trials. Drug loading and release from PSi powders [215] or PSi pieces [216] have been demonstrated using Papain as a model drug. Table 7.1 highlights some of the properties of Papain.

Property	Typical Value	Reference
Molecular Weight, *MW*	23 406 Dalton	[415]
Percent Absorption Coefficient (1 % or 10 mg·mL^{-1} solution), $\varepsilon^{1\%}$ at 278 nm	25 L·g^{-1}·cm^{-1}	[417]
Molar Absorption Coefficient, ε	58515 L·mol^{-1}·cm^{-1}	calculated
Optimal pH for activity	6.0 to 7.0	[418]
Optimal temperature for activity	65 °C	[419]

Table 7.1: Some physical properties and kinetics of Papain. The molar absorption coefficient was calculated as 0.1 x $\varepsilon^{1\%}$ x *MW*.

7.2.2 Methods and Procedure

A typical protocol of protein labelling involves the preparation of the protein and the fluorescent dye, the incubation and conjugation of the fluorescent dye with the protein and, finally, the separation of non-reacted fluorescent dye from the mixture.

For the labelling of Papain, the 5(6)-Carboxyfluorescein *N*-hydroxysuccinimide (NHS) ester (FLUOS) was preferred as the fluorescent dye. FLUOS is one of the derivatives of fluorescein isothiocyanate (FITC), which is more widely used due to its higher quantum efficiency [420]. However, FLUOS has an advantage over FITC because the NHS esters react with the primary amino groups in proteins to form more stable carboxamide bonds as opposed to the thiol-urea bond formed by FITC [421]. These carboxamide bonds are relatively more resistant to hydrolysis [420]. Some of the properties of FLUOS are summarised in Table 7.2.

Property	Typical Value
Molecular Weight, *MW*	473.4 Dalton
Molar Absorption Coefficient, ε	70 000 $L \cdot mol^{-1} \cdot cm^{-1}$
Excitation Wavelength, λ_{EX}	494 nm
Emission Wavelength, λ_{EM}	518 nm
Optimum pH for labelling	7.0 to 9.0; 8.5 for 50 mM borate buffer

Table 7.2: Some physical properties of FLUOS (adapted from [422]).

The lyophilised Papain powder (P4762, Sigma-Aldrich Company Ltd., UK) and the lyophilised FLUOS powder from a Roche Protein Labelling kit (1386093, Roche Applied Science) were used as received. All the solvents were of reagent grade and were used without further purification, except for dimethylsulfoxide (DMSO), which was filtered using a 0.2 μm membrane filter. The de-ionised (DI) water was from ELGA® PURELAB Ultra system with a typical resistivity of 18.2 MΩ·cm and a pH value of 7.0.

Papain was prepared by first dissolving 2.7 mg of the lyophilised Papain into 270 μL of DI water (as the buffer solution). Then, 100 μL of the solution was diluted with 900 μL of DI water to make up 1 mL of Papain stock solution of a concentration of 1 $mg \cdot mL^{-1}$. Next, 1 mg of the lyophilised FLUOS powder was reconstituted with 50 μL of filtered, analytical grade DMSO to produce a FLUOS solution with a

concentration of 20 mg·mL^{-1} [421]. Papain has 10 side chains of lysine within its amino acid chains [415], which could be available for conjugation to FLUOS. Hence, a fluorophore to protein molar ratio of 10:1 was selected for the conjugation reaction. 10.11 μL of the reconstituted FLUOS solution (concentration of 20 mg·mL^{-1}), as calculated using equation 7.1, was used to react with 1 mL of the Papain stock solution (concentration of 1 mg·mL^{-1}). The mixed solution was then incubated for 2 hours, in the dark, at room temperature, with gentle stirring.

Next, the free, unconjugated fluorophores were removed from the conjugation mixture. Instead of using the column separation technique, as suggested by the product information sheet [421], dialysis was preferred. Dialysis is the diffusion of molecules through a semi-permeable membrane, from the higher concentration side to a lower concentration side of the membrane, in an attempt to achieve equilibrium in concentration. A Slide-A-Lyzer® dialysis cassette (66382, Thermo Science Pierce) with a molecular weight cut-off (MWCO) of 10,000 Dalton and capacity of 0.5 mL to 3 mL, was used. The conjugated FLUOS-Papain mixture was dialysed over 4 changes, against 1 L of DI water. The purified FLUOS-labelled Papain was stored in the freezer until use.

7.2.3 Protein Concentration and Labelling Efficiency

In the quantitative determination of protein concentration, ultraviolet / visible (UV / Vis) absorption spectrophotometry is widely used in conjunction with colorimetric protein assays, such as the Lowry assay, the Bradford assay, the Biuret assay or the bicinchoninic acid assay [423-425]. The most straight-forward method of quantifying proteins, however, is to measure the UV absorbance of the protein solution, typically at the wavelength of 280 nm or 205 nm [425, 426]. Most proteins have intrinsic absorbance at ~ 280 nm due to the aromatic amino acids, such as the tryptophan, tyrosine, phenylalanine and histidine [424]. Sometimes, the fraction of tryptophan or tyrosine residues of a protein can be too low for a measurable absorbance at 280 nm. In this case, measuring the absorbance at 205 nm is generally used, since this indicates the absorbance due to the peptide bonds of a protein [426].

In order to determine the efficiency of the labelling of Papain with FLUOS and to establish the concentration of Papain in the recovered mixture after the

dialysis, a UV / Vis spectrophotometer (Varian Cary® 50) was used. For the measurement, 200 µL of the recovered, dialysed FLUOS-labelled Papain solution, was first diluted with 800 µL of DI water (5-fold dilution). About 120 µL of the diluted sample was dispensed, by using a pipette, into a cleaned cuvette (105.253 QS, Hellma Ltd., UK). The absorbance of the diluted FLUOS-labelled Papain solution was measured, between the wavelength of 200 nm and 800 nm, with a scan speed of 4800 nm·s^{-1}, and recorded using the software *Cary WinUV*. Two sets of measurements, using two different diluted samples (same dilution factor), were performed, with each run repeated 5 times. A typical baseline-corrected absorption spectrum of the 5-fold diluted FLUOS-labelled Papain solution is depicted in Figure 7.1.

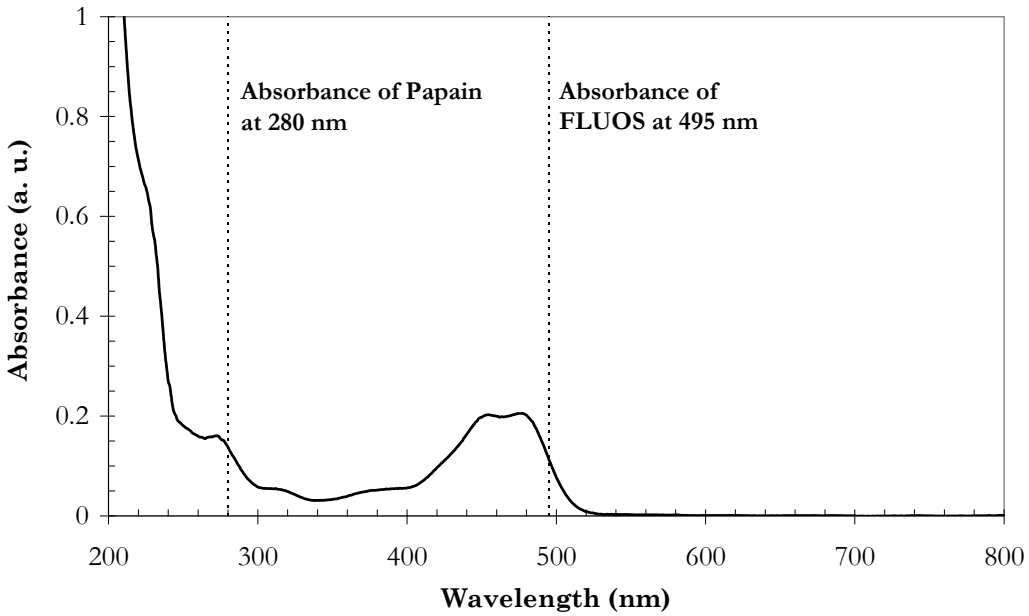

Figure 7.1: A typical corrected absorption spectrum of the 5-fold diluted FLUOS-labelled Papain (a. u. denotes arbitrary unit).

The concentration of the FLUOS-labelled Papain, recovered from the dialysis process, was determined; the absorbance value at 280 nm, A_{280}, was obtained from the UV / Vis spectrophotometry of the 5-fold diluted solution. Due to the presence of the fluorophore (FLUOS), a correction factor, *CF* of 0.255, deduced from [421], was introduced into the typical Beer-Lambert's equation. The concentration of Papain (in mg·mL^{-1}), C_{Papain} is therefore:

$$C_{Papain} = \frac{A_{280} - (CF \times A_{495})}{\varepsilon_{Papain} \times l} \times MW_{Papain} \times DF \tag{7.2}$$

where ε_{Papain} and MW_{Papain} are the molar absorption coefficient and the molecular weight of Papain, respectively; l is the path length of the cuvette, A_{495} is the absorbance value at 495 nm (of FLUOS) and DF is the dilution factor. The ε_{Papain} value of 58 515 $L \cdot mol^{-1} \cdot cm^{-1}$ (see Table 7.1) was used in the calculation by assuming that the absorbance of Papain was not altered by the conjugation. The average concentration of Papain, based on the baseline-corrected spectra, was calculated to be (0.218 ± 0.003) $mg \cdot mL^{-1}$.

The molar fluorophore to protein (F/P) ratio of the dialysed FLUOS-labelled Papain was then determined by taking the ratio of the molar concentration of FLUOS, $C_{M,FLUOS}$ over the molar concentration of Papain, $C_{M,Papain}$ as follows:

$$F/P = \frac{C_{M,FLUOS}}{C_{M,Papain}} = \frac{A_{495}}{A_{280} - (CF \times A_{495})} \times \frac{\varepsilon_{Papain}}{\varepsilon_{FLUOS}} \tag{7.3}$$

where ε_{FLUOS} is the molar absorption coefficient of the free FLUOS. The average molar F/P ratio, based on the baseline-corrected spectra, was calculated to be 0.875 ± 0.011; this implies a labelling efficiency of less than 8.8 % since the initial molar reaction used was 10:1. Some of the Papain molecules may not be labelled and this may result in a low estimate to the actual concentration of Papain when analysed using spectrofluorimetry.

7.3 Protein Loading

7.3.1 Methods and Procedure

The purified FLUOS-labelled Papain was loaded into selected PSi membrane devices using the impregnation technique with the vacuum drying method (see §7.1.1), this is similar to the approach described by Prestidge *et al.* [216]. The devices were first pre-wetted in methanol (at least overnight), in order to enhance the hydrophilicity of

the porous surface. Prior to the loading process, the methanol was replaced with DI water, in a series of steps of reducing methanol concentration, to preserve the hydrophilicity of the devices and to avoid building up of air bubbles which could be problematic during the loading process. The devices pre-wetted in methanol were first immersed into a 1:3 DI water:methanol solution for 2 hours, with gentle stirring. Then the devices were immersed into a 1:1 DI water:methanol solution, followed by a 3:1 DI water: methanol solution, each for 2 hours while being gently stirred. Lastly, the devices were individually placed into separate glass specimen bottles filled with ~ 5 mL DI water. The devices were kept in the bottles for at least 1 hour prior to the protein loading process.

During the loading process, the devices were placed, one at a time, in a vacuum chamber of a mini sputter-coater (Polaron SC7620, Quorum Technologies Ltd., UK) while retaining the wetness. Typically, either 2.5 μL or 5.0 μL of FLUOS-labelled Papain solution was carefully dispensed, using a pipette, onto the centre of the membrane cavity. The chamber was then closed and the vacuum pump was started. The aqueous solution would be slowly evaporated due to the vacuum, which typically takes about 5 minutes of vacuum pumping. The process was completed when the pressure finally reached 3 x 10^{-2} mbar. The devices were then examined by fluorescence microscopy and SEM to investigate the extent of the loading process.

7.3.2 Analysis of Papain Loading

Some of the membranes were observed to crack or break into pieces, during the initial stages of the vacuum drying process. The PSi membrane device was attached to the sample holder, which was merely a SEM stub, with carbon adhesive tape, hence creating a gap due to the finite thickness of the tape. Any water droplets trapped between the gap of the device and the sample holder, could have introduced additional stress to the weak-point (such as at the pinholes, see Chapter 6, §6.3.1.1) of the membrane, hence causing the cracks on the membrane.

Quantifying the extent of drug loading into a porous matrix is not always straight-forward; it is difficult to distinguish between the fraction of drug on the surface of the porous structure and the fraction impregnated into the pores. In an attempt to investigate the efficiency of the loading process, the PSi membrane

devices loaded with FLUOS-labelled Papain, were examined using an inverted fluorescence microscope (Axio Observer.Z1, Carl Zeiss) and a SEM (LEO 1455VP). The fluorescence microscope is fitted with a monochromatic charge coupled camera (1388 x 1040 pixels, AxioCam HR3, Carl Zeiss) for image acquisition and equipped with a 100 W mercury arc lamp (HBO 100, Carl Zeiss). The Zeiss 09 filter set (488009-9901-00, Carl Zeiss), with a band pass between 450 nm and 490 nm for the excitation, a dichroic beam splitter at 510 nm and a long pass filter with a cut-off at 515 nm for the emission spectrum, was used. The accompanied software, AxioVision 4.6.3, was used for image acquisition and image processing.

In general, a broad-ring pattern, as depicted in the SEM micrograph of Figure 7.2, could be observed on most of the devices after the loading process. The formation of such a ring pattern is a common phenomenon during drying from the receeding meniscus of aqueous solutions, including biological polyelectrolyte solutions [427]. A SEM micrograph, as depicted in Figure 7.3, confirms the formation of the aggregation on the surface of the PSi membrane.

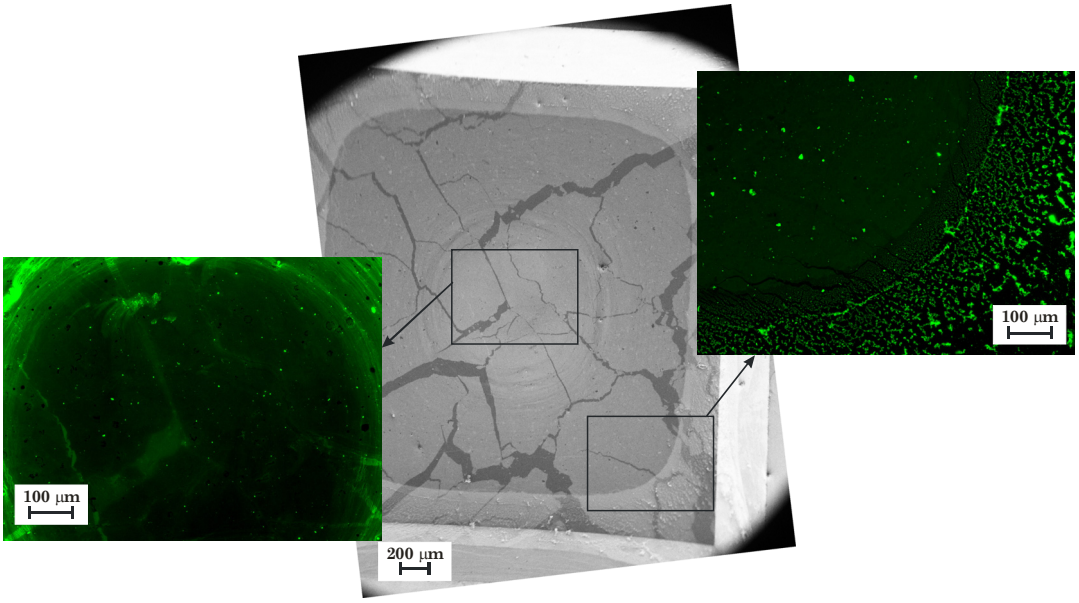

Figure 7.2: Plane-view SEM micrograph of device *b2P06S43*, imaged in low magnification, showing almost the entire area of the PSi membrane surface. The fluorescence microscope images (with false colour) were acquired at the respective boxed areas of the device, highlighting the present of the FLUOS-labelled Papain.

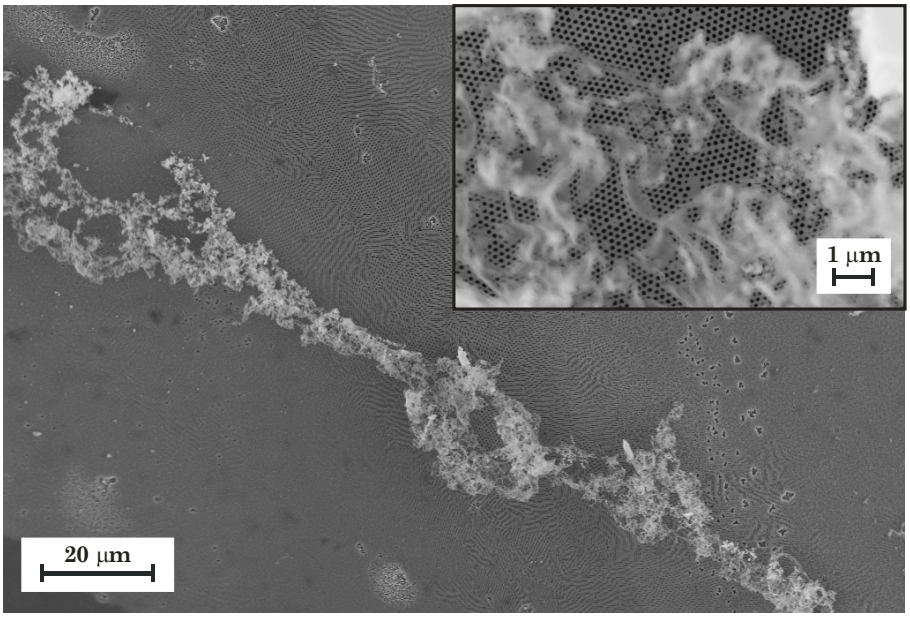

Figure 7.3: Plane-view SEM micrographs of device *b2P06S63* after the protein loading process, clearly demonstrate the present of FLUOS-labelled Papain on the surface of the PSi membrane. The inset shows a magnified view of the same sample.

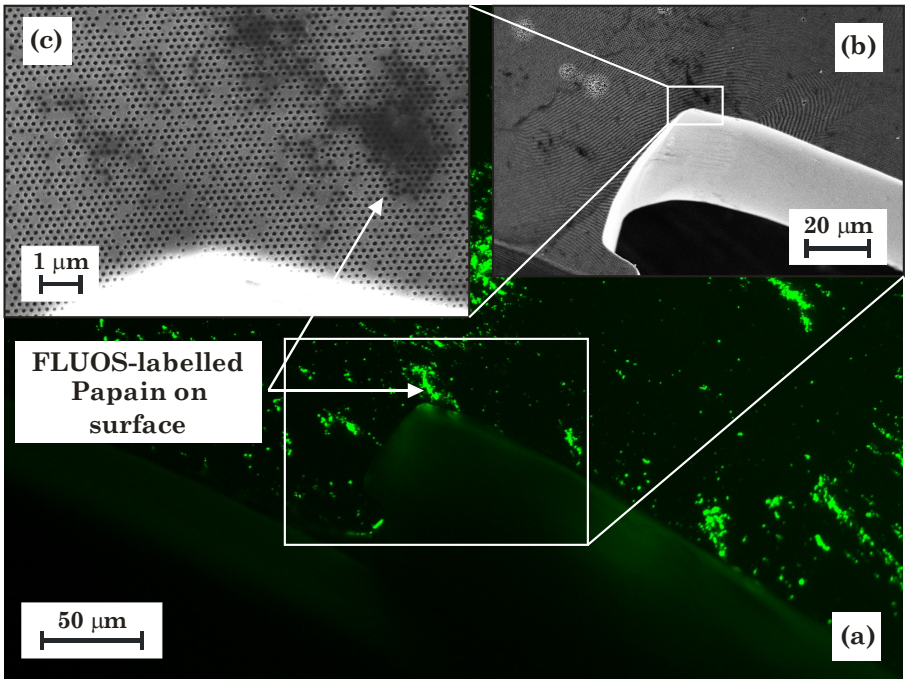

Figure 7.4: (a) Fluorescence microscope image (with false colour); and (b) its corresponding plane-view SEM micrograph at the boxed area, of device *P03S32*, after several washes in DI water. The inset (c) depicts a magnified view of the boxed area in (b).

In an attempt to remove the weakly surface bound Papain, device *P03S32* (see Appendix E, §E.1 for additional SEM micrograph) which was loaded with 2.5 μL of FLUOS-labelled Papain solution, was washed several times under a stream of running DI water. The combined SEM-fluorescence microscopy, as depicted in Figure 7.4, of the device indicates a significant reduction in the extent of unspecific binding of FLUOS-labelled Papain on the surface of the PSi membrane. Some of the protein was observed over the pores, as shown by the arrows in Figure 7.4. However, it was not easy to establish if any of the protein was trapped within the pores.

Fluorescence microscopy provides a good indication of the distribution of FLUOS across the sample; areas where the fluorescent signals are high indicate a relatively high concentration of FLUOS-labelled Papain. However, the fluorescence microscope does not quantify the amount of the detected Papain, nor is it possible to determine if the FLUOS-labelled Papain was indeed inside the ~ 100 nm diameter pores or just attached to the surface. By using the SEM, the FLUOS-labelled Papain could be easily detected on the surface.

7.4 Passive Release of Protein

7.4.1 Methods and Procedure

To investigate the release of the loaded FLUOS-labelled Papain at different temperature conditions, three PSi membrane devices, with the characteristic of the PSi structure as summarised in Table 7.3, were used. The sample *b2P06S51* cracked and broke into two during the protein loading process, hence only half of the chip was used. The sample *b2N07S51* does not have the PSi structure and was used as a control. The passive release at two temperature conditions was performed: one at 37 °C, to simulate the conditions of body temperature and the other at 60 °C, to replicate an elevated temperature caused by the actuation of the integrated heater.

Firstly, in an attempt to remove the FLUOS-labelled Papain attached to the surface, the PSi membrane devices were leached at 37 °C for 24 hours. Here, ~ 5 mL of DI water was filled into a glass specimen bottle. A PSi membrane device, with pre-

loaded FLUOS-labelled Papain, was then immersed into the DI water, with the side containing the PSi structure (the back-side) facing up. The specimen bottle was capped and wrapped with aluminium foil to prevent photobleaching of the fluorophores. The bottle was then put in a water bath (JB1, Grant Instruments Ltd., UK) and subjected to a constant temperature of 37 °C. After 24 hours, the specimen bottle was removed from the water bath and the device was rinsed and dried.

Device	PSi characteristic		Protein solution used (μL)	Comment
	Pore width	Pore depth		
b2P06S51	111 nm ± 7 nm	545 nm ± 32 nm (inclusive of SiO_2 hard mask)	5.0	~ Half chip (~ 2 mm by 4 mm membrane size); SiO_2 hard mask still intact
b2N07S62	112 nm ± 10 nm	340 nm ± 36 nm	2.5	Full chip (4 mm by 4 mm membrane size); SiO_2 hard mask removed
b2N07S51	Without PSi structure		5.0	Full chip (4 mm by 4 mm membrane size) with SiO_2 layer; used as control

Table 7.3: The characteristics of the devices used in the protein release experiments (see Appendix E, §E.2 and §E.3 for SEM micrographs of *b2P06S51* and *b2N07S62*, respectively).

The same procedure was used for the passive release at 37 °C. The leached PSi membrane devices were individually immersed into glass specimen bottles filled with ~ 5 mL of DI water. The bottles were placed into the water bath (set at 37 °C) and the passive release was carried out for 24 hours. After that, the specimen bottle was removed from the water bath. The device was rinsed with 1 mL of DI water with the fraction collected into the glass specimen bottle. After drying with a nitrogen gun, the PSi membrane device was inspected under a fluorescence microscope. 1 mL of the solution in the specimen bottle was collected for later analysis using the spectrofluorimetry. The devices were then placed in new, DI water-filled (~ 5 mL), glass specimen bottles and the release process was repeated for another 24 hours, but with the water bath set at 60 °C. Similarly, after 24 hours, the devices were rinsed with 1 mL of DI water, dried and inspected, while 1 mL of the solution in the specimen bottle was collected for further analysis.

7.4.1.1 Quantification of Released Protein

The concentration of FLUOS-labelled Papain, released in the passive release experiments, was expected to be very low; hence a more sensitive technique than the

UV / Vis spectrophotometry was required to determine the concentration. Hence, the spectrofluorimetry or fluorescence spectroscopy technique, based on the fluorescence emission of the conjugated FLUOS, was used.

A standard curve of fluorescence emission intensity, as a function of concentration, was first obtained. Here, the remainder of the 5-fold diluted FLUOS-labelled Papain solution, previously used in the UV / Vis spectrophotometry measurement (see §7.2.3), was used as the stock solution for a series of dilutions (up to 50 000-fold dilution). To measure the fluorescence intensity of the emission spectra, a luminescence spectrometer (PerkinElmer® LS-50B), was used. Typically, ~ 55 μL of the diluted FLUOS-labelled Papain solution was dispensed, by using a pipette, into a cleaned, 3-window, fluorescence quartz cuvette (105.254 QS, Hellma Ltd., UK). An excitation wavelength of 495 nm was used; while the emission wavelength was scanned from 505 nm to 605 nm, to obtain the fluorescence emission spectrum. The width of the excitation and emission slits was fixed at 5.0 nm and 5.5 nm, respectively. The spectrum was typically recorded at 20 °C, using the software *FL WinLab*™, at a scan speed of 50 nm·min^{-1}.

The fractions of FLUOS-labelled Papain solution, collected from the passive release experiments, were first freeze-dried and then reconstituted with 100 μL of DI water. The fluorescence emission spectrum of the concentrated FLUOS-labelled Papain was then obtained, using the same procedure and parameters as described above. The concentration of the FLUOS-labelled Papain was then deduced from the standard curve.

7.4.1.2 Spectrofluorimetry Standard Curve

For spectrofluorimetric determination of protein concentration, the area under the fluorescent emission spectrum was computed to provide the total emission intensity, using the widely-used *Simpson's rule* of numerical integration method [428]. The composite *Simpson's rule* is given as:

$$\int_{\lambda_a}^{\lambda_b} I(\lambda)\, d\lambda \approx \frac{h}{3} \cdot \left[I(\lambda_0) + 4 \cdot I(\lambda_1) + 2 \cdot I(\lambda_2) + 4 \cdot I(\lambda_3) + \cdots + 4 \cdot I(\lambda_{n-1}) + I(\lambda_n) \right] \tag{7.4}$$

where $I(\lambda)$ is the intensity curve within an interval $[\lambda_a, \lambda_b]$ which is split up to n sub-intervals, with n an even number; and $\lambda_i = \lambda_a + ih$ for $i = 0, 1, \ldots, n–1$, n with $h = (\lambda_b – \lambda_a) / n$. The area under the curve was computed for wavelengths between 510 nm and 600 nm, with 180 sub-intervals ($\lambda_0 = \lambda_a = 510$ nm, $\lambda_n = \lambda_b = 600$ nm, $n = 180$, $h = 0.5$).

The concentration of the diluted FLUOS-labelled Papain was deduced from a stock concentration of 0.218 mg·mL^{-1} (based on the baseline-corrected calculation, as discussed in §7.2.3). Based on the uncorrected emission spectra, a standard curve, as depicted in Figure 7.5, was produced. The standard curve could be best fitted with a linear fit, with a slope of 2.12 and a y-intercept of 14.81, and this was used to approximate the concentration of the FLUOS-labelled Papain released.

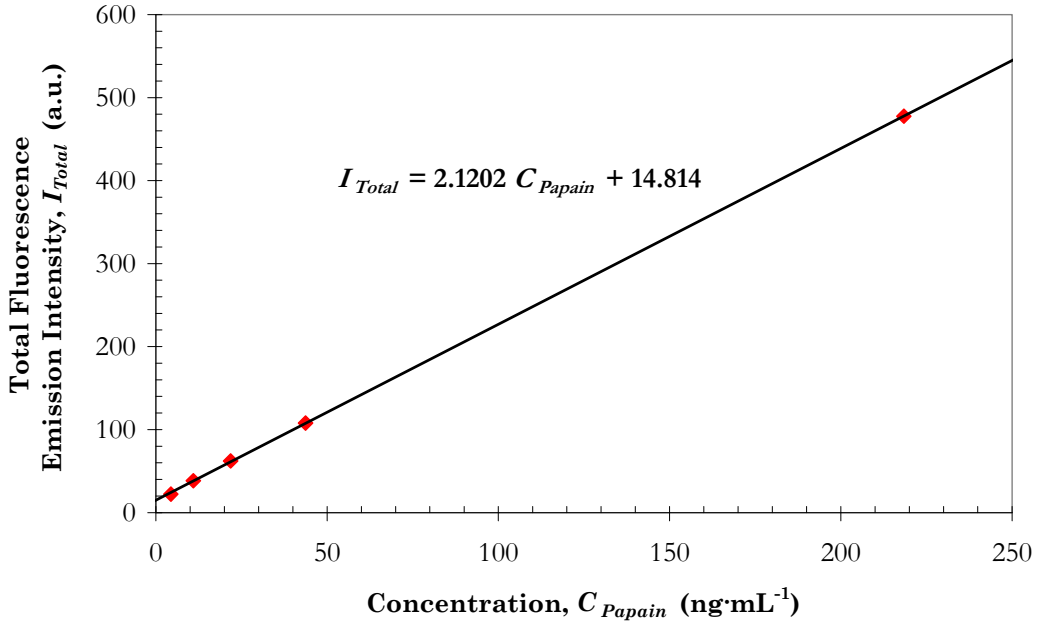

Figure 7.5: The standard curve of the fluorescence emission intensity of FLUOS-labelled Papain, of various concentrations, excited at 495 nm.

7.4.2 Passive Release of Papain

The *in vitro* passive release of the FLUOS-labelled Papain, of the three devices, was performed at 37 °C and 60 °C, over 24 hours. The fluorescence microscopy technique was used to provide a rapid, qualitative comparison and estimation of the extent of the Papain released in the experiments. Figure 7.6 depicts a series of fluorescence

microscope images of device *b2N07S62* acquired after the protein loading process, the leaching process, and the passive release at 37 °C and at 60 °C. By using the AxioVision software, the mean intensity was computed from the gray scale histogram of the acquired 14-bit raw image (16384 gray levels, 0 being lowest intensity, 16383 being the highest intensity). Figure 7.6 (a) shows a low mean intensity (241.1) due to a much shorter exposure time (of 7.2 ms compared to ~ 38 ms for others) used during the image acquisition. After the leaching process, a significant reduction in fluorescence signal was observed visually, as depicted in Figure 7.6 (b). It is therefore postulated that most of the weakly surface bound FLUOS-labelled Papain was removed by the leaching process. After the passive release at 37 °C and at 60 °C, the fluorescence microscope images, as depicted in Figure 7.6 (c) and (d) respectively, demonstrated a decrease in the mean intensity as

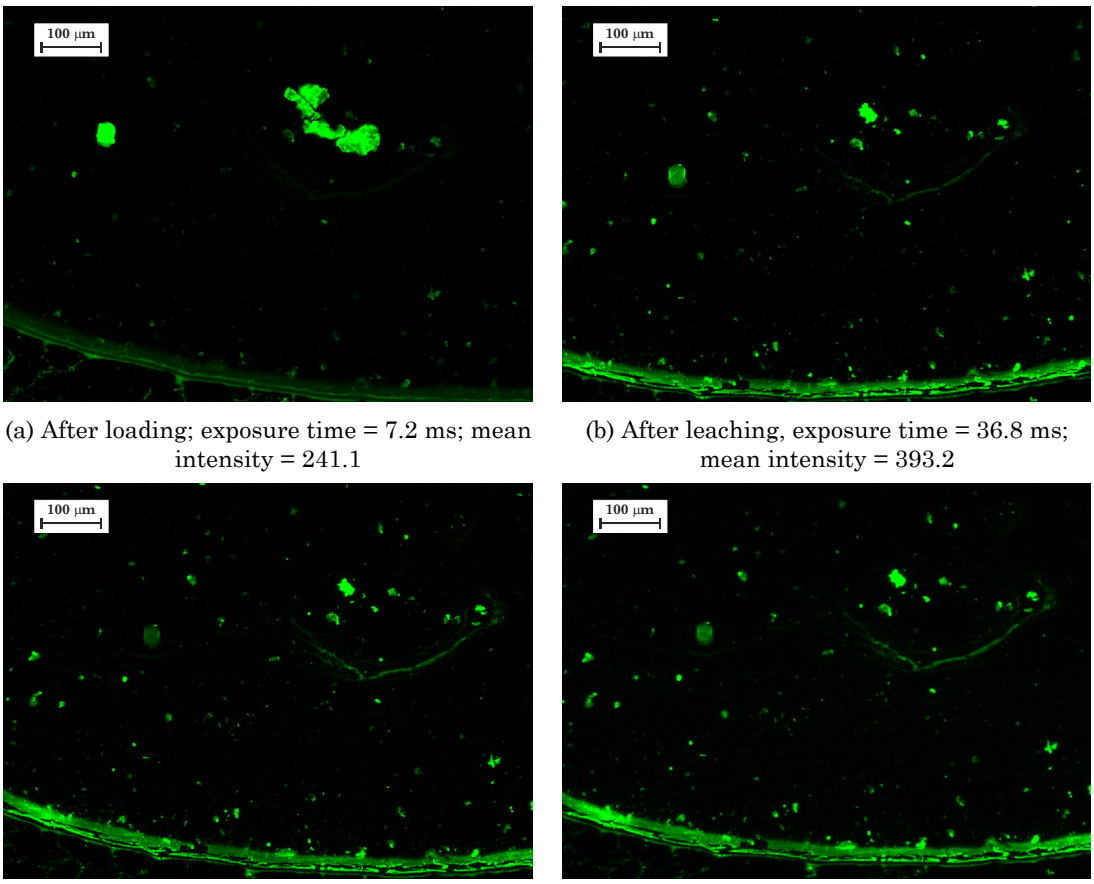

(a) After loading; exposure time = 7.2 ms; mean intensity = 241.1

(b) After leaching, exposure time = 36.8 ms; mean intensity = 393.2

(c) After release in 37 °C; exposure time = 38.8 ms; mean intensity = 245.7

(d) After release in 60 °C; exposure time = 38.8 ms; mean intensity = 207.6

Figure 7.6: Fluorescence microscope images (with false colour) of device *b2N07S62* after (a) the loading process; (b) the leaching process; (c) the passive release in 37 °C and (d) the passive release in 60 °C. The images were acquired at approximately the same area of the sample, with exposure times of (a) 7.2 ms; (b) 36.8 ms and (c) and (d) 38.8 ms.

compared to Figure 7.6 (b) (after leaching), although they appeared similar visually. The small decrease in the mean intensity suggests that a marginal amount of Papain was released during both the passive release at 37 °C and at 60 °C.

The aqueous fraction of FLUOS-labelled Papain collected from the release experiments was quantitatively determined using the spectrofluorimetry (as discussed in §7.4.1.1). A typical, uncorrected fluorescence emission spectrum, obtained using the spectrofluorimetry, is depicted in Figure 7.7. The fluorescence emission was excited at a wavelength of 495 nm, with a Stoke shift anticipated to be between 10 nm and 13 nm (emission peak around 515 nm and 518 nm). As depicted in Figure 7.7, the majority of the fraction of FLUOS-labelled Papain, from the release experiments, does not exhibit a well-defined emission peak.

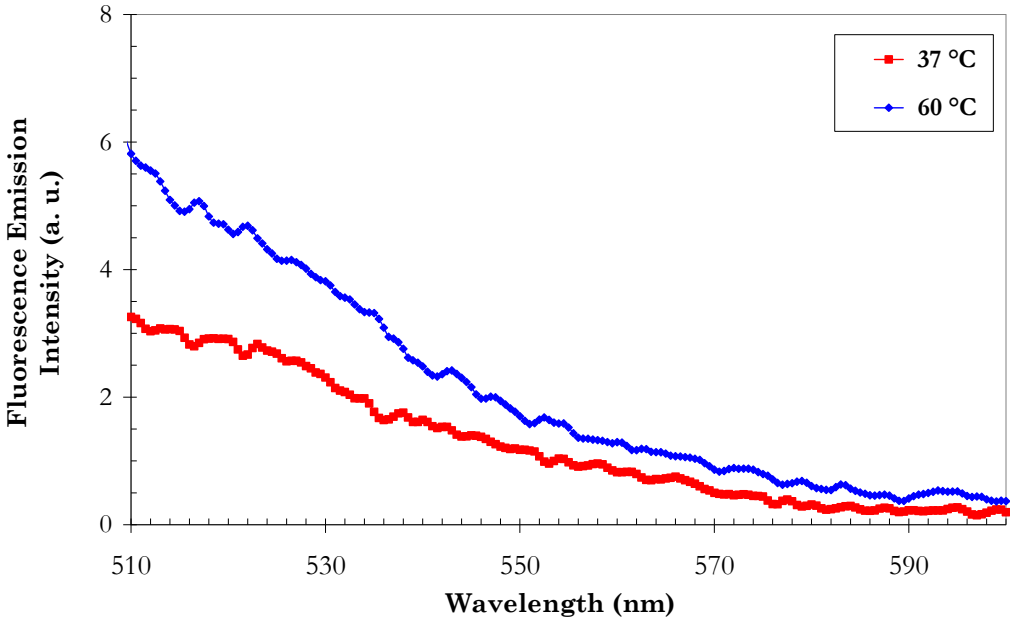

Figure 7.7: Plot of the fluorescence emission intensity against the wavelength, excited at 495 nm, of device *b2N07S62,* after the passive release experiments in 37 °C (■) and 60 °C (◆) for 24 hours.

The concentration of the released FLUOS-labelled Papain was interpolated from the standard curve depicted in Figure 7.5. The interpolated concentration was then corrected as the measurement was performed using a more concentrated fraction, obtained after reconstitution of the freeze-dried Papain. The results are summarised in Table 7.4. The absolute quantity of FLUOS-labelled Papain was then estimated, based on a total volume of 6 mL (5 mL used in the specimen bottle and 1

mL from the rinsing step), and summarised in Table 7.5. The amount of Papain released was significantly less than the estimated amount of Papain loaded into the PSi membrane. This is expected since the majority of the Papain, very likely bound to the surface of the PSi membrane, was removed during the leaching process (as depicted in Figure 7.6 (b)). However, importantly, it is clear, from both Table 7.4 and Table 7.5, that the passive release of Papain appeared to be enhanced at 60 °C, as all three devices, including the control, were found to have an increased amount of released Papain. Interestingly, the percent of Papain released (see Table 7.5), both at 37 °C and at 60 °C, from the device with nanostructured PSi (*b2P06S51* and *b2N07S51*), was relatively higher (> 5.2 %) than that obtained from the control device (< 3.5 %), which was without any PSi structure. Therefore, it is believed that the release profile from devices *b2P06S51* and *b2N07S51* are heterogeneous; Papain molecules that were bound on the surface and trapped inside the pores, both contributed to the release profile. It is postulated, based on the percent of Papain released, as summarised in Table 7.5, that the nanostructured PSi indeed enhances the release of Papain.

Device	**PSi characteristics**	**Interpolated concentration (ng·mL^{-1})**		
		At 37 °C	**At 60 °C**	**Difference**
b2P06S51	Pore width: 111 nm ± 7 nm Pore depth: 545 nm ± 32 nm (include SiO_2) Membrane size: ~ 2 mm x 4 mm	4.851	5.303	0.452
b2N07S62	Pore width: 112 nm ± 10 nm Pore depth: 340 nm ± 36 nm Membrane size: 4 mm x 4 mm	4.699	8.284	3.585
b2N07S51	Without PSi structure Membrane size: 4 mm x 4 mm	3.226	6.439	3.213

Table 7.4: The concentration (in ng·mL^{-1}) of the FLUOS-labelled Papain obtained from the passive release experiments. The concentration was interpolated from the standard curve in Figure 7.5 and divided by 10 to take into account the concentration factor.

Device	**Estimated Papain released (ng)**			**Estimated Papain loaded (ng)**
	At 37 °C	**At 60 °C**	**Difference**	
b2P06S51	29.11 (5.3 %)	31.82 (5.8 %)	2.71	545*
b2N07S62	28.20 (5.2 %)	49.71 (9.1 %)	21.51	545
b2N07S51	19.36 (1.8 %)	38.64 (3.5 %)	19.28	1090

Table 7.5: The estimated absolute quantity (in ng) of the FLUOS-labelled Papain obtained from the passive release experiments. The percent (%) released was based on the estimated Papain loaded into the device (see Table 7.3). * Device *b2P06S51* was broken during the loading process; only half of the amount loaded was assumed in the calculation.

7.5 Conclusion

The proof of concept of using the fabricated PSi membrane device, for drug delivery, was demonstrated. Fluorescently labelled model protein, Papain (*MW* = 23 406 Dalton), which has a similar molecular weight to the BMP-2 (*MW* ≈ 26 000 Dalton), was used. By using the impregnation method, with vacuum drying, the FLUOS-labelled Papain was found to be predominantly bound to the surface, as demonstrated using the combined fluorescence microscopy and SEM (see Figure 7.2 and Figure 7.3) techniques. The amount of protein loaded into the PSi membrane devices, however, could not be quantitatively determined by using these techniques; other alternative methods are needed. An improved loading strategy, perhaps by using other drying approaches or by surface functionalising the PSi structure [211, 212], may be required to optimise the loading efficacy and improve the penetration of protein into the pores.

A passive release, of the FLUOS-labelled Papain in DI water, was performed at 37 °C and at 60 °C, over 24 hours. Two interesting and promising findings were observed. Firstly, an increase in the concentration of FLUOS-labelled Papain, which was released at 60 °C, was observed in the three devices investigated (see Table 7.4 and Table 7.5). This is a useful finding as the nanostructured PSi and the Papain appeared to respond to a thermal stimulus. Secondly, the nanostructured PSi is believed to enhance the release of Papain, both at 37 °C and at 60°C. This proposal is supported based on the increase in percentage of Papain released (> 5.2 %, see Table 7.5) by the devices with PSi structure (*b2P06S51* and *b2N07S62*), as compared to the control device (< 3.5 %), which does not contain any PSi structure.

Further investigations, to establish the impact of factors such as the pH level and type of release medium, the physical properties (porosity, pore sizes and pore depths) of the PSi and the dissolution kinetic of the PSi, on the release of Papain, will enhance the understanding of the PSi membrane device for drug delivery. The next step will be to study the controlled release of protein by active release using the integrated heater of the PSi membrane drug delivery device.

Chapter 8

Conclusion and Suggestions for Future Work

8.1 Thesis Summary and Conclusion

The ability to deliver therapeutic agents, to a targeted site, in a controlled manner, is pivotal in achieving the full therapeutic potentials of many pharmaceuticals. Thus, the aim of this thesis work was to design and produce, using microfabrication technologies, a novel, integrated, electrically-addressable drug delivery device for the site-specific, controlled release of therapeutic agents. In particular, the device is designed to locally deliver bone morphogenetic protein-2 in a controlled manner, as the first step to an intelligent therapeutic system for skeletal regeneration.

Ideally, for a localised delivery, the drug delivery microdevice should be implantable. In fact, based on a literature review, implantable drug delivery microdevices with integrated electronics, such as the microchip developed by Langer and co-workers [125], stand-out as the most promising candidates to offer a personalised, responsive and controlled delivery of therapeutic agents. These microdevices are equipped with one or more micromachined physical containers as drug reservoirs, which are usually capped with biocompatible membranes [125, 130]. A major concern of such a design is the potential for dose-dumping upon device failure, especially the accidental rupture of the membrane.

A porous drug reservoir, with better entrapment and retention of the drug molecules, could address this concern. In particular, porous silicon (PSi) is a promising candidate; PSi in particulate forms has been used as a drug delivery vehicle [54, 55]. PSi is biocompatible and can be made bioinert, bioactive or biodegradable depending on its microstructural properties (such as porosity and pore morphology) [60, 61, 207]. The biodegradable PSi can be readily and safely dissolved in the human body [62], thus introducing the therapeutic agents; while bioinert PSi can rely on the desorption or diffusion of drugs into the human body. These means of passive release form the basis of a sustainable drug delivery. By incorporating an active control mechanism into a porous drug reservoir, a controlled release can be realised. Hence, a novel drug delivery system with a silicon-based porous drug reservoir and an integrated, electro-thermal actuated active control mechanism was proposed.

A prototype device based on a porous polysilicon (PPSi) drug reservoir was conceptualised by C. Kaminski [247]. In the design, a pair of electrodes was integrated into the device for electro-thermal actuation. By applying a current across the resistive PPSi drug reservoir, via the pair of electrodes, the entrapped drug could be released by Joule heating. The fabrication of the prototype device went swiftly until the formation of the PPSi structure; considerable amount of effort was put into creating a PPSi structure that is suitable as a drug reservoir.

The initial studies included fabrication of a PPSi structure using a chemical stain etching method. The stain etching method was preferred over the conventional anodisation approach due to the straight-forward implementation and relatively inexpensive experimental setup. Various volume ratios of $HF:HNO_3:H_2O$ and etching times were investigated; mixed results were obtained. By using 1.3:6:15 volume ratio of $HF:HNO_3:H_2O$, a PPSi structure, with random, branched pores of sizes estimated in the range of 30 nm to 50 nm and a porous film thickness of ~ 250 nm, was produced on a polysilicon substrate with a R_s of (28.67 ± 0.59) Ω/sq. In contrast, most samples prepared by the stain etching process, did not yield a PPSi film with distinct microstructural characteristics; hillocks, cracks and rough surfaces were observed when the produced PPSi structures were examined using SEM and AFM techniques. This study, like others [180, 225, 242, 249], demonstrated the poor reproducibility and non-uniformity of porous structure produced using the stain etching method.

The random pore structure, the self-limiting thickness of PPSi films and the lack of success in obtaining well-characterised PPSi structures formed by using the stain etching method prompted an investigation into using alternative fabrication approaches. In addition, the pore size range of 50 nm to 100 nm is deemed more suitable due to typical sizes of proteins and peptides, which are in the range of 5 nm to 20 nm [61, 228]; the protein of interest, the BMP-2, has dimensions of 7.0 nm x 3.5 nm x 3.0 nm [28].

Two alternative, novel approaches to fabricate a more orderly, reproducible PPSi structure, with sizes between 50 nm and 100 nm, were investigated. Both approaches employ the concept of using a dry etching process through a well-defined masking template. The first approach used a porous anodic alumina (PAA) film as a template. In this approach, a thick (> 7 μm) aluminium layer was first deposited on top of a polysilicon surface by thermal evaporation. A PAA film was formed by electrochemical etching (anodisation) of the aluminium layer; here, a process developed by M. E. Nasir [288], which includes electrochemical polishing and multistep anodisation, was used. Due to non-uniformity in the thickness of the deposited aluminium, an uncharacteristic anodisation behaviour was observed. As a result, most PAA films were found to have detached from the polysilicon surface after the anodisation process. In addition, some of the pores were not vertical. Although a quasi-ordered PAA film with desirable pore dimensions (pore diameter ~ 50 nm; interpore distance of ~ 100 nm) was obtained, due to the poor contact between the PAA film and the polysilicon surface, and the angled pore structure, the PAA film was considered to be non-ideal for the use as a masking template during the RIE of the polysilicon layer.

The second approach employed the nanosphere lithography (NSL) technique to create the template. Nanospheres, of 500 nm or 200 nm in diameter, were first self-assembled on top of a polysilicon substrate to form a monolayer, hexagonally close-packed array. Next, the size of the nanospheres was reduced by a RIE process, thus creating a non-close-packed nanosphere array arranged in a hexagonal lattice. A thin metal film was then deposited. Subsequent removal (lift-off) of the nanospheres thus produced a metal film with array of holes. This metal film was used as a masking template for the RIE of the polysilicon to realise the PPSi structure.

In principle, the NSL technique provides an inexpensive and practical approach for pattern generation of hexagonally-arranged holes, with tuneable diameter and spacing (or pitch size) of the holes – the initial size of the nanospheres defines the pitch size; while the size of the etched nanospheres determines the eventual diameter of the holes. In practise, however, there is a limit to the reasonable size that can be reduced; the smaller the size-reduced nanospheres, the thinner the metal mask has to be, so that the subsequent removal of nanospheres is possible. However, a thin metal mask limits the etch depth of the polysilicon using the RIE process. Therefore, a good compromise is needed; in most cases, the size of the nanospheres was not reduced (by RIE) by more than half the original size. A metal mask, with total thickness of 20 nm, was found to produce successful lift-off and yet, sufficiently robust during the RIE of the polysilicon layer.

The RIE of the polysilicon was achieved using the "black silicon" process [383]. Typically, the RIE resulted in a positively tapered etch profile. For nanospheres with initial diameter of 500 nm, a tapered PPSi structure with pore width of, for instance, 370 nm ± 30 nm and pore depth around 417 nm were achieved. Although the quasi-ordered PPSi exhibited a tapered profile, this is the first demonstration of the fabrication of PPSi with ordered pores of sizes in the macropore range of ~ 370 nm. PPSi structures, which were fabricated using metal mask formed using the 200 nm initial-sized nanospheres, typically exhibited a microneedle-like, spiked triangular pyramidal shape, as a result of lateral through-etching between the pores at the upper surface. It was proposed that by using a silicon substrate (instead of polysilicon) or with different etching tools, the geometry of the pores could be improved, so that the sidewalls are straight.

Subsequently, an improved, second generation, prototype drug delivery device, using a silicon membrane substrate, with an alternative electro-thermal actuation method, was proposed. The silicon membrane substrate consists of a nanostructured, quasi-ordered PSi drug reservoir, fabricated at the back-side of the membrane. An integrated heater and temperature sensor was designed at the front-side of the silicon membrane. It was envisaged that, by Joule heating, the heater provide a rapid increase in temperature, for a short period of time, to the PSi structure, therefore promoting the release of the loaded therapeutic agents from the pores.

A modified NSL technique, with an improved RIE of silicon using a STS LPX Pegasus system, was used to fabricate quasi-ordered, vertical, cylindrical PSi structures. Nanospheres with a mean diameter of 200 nm were used, thus resulting in the interpore distance of ~ 200 nm of the eventual PSi structures. The nanospheres were typically reduced to a diameter of 86 nm ± 3 nm by a one-minute O_2 RIE process. To improve the success of the removal of nanospheres, a 10 nm thick Cr layer and an ultrasonication time of < 60 s, were used. By exploiting the LF process and the parameter ramping feature of the STS LPX Pegasus system, PSi structures with mean pore diameters between ~ 75 nm and ~ 120 nm, and a pore depth in the range of ~ 330 nm to 500 nm, were fabricated. The theoretical porosity was calculated to be between 12.8 % and 32.6 %. The aspect ratio was found to be < 5:1; higher aspect ratios might potentially be achieved using an optimised process in the STS LPX Pegasus system. This novel nanofabrication technique is versatile and various other nanostructures, such as nanopillars (see Appendix E, §E.6) and nanowires (see Appendix E, §E.7), have been successfully fabricated. It is a "materials general" technique and has been successfully demonstrated on both p-type and n-type silicon substrates; ordered PSi with cylindrical pores in 100 nm diameter range has been difficult to achieve using conventional electrochemical etching method.

An integrated heater and temperature sensor was incorporated at the front-side of the PSi membrane device. Three configurations (meander, spiral and coil) of the heater and temperature sensor were designed and fabricated using the lift-off method. Higher than simulated peak temperatures were first observed when the meander heater was actuated with voltages from 3 V to 5 V, with heater on-times of 0.1 s to 1.0 s. This was believed to be due to a higher than desired deposited thickness of Ti and Au (hence, a reduced resistance) and the smaller than expected TCR values. A revised simulation, however, demonstrated a good agreement with the experimental result. Hence, it was proposed and verified, both by experiment and simulation, that an actuation voltage of 3 V and a heater on-time of 0.5 s was sufficient to provide a rapid local heating (up to 60 °C ± 10 °C) with minimal heat dissipation to the surrounding environment.

The proof of concept of using the fabricated PSi membrane device, for drug delivery, was demonstrated. Fluorescently labelled model protein, Papain, which has

similar molecular weight with BMP-2, was used. The FLUOS-labelled Papain was found to be predominantly bound to the surface; the amount of protein loaded into the pores of the nanostructured PSi drug reservoir could not be quantitatively determined. A passive release, of the FLUOS-labelled Papain in DI water, was performed at 37 °C and at 60 °C, over 24 hours. Two interesting and promising findings were observed – i) the nanostructured PSi and the Papain appeared to respond to a thermal stimulus since an increase in the concentration of FLUOS-labelled Papain was observed at a release temperature of 60 °C; ii) the nanostructured PSi appeared to enhance the release of Papain, both at 37 °C and at 60°C, as demonstrated by an increase in percentage of Papain released as compared to the control device (without PSi structure).

The commercially available INFUSE® Bone Graft with ACS carrier (7.5 cm x 10 cm in size), was demonstrated to accelerate open tibial fracture healing when used in a concentration of 1.50 $mg \cdot mL^{-1}$ (total dose of 12 mg) [20]. Hypothetically, the concentration of rhBMP-2 delivered, normalised to the area of the ACS carrier, amounts to 0.02 $mg \cdot mL^{-1} \cdot cm^{-2}$ (or 0.16 $mg \cdot cm^{-2}$). In comparison, the PSi membrane drug delivery device developed here, with a membrane size of 0.4 cm x 0.4 cm, is capable of passive delivery of ~ 4.7 $ng \cdot mL^{-1}$ (28.2 ng) model protein at 37 °C. The normalised concentration is calculated to be ~ 0.03 $mg \cdot mL^{-1} \cdot cm^{-2}$ (or ~ 0.18 $mg \cdot cm^{-2}$); this is comparable to the delivery capacity of the ACS carrier. However, the PSi membrane device is potentially capable of an active, controlled release, which is lacking in the ACS carrier.

The proof-of-concept prototype drug delivery microchip device developed by Langer and co-workers was demonstrated to produce a pulsatile controlled release of microgram quantities of either single or multiple substances [125]. However, in order to provide a sustained release, the microchip has to be operated periodically; each of the drug reservoirs has to be actuated to maintain the plasma concentration. In contrast, the PSi membrane device developed here was designed to provide the sustained delivery by passive release. The active control mechanism could potentially be used as a bolus dose, when a higher concentration of therapeutic agents is required, thus realising the pulsatile controlled release. This, unlike the Langer's device where the delivery of therapeutic agents has to be actuated, is a much safer strategy as the active control mechanism is only used when required;

issue of dose-dumping upon device failure (which could occur in Langer's device) is of a lesser risk. The microchip by Langer was able to release multiple substances (due to individual loading of substances into each reservoir); this feature may be difficult to achieve with the current PSi membrane device developed here.

In summary, it has been demonstrated that the NSL technique and an improved RIE process using the STS LPX Pegasus system can be used to fabricate a quasi-ordered PSi structure with cylindrical pores of ~ 100 nm in diameter. By incorporating the nanostructured PSi as a drug reservoir and an integrated heater and temperature sensor as an active control mechanism, a drug delivery device was realised. A passive release of an intermediate-sized model protein was demonstrated using the microdevice, and preliminary results suggested that an increment in release quantity was achieved by using the nanostructured PSi drug reservoir.

8.2 Suggestions for Future Work

The aim of the research is to fabricate an electrically-addressable drug delivery device; it is desirable to demonstrate the potential of this technology in skeletal regeneration, by using the BMP-2. This thesis has demonstrated the potential benefit of incorporating a PSi structure for the delivery of a model protein by passive desorption. Thus, the logical next step would be to demonstrate the full potential of the designed device by releasing the model protein using the active control mechanism. The integrated heater can be actuated periodically and the released protein can be monitored and quantified. These measurements can be compared with a device (as the control) operating under passive release condition. Subsequently, upon successful demonstration of the functionality of the PSi membrane drug delivery device, the actual BMP-2 can be used in conjunction with human mesenchymal stem cell, to demonstrate and optimise the use of the device, both by the passive release and active control mechanism.

Currently, the driver circuit was designed to actuate the heater by passing a current (with an applied voltage) in a specific time frame. The heat generated, hence the resultant temperature, was therefore not modulated. Alternatively, a feedback

control with a simple proportional-integral-derivative (PID) and a comparator circuit can be devised to modulate the temperature; this ensures the heater is actuated to produce the required temperature within the time limit. The electrical connection of the heater and the temperature sensor, to the external world, could also be improved by using wire bonding to a custom-made dual in-line package.

An improved loading strategy is desirable to enhance the penetration of protein into the pores of the nanostructured PSi drug reservoir of the devices fabricated during this thesis. Other drying approaches, such as freeze-drying or supercritical drying, can be employed. Alternatively, by surface functionalisation of PSi structure [211, 212], the pores can be chemically modified to provide a suitable covalent attachment of the therapeutic agents. The quantification of drug loaded into the pores remains a challenge; a combination of analytical techniques may be required instead. Thermal analysis methods (such as thermogravimetry [429] and different scanning calorimetry [70, 429]), helium pycnometry [54] and N_2 adsorption / desorption methods [54], have been used to investigate the loading of model drugs into PSi microparticles, and can be potentially used here. Other techniques such as secondary-ions mass spectrometry (SIMS) can be used to provide qualitative determination of protein within the pores, by examining the cross-section of the PSi structure, as demonstrated by Prestidge *et al.* [216].

This thesis work investigated the microstructural characteristics, primarily using the SEM, of the fabricated PPSi and PSi structures extensively. Based on the dimensions and theoretical porosity determined from these investigations, and a comparison to the literature [61, 208], the ordered PPSi and PSi structures could be bioinert. Therefore, it is desirable to experimentally establish the bioactivity and biocompatibility of these fabricated structures. In particular, the dissolution (or non-dissolution) of these structures in the simulated body fluids, under an electro-thermal stimulus from the integrated heater, could be an interesting investigation which can enhance the understanding of the drug release by these structures.

The most studied property of PPSi and PSi is its photoluminescent behaviour [134, 145, 158, 176, 178-189] due to a great interest in integrating PSi and PPSi into optoelectronics devices. Hence, it would be very interesting to also interrogate the optical properties of the fabricated ordered PPSi and PSi structure with respect to

conventionally fabricated PPSi and PSi structures. Temperature and power dependent PL and EL measurement, and reflectance and light scattering measurements using integrating sphere are two examples of many possible optical interrogations; findings from these optical characterisation will provide more insight into the potential of these ordered porous structures in the application of optoelectronics and as an anti-reflective layer for solar cell applications.

The PSi membrane drug delivery device was fabricated satisfactorily; however, there is plenty of room for improvement. Three possible improvements to the current fabrication process are identified here. Firstly, the fabrication of the silicon membrane using TMAH timed-etch was not ideal. The timed-etch requires that the etch depth is measured, intermittently, during the etching process to estimated an etch rate and hence the total etch time needed; this is only feasible if the initial thickness of the wafer is known. Alternatively, an *in-situ* optical monitoring [385, 386] can be used to control the etching. A boron-doped layer can also be used as an etch stop or a SOI wafer can be used since the insulator layer readily providing the etch stop. Some fabrication issues were experienced post-TMAH etch, which were believed to be caused by the cracking or pinholes on the fabricated silicon membrane. It was proposed that these undesirable cracking and pinholes were a result of the failure of the SiO_2-Si_3N_4 masking layers, both at the front- and back-side of the wafers. Therefore, it is imperative that a good working practice is maintained to ensure the integrity of these masking layers during standard wafer handling processes. Thicker SiO_2-Si_3N_4 layers can also be used to provide better protection during the TMAH etching.

Secondly, the RIE using STS LPX Pegasus system produced PSi structures with mean pore diameters between ~ 75 nm and ~ 120 nm and a pore depth in the range of ~ 330 nm to 500 nm; the aspect ratio was < 5:1. In order to improve the retention capability, pores with higher aspect ratio will be ideal. The RIE process could be optimised to achieve that. Longer total process times can be used to increase the etch depth, hence the aspect ratio. In addition, when using the LF process, the pulsing generator feature can be explored; this feature was not used in the current fabrication process. A pulsing generator switches the platen on and off during the etch cycle, hence reducing the notching effect typically observed when etching SOI wafers. Thus it is proposed to explore the potential benefit of using a pulsing

generator, during the LF process, to improve the etch depth and the aspect ratio of the PSi structure.

Lastly, the lift-off process to realise the integrated heater and temperature sensor can be better performed using alternative approaches. In the current fabrication process, the lift-off was performed using a thick photoresist with a subsequent surface modification step to provide the required undercut. However, a positive taper profile with shallow undercut was often obtained. Although a successful lift-off was demonstrated (in most samples), the fabricated heater and temperature sensor exhibited a curved edge that followed the taper profile of the photoresist. Therefore, alternative lift-off strategies can be used to provide a better undercut profile. These include using a bi-layer photoresist process, which uses a dedicated lift-off photoresist (such as MicroChem's PMGI or LOR 10B) as a sacrificial layer, and a standard pattern-generation photoresist on top. The dedicated lift-off photoresist dissolves faster in the developer, hence creating an overhang with good undercut. An image reversal process [42] is also frequently used to change the taper profile (typically observed in positive tone photoresist) into an undercut profile that is suitable for lift-off process.

The work presented in this thesis provides the basis for many exciting applications. In drug delivery, the PSi membrane device can be further developed to incorporate appropriate sensors, integrated electronics and non-biofouling packaging, and thus potentially realising an implantable, responsive and controlled release drug delivery system. The quasi-ordered PSi, fabricated using the NSL technique and Bosch-based RIE process, is uniquely interesting; its application could potentially be extended to include, for instance, bio-sensing, tissue engineering and optoelectronics.

Appendix A

Process Listings

A.1 Batch K2714s – Intelligent Drug Delivery Device

Running k2714s

	1	2	3	4	5	6	ID	Description	Count
1	☑						P-EM	E-BEAM Mask/Reticle Writing	0
2	☑						G-S1	* Title Page: 20 wafers, MATERIAL:Si p-type #1-12, Si n-type #13-16,+4 n-type checkwafers	20
3	☑						G-1P	Lithography Notes	0
4	☑						G-1	Notebook page	0
5	☑						W-C1	* RCA clean	20
6	☑						F4-W	* Wet oxidation; 600nm+-20nm, 1100degC, IdO2,rmpO2,x'wetO2,unldN2	20
7	☑						LP-0	* Blank sheet for LPCVD PSi. PolySi deposition: 1000nm+-25nm at 610 degC SiH4 10nm/min	20
8	☑						IB-0	* Implant B+: 5e15 B+ 80keV #1-4 +checkwf 1	5
9	☑						IB-0	* Implant B+: 1e16 B+ 80keV #5-8 +checkwf 2	5
10	☑						IB-50	* Implant Boron: 5E14 B+ 50 KeV #9-12 +checkwf3	5
11	☑						IP-80	* Implant Phos+: 1.8E12 P+ 100KeV #13-16 +checkwf4	5
12	☑						W-C1	* RCA clean	20
13	☑						LO-3(	* LTO deposition: 300nm +- 30nm at 400degC SiH4 and O2	20
14	☑						F10-0	Phosphorus Drive-In in N2: 200min,1150degC	20
15	☑						WH-7	Strip all SiO2 from wafer: 7:1 BHF 25degC, 4 Checkwafers	4
16	☑						X-R1	Measure polysilicon sheet resistance on 4 Checkwafers.	4
17	☑						LN-1	* Deposit Si3N4 130nm+-20nm @ 740degC DCS:NH4 1:4, 2.3nm/m.	16
18	☑						P-G1	* Photolith mask KB35M, dark Field: nom. 1.1um resist STANDARD	16
19	☑						P-RH	* Hardbake for dry etch	16
20	☐						D-N1	Etch Si3N4. Anisot. D/F EBMF/OPTICAL resist OPT80+ CHF3+Ar	-2
21	☐						D-01	Etch SiO2 . (300nm) Anisot. For D/F EBMF/OPTICAL resist OPT80+ CHF3+Ar	0
22	☐						P-RS	* Resist strip	0
23	☐						W-C2	* Fuming Nitric acid clean	0
24	☐						WS-0	stain etching in HF:HNO3:H20 (4:1:5) ; (same as batch k2618dt)	0
25	☐						P-G1	* Photolith mask KB35M, dark Field: nom. 1.1um resist STANDARD	0
26	☐						P-GL	* PMGI Lift-off Hardbake + Descum	0
27	☐						ME-A	Evaporate pure Al 1000nm +- 100nm	0
28	☐						P-GL	* LIFT-OFF metal (PMGI process)	0

A.2 Silicon Membrane Device (at Chalmers University of Technology)

No	Description	Count
1	Mask Writing (3 x 7" + 2 x 5" Mask Plates)	5
2	Title Page: Total 13 Wafers, Materials: Si Prime, DSP with Primary flat in accordance to SEMI standard. All wafers 150 mm dia., 525 µm ± 15 µm thick and in <100> orientation. Wafers breakdown: SIX Si p-type, Boron, (1 - 10) Ωcm, *#P01 - P06* SIX Si n-type, Phosphorus, (1 - 10) Ωcm, *#N07 - N12* ONE TEST WAFER Si p-type, Boron, (1 - 10) Ωcm, *#T01*	13
3	RCA Clean (SC1 & SC2)	13
4	Dry Oxide 40 nm ± 5 nm (FRONT & BACK)	13
5	LPCVD Si_3N_4 160 nm ± 20 nm @ 770°C (Stoichiometric Standard Recipe) (FRONT & BACK)	13
	*** START OF TEST WAFER (*Evaluation of Al for PAA Template*) ***	
6	Photolithography Mask *UoS-TM-CFC-M2* (FRONT) - *#T01* Dark Field: nom. 1.1 µm resist STANDARD [Align to flat] USE SOFT CONTACT TO MINIMISE DAMAGE TO PHOTORESIST	1
7	Hardbake for dry etch (FRONT) - *#T01*	1
8	General Inspection - *#T01* Inspect photolithography quality - resolution on alignment marks, for any damage to resist in large patterned areas	1
9	Etch nom. 160 nm Si_3N_4 Aniso. D/F OPTICAL resists, $CF_4 + O_2$ plus short over etch (FRONT) - *#T01*	1
10	Etch nom. 40 nm SiO_2 Aniso. D/F OPTICAL resists, $CF_4 + O_2$ plus short over etch (FRONT) - *#T01*	1
11	Resist Strip Plasma O_2 in the same chamber (FRONT) - *#T01*	1
12	Al Sputter 4 µm with Ar Plasma clean to remove native oxide (FRONT) - *#T01*	1
13	Etch nom. 160 nm Si_3N_4 Aniso. D/F OPTICAL resists, $CF_4 + O_2$ plus short over etch (BACK) - *#T01*	1
14	Etch nom. 40 nm SiO_2 Aniso. D/F OPTICAL resists, $CF_4 + O_2$ plus short over etch (BACK) - *#T01*	1
15	Ti / Au Sputter 10 nm / 300 nm (BACK) - *#T01*	1
16	Spin resist for protection (FRONT) - *#T01*	1
17	Saw into 10 mm x 10 mm chips [follow the scribe line created with M2] - *#T01*	1
18	Optical inspections for surface smoothness and adhesion quality of Sputtered Al film	1

19	Send to Southampton for External Processing	1
	*** END OF TEST WAFER *** Processing continues with Device Wafers (*#P01-P06* & *#N07-N12*)	
20	Photolithography Mask *UoS-TM-CFC-M1* (BACK) Dark Field: nom. 1.1 µm resist STANDARD [Right reading on "Align to flat", wrong reading on Mask ID] USE SOFT CONTACT TO MINIMISE DAMAGE TO PHOTORESIST	12
21	Hardbake for dry etch (BACK)	12
22	General Inspection Inspect photolithography quality - resolution on alignment marks, for any damage to resist in large patterned areas	12
23	Etch nom. 160 nm Si_3N_4 Aniso. D/F OPTICAL resists, $CF_4 + O_2$ plus short over etch (BACK)	12
24	Etch nom. 40 nm SiO_2 Aniso. D/F OPTICAL resists, $CF_4 + O_2$ plus short over etch (BACK)	12
25	Resist Strip Plasma O_2 in the same chamber (BACK)	12
	*** START OF DEVELOPMENT WAFER ***	
26	TMAH Etch. Timed-etch (etch and measure) to achieve membrane thickness of 50 µm (BACK)	1
27	Ti / Au Sputter 10 nm / 300 nm (BACK)	1
28	Photolithography Mask *UoS-TM-CFC-M2* (FRONT) Dark Field: nom. 1.1 µm resist STANDARD [Mask reads "Right Side Up"; Captured image reads "Wrong Side Up"] USE HARD CONTACT / LOW VAC for Double-sided alignment	1
29	Hardbake for dry etch (FRONT)	1
30	General Inspection (FRONT) Inspect photolithography quality - resolution on alignment marks, for any damage to resist in large patterned areas	1
31	Etch nom. 160 nm Si_3N_4 Aniso. D/F OPTICAL resists, $CF_4 + O_2$ plus short over etch (FRONT)	1
32	Etch nom. 40nm SiO_2 Aniso. D/F OPTICAL resists, $CF_4 + O_2$ plus short over etch (FRONT)	1
33	Photoresist Strip with Plasma O_2 in the same chamber (FRONT)	1
34	Spin resist for protection (FRONT)	1
35	Saw into Chips	1
36	Send to Southampton for External Processing	1
	*** END OF DEVELOPMENT WAFER *** Processing continues with Device Wafers	
37	TMAH Etch. Timed-etch based on development of Step 26 to achieve membrane thickness of 50 µm (BACK)	11

38	Photolithography Mask *UoS-TM-CFC-M2* (FRONT) Dark Field: nom. 1.1 µm resist STANDARD [Mask reads "Right Side Up"; Captured image reads "Wrong Side Up"] USE HARD CONTACT / LOW VAC for Double-sided alignment	11
39	Hardbake for dry etch (FRONT)	11
40	General Inspection (FRONT) Inspect photolithography quality - resolution on alignment marks, for any damage to resist in large patterned areas	11
41	Etch nom. 160 nm Si_3N_4 Aniso. D/F OPTICAL resists, CF_4 + O_2 plus short over etch (FRONT)	11
42	Etch nom. 40 nm SiO_2 Aniso. D/F OPTICAL resists, CF_4 + O_2 plus short over etch (FRONT)	11
43	Photoresist Strip with Plasma O_2 in the same chamber (FRONT)	11
	*** START OF SPLIT BATCH (*for PAA Template*) (*#P04-P06* & *#N07-N09*) ***	
44	Ti / Au Sputter 10 nm / 300 nm (BACK)	6
45	Aluminium Sputter 4 µm with Ar Plasma clean to remove native oxide (FRONT)	6
46	Spin photoresist for protection (BACK)	6
47	Photolithography Mask *UoS-TM-CFC-M3* (FRONT) Dark Field: nom. 2.2 µm resist STANDARD USE SOFT CONTACT TO MINIMISE DAMAGE TO PHOTORESIST	6
48	Postbake for wet etch (FRONT)	6
49	General Inspection (FRONT) Inspect photolithography quality - for any defects or pin-holes on resist in device areas	6
50	Aluminium Wet Etch to reveal scribe lines	6
	*** END OF SPLIT BATCH ***	
51	Spin resist for protection (FRONT)	11
52	Saw into Chips	11
53	Completion of Listing / Section Send wafers to Southampton for processing	11

Appendix B

Mask Layouts

B.1 Batch K2714s – Intelligent Drug Delivery Device

B.1.1 Mask 1 – *KB35M-AA*

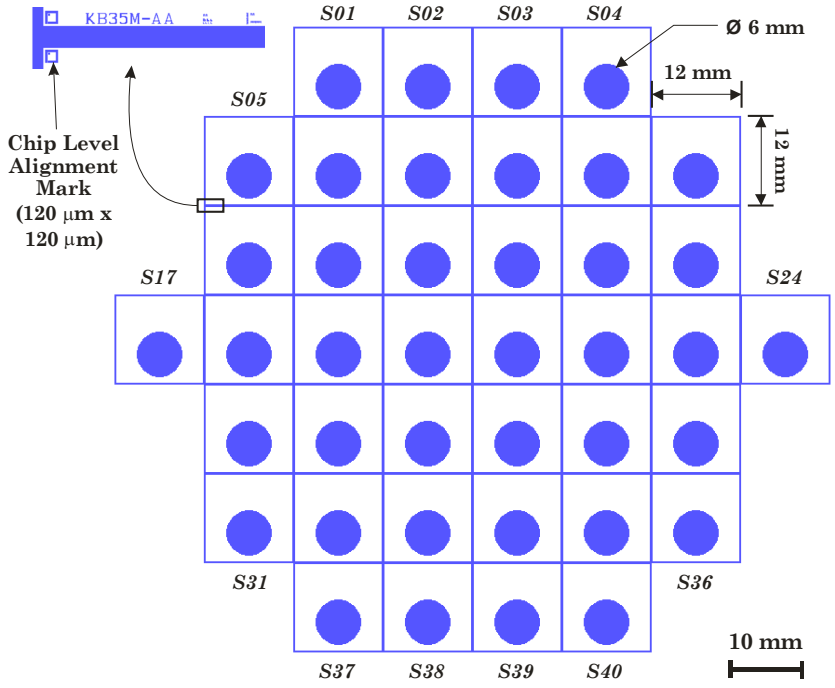

Figure B.1: Layout of mask *KB35M-AA*, showing the 6 mm diameter circular region, which defines the area for the fabrication of porous polysilicon. The samples were denoted by *Sxx*, where *xx* is their positions on the wafer, assumed from left to right and top to bottom.

B.1.2 Mask 2 – *KB35M-M1*

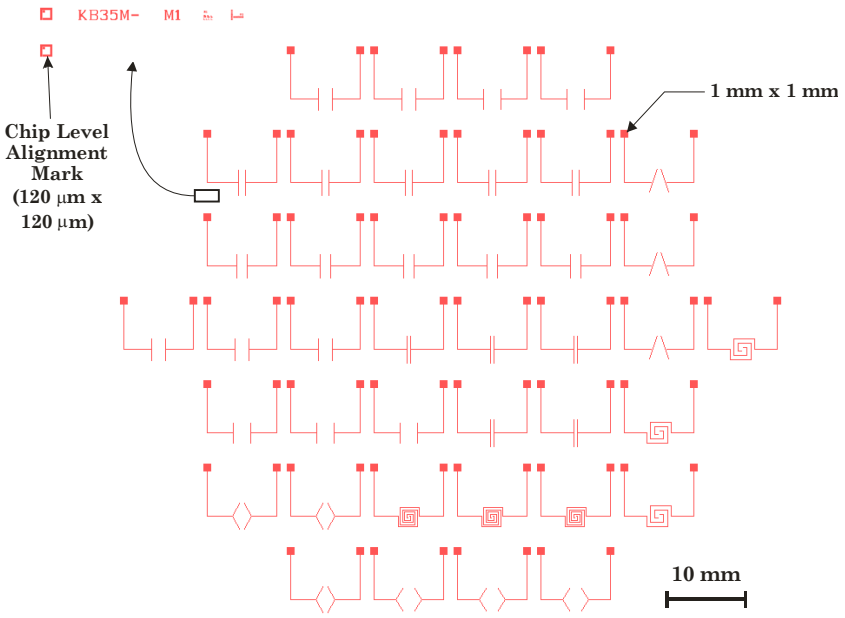

Figure B.2: Layout of mask *KB35M-M1*, showing the various patterns of the electrodes.

B.1.3 Revised Mask 2

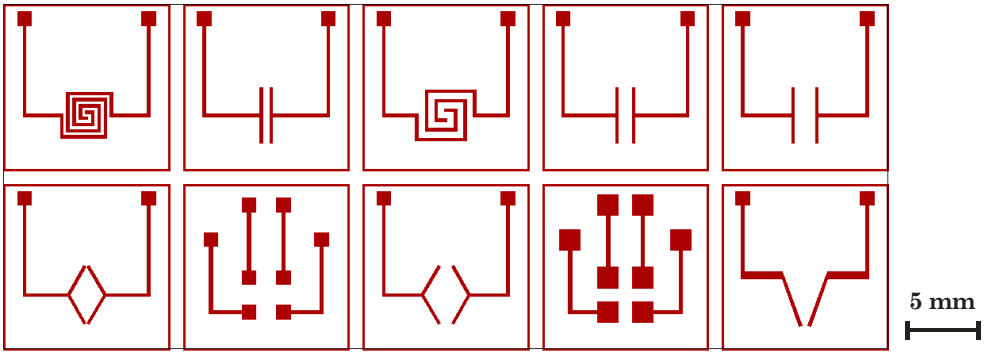

Figure B.3: Layout of the revised, 3-inch emulsion mask (of *KB35M-M1*), used for the lift-off development in University of Manchester.

B.2 Porous Silicon Membrane Drug Delivery Device

B.2.1 Mask 1 – *UoS-TM-CFC-M1*

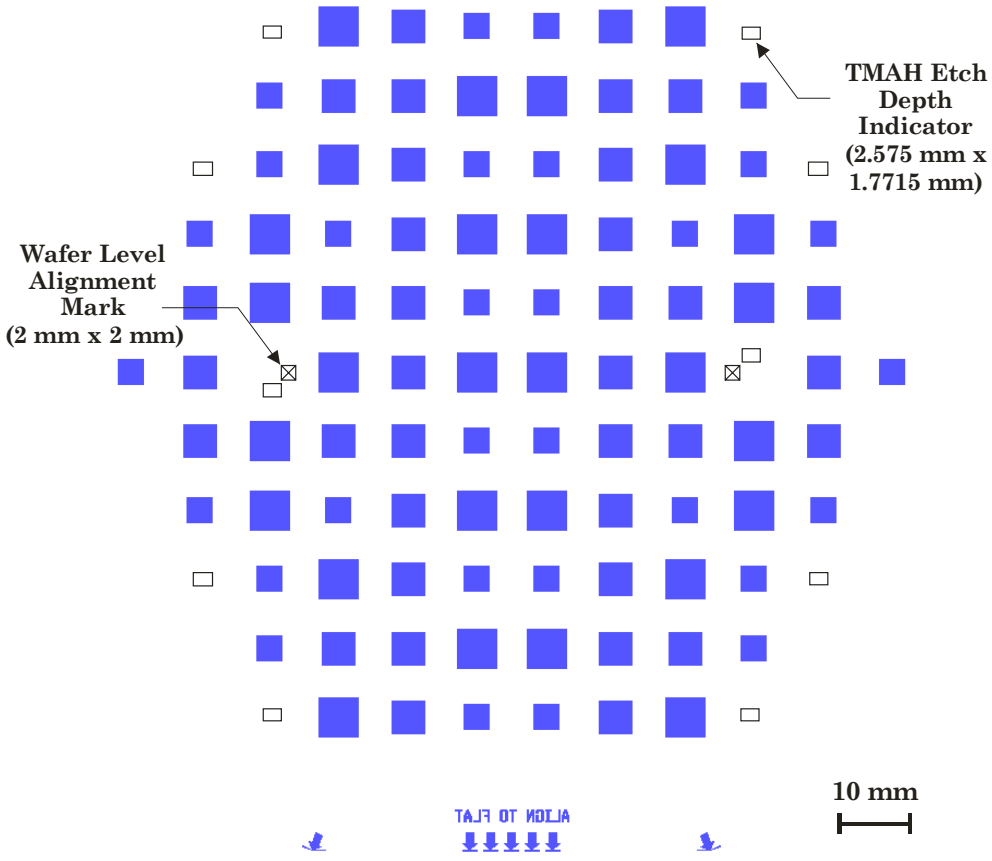

Figure B.4: Layout of mask *UoS-TM-CFC-M1*, which defines the opening for TMAH etch, to realise the silicon membranes, at the back-side of the wafers.

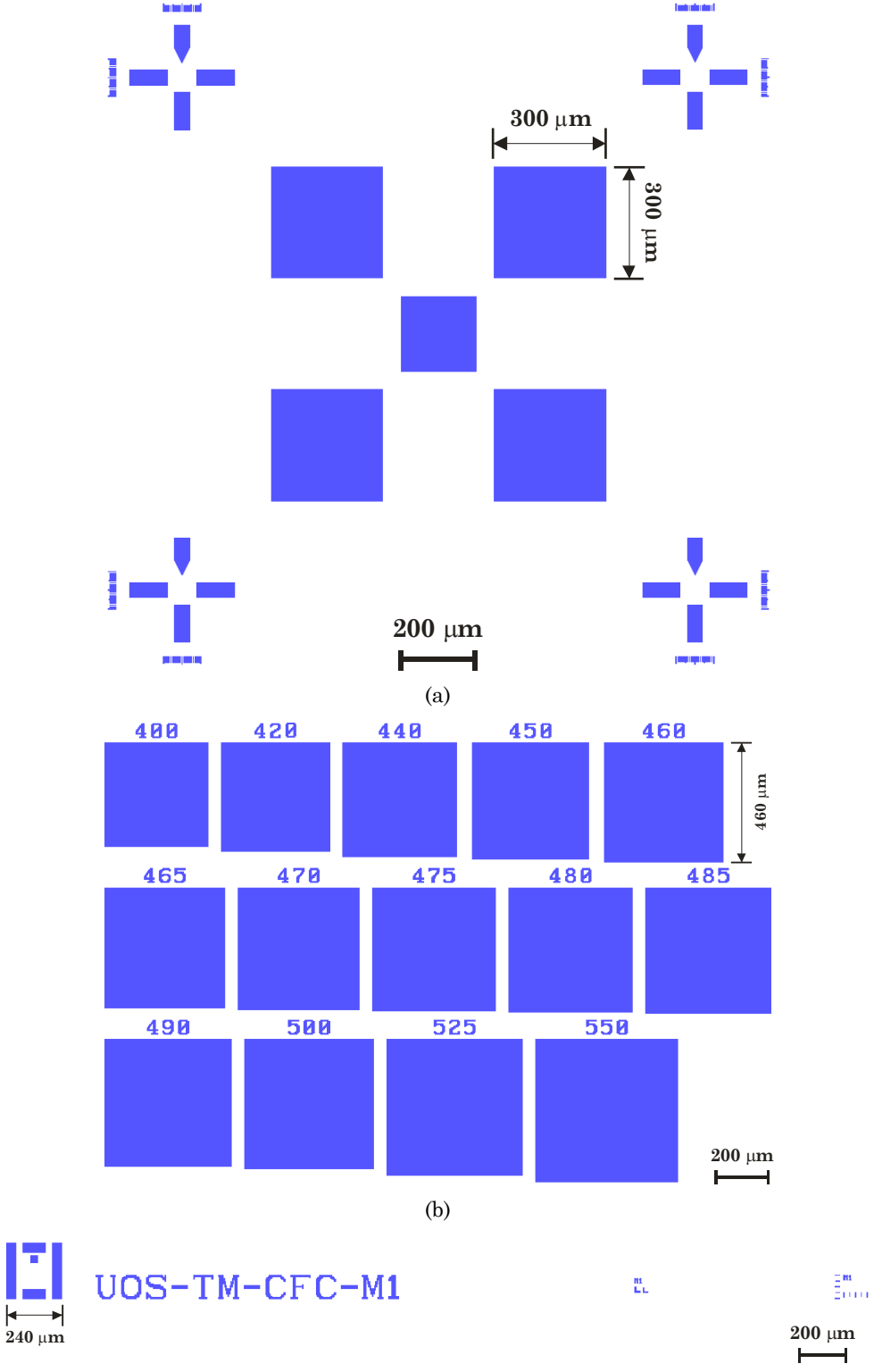

Figure B.5: Detailed layout of mask *UoS-TM-CFC-M1*, showing (a) the wafer level alignment mark; (b) the TMAH etch-depth indicator; and (c) the chip level alignment mark and identification.

B.2.2 Mask 2 – *UoS-TM-CFC-M2*

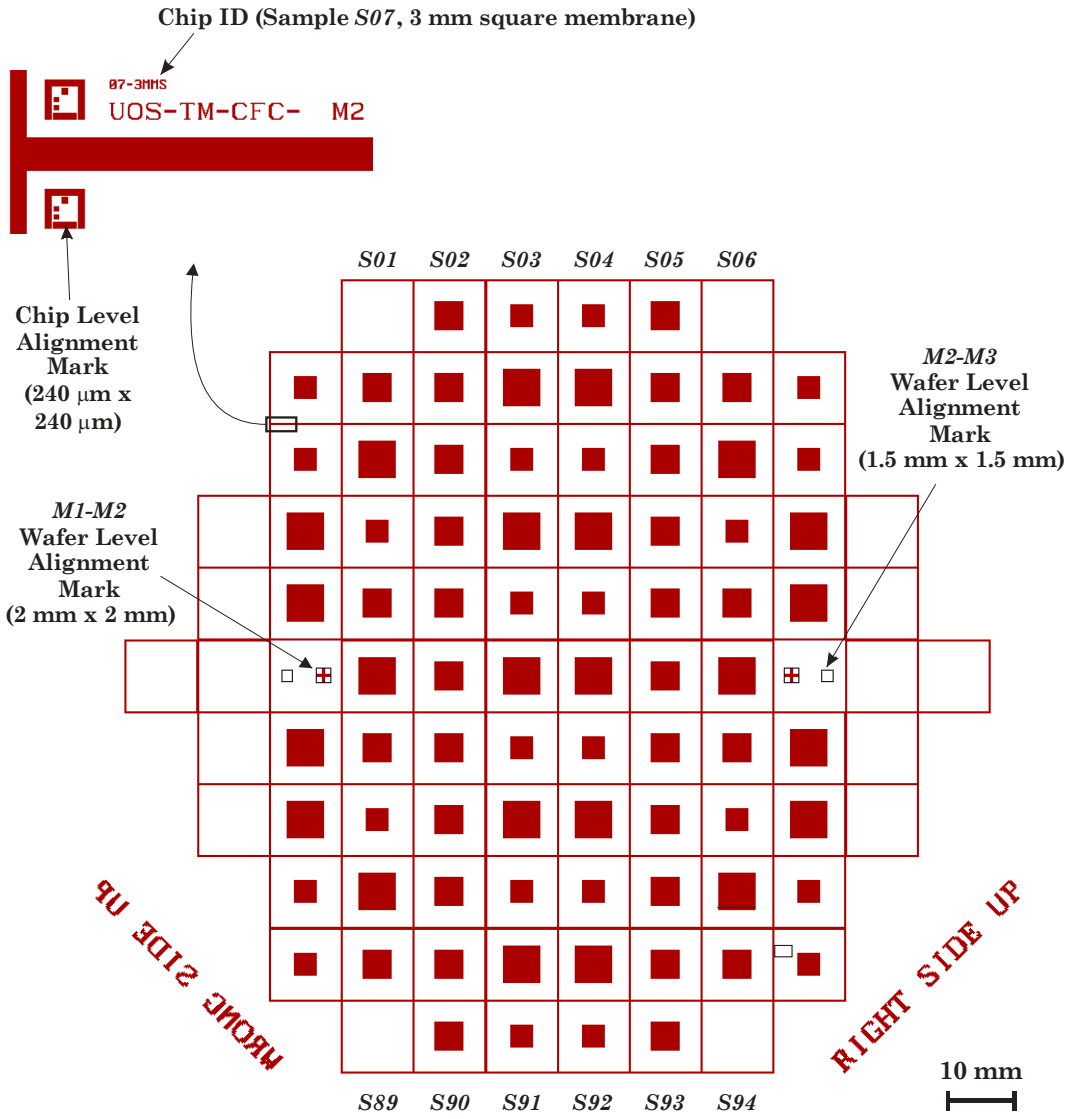

Figure B.6: Layout of mask *UoS-TM-CFC-M2*, which defines the sawing tracks and opening of the front membrane, intended for the formation of PAA. The samples were denoted by *Sxx*, where *xx* is their positions on the wafer, assumed from left to right and top to bottom.

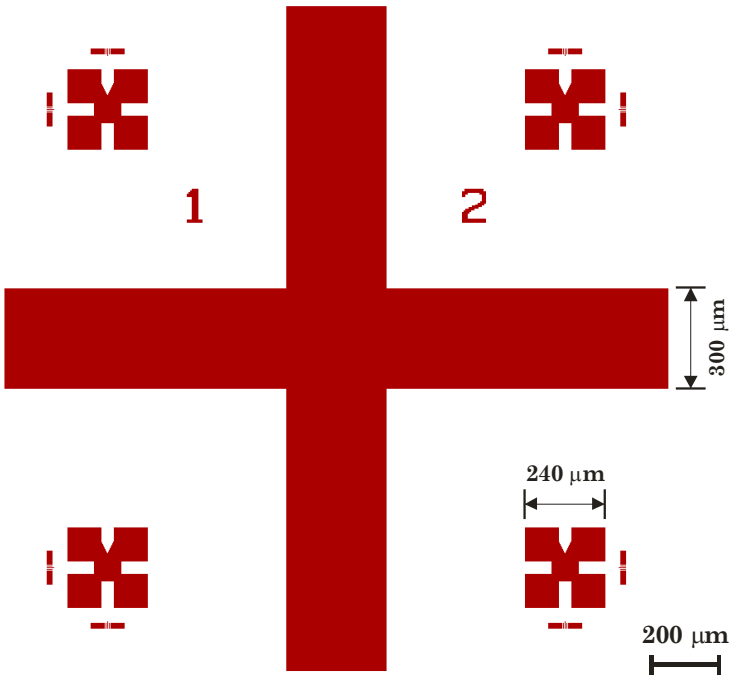

(a)

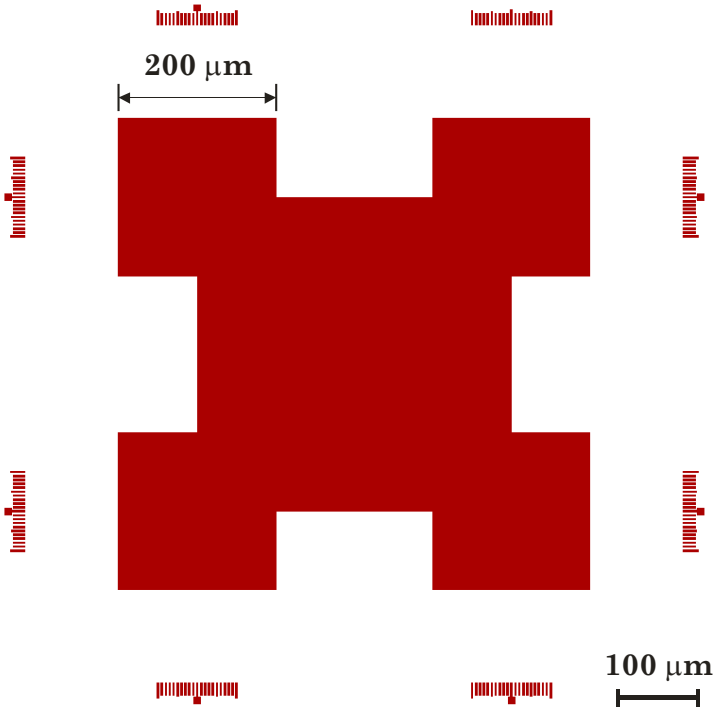

(b)

Figure B.7: Detailed layout of mask *UoS-TM-CFC-M2*, showing (a) the *M1* to *M2*; and (b) *M2* to *M3*, wafer level alignment marks.

B.2.3 Mask 3 – *UoS-TM-CFC-M3*

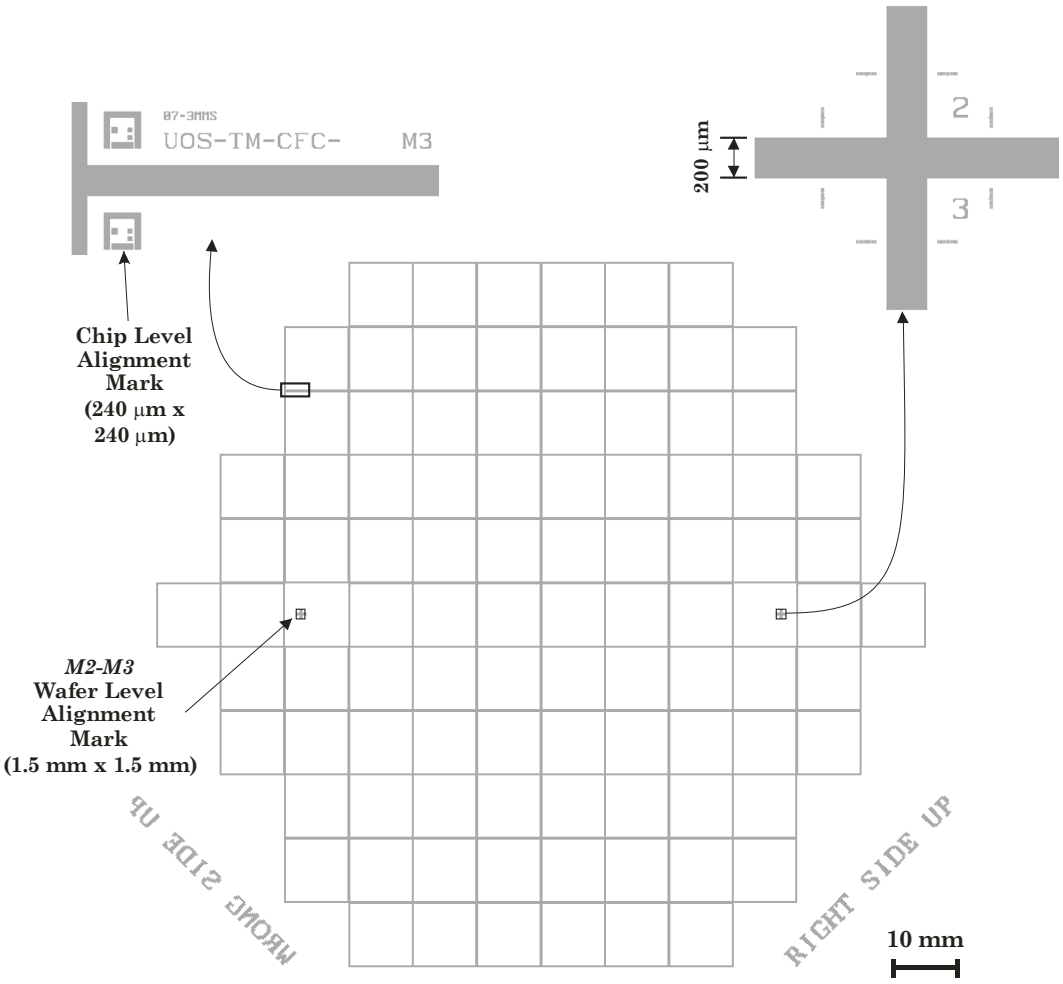

Figure B.8: Layout of mask *UoS-TM-CFC-M3*, which defines the sawing tracks for the wet chemical etching of aluminium.

B.2.4 Mask 4 – *UoS-TM-CFC-M4*

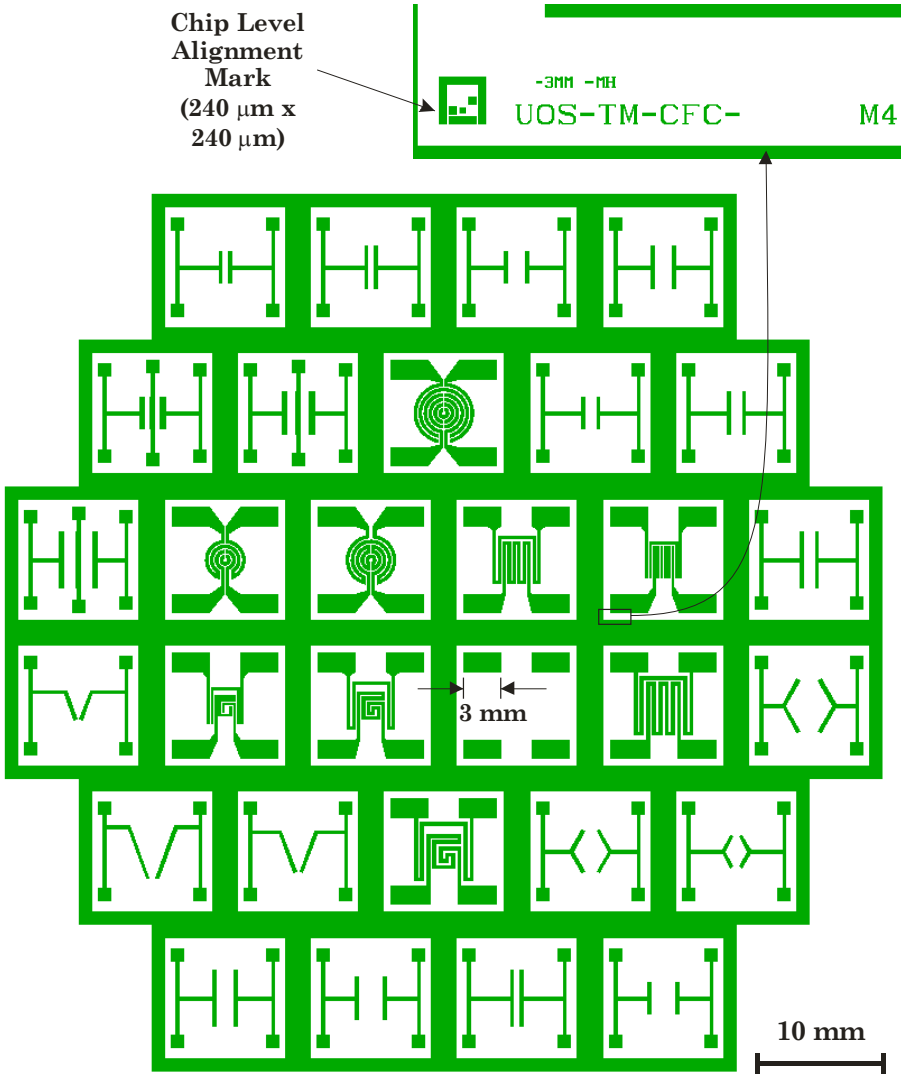

Figure B.9: Layout of mask *UoS-TM-CFC-M4*, which defines the various electrode designs and the integrated heater and temperature sensor designs.

Appendix C

Process Simulation – Example Input File used in *Athena*

C.1 Simulation with Boron Implantation of 5 x 10^{15} cm^{-2} and Energy of 80 keV

```
# ------------------------------------------------------------  #
# Filename    : k2714s_01.in                                    #
# Description : Process simulation of batch K2714s Wafer 1-4    #
# Author      : C. F. Chau (cfc03r@ecs.soton.ac.uk)             #
# Created     : 31 March 2006                                   #
# Comment     : Using SIMS Verified Dual Pearson (SVDP)         #
#               ion implantation model                          #
# ------------------------------------------------------------  #

go athena

set prefix=k2714s_01
set cutline=0.5

set implant_dose=5e15
set implant_eneg=80
set poly_thick=1.0


# Establish the grid locations and densities
# ------------------------------------------
line x loc=0.00 spac=0.05
line x loc=0.50 spac=0.01
```

```
line x loc=1.00 spac=0.05

line y loc=0.00 spac=0.01
line y loc=0.50 spac=0.05
line y loc=1.00 spac=0.1
line y loc=2.00 spac=0.5

# Initialize the silicon wafer
# ----------------------------
init silicon boron resistivity=25 orientation=100 two.d

# Grow pad oxide layer
# --------------------
method fermi grid.oxide=0.05

diffuse time=15 temp=750 t.final=1000 dryo2 press=1.0 hcl.pc=0.0
diffuse time=105 temp=1000 weto2 press=1.0 hcl.pc=0.0
diffuse time=30 temp=1000 t.final=750 nitrogen press=1.0 hcl.pc=0.0

extract name="Pad Oxide Thickness" thickness material="SiO~2" \
       mat.occno=1 x.val=$cutline datafile="k2714s_01_para.dat"

# LPCVD Polysilicon
# -----------------
deposit polysilicon thick=$poly_thick div=20

extract name="Polysilicon Thickness" thickness material="Polysilicon" \
       mat.occno=1 x.val=$cutline datafile="k2714s_01_para.dat"

# Dope Polysilicon with Ion Implantation
# --------------------------------------
implant boron dose=$implant_dose energy=$implant_eneg tilt=0 rotation=0 \
       amorph unit.damage dam.factor=1.0

struct outfile=$"prefix"_implant.str
extract name="Simulated_dose" area from curve(depth, impurity="Boron" \
        material="Polysilicon" mat.occno=1 x.val=$cutline)*1e-4 \
       datafile="k2714s_01_para.dat"
extract name="Percent diff" abs($Simulated_dose - $implant_dose)*\
       100/$implant_dose datafile="k2714s_01_para.dat"
extract name="Surface Conc after Implant" surf.conc impurity="Net Doping" \
       material="Polysilicon" mat.occno=1 x.val=$cutline \
       datafile="k2714s_01_para.dat"
extract name="Sheet_Res_after_implant" sheet.res material="Polysilicon" \
       mat.occno=1 x.val=$cutline semi.poly datafile="k2714s_01_para.dat"
extract name="Polysi_Thick_after_implant" thickness material="Polysilicon" \
```

```
       mat.occno=1 x.val=$cutline datafile="k2714s_01_para.dat"
extract name="Res after Implant (Ohm*cm)" \
       $Sheet_Res_after_implant*$Polysi_Thick_after_implant/1e8 \
       datafile="k2714s_01_para.dat"

# Deposit LTO to reduce stress of nitride layer
# ---------------------------------------------
deposit oxide thick=0.3 div=10

extract name="LTO Thickness" thickness material="SiO~2" \
       mat.occno=1 x.val=$cutline datafile="k2714s_01_para.dat"

# Drive-in
# --------
diffus time=200 temp=1150 nitrogen press=1.00

struct outfile=$"prefix"_drivein.str

# LPCVD Silicon nitride
# ---------------------
deposit nitride thick=0.16 div=10

struct outfile=$"prefix"_final.str
extract name="Nitride Thickness" thickness material="Si~3N~4" \
       mat.occno=1 x.val=$cutline datafile="k2714s_01_para.dat"
extract name="Surface Conc after Drive-in" surf.conc impurity="Net Doping" \
       material="Polysilicon" mat.occno=1 x.val=$cutline \
       datafile="k2714s_01_para.dat"
extract name="Sheet_Res_after_drivein" sheet.res material="Polysilicon" \
       mat.occno=1 x.val=$cutline semi.poly datafile="k2714s_01_para.dat"
extract name="Polysi_Thick_after_drivein" thickness material="Polysilicon" \
       mat.occno=1 x.val=$cutline datafile="k2714s_01_para.dat"
extract name="Res after Drive-in (Ohm*cm)" \
       $Sheet_Res_after_drivein*$Polysi_Thick_after_drivein/1e8 \
       datafile="k2714s_01_para.dat"

quit
```

Appendix D

COMSOL Simulation

D.1 AC / DC Module

The AC / DC Module comprises several application modes aimed to solve the diverse problems in electromagnetic. The application modes can be divided into two main fields: electrostatic fields, and magnetostatic and quasi-static fields. The *Conductive Media DC* and *Shell, Conductive Media DC* application modes, used in this simulation, are part of the electrostatic fields. The following descriptions are adopted from COMSOL's *AC / DC Module User's Guide* [430].

D.1.1 *Conductive Media DC* Application Mode

The Conductive Media DC application mode solves the following partial differential equation (PDE):

$$-\nabla \cdot \left(\sigma \nabla V - \mathbf{J}^e\right) = \mathbf{Q}_j \tag{D.1}$$

where V is the electrical potential, $\mathbf{J}^e$ is an externally generated current density, and $\mathbf{Q}_j$ is the current source. The σ is the electrical conductivity of the conductive media, which is the only governing material property. For a strongly coupled simulation, the conductivity is temperature-dependent, as described by the following equation:

$$\sigma = \frac{1}{\rho_0\left[1 + \alpha\left(T - T_0\right)\right]} \tag{D.2}$$

where ρ_0 is the resistivity at the reference temperature T_0, α is the temperature coefficient of resistivity (TCR), and T is the current temperature (in Joule heating multiphysics coupling, this is obtained from a heat transfer application mode). The relevant interface condition at the interface between two different media (1 and 2) is

$$\mathbf{n}_2 \cdot \left(\mathbf{J}_1 - \mathbf{J}_2\right) = 0 \tag{D.3}$$

where **n** is the normal vector. The equation D.3 is fulfilled by the following natural boundary condition:

$$\mathbf{n} \cdot \left[\left(\sigma \nabla V - \mathbf{J}^e\right)_1 - \left(\sigma \nabla V - \mathbf{J}^e\right)_2\right] = -\mathbf{n} \cdot \left(\mathbf{J}_1 - \mathbf{J}_2\right) = 0 \tag{D.4}$$

Therefore, the boundary conditions typically used in this model include:

Boundary Condition	Description
$-\mathbf{n} \cdot \mathbf{J} = J_n$	Inward current flow
$\mathbf{n} \cdot \mathbf{J} = 0$	Electrical insulation
$V = V_0$	Electrical potential
$V = 0$	Ground

Table D.1: The boundary conditions typically used in the *Conductive Media DC* application mode.

D.1.2 *Shell, Conductive Media DC* Application Mode

The *Shell, Conductive Media DC* application mode models thin layers of conductive media by solving the problem on 2D surfaces in a 3D geometry. It is similar to the 2D *Conductive Media DC* application mode, as described by the following PDE:

$$-\nabla_t \cdot d_s\left(\sigma \nabla_t V - \mathbf{J}^e\right) = d_s \mathbf{Q}_j \tag{D.5}$$

where d_s is the thickness of the layer (or shell) and the operator ∇_t represents the tangential derivative along the layer.

D.2 Heat Transfer Module

The Heat Transfer Module covers all the fundamental mechanisms in heat transfer, including different combinations of conductive, convective and radiative heat transfer (with both surface-to-surface and surface-to-ambient radiation). The *General Heat Transfer* is the main application mode within this module. The following descriptions are adopted from COMSOL's *Heat Transfer Module User's Guide* [431].

D.2.1 *General Heat Transfer* Application Mode

For the conductive heat transfer analysis, COMSOL solves for the following PDE:

$$Q = \rho C \frac{\partial T}{\partial t} - \nabla \cdot \left(k \nabla T \right) \tag{D.6}$$

where Q is the heat source, ρ is the density, C is the specific heat capacity, T is the temperature, t is time and k is the thermal conductivity. For the steady-state simulation, the first term containing ρ and C vanishes, and the only governing material property is the thermal conductivity, k. The boundary conditions available with this model include:

Boundary Condition	Description
$-\mathbf{n} \cdot \left(-k \nabla T \right) = q_0 + h\left(T_{inf} - T \right)$	Heat flux
$\mathbf{n} \cdot \left(k \nabla T \right) = 0$	Insulation or symmetry
$T = T_0$	Prescribed temperature
$-\mathbf{n}_u \cdot \left(-k_u \nabla T_u \right) - \mathbf{n}_d \cdot \left(-k_d \nabla T_d \right) = 0$	Continuity for interior boundary

Table D.2: The boundary conditions available in the *General Heat Transfer* application mode.

where q_0 is the inward heat flux, h is the heat transfer coefficient and T_{inf} is the temperature of surrounding environment. $\mathbf{n}$ is the normal vector, with the subscripts u and d denote the upside and downside of the boundary, respectively.

The *Highly Conductive Layers* feature, of the *General Heat Transfer* application mode, provide efficient modelling of heat transfer in thin layers without the need to geometrically create a fine mesh for them. The feature assumes that no variations in temperature and in-plane heat flux exist along the direction of the thickness of the layer. In doing so, it simplifies the geometry and significantly reduces the required number of mesh elements.

$$d_s \rho_s C_s \frac{\partial T}{\partial t} + \nabla_t \cdot \left(- d_s k_s \nabla_t T\right) = q_{\partial\Omega} - q_\Omega \tag{D.7}$$

$$q_{\partial\Omega} = q_0 + h\left(T_{inf} - T\right) \tag{D.8}$$

$$q_\Omega = - \mathbf{n} \cdot \left(- k\nabla T + \rho C T \mathbf{u}\right) \tag{D.9}$$

where d_s is the layer thickness, ρ_s is the layer density, C_s is the layer specific heat capacity, k_s is the layer thermal conductivity, $q_{\partial\Omega}$ is the heat flux from the boundary into the layer and q_Ω is the heat flux from the layer into the subdomain.

D.3 2D Simulation

A 2D, steady-state simulation was performed to investigate the effect of the insulating layers (Si_3N_4 and SiO_2), on the heat transfer of the silicon membrane device. The steady-state simulation used the application modes *Conductive Media DC* and *General Heat Transfer* to model the conductive heat transfer due to the Joule heating. The insulating layers (Si_3N_4 and SiO_2) were modelled as one single 200 nm thick Si_3N_4 layer. For comparison, two simulations were performed – i) with the heater on the insulating layer; and ii) with the heater on the silicon membrane.

D.3.1 Settings for *Conductive Media DC* Application Mode

Only the gold heater was set to be active in this application mode. The conductivity of the gold heater was modelled using equation D.2 with properties that are

summarised in Table D.3. An inward current flow of 1.67 x 10^{11} A·m^{-2}, which is based on an input current of 10 A, was used in the simulation.

Parameter	Value	Unit	Reference
Resistivity, ρ_0	2.2 x 10^{-8}	Ωm	[389]
Reference Temperature, T_0	293.15	K	[389]
TCR, α	0.00372	K^{-1}	[388]

Table D.3: The properties of Au used in the subdomain settings of the *Conductive Media DC* application mode.

D.3.2 Settings for *General Heat Transfer* Application Mode

The thermal properties, for the various materials, used in the simulation are presented in Table D.4. The PSi layer was assumed to be 25 % porous (porosity, P = 0.25), and its thermal conductivity, k_{PSi} and specific heat capacity, C_{PSi} were assumed by the following [393]:

$$k_{PSi} = k_{exp} \times (1 - P)^3 \tag{D.10}$$

$$\rho_{PSi} C_{PSi} = \rho_{Si} C_{Si} \times (1 - P) \tag{D.11}$$

where k_{exp} is an experimentally determined fitting parameter (here assumed to be the thermal conductivity of the bulk silicon), ρ_{PSi} and ρ_{Si} are the density of porous silicon and the bulk silicon, respectively, and C_{Si} is the specific heat capacity of the bulk silicon. The density of PSi was assumed to be the same as the density of silicon. A prescribed temperature of 37 °C was set at the boundary of the PSi.

Material	Thickness (μm)	Density, ρ (kgm^{-3})	Thermal Conductivity, k (Wm^{-1}K^{-1})	Specific Heat Capacity, C (Jkg^{-1}K^{-1})
Gold, Au	0.3	19300	317	129
Silicon nitride, Si_3N_4	0.2	3100	20	700
Silicon, Si	50	2330	163	703
Porous silicon, PSi	0.5	2330	68.8	527.3

Table D.4: The thermal properties used in the 2D simulation.

D.3.3 Results

The 2D temperature distribution of both simulations was compared. A temperature line profile was made along the depth of the simulated device structure, for both of the simulations. It was observed that the simulated temperature gradient, at the heater layer, differs by about 3 °C; the model with the heater on the Si_3N_4 layer exhibits higher temperature at steady-state, as depicted in Figure D.1. However, the temperature gradient at the silicon membrane layer (depth from -25.0 µm to 25.0 µm) is very similar (with ~ 1 °C difference). At the PSi structure (depth from -25.5 µm to -25.0 µm) the temperature gradients of both simulations are almost identical, suggesting that the effect of omitting the Si_3N_4 layer was negligible.

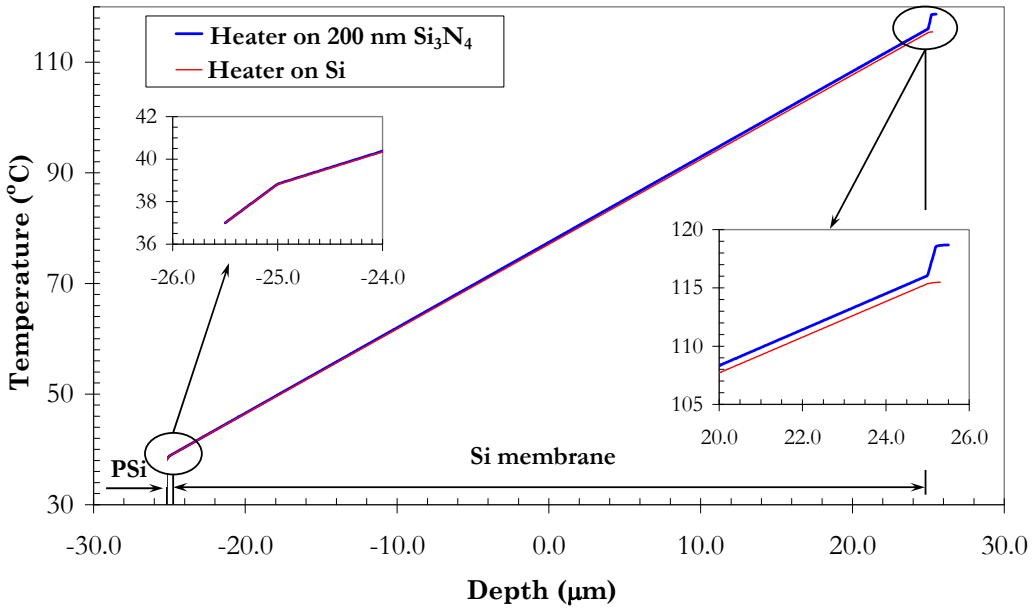

Figure D.1: Simulated steady-state temperature profiles, along the depth of the simulated 2D device structure, of both simulations.

D.4 Revised 3D Simulation

For the revised simulation, the measured total thickness of the metal layers (Ti and Au) and the calculated TCR value were used. Therefore, for sample *b2P02S51*, the metal thickness (d_s) of 443 nm and the TCR value of 0.003 K^{-1} were used. The

natural convective heat transfer coefficients, h_c of 20, 200, 1000 and 2000 were used. The actuation voltage was fixed at 3 V with a heater on-time of 0.5 s. It can be observed, from Figure D.2, that the peak temperature and the cooling rate differ greatly with the different values of h_c used in the simulation.

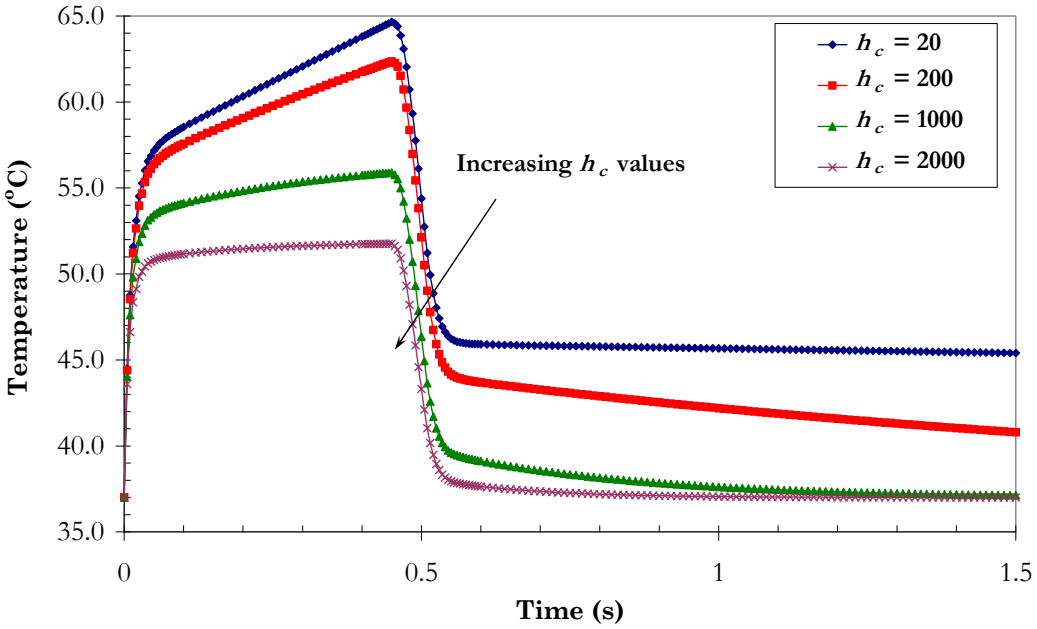

Figure D.2: Simulated temperature profile over time, at the centre of the meander heater, after applying actuation voltages of 3 V, for 0.5 s, with h_c values of 20 (♦), 200 (■), 1000 (▲) and 2000 (×). The metal thickness of 443 nm and the TCR value of 0.003 K^{-1} were used.

Appendix E

Additional SEM Micrographs of the Fabricated PSi Structures

E.1 Sample *P03S32*

Sample *P03S32* was used in the protein loading experiment and discussed in Chapter 7, §7.3.2. The SEM micrograph was acquired with the SiO_2 hard mask still intact.

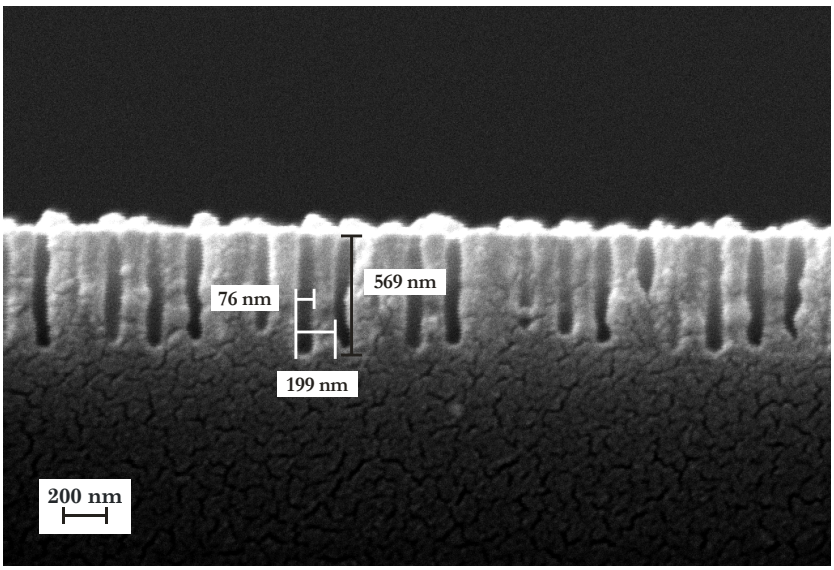

Figure E.1: Cross-sectional view SEM micrograph of sample *P03S32* after the RIE process using the STS LPX Pegasus system.

E.2 Sample *b2P06S51*

Sample *b2P06S51* was used in the protein release experiment and discussed in Chapter 7, §7.4. The SEM micrographs were acquired with the SiO_2 hard mask still intact.

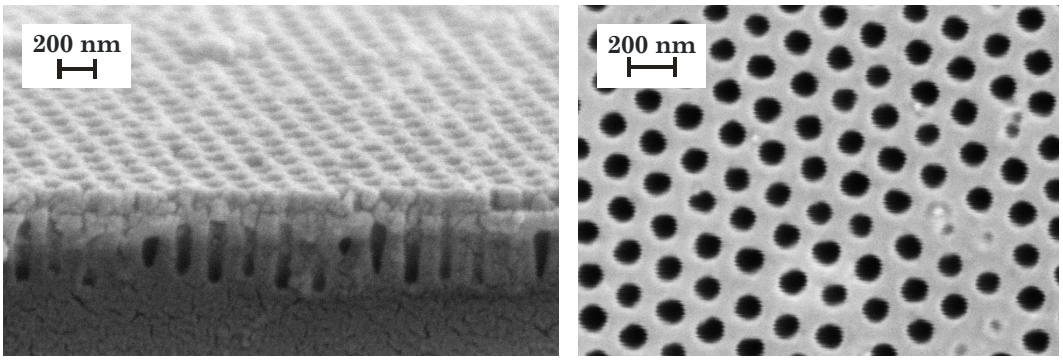

(a) (b)

Figure E.2: (a) Oblique, cross-sectional view and (b) plane-view SEM micrographs of sample *b2P06S51* after the RIE process using the STS LPX Pegasus. The mean diameter of the pores was calculated to be 111 nm ± 7 nm, with a pore depth of 545 nm ± 32 nm (inclusive of the thickness of the SiO_2 hard mask).

E.3 Sample *b2N07S62*

Sample *b2N07S62* was used in the protein release experiment and discussed in Chapter 7, §7.4. The SiO_2 hard mask was etched before the SEM.

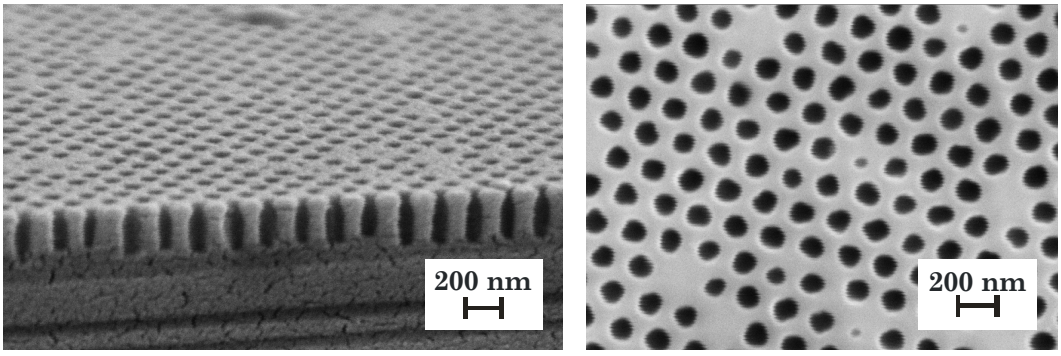

(a) (b)

Figure E.3: (a) Oblique, cross-sectional view and (b) plane-view SEM micrographs of sample *b2N07S62* after the RIE process using the STS LPX Pegasus. The mean diameter of the pores was calculated to be 112 nm ± 10 nm, with a pore depth of 340 nm ± 36 nm.

E.4 Sample *b2N07S43*

These SEM micrographs of sample *b2N07S43* were acquired with the SiO_2 hard mask still intact.

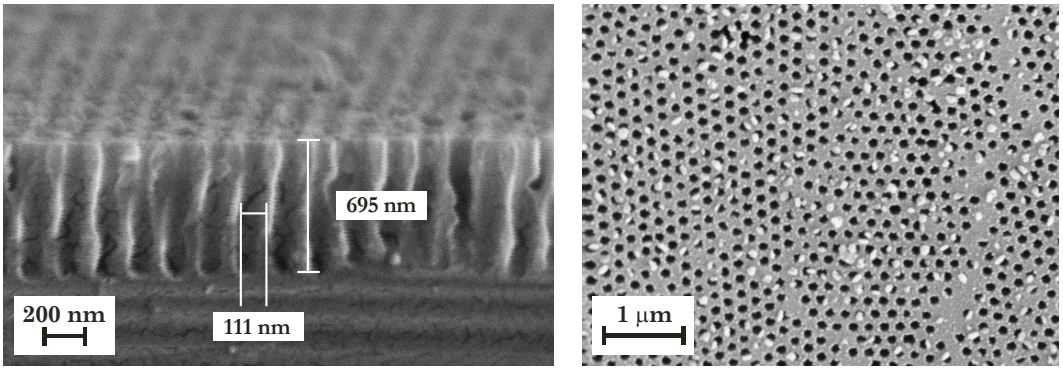

(a) (b)

Figure E.4: (a) Oblique, cross-sectional view and (b) plane-view SEM micrographs of sample *b2N07S43* after the RIE process using the STS LPX Pegasus.

E.5 Sample *b2P06S23*

These SEM micrographs of sample *b2P07S23* were acquired with the SiO_2 hard mask still intact.

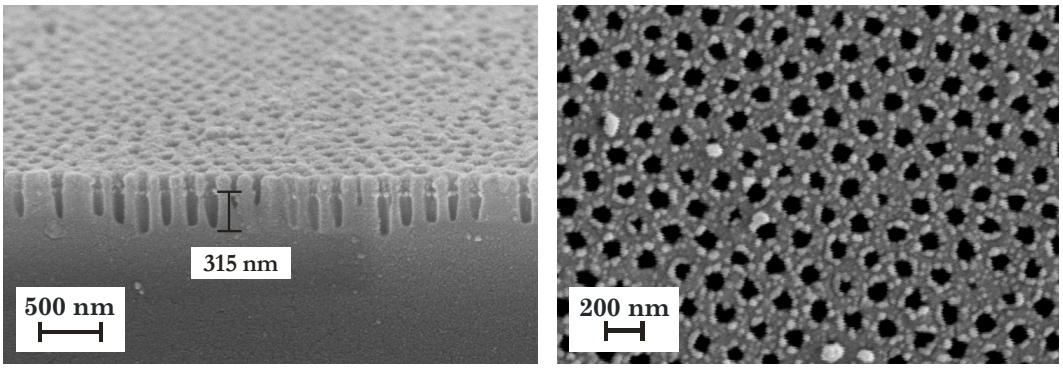

(a) (b)

Figure E.5: (a) Oblique, cross-sectional view and (b) plane-view SEM micrographs of sample *b2P06S23* after the RIE process using the STS LPX Pegasus.

E.6 Sample *b2P02S46*

Sample *b2P02S46* was deposited with nanospheres that were subsequently etched for 40 s using an O_2 RIE process. The RIE of silicon using the STS LPX Pegasus was then performed for 10 minutes to realise the nanopillars.

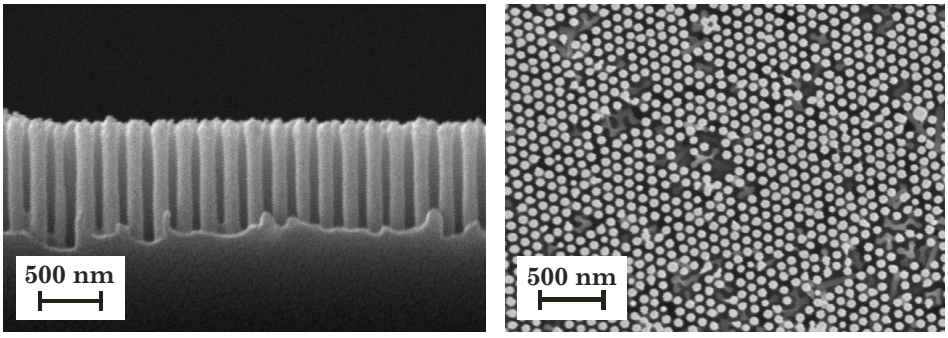

(a) (b)

Figure E.6: (a) Cross-sectional view and (b) plane-view SEM micrographs of sample *b2P02S46* after the RIE of silicon. Nanopillars of ~ 107 nm in diameter and ~ 894 nm in length were fabricated.

E.7 Sample *b2P02S56*

Sample *b2P02S56* was deposited with nanospheres that were subsequently etched for 50 s using an O_2 RIE process. The RIE of silicon using the STS LPX Pegasus was then performed for 15 minutes to realise the nanowires.

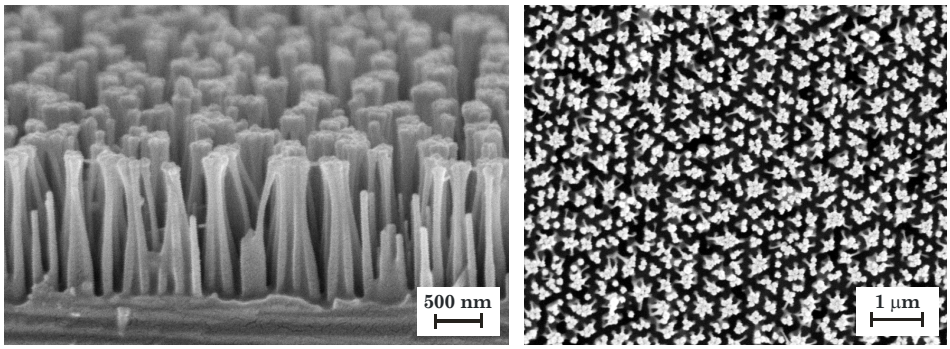

(a) (b)

Figure E.7: (a) Oblique, cross-sectional view and (b) plane-view SEM micrographs of sample *b2P02S56* after the RIE of silicon. Nanowires of ~ 97 nm in diameter and ~ 1369 nm in length were fabricated.

Appendix F

Publications

F.1 Journal and Conferences

1) C. F. Chau and T. Melvin, "The fabrication of macroporous polysilicon by nanosphere lithography," *J. Micromech. Microeng.*, **18** (6), 064012 (9pp.), 2008.

2) C. F. Chau and T. Melvin, (Talk) "Fabrication of macroporous polysilicon using nanosphere lithography technique," in *Biomimetic on the Nanoscale (IoP Day Meeting)*, Southampton, UK, Feb. 2008.

3) C. F. Chau and T. Melvin, (Poster) "Fabrication of macroporous polysilicon by using nanosphere lithography," in *18th Workshop on Micromachining, Micromechanics and Microsystems (MME 2007)*, Guimaraes, Portugal, pp. 273-276, Sep. 2007.

4) C. F. Chau, T. Melvin, and B. Hamilton, (Poster) "Fabrication of a nanoporous polysilicon device for drug delivery," in *Nanoscale Physics and Technology: the Interface with Medical and Biological Sciences (IoP Meeting)*, Southampton, UK, Mar. 2007.

5) S. Mohmad, C. F. Chau, T. Melvin, S. Atri, and C. Kaminski, (Talk) "Nano-porous polysilicon fabrication for micro electro mechanical system (MEMS) drug delivery device," *IFMBE for the 3rd Kuala Lumpur International Conference on*

Biomedical Engineering 2006 (Biomed 2006), Kuala Lumpur, Malaysia, Dec. 2006.

F.2 Supporting Publications

1) C. F. Chau and T. Melvin, (Talk) "Design and fabrication of passive mixing channels to be incorporated into a centrifugally driven microfluidic lab-on-a-disc," in *7th Postgraduate Research Conference in Electronics, Photonics, Communications and Software (PREP 2005)*, Lancaster, UK, 2005.

2) B. Mills, C. F. Chau, E. T. F. Rogers, J. Grant-Jacob, S. L. Stebbings, M. Praeger, A. M. De Paula, C. A. Froud, R. T. Chapman, T. J. Butcher, J. J. Baumberg, W. S. Brocklesby and J. G. Frey, "Direct measurement of the complex refractive index in the extreme ultraviolet spectral region using diffraction from a nanosphere array," *Appl. Phys. Lett.*, **93** (23), 231103 (3pp.), 2008.

3) B. Mills, C. F. Chau, E. T. F. Rogers, J. Grant-Jacob, S. L. Stebbings, M. Praeger, C. A. Froud, R. T. Chapman, T. J. Butcher, D. C. Hanna, J. J. Baumberg, W. S. Brocklesby and J. G. Frey, (Talk) "XUV diffraction from a self-assembled 2D array of close-packed 200nm diameter PMMA spheres," in *Optics and Photonics Conf. 2008 (Photon 08)*, Edinburg, UK, August 2008.

4) B. Mills, C. F. Chau, E. T. F. Rogers, J. Grant-Jacob, S. L. Stebbings, M. Praeger, C. A. Froud, R. T. Chapman, T. J. Butcher, D. C. Hanna, J. J. Baumberg, W. S. Brocklesby and J. G. Frey, (Talk) "XUV diffraction from a self-assembled 2D array of close-packed 200nm diameter PMMA spheres," in *European Conf. X-Ray Spectrometry (EXRS 2008)*, Dubrovnik, Croatia, June 2008.

References

[1] C. Holroyd, C. Cooper and E. Dennison, "Epidemiology of osteoporosis," *Best Pract. Res. Clin. Endocrinol. Metab.*, **22** (5), pp. 671-685, 2008.

[2] National Osteoporosis Society England, *The NOS Menifesto 2009: Protecting fragile bones - A strategy to reduce the impact of osteoporosis and fragility fractures in England*, http://www.nos.org.uk/NetCommunity/Document.Doc?id=490, last accessed in Jul. 2009.

[3] S. Parrott, *The economic cost of hip fracture in the UK*. A paper commissioned by Health Promotion England on behalf of the Department of Trade and Industry York, UK: Centre for Health Economics, University of York, Jun. 2000.

[4] T. P. van Staa, E. M. Dennison, H. G. M. Leufkens and C. Cooper, "Epidemiology of fractures in England and Wales," *Bone*, **29** (6), pp. 517-522, 2001.

[5] G. F. Muschler, C. Nakamoto and L. G. Griffith, "Engineering principles of clinical cell-based tissue engineering," *J. Bone Joint Surg. Am.*, **86** (7), pp. 1541-1558, 2004.

[6] P. V. Giannoudis, T. A. Einhorn and D. Marsh, "Fracture healing: The diamond concept," *Injury, Int. J. Care Injured*, **38** (Supplement 4), pp. S3-S6, 2007.

[7] S. B. Trippel, R. D. Coutts, T. A. Einhorn, G. R. Mundy and R. G. Rosenfeld, "Instructional Course Lectures, The American Academy of Orthopaedic Surgeons - Growth factors as therapeutic agents," *J. Bone Joint Surg. Am.*, **78A** (8), pp. 1272-1286, 1996.

[8] S. R. Winn, H. Uludag and J. O. Hollinger, "Sustained release emphasizing recombinant human bone morphogenetic protein-2," *Adv. Drug Deliv. Rev.*, **31** (3), pp. 303-318, 1998.

[9] M. R. Urist, "Bone: Formation by autoinduction," *Science*, **150** (3698), pp. 893-899, 1965.

[10] M. R. Urist and B. S. Strates, "Bone morphogenetic protein," *J. Dent. Res.*, **50** (6), pp. 1392-1406, 1971.

[11] H. Cheng, W. Jiang, F. M. Phillips, R. C. Haydon, Y. Peng, L. Zhou, H. H. Luu, N. An, B. Breyer, P. Vanichakarn*, et al.*, "Osteogenic activity of the fourteen types of human bone morphogenetic proteins (BMPs)," *J. Bone Joint Surg. Am.*, **85A** (8), pp. 1544-1552, 2003.

[12] O. P. Gautschi, S. P. Frey and R. Zellweger, "Bone morphogenetic proteins in clinical applications," *ANZ J. Surg.*, **77** (8), pp. 626-631, 2007.

[13] D. Chen, M. Zhao and G. R. Mundy, "Bone morphogenetic proteins," *Growth Factors*, **22** (4), pp. 233 - 241, 2004.

[14] M. F. Termaat, F. C. Den Boer, F. C. Bakker, P. Patka and H. J. T. M. Haarman, "Bone Morphogenetic Proteins. Development and clinical efficacy in the treatment of fractures and bone defects," *J. Bone Joint Surg. Am.*, **87** (6), pp. 1367-1378, 2005.

[15] W. F. McKay, S. M. Peckham and J. M. Badura, "A comprehensive clinical review of recombinant human bone morphogenetic protein-2 (INFUSE® Bone Graft)," *Int. Orthop.*, **31** (6), pp. 729-734, 2007.

[16] G. Schmidmaier, P. Schwabe, B. Wildemann and N. P. Haas, "Use of bone morphogenetic proteins for treatment of non-unions and future perspectives," *Injury, Int. J. Care Injured*, **38** (Supplement 4), pp. S35-S41, 2007.

[17] J. M. Schmitt, K. Hwang, S. R. Winn and J. O. Hollinger, "Bone morphogenetic proteins: An update on basic biology and clinical relevance," *J. Orthop. Res.*, **17** (2), pp. 269-278, 1999.

[18] J. K. Burkus, M. F. Gornet, C. A. Dickman and T. A. Zdeblick, "Anterior lumbar interbody fusion using rhBMP-2 with tapered interbody cages," *J. Spinal Disord. Tech.*, **15** (5), pp. 337-349, 2002.

[19] G. E. Friedlaender, C. R. Perry, J. D. Cole, S. D. Cook, G. Cierny, G. F. Muschler, G. A. Zych, J. H. Calhoun, A. J. LaForte and S. Yin, "Osteogenic protein-1 (bone morphogenetic protein-7) in the treatment of tibial nonunions: A prospective, randomized clinical trial comparing rhOP-1 with fresh bone autograft," *J. Bone Joint Surg. Am.*, **83A** (Supp. 1, Part 2), pp. S151-S158, 2001.

[20] BMP-2 Evaluation in Surgery for Tibial Trauma (BESTT) Study Group, S. Govender, C. Csimma, H. K. Genant, A. Valentin-Opran, Y. Amit, R. Arbel, H. Aro, D. Atar, M. Bishay, *et al.*, "Recombinant human bone morphogenetic protein-2 for treatment of open tibial fractures: A prospective, controlled, randomized study of four hundred and fifty patients," *J. Bone Joint Surg. Am.*, **84A** (12), pp. 2123-2134, 2002.

[21] H. Seeherman and J. M. Wozney, "Delivery of bone morphogenetic proteins for orthopedic tissue regeneration," *Cytokine Growth Factor Rev.*, **16** (3), pp. 329-345, 2005.

[22] G. Schmidmaier, P. Schwabe, C. Strobel and B. Wildemann, "Carrier systems and application of growth factors in orthopaedics," *Injury, Int. J. Care Injured*, **39** (Supplement 2), pp. S37-S43, 2008.

[23] E. Anitua, M. Sánchez, G. Orive and I. Andia, "Delivering growth factors for therapeutics," *Trends Pharmacol. Sci.*, **29** (1), pp. 37-41, 2008.

[24] M. Geiger, R. H. Li and W. Friess, "Collagen sponges for bone regeneration with rhBMP-2," *Adv. Drug Deliv. Rev.*, **55** (12), pp. 1613-1629, 2003.

[25] W. G. De Long, Jr., T. A. Einhorn, K. Koval, M. McKee, W. Smith, R. Sanders and T. Watson, "Bone grafts and bone graft substitutes in orthopaedic trauma surgery. A critical analysis," *J. Bone Joint Surg. Am.*, **89** (3), pp. 649-658, 2007.

[26] B. McKay and H. S. Sandhu, "Use of recombinant human bone morphogenetic protein-2 in spinal fusion applications," *Spine*, **27** (16S), pp. S66-S85, 2002.

[27] R. Ruppert, E. Hoffmann and W. Sebald, "Human bone morphogenetic protein 2 contains a Heparin-binding site which modifies its biological activity," *Eur. J. Biochem.*, **237** (1), pp. 295-302, 1996.

[28] C. Scheufler, W. Sebald and M. Hülsmeyer, "Crystal structure of human bone morphogenetic protein-2 at 2.7 Å resolution," *J. Mol. Biol.*, **287** (1), pp. 103-115, 1999.

[29] M. Laub, H. P. Jennissen, T. Seul and E. Schmachtenberg, "Molecular modelling of bone morphogenetic protein-2 (BMP-2) by 3D-rapid prototyping," *Materwiss. Werksttech.*, **32** (12), pp. 926-930, 2001.

[30] H. Ohta, S. Wakitani, K. Tensho, H. Horiuchi, S. Wakabayashi, N. Saito, Y. Nakamura, K. Nozaki, Y. Imai and K. Takaoka, "The effects of heat on the biological activity of recombinant human bone morphogenetic protein-2," *J. Bone Miner. Metab.*, **23** (6), pp. 420-425, 2005.

[31] R. D'Aquino, "Good drug therapy: It's not just the molecule - It's the delivery," in *Chem. Eng. Prog. magazine*, **100** (2), pp. 15S-17S, 2004.

[32] J. T. Santini, A. C. Richards, R. Scheidt, M. J. Cima and R. Langer, "Microchips as controlled drug-delivered devices," *Angew. Chem. Int. Ed.*, **39** (14), pp. 2397-2407, 2000.

[33] F. J. Martin and C. Grove, "Microfabricated drug delivery systems: Concepts to improve clinical benefit," *Biomed. Microdevices*, **3** (2), pp. 97-108, 2001.

[34] S. Sharma, A. J. Nijdam, P. M. Sinha, R. J. Walczak, X. Liu, M. M. C. Cheng and M. Ferrari, "Controlled-release microchips," *Expert Opin. Drug Deliv.*, **3** (3), pp. 379-394, 2006.

[35] J. Z. Hilt and N. A. Peppas, "Microfabricated drug delivery devices," *Int. J. Pharm.*, **306** (1-2), pp. 15-23, 2005.

[36] S. Zafar Razzacki, P. K. Thwar, M. Yang, V. M. Ugaz and M. A. Burns, "Integrated microsystems for controlled drug delivery," *Adv. Drug Deliv. Rev.*, **56** (2), pp. 185-198, 2004.

[37] O. H. Chan and B. H. Stewart, "Physicochemical and drug-delivery considerations for oral drug bioavailability," *Drug Discov. Today*, **1** (11), pp. 461-473, 1996.

[38] L. F. Chasseaud and T. Taylor, "Bioavailability of drugs from formulations after oral administration," *Annu. Rev. of Pharmacol.*, **14**, pp. 35-46, 1974.

[39] G. Walsh, "Biopharmaceuticals: Recent approvals and likely directions," *Trends Biotechnol.*, **23** (11), pp. 553-558, 2005.

[40] S. D. Senturia, *Microsystem Design*, Boston, USA: Kluwer Academic, 2002.

[41] G. T. A. Kovacs, *Micromachined Transducers Sourcebook*, Boston, USA: McGraw-Hill, 1998.

[42] M. J. Madou, *Fundamentals of Microfabrication: The Science of Miniaturization*, 2nd ed., Boca Raton , USA: CRC Press, 2002.

[43] M. Hu and R. Zengerle, "Microfabricated devices for controlled biochemical release," in *10th International Conference on New Actuators and the 4th International Exhibition on Smart Actuators and Drive Systems (Actuator 2006)*, Bremen, Germany, pp. 263-271, Jun. 2006.

[44] A. C. Richards Grayson, R. S. Shawgo, Y. Li and M. J. Cima, "Electronic MEMS for triggered delivery," *Adv. Drug Deliv. Rev.*, **56** (2), pp. 173-184, 2004.

[45] M. L. Reed and W.-K. Lye, "Microsystems for drug and gene delivery," *Proc. IEEE*, **92** (1), pp. 56-75, 2004.

[46] D. A. LaVan, T. McGuire and R. Langer, "Small-scale systems for in vivo drug delivery," *Nat. Biotechnol.*, **21** (10), pp. 1184-1191, 2003.

[47] R. S. Shawgo, A. C. R. Grayson, Y. Li and M. J. Cima, "BioMEMS for drug delivery," *Curr. Opin. Solid State Mater. Sci.*, **6** (4), pp. 329-334, 2002.

[48] A. C. Richards Grayson, R. S. Shawgo, A. M. Johnson, N. T. Flynn, Y. Li, M. J. Cima and R. Langer, "A BioMEMS review: MEMS technology for physiologically integrated devices," *Proc. IEEE*, **92** (1), pp. 6-21, 2004.

[49] M. Staples, K. Daniel, M. J. Cima and R. Langer, "Application of micro- and nano-electromechanical devices to drug delivery," *Pharm. Res.*, **23** (5), pp. 847-863, 2006.

[50] S. L. Tao and T. A. Desai, "Microfabricated drug delivery systems: From particles to pores," *Adv. Drug Deliv. Rev.*, **55** (3), pp. 315-328, 2003.

[51] D. T. Birnbaum and L. Brannon-Peppas, "Microparticle drug delivery systems," in *Drug Delivery Systems in Cancer Therapy*, D. M. Brown (Ed.), Totowa, NJ, USA: Humana Press, 2004, pp. 117-136.

[52] M. N. V. Ravi Kumar, "Nano and microparticles as controlled drug delivery devices," *J. Pharm. Pharm. Sci.*, **3** (2), pp. 234-258, 2000.

[53] G. A. Hughes, "Nanostructure-mediated drug delivery," *Nanomed. Nanotechnol. Biol. Med.*, **1** (1), pp. 22-30, 2005.

[54] J. Salonen, A. M. Kaukonen, J. Hirvonen and V.-P. Lehto, "Mesoporous silicon in drug delivery applications," *J. Pharm. Sci.*, **97** (2), pp. 632-653, 2008.

[55] E. J. Anglin, L. Cheng, W. R. Freeman and M. J. Sailor, "Porous silicon in drug delivery devices and materials," *Adv. Drug Deliv. Rev.*, **60** (11), pp. 1266-1277, 2008.

[56] M. Ferrari, "Cancer nanotechnology: Opportunities and challenges," *Nat. Rev. Cancer*, **5** (3), pp. 161-171, 2007.

[57] W. R. Sanhai, J. H. Sakamoto, R. Canady and M. Ferrari, "Seven challenges for nanomedicine," *Nat. Nanotechnol.*, **3** (5), pp. 242-244, 2008.

[58] C. E. Webb, "Chip shots," in *IEEE Spectrum magazine*, **41** (10), pp. 48-53, 2004.

[59] S. K. Deo, E. A. Moschou, S. F. Peteu, L. G. Bachas, S. Daunert, P. E. Eisenhardt and M. J. Madou, "Responsive drug delivery systems," *Anal. Chem.*, **75** (9), pp. 206A-213A, 2003.

[60] L. T. Canham, "Bioactive silicon structure fabrication through nanoetching techniques," *Adv. Mater.*, **7** (12), pp. 1033-1037, 1995.

[61] ---, "Biomedical applications of porous silicon," in *Properties of Porous Silicon (EMIS Datareview Series No. 18)*, L. T. Canham (Ed.), London, UK: INSPEC, the Institution of Electrical Engineers, 1997, pp. 371-376.

[62] S. H. C. Anderson, H. Elliott, D. J. Walllis, L. T. Canham and J. J. Powell, "Dissolution of different forms of partially porous silicon wafers under simulated physiological conditions," *Phys. Status Solidi A*, **197** (2), pp. 331-5, 2003.

[63] S. L. Tao and T. A. Desai, "Micromachined devices: The impact of controlled geometry from cell-targeting to bioavailability," *J. Controlled Release*, **109** (1-3), pp. 127-138, 2005.

[64] K. M. Ainslie, C. M. Kraning and T. A. Desai, "Microfabrication of an asymmetric, multi-layered microdevice for controlled release of orally delivered therapeutics," *Lab Chip*, **8** (7), pp. 1042-1047, 2008.

[65] A. Ahmed, C. Bonner and T. A. Desai, "Bioadhesive microdevices with multiple reservoirs: a new platform for oral drug delivery," *J. Controlled Release*, **81** (3), pp. 291-306, 2002.

[66] S. L. Tao and T. A. Desai, "Micromachined polymeric devices for applications in targeted drug delivery," *JALA J. Assoc. Lab. Autom.*, **9** (3), pp. 155-8, 2004.

[67] ---, "Microfabrication of multilayer, asymmetric, polymeric devices for drug delivery," *Adv. Mater.*, **17** (13), pp. 1625-1630, 2005.

[68] M. H. Cohen, K. Melnik, A. A. Boiarski, M. Ferrari and F. J. Martin, "Microfabrication of silicon-based nanoporous particulates for medical applications," *Biomed. Microdevices*, **5** (3), pp. 253-259, 2003.

[69] A. B. Foraker, R. J. Walczak, M. H. Cohen, T. A. Boiarski, C. F. Grove and P. W. Swaan, "Microfabricated porous silicon particles enhance paracellular delivery of insulin across intestinal Caco-2 cell monolayers," *Pharm. Res.*, **20** (1), pp. 110-116, 2003.

[70] J. Salonen, L. Laitinen, A. M. Kaukonen, J. Tuura, M. Björkqvist, T. Heikkilä, K. Vähä-Heikkilä, J. Hirvonen and V.-P. Lehto, "Mesoporous silicon microparticles for oral drug delivery: Loading and release of five model drugs," *J. Controlled Release*, **108** (2-3), pp. 362-374, 2005.

[71] E. Tasciotti, X. Liu, R. Bhavane, K. Plant, A. D. Leonard, B. K. Price, M. M.-C. Cheng, P. Decuzzi, J. M. Tour, F. Robertson, *et al.*, "Mesoporous silicon particles as a multistage delivery system for imaging and therapeutic applications," *Nat. Nanotechnol.*, **3** (3), pp. 151-157, 2008.

[72] L. Brown and R. Langer, "Transdermal delivery of drugs," *Ann. Rev. Med.*, **39**, pp. 221-229, 1988.

[73] R. B. Stoughton, "Percutaneous Absorption of Drugs," *Annu. Rev. Pharmacol Toxicol*, **29**, pp. 55-69, 1989.

[74] V. V. Ranade, "Drug delivery systems. 6. Transdermal drug delivery," *J. Clin. Pharmacol.*, **31** (5), pp. 401-418, 1991.

[75] R. Kumar and A. Philip, "Modified transdermal technologies: Breaking the barriers of drug permeation via the skin," *Trop. J. Pharm. Res.*, **6** (1), pp. 633-644, 2007.

[76] M. R. Prausnitz, S. Mitragotri and R. Langer, "Current status and future potential of transdermal drug delivery," *Nat Rev Drug Discov*, **3** (2), pp. 115-124, 2004.

[77] C. H. Dublin, "Transdermal delivery becoming more active," in *Drug Deliv. Technol. magazine*, **8** (7), pp. 38-43, 2008.

[78] T. Tanner and R. Marks, "Delivering drugs by the transdermal route: Review and comment," *Skin Res. Technol.*, **14** (3), pp. 249-260, 2008.

[79] K. Chiarello, "Breaking the barrier: Advances in transdermal technology," in *Pharm. Technol. magazine*, **28** (10), pp. 46-56, 2004.

[80] M. R. Prausnitz, "Microneedles for transdermal drug delivery," *Adv. Drug Deliv. Rev.*, **56** (5), pp. 581-587, 2004.

[81] D. V. McAllister, M. G. Allen and M. R. Prausnitz, "Microfabricated microneedles for gene and drug delivery," *Annu. Rev. Biomed. Eng.*, **2**, pp. 289-313, 2000.

[82] J. C. Birchall, "Microneedle array technology: the time is right but is the science ready?," *Expert Rev. Med. Devices*, **3** (1), pp. 1-4, 2006.

[83] H. S. Gill and M. R. Prausnitz, "Coated microneedles for transdermal delivery," *J. Controlled Release*, **117** (2), pp. 227-237, 2007.

[84] D. V. McAllister, P. M. Wang, S. P. Davis, J.-H. Park, P. J. Canatella, M. G. Allen and M. R. Prausnitz, "Microfabricated needles for transdermal delivery of macromolecules and nanoparticles: Fabrication methods and transport studies," *Proc. Natl. Acad. Sci. USA*, **100** (24), pp. 13755-13760, 2003.

[85] S. Mitragotri, "Immunization without needles," *Nat. Rev. Immunol.*, **5** (12), pp. 905-916, 2005.

[86] K. D. Wise, J. B. Angell and A. Starr, "An integrated-circuit approach to extracellular microelectrodes," *IEEE Trans. Biomed. Eng.*, **17** (3), pp. 238-247, 1970.

[87] J. Chen, K. D. Wise, J. F. Hetke and S. C. Bledsoe, Jr., "A multichannel neural probe for selective chemical delivery at the cellular level," *IEEE Trans. Biomed. Eng.*, **44** (8), pp. 760-769, 1997.

[88] L. Lin and A. P. Pisano, "Silicon-processed microneedles," *J. Microelectromech. Syst.*, **8** (1), pp. 78-84, 1999.

[89] J. D. Zahn, A. Deshmukh, A. P. Pisano and D. Liepmann, "Continuous on-chip micropumping for microneedle enhanced drug delivery," *Biomed. Microdevices*, **6** (3), pp. 183-90, 2004.

[90] S. Henry, D. V. McAllister, M. G. Allen and M. R. Prausnitz, "Microfabricated microneedles: A novel approach to transdermal drug delivery," *J. Pharm. Sci.*, **87** (8), pp. 922-925, 1998.

[91] H. Jansen, M. de Boer, R. Legtenberg and M. Elwenspoek, "The Black Silicon method: A universal method for determining the parameter setting of a fluorine-based reactive ion etcher in deep silicon trench etching with profile control," *J. Micromech. Microeng.*, **5** (2), pp. 115-120, 1995.

[92] S. Kaushik, A. H. Hord, D. D. Denson, D. V. McAllister, S. Smitra, M. G. Allen and M. R. Prausnitz, "Lack of pain associated with microfabricated microneedles," *Anesth. Analg.*, **92** (2), pp. 502-504, 2001.

[93] D. P. Wermeling, S. L. Banks, D. A. Hudson, H. S. Gill, J. Gupta, M. R. Prausnitz and A. L. Stinchcomb, "Microneedles permit transdermal delivery of a skin-impermeant medication to humans," *Proc. Natl. Acad. Sci. USA*, **105** (6), pp. 2058-2063, 2008.

[94] B. Stoeber and D. Liepmann, "Arrays of hollow out-of-plane microneedles for drug delivery," *J. Microelectromech. Syst.*, **14** (3), pp. 472-479, 2005.

[95] F. Lärmer and A. Schilp, "Method of Anisotropically Etching Silicon." Robert Bosch GmbH, Stuttgart, Germany: U.S. Patent 5501893, 1996.

[96] P. Griss and G. Stemme, "Side-opened out-of-plane microneedles for microfluidic transdermal liquid transfer," *J. Microelectromech. Syst.*, **12** (3), pp. 296-301, 2003.

[97] H. J. G. E. Gardeniers, R. Luttge, E. J. W. Berenschot, M. J. de Boer, S. Y. Yeshurun, M. Hefetz, R. van't Oever and A. van den Berg, "Silicon micromachined hollow microneedles for transdermal liquid transport," *J. Microelectromech. Syst.*, **12** (6), pp. 855-62, 2003.

[98] W. Lin, M. Cormier, A. Samiee, A. Griffin, B. Johnson, C.-L. Teng, G. E. Hardee and P. E. Daddona, "Transdermal delivery of antisense oligonucleotides with microprojection patch (Macroflux®) technology," *Pharm. Res.*, **18** (12), pp. 1789-1793, 2001.

[99] G. Widera, J. Johnson, L. Kim, L. Libiran, K. Nyam, P. E. Daddona and M. Cormier, "Effect of delivery parameters on immunization to ovalbumin following intracutaneous administration by a coated microneedle array patch system," *Vaccine*, **24** (10), pp. 1653-1664, 2006.

[100] J. A. Matriano, M. Cormier, J. Johnson, W. A. Young, M. Buttery, K. Nyam and P. E. Daddona, "Macroflux® microprojection array patch technology: A new and efficient approach for intracutaneous immunization," *Pharm. Res.*, **19** (1), pp. 63-70, 2002.

[101] J. W. Lee, J.-H. Park and M. R. Prausnitz, "Dissolving microneedles for transdermal drug delivery," *Biomaterials*, **29** (13), pp. 2113-24, 2008.

[102] S. P. Sullivan, N. Murthy and M. R. Prausnitz, "Minimally invasive protein delivery with rapidly dissolving polymer microneedles," *Adv. Mater.*, **20** (5), pp. 933-938, 2008.

[103] J.-H. Park, M. Allen and M. Prausnitz, "Polymer microneedles for controlled-release drug delivery," *Pharm. Res.*, **23** (5), pp. 1008-1019, 2006.

[104] J.-H. Park, M. G. Allen and M. R. Prausnitz, "Biodegradable polymer microneedles: Fabrication, mechanics and transdermal drug delivery," *J. Controlled Release*, **104** (1), pp. 51-66, 2005.

[105] J. H. Park, Y. K. Yoon, S. O. Choi, M. R. Prausnitz and M. G. Allen, "Tapered conical polymer microneedles fabricated using an integrated lens technique for transdermal drug delivery," *IEEE Trans. Biomed. Eng.*, **54** (5), pp. 903-913, 2007.

[106] T. Miyano, Y. Tobinaga, T. Kanno, Y. Matsuzaki, H. Takeda, M. Wakui and K. Hanada, "Sugar micro needles as transdermic drug delivery system," *Biomed. Microdevices*, **7** (3), pp. 185-188, 2005.

[107] J. Ji, F. E. H. Tay, J. Miao and C. Iliescu, "Microfabricated microneedle with porous tip for drug delivery," *J. Micromech. Microeng.*, **16** (5), pp. 958-964, 2006.

[108] J. Ji, F. E. H. Tay, M. Jianmin and C. Iliescu, "Microfabricated silicon microneedle array for transdermal drug delivery," in *International MEMS Conference 2006*, Singapore, pp. 1127-31, May 2006.

[109] B. Chen, J. Wei, F. E. H. Tay, Y. T. Wong and C. Iliescu, "Silicon microneedle array with biodegradable tips for transdermal drug delivery," *Microsyst. Technol.*, **14** (7), pp. 1015-1019, 2008.

[110] V. V. Ranade, "Drug delivery systems. 4. Implants in drug delivery," *J. Clin. Pharmacol.*, **30** (10), pp. 871-889, 1990.

[111] N.-C. Tsai and C.-Y. Sue, "Review of MEMS-based drug delivery and dosing systems," *Sens. Actuators A*, **134** (2), pp. 555-64, 2007.

[112] A. Nisar, N. Afzulpurkar, B. Mahaisavariya and A. Tuantranont, "MEMS-based micropumps in drug delivery and biomedical applications," *Sens. Actuators B*, **130** (2), pp. 917-942, 2008.

[113] J. T. Santini, A. C. Richards, R. A. Scheidt, M. J. Cima and R. S. Langer, "Microchip technology in drug delivery," *Ann. Med.*, **32** (6), pp. 377 - 379, 2000.

[114] N.-T. Nguyen and S. T. Wereley, *Fundamentals and Applications of Microfluidics*, Boston, USA: Artech House, 2002.

[115] B. Husband, *The Design and Fabrication of a Magnetically Actuated Microfluidic Dispensing Device*, Ph.D. Dissertation, University of Southampton, 2007.

[116] A. Geipel, F. Goldschmidtboeing, P. Jantscheff, N. Esser, U. Massing and P. Woias, "Design of an implantable active microport system for patient specific drug release," *Biomed. Microdevices*, **10** (4), pp. 469-478, 2008.

[117] A. Geipel, A. Doll, F. Goldschmidtboing, P. Jantscheff, N. Esser, U. Massing and P. Woias, "Pressure-independent micropump with piezoelectric valves for low flow drug delivery systems," in *Proc. 19th IEEE International Conference on Micro Electro Mechanical Systems (MEMS 2006)*, Istanbul, Turkey, pp. 786-789, Jan. 2006.

[118] A. Geipel, A. Doll, P. Jantscheff, N. Esser, U. Massing, P. Woias and F. Goldschmidtboeing, "A novel two-stage backpressure-independent micropump: Modeling and characterization," *J. Micromech. Microeng.*, **17** (5), pp. 949-59, 2007.

[119] D. Maillefer, S. Gamper, B. Frehner, P. Balmer, H. Van Lintel and P. Renaud, "A high-performance silicon micropump for disposable drug delivery systems," in *Tech. Digest 14th IEEE International Conference on Micro Electro Mechanical Systems (MEMS 2001)*, Interlaken, Switzerland, pp. 413-417, Jan. 2001.

[120] D. Maillefer, H. van Lintel, G. Rey-Mermet and R. Hirschi, "A high-performance silicon micropump for an implantable drug delivery system," in *Proc. 12th IEEE International Conference on Micro Electro Mechanical Systems (MEMS 1999)*, Orlando, FL, USA, pp. 541-546, Jan. 1999.

[121] Y.-C. Su and L. Lin, "A water-powered micro drug delivery system," *J. Microelectromech. Syst.*, **13** (1), pp. 75-82, 2004.

[122] W. Ryu, Z. Huang, F. B. Prinz, S. B. Goodman and R. Fasching, "Biodegradable micro-osmotic pump for long-term and controlled release of basic fibroblast growth factor," *J. Controlled Release*, **124** (1-2), pp. 98-105, 2007.

[123] *Viadur® Press Release (12 Dec. 2007)*, http://www.bayerviadur.com/pdfs/Final_Press_Release_Viadur_122007.pdf, last accessed in Sep. 2008.

[124] *DUROS® Fact Sheet*, http://www.durect.com/pdf/duros_fact_sheet2001.pdf, last accessed in Sep. 2008.

[125] J. T. Santini, M. J. Cima and R. Langer, "A controlled-release microchip," *Nature*, **397** (6717), pp. 335-338, 1999.

[126] J. M. Maloney, S. A. Uhland, B. F. Polito, N. F. Sheppard Jr, C. M. Pelta and J. T. Santini Jr, "Electrothermally activated microchips for implantable drug delivery and biosensing," *J. Controlled Release*, **109** (1-3), pp. 244-255, 2005.

[127] J. Prescott, T. Krieger, S. Lipka and M. Staples, "Dosage form development, in vitro release kinetics, and in vitro–in vivo correlation for Leuprolide released from an implantable multi-reservoir array," *Pharm. Res.*, **24** (7), pp. 1252-1261, 2007.

[128] J. H. Prescott, S. Lipka, S. Baldwin, N. F. Sheppard, J. M. Maloney, J. Coppeta, B. Yomtov, M. A. Staples and J. T. Santini, "Chronic, programmed polypeptide delivery from an implanted, multireservoir microchip device," *Nat. Biotechnol.*, **24** (4), pp. 437-438, 2006.

[129] E. R. Proos, J. H. Prescott and M. A. Staples, "Long-term stability and *in vitro* release of hPTH(1–34) from a multi-reservoir array," *Pharm. Res.*, **25** (6), pp. 1387-1395, 2008.

[130] A. C. Richards Grayson, I. S. Choi, B. M. Tyler, P. P. Wang, H. Brem, M. J. Cima and R. Langer, "Multi-pulse drug delivery from a resorbable polymeric microchip device," *Nat. Mater.*, **2** (11), pp. 767-772, 2003.

[131] F. Martin, R. Walczak, A. Boiarski, M. Cohen, T. West, C. Cosentino, J. Shapiro and M. Ferrari, "Tailoring width of microfabricated nanochannels to solute size can be used to control diffusion kinetics," *J. Controlled Release*, **102** (1), pp. 123-133, 2005.

[132] P. M. Sinha, G. Valco, S. Sharma, L. Xuewu and M. Ferrari, "Nanoengineered device for drug delivery application," *Nanotechnology*, **15** (10), pp. 585-9, 2004.

[133] G. B. Lesinski, S. Sadhana, K. A. Varker, P. Sinha, M. Ferrari and I. I. I. W. Carson, "Release of biologically functional interferon-alpha from a nanochannel delivery system," *Biomed. Microdevices*, **7** (1), pp. 71-9, 2005.

[134] L. T. Canham, "Silicon quantum wire array fabrication by electrochemical and chemical dissolution of wafers," *Appl. Phys. Lett.*, **57** (10), pp. 1046-50, 1990.

[135] V. Lehmann and U. Gösele, "Porous silicon formation: A quantum wire effect," *Appl. Phys. Lett.*, **58** (8), pp. 856-858, 1991.

[136] J. Salonen and V.-P. Lehto, "Fabrication and chemical surface modification of mesoporous silicon for biomedical applications," *Chem. Eng. J.*, **137** (1), pp. 162-172, 2008.

[137] A. G. Cullis, L. T. Canham and P. D. J. Calcott, "The structural and luminescence properties of porous silicon," *J. Appl. Phys.*, **82** (3), pp. 909-965, 1997.

[138] V. Lehmann, "Trends in fabrication and applications of macroporous silicon," *Phys. Status Solidi A*, **197**, pp. 13-15, 2003.

[139] M. J. Sailor, "Sensor applications of porous silicon," in *Properties of Porous Silicon (EMIS Datareview Series No. 18)*, L. T. Canham (Ed.), London, UK: INSPEC, the Institution of Electrical Engineers, 1997, pp. 364-370.

[140] E. Lorenzo, C. J. Oton, N. E. Capuj, M. Ghulinyan, D. Navarro-Urrios, Z. Gaburro and L. Pavesi, "Porous silicon-based rugate filters," *Appl. Opt.*, **44** (26), pp. 5415-5421, 2005.

[141] A. Janshoff, K.-P. S. Dancil, C. Steinem, D. P. Greiner, V. S.-Y. Lin, C. Gurtner, K. Motesharei, M. J. Sailor and M. R. Ghadiri, "Macroporous p-type silicon Fabry-Pérot layers. Fabrication, characterization, and applications in biosensing," *J. Am. Chem. Soc.*, **120** (46), pp. 12108-12116, 1998.

[142] M. Thönissen, M. Krüger, G. Lerondel and R. Romestain, "Optical applications of porous silicon," in *Properties of Porous Silicon (EMIS Datareview Series No. 18)*, L. T. Canham (Ed.), London, UK: INSPEC, the Institution of Electrical Engineers, 1997, pp. 349-355.

[143] V. P. Bondarenko and V. A. Yakovtseva, "Optoelectronic applications of porous silicon," in *Properties of Porous Silicon (EMIS Datareview Series No. 18)*, L. T. Canham (Ed.), London, UK: INSPEC, the Institution of Electrical Engineers, 1997, pp. 356-363.

[144] N. M. Kalkhoran, F. Namavar and H. P. Maruska, "Optoelectronic applications of porous polycrystalline silicon," *Appl. Phys. Lett.*, **63** (19), pp. 2661-2663, 1993.

[145] V. Lehmann, B. Jobst, T. Muschik, A. Kux and V. Petrova-Koch, "Correlation between optical properties and crystallite size in porous silicon," *Jpn. J. Appl. Phys., Part 1 Regul. Pap. Short Note Rev. Pap.*, **32** (5A), pp. 2095-2099, 1993.

[146] S. Gardelis, U. Bangert and B. Hamilton, "Correlation between structural and optical properties of luminescent porous silicon," *Thin Solid Films*, **255** (1-2), pp. 167-170, 1995.

[147] J. Z. Wallner and P. L. Bergstrom, "A porous silicon based particle filter for microsystems," *Phys. Status Solidi A*, **204** (5), pp. 1469-1473, 2007.

[148] X. G. Zhang, "Morphology and formation mechanisms of porous silicon," *J. Electrochem. Soc.*, **151** (1), pp. C69-C80, 2004.

[149] V. N. Tondare, B. C. Gierhart, D. G. Howitt, R. L. Smith, S. J. Chen and S. D. Collins, "An electron microscopy investigation of the structure of porous silicon by oxide replication," *Nanotechnology*, **19** (22), pp. 225301 (4 pp), 2008.

[150] J. Dian, A. Macek, D. Nižňanský, I. Němec, V. Vrkoslav, T. Chvojka and I. Jelínek, "SEM and HRTEM study of porous silicon - Relationship between fabrication, morphology and optical properties," *Appl. Surf. Sci.*, **238** (1-4), pp. 169-174, 2004.

[151] R. J. Martín-Palma, P. Herrero, R. Guerrero-Lemus, J. D. Moreno and J. M. Martínez-Duart, "Cross-section TEM and optical characterization of porous silicon multilayer stacks," *J. Mater. Sci. Lett.*, **17** (10), pp. 845-847, 1998.

[152] S. Shih, K. H. Jung, R. Z. Qian and D. L. Kwong, "Transmission electron microscopy study of chemically etched porous Si," *Appl. Phys. Lett.*, **62** (5), pp. 467-469, 1993.

[153] R. Hérino, "Pore size distribution in porous silicon," in *Properties of Porous Silicon (EMIS Datareview Series No. 18)*, L. T. Canham (Ed.), London, UK: INSPEC, the Institution of Electrical Engineers, 1997, pp. 89-96.

[154] R. Hérino, G. Bomchil, K. Barla, C. Bertrand and J. L. Ginoux, "Porosity and pore size distributions of porous silicon layers," *J. Electrochem. Soc.*, **134** (8), pp. 1994-2000, 1987.

[155] G. Bomchil, R. Hérino, K. Barla and J. C. Pfister, "Pore size distribution in porous silicon studied by adsorption isotherms," *J. Electrochem. Soc.*, **130** (7), pp. 1611-14, 1983.

[156] P. G. Abramof, A. F. Beloto, A. Y. Ueta and N. G. Ferreira, "X-ray investigation of nanostructured stain-etched porous silicon," *J. Appl. Phys.*, **99** (2), pp. 24304(5pp), 2006.

[157] S. Gardelis, U. Bangert, A. J. Harvey and B. Hamilton, "Double-crystal X-ray diffraction, electron diffraction, and high resolution electron microscopy of luminescent porous silicon," *J. Electrochem. Soc.*, **142** (6), pp. 2094-2101, 1995.

[158] T. K. Sham, D. T. Jiang, I. Coulthard, J. W. Lorimer, X. H. Feng, K. H. Tan, S. P. Frigo, R. A. Rosenberg, D. C. Houghton and B. Bryskiewicz, "Origin of luminescence from porous silicon deduced by synchrotron-light-induced optical luminescence," *Nature*, **363** (6427), pp. 331-334, 1993.

[159] P. G. Abramof, N. G. Ferreira, A. F. Beloto and A. Y. Ueta, "Investigation of nanostructured porous silicon by Raman spectroscopy and atomic force microscopy," *J. Non-Cryst. Solids*, **338-340**, pp. 139-142, 2004.

[160] R. J. Martín-Palma, L. Vázquez, P. Herrero, J. M. Martínez-Duart, M. Schnell and S. Schaefer, "Morphological, optical and electrical characterization of antireflective porous silicon coatings for solar cells," *Opt. Mater.*, **17** (1-2), pp. 75-78, 2001.

[161] C. Wongmanerod, S. Zangooie and H. Arwin, "Determination of pore size distribution and surface area of thin porous silicon layers by spectroscopic ellipsometry," *Appl. Surf. Sci.*, **172** (1-2), pp. 117-125, 2001.

[162] W. J. Salcedo, F. J. Ramirez Fernandez and E. Galeazzo, "Structural characterization of photoluminescent porous silicon with FTIR spectroscopy," *Braz. J. Phys.*, **27A** (4), pp. 158-161, 1997.

[163] J. Rouquérol, D. Avnir, C. W. Fairbridge, D. H. Everett, J. H. Haynes, N. Pernicone, J. D. F. Ramsay, K. S. W. Sing and K. K. Unger, "Recommendations for the characterization of porous solids (IUPAC Technical Report)," *Pure Appl. Chem.*, **66** (8), pp. 1739-1758, 1994.

[164] K. S. W. Sing, D. H. Everett, R. A. W. Haul, L. Moscou, R. A. Pierotti, J. Rouquérol and T. Siemieniewska, "Reporting physisorption data for gas/solid systems with special reference to the determination of surface area and porosity (IUPAC Recommendations 1984)," *Pure Appl. Chem.*, **57** (4), pp. 603-619, 1985.

[165] H. Föll, M. Christophersen, J. Carstensen and G. Hasse, "Formation and application of porous silicon," *Mater. Sci. Eng. R Rep.*, **R39** (4), pp. 93-141, 2002.

[166] A. F. Vyatkin, "Macroporous silicon: Material science and technology," in *Proc. SPIE - Micro- and Nanoelectronics 2003*, Zvenigorod, Russia, pp. 187-191, Oct. 2003.

[167] V. Lehmann and U. Gösele, "The limits of macropore array fabrication," *Thin Solid Films*, **297** (1-2), pp. 13-17, 1997.

[168] H. Föll, J. Carstensen and S. Frey, "Porous and nanoporous semiconductors and emerging applications," *J. Nanomater.*, **2006**, pp. 91635 (10pp), 2006.

[169] L. Santinacci and T. Djenizian, "Electrochemical pore formation onto semiconductor surfaces," *C. R. Chimie*, **11** (9), pp. 964-983, 2008.

[170] L. T. Canham, "Pore type, shape, size, volume and surface area in porous silicon," in *Properties of Porous Silicon (EMIS Datareview Series No. 18)*, L. T. Canham (Ed.), London, UK: INSPEC, the Institution of Electrical Engineers, 1997, pp. 83-88.

[171] E. S. Kooij and J. J. Kelly, "Chemiluminescence from porous silicon," in *Properties of Porous Silicon (EMIS Datareview Series No. 18)*, L. T. Canham (Ed.), London, UK: INSPEC, the Institution of Electrical Engineers, 1997, pp. 276-279.

[172] X. G. Zhang, "Mechanism of pore formation on n-type silicon," *J. Electrochem. Soc.*, **138** (12), pp. 3750-3756, 1991.

[173] C. Lévy-Clément, A. Lagoubi and M. Tomkiewicz, "Morphology of porous n-type silicon obtained by photoelectrochemical etching," *J. Electrochem. Soc.*, **141** (4), pp. 958-967, 1994.

[174] C. Pickering, M. I. J. Beale, D. J. Robbins, P. J. Pearson and R. Greef, "Optical studies of the structure of porous silicon films formed in p-type degenerate and non-degenerate silicon," *J. Phys. C: Solid State Phys.*, **17** (35), pp. 6535-6552, 1984.

[175] M. du Plessis, "Relationship between specific surface area and pore dimension of high porosity nanoporous silicon - Model and experiment," *Phys. Status Solidi A*, **204** (7), pp. 23219-28, 2007.

[176] K. H. Jung, S. Shih and D. L. Kwong, "Developments in luminescent porous Si," *J. Electrochem. Soc.*, **140** (10), pp. 3046-3064, 1993.

[177] B. Hamilton, "Porous silicon," *Semicond. Sci. Technol.*, **10** (9), pp. 1187-1207, 1995.

[178] A. G. Cullis and L. T. Canham, "Visible light emission due to quantum size effects in highly porous crystalline silicon," *Nature*, **353** (6342), pp. 335-338, 1991.

[179] S. Gardelis, J. S. Rimmer, P. Dawson, B. Hamilton, R. A. Kubiak, T. E. Whall and E. H. C. Parker, "Evidence for quantum confinement in the photoluminescence of porous Si and SiGe," *Appl. Phys. Lett.*, **59** (17), pp. 2118-2220, 1991.

[180] R. W. Fathauer, T. George, A. Ksendzov and R. P. Vasquez, "Visible luminescence from silicon wafers subjected to stain etches," *Appl. Phys. Lett.*, **60** (8), pp. 995-997, 1992.

[181] J. Sarathy, S. Shih, K. Jung, C. Tsai, K. H. Li, D. L. Kwong, J. C. Campbell, Y. Shueh-Lin and A. J. Bard, "Demonstration of photoluminescence in nonanodized silicon," *Appl. Phys. Lett.*, **60** (13), pp. 1532-1534, 1992.

[182] A. J. Steckl, J. Xu and H. C. Mogul, "Photoluminescence from stain-etched polycrystalline Si thin films," *Appl. Phys. Lett.*, **62** (17), pp. 2111-2113, 1993.

[183] A. G. Cullis, L. T. Canham, G. M. Williams, P. W. Smith and O. D. Dosser, "Correlation of the structural and optical properties of luminescent, highly oxidized porous silicon," *J. Appl. Phys.*, **75** (1), pp. 493-501, 1994.

[184] Y. Gao, D. G. Uttamchandani and B. Culshaw, "Comparative study on photoluminescence of porous silicon fabricated by different methods," in *Proc. SPIE - 2nd International Conference on Optoelectronic Science and Engineering '94*, Beijing, China, pp. 68-70, Aug. 1994.

[185] S. Gardelis and B. Hamilton, "The effect of surface modification on the luminescence of porous silicon," *J. Appl. Phys.*, **76** (9), pp. 5327-5333, 1994.

[186] U. Gösele and V. Lehmann, "Light-emitting porous silicon," *Mater. Chem. Phys.*, **40** (4), pp. 253-259, 1995.

[187] D. Dimova-Malinovska, M. Sendova-Vassileva, M. Kamenova, N. Tzenov and M. Tzolov, "On the origin of the visible luminescence from porous silicon," *Vacuum*, **47** (9), pp. 1133-1138, 1996.

[188] W. N. Huang, K. Y. Tong and P. W. Chan, "Photoluminescence in porous sputtered polysilicon films formed by chemical etching," *Semicond. Sci. Technol.*, **12** (2), pp. 228-233, 1997.

[189] S. Cheylan, T. Trifonov, A. Rodriguez, L. F. Marsal, J. Pallares, R. Alcubilla and G. Badenes, "Visible light emission from macroporous Si," *Opt. Mater.*, **29** (2-3), pp. 262-267, 2006.

[190] G. M. Williams, "Cathodoluminescence properties of porous silicon," in *Properties of Porous Silicon (EMIS Datareview Series No. 18)*, L. T. Canham (Ed.), London, UK: INSPEC, the Institution of Electrical Engineers, 1997, pp. 270-275.

[191] A. Biaggi-Labiosa, L. F. Fonseca, O. Resto and I. Balberg, "Tuning the cathodoluminescence of porous silicon films," *J. Lumin.*, **128** (3), pp. 321-327, 2008.

[192] L. T. Canham, W. Y. Leong, M. I. J. Beale, T. I. Cox and L. Taylor, "Efficient visible electroluminescence from highly porous silicon under cathodic bias," *Appl. Phys. Lett.*, **61** (21), pp. 2563-2565, 1992.

[193] S. Lazarouk, V. Bondarenko, P. Jaguiro, N. Lacquaniti, S. La Monica, G. Maiello, G. Masini and A. Ferrari, "Electrical characterization of visible emitting electroluminescent Schottky diodes based on n-type porous silicon and on highly doped n-type porous polysilicon," *J. Non-Cryst. Solids*, **198-200** (Part 2), pp. 973-976, 1996.

[194] N. Yamamoto, A. Sumiya and H. Takai, "Electroluminescence (EL) from photo-chemically etched silicon," *Mater. Sci. Eng. B Solid-State Mater. Adv. Technol.*, **69-70**, pp. 205-209, 2000.

[195] E. S. Kooij, R. W. Despo and J. J. Kelly, "Electroluminescence from porous silicon due to electron injection from solution," *Appl. Phys. Lett.*, **66** (19), pp. 2552-2554, 1995.

[196] W. N. Huang, K. Y. Tong and P. W. Chan, "Electroluminescence in porous polycrystalline silicon," *Int. J. Electron.*, **85** (4), pp. 419-423, 1998.

[197] J. Xu and A. J. Steckl, "Visible electroluminescence from stain-etched porous Si diodes," *IEEE Electron Device Lett.*, **15** (12), pp. 507-509, 1994.

[198] E. S. Kooij, K. Butter and J. J. Kelly, "Hole injection at the silicon/aqueous electrolyte interface: A possible mechanism for chemiluminescence from porous silicon," *J. Electrochem. Soc.*, **145** (4), pp. 1232-1238, 1998.

[199] L. T. Canham, "Storage of porous silicon," in *Properties of Porous Silicon (EMIS Datareview Series No. 18)*, L. T. Canham (Ed.), London, UK: INSPEC, the Institution of Electrical Engineers, 1997, pp. 44-50.

[200] S. Godefroo, M. Hayne, M. Jivanescu, A. Stesmans, M. Zacharias, O. I. Lebedev, G. Van Tendeloo and V. V. Moshchalkov, "Classification and control of the origin of photoluminescence from Si nanocrystals," *Nat. Nanotechnol.*, **3** (3), pp. 174-178, 2008.

[201] C. L. Curtis, V. V. Doan, G. M. Credo and M. J. Sailor, "Observation of optical cavity modes in photoluminescent porous silicon films," *J. Electrochem. Soc.*, **140** (12), pp. 3492-3494, 1993.

[202] J. D. Birchall, "The essentiality of silicon in biology," *Chem. Soc. Rev.*, **24** (5), pp. 351-357, 1995.

[203] C. Pacholski, M. Sartor, M. J. Sailor, F. Cunin and G. M. Miskelly, "Biosensing using porous silicon double-layer interferometers: Reflective interferometric fourier transform spectroscopy," *J. Am. Chem. Soc.*, **127**, pp. 11636-11645, 2005.

[204] E. J. Anglin, M. P. Schwartz, V. P. Ng, L. A. Perelman and M. J. Sailor, "Engineering the chemistry and nanostructure of porous silicon Fabry-Pérot films for loading and release of a steroid," *Langmuir*, **20** (25), pp. 11264-11269, 2004.

[205] D. F. Williams, "On the mechanisms of biocompatibility," *Biomaterials*, **29** (20), pp. 2941-53, 2008.

[206] B. D. Ratner and S. J. Bryant, "BIOMATERIALS: Where we have been and where we are going," *Annu. Rev. Biomed. Eng.*, **6** (1), pp. 41-75, 2004.

[207] L. T. Canham, C. L. Reeves, J. P. Newey, M. R. Houlton, T. I. Cox, J. M. Buriak and M. P. Stewart, "Derivatized mesoporous silicon with dramatically improved stability in simulated human blood plasma," *Adv. Mater.*, **11** (18), pp. 1505-1507, 1999.

[208] M. Arroyo-Hernández, J. Pérez-Rigueiro, M. Manso-Silván and J. M. Martínez-Duart, "Bioactivity test for amine-based functionalized meso- and macro-porous silicon substrates," *Mater. Sci. Eng. C, Biomin. Supramol. Syst.*, **27** (5-8), pp. 1211-14, 2007.

[209] L. T. Canham, "Nanoscale semiconducting silicon as a nutritional food additive," *Nanotechnology*, **18** (18), pp. 185704, 2007.

[210] W. Y. Leong, A. Loni and L. T. Canham, "Electrically enhanced erosion of porous Si material in electrolyte by pH modulation and its application in chronotherapy," *Phys. Status Solidi A*, **204** (5), pp. 1486-90, 2007.

[211] J.-N. Chazalviel and F. Ozanam, "Surface modification of porous silicon," in *Properties of Porous Silicon (EMIS Datareview Series No. 18)*, L. T. Canham (Ed.), London, UK: INSPEC, the Institution of Electrical Engineers, 1997, pp. 59-65.

[212] J. H. Song and M. J. Sailor, "Chemical modification of crystalline porous silicon surfaces," *Comments Inorg. Chem.*, **21** (1), pp. 69-84, 1999.

[213] L. Vaccari, D. Canton, N. Zaffaroni, R. Villa, M. Tormen and E. Fabrizio, "Porous silicon as drug carrier for controlled delivery of doxorubicin anticancer agent," *Microelectron. Eng.*, **83** (4-9), pp. 1598-1601, 2006.

[214] A. M. Kaukonen, L. Laitinen, J. Salonen, J. Tuura, T. Heikkilä, T. Limnell, J. Hirvonen and V.-P. Lehto, "Enhanced *in vitro* permeation of furosemide loaded into thermally carbonized mesoporous silicon (TCPSi) microparticles," *Eur. J. Pharm. Biopharm*, **66** (3), pp. 348-356, 2007.

[215] C. A. Prestidge, T. J. Barnes, A. Mierczynska-Vasilev, W. Skinner, F. Peddie and C. Barnett, "Loading and release of a model protein from porous silicon powders," *Phys. Status Solidi A*, **204** (10), pp. 3361-3366, 2007.

[216] C. A. Prestidge, T. J. Barnes, A. Mierczynska-Vasilev, I. Kempson, F. Peddie and C. Barnett, "Peptide and protein loading into porous silicon wafers," *Phys. Status Solidi A*, **205** (2), pp. 311-315, 2008.

[217] J. C. Thomas, C. Pacholski and M. J. Sailor, "Delivery of nanogram payloads using magnetic porous silicon microcarriers," *Lab Chip*, **6** (6), pp. 782-7, 2006.

[218] Y. Koh, S. Jang, J. Kim, S. Kim, Y. C. Ko, S. Cho and H. Sohn, "DBR PSi/PMMA composite materials for smart patch application," *Colloids Surf. A Physicochem. Eng. Asp.*, **313-314**, pp. 328-331, 2008.

[219] W. Sun, J. E. Puzas, T.-J. Sheu, X. Liu and P. M. Fauchet, "Nano- to microscale porous silicon as a cell interface for bone-tissue engineering," *Adv. Mater.*, **19** (7), pp. 921-924, 2007.

[220] W. Sun, J. E. Puzas, T.-J. Sheu and P. M. Fauchet, "Porous silicon as a cell interface for bone tissue engineering," *Phys. Status Solidi A*, **204** (5), pp. 1429-33, 2007.

[221] A. S.-W. Goh, A. Y.-F. Chung, R. H.-G. Lo, T.-N. Lau, S. W.-K. Yu, M. Chng, S. Satchithanantham, S. L.-E. Loong, D. C.-E. Ng, B.-C. Lim, *et al.*, "A novel approach to brachytherapy in hepatocellular carcinoma using a phosphorous^{32} (^{32}P) brachytherapy delivery device - A first-in-man study," *Int. J. Radiation Oncology Biol. Phys.*, **67** (3), pp. 786-792, 2007.

[222] A. Uhlir, "Electrolytic shaping of germanium and silicon," *Bell Syst. Tech. J.*, **35** (2), pp. 333-347, 1956.

[223] C. S. Fuller and J. A. Ditzenberger, "Diffusion of donor and acceptor elements in silicon," *J. Appl. Phys.*, **27** (5), pp. 544-553, 1956.

[224] D. R. Turner, "Electropolishing silicon in hydrofluoric acid solutions," *J. Electrochem. Soc.*, **105** (7), pp. 402-408, 1958.

[225] R. J. Archer, "Stain films on silicon," *J. Phys. Chem. Solids*, **14**, pp. 104-110, 1960.

[226] Y. Watanabe, Y. Arita, T. Yokoyama and Y. Igarashi, "Formation and properties of porous silicon and its application," *J. Electrochem. Soc.*, **122** (10), pp. 1351-1355, 1975.

[227] A. Halimaoui, "Porous silicon formation by anodisation," in *Properties of Porous Silicon (EMIS Datareview Series No. 18)*, L. T. Canham (Ed.), London, UK: INSPEC, the Institution of Electrical Engineers, 1997, pp. 12-22.

[228] V. Lehmann, *Electrochemistry of Silicon: Instrumentation, Science, Materials and Applications*, Verlag, Germany: Wiley-VCH, 2002.

[229] V. Lehmann, R. Stengl and A. Luigart, "On the morphology and the electrochemical formation mechanism of mesoporous silicon," *Mater. Sci. Eng. B Solid-State Mater. Adv. Technol.*, **69**, pp. 11-22, 2000.

[230] M. L. Ngan, K. C. Lee and K. W. Cheah, "Photochemical etching of silicon," *J. Porous Mater.*, **7** (1-3), pp. 41-45, 2000.

[231] K. W. Kolasinski, D. Mills and M. Nahidi, "Laser assisted and wet chemical etching of silicon nanostructures," *J. Vac. Sci. Technol. A*, **24** (4), pp. 1474-1479, 2006.

[232] Q. Chen, J. Zhu, X. G. Li and C. G. Fan, "Photoluminescence in porous silicon obtained by hydrothermal etching," *Phys. Lett. A*, **220** (4-5), pp. 293-296, 1996.

[233] E. A. De Vasconcelos, E. F. Da Silva Jr, B. E. C. A. Dos Santos, W. M. De Azevedo and J. A. K. Freire, "A new method for luminescent porous silicon formation: Reaction-induced vapor-phase stain etch," *Phys. Status Solidi A*, **202** (8), pp. 1539-1542, 2005.

[234] C. M. A. Ashruf, P. J. French, P. M. M. C. Bressers and J. J. Kelly, "Galvanic porous silicon formation without external contacts," *Sens. Actuators A*, **74** (1-3), pp. 118-122, 1999.

[235] X. Li and P. W. Bonn, "Metal-assisted chemical etching in HF/H_2O_2 produces porous silicon," *Appl. Phys. Lett.*, **77** (16), pp. 2572-2574, 2000.

[236] A. Splinter, J. Stüermann and W. Benecke, "Novel porous silicon formation without external contact," in *Proc. SPIE - Micromachining and Microfabrication Process Technology VI*, Santa Clara, CA, USA, pp. 398-405, Sep. 2000.

[237] ---, "New porous silicon formation technology using internal current generation with galvanic elements," *Sens. Actuators A*, **92** (1-3), pp. 394-399, 2001.

[238] K. Tsujino and M. Matsumura, "Boring deep cylindrical nanoholes in silicon using silver nanoparticles as a catalyst," *Adv. Mater.*, **17** (8), pp. 1045-1047, 2005.

[239] P. Allongue, "Porous silicon formation mechanisms," in *Properties of Porous Silicon (EMIS Datareview Series No. 18)*, L. T. Canham (Ed.), London, UK: INSPEC, the Institution of Electrical Engineers, 1997, pp. 3-11.

[240] X. G. Zhang, "Porous Silicon," in *Electrochemistry of Silicon and Its Oxide*, New York, USA: Kluwer Academic / Plenum, 2001, pp. 353-439.

[241] J. L. Coffer, "Porous silicon formation by stain etching," in *Properties of Porous Silicon (EMIS Datareview Series No. 18)*, L. T. Canham (Ed.), London, UK: INSPEC, the Institution of Electrical Engineers, 1997, pp. 23-29.

[242] S. Shih, K. H. Jung, T. Y. Hsieh, J. Sarathy, J. C. Campbell and D. L. Kwong, "Photoluminescence and formation mechanism of chemically etched silicon," *Appl. Phys. Lett.*, **60** (15), pp. 1863-1865, 1992.

[243] D. R. Turner, "On the mechanism of chemically etching Germanium and Silicon," *J. Electrochem. Soc.*, **107** (10), pp. 810-816, 1960.

[244] M. T. Kelly, J. K. M. Chun and A. B. Bocarsly, "High efficiency chemical etchant for the formation of luminescent porous silicon," *Appl. Phys. Lett.*, **64** (13), pp. 1693-1695, 1994.

[245] É. Vázsonyi, E. Szilágyi, P. Petrik, Z. E. Horváth, T. Lohner, M. Fried and G. Jalsovszky, "Porous silicon formation by stain etching," *Thin Solid Films*, **388** (1-2), pp. 295-302, 2001.

[246] E. A. Starostina, V. V. Starkov and A. F. Vyatkin, "Porous-silicon formation in HF-HNO_3-H_2O etchants," *Russ. Microelectron.*, **31** (2), pp. 88-96, 2002.

[247] C. Kaminski, *Intelligent Drug Delivery Device from Nanoporous Silicon*, Diploma Dissertation, Universität Karlsruhe (TH, Germany) and University of Southampton (UK), 2004.

[248] M. I. J. Beale, J. D. Benjamin, M. J. Uren, N. G. Chew and A. G. Cullis, "The formation of porous silicon by chemical stain etches," *J. Cryst. Growth*, **75** (3), pp. 408-414, 1986.

[249] A. J. Steckl, J. Xu, H. C. Mogul and S. Mogren, "Doping-induced selective area photoluminescence in porous silicon," *Appl. Phys. Lett.*, **62** (16), pp. 1982-1984, 1993.

[250] J. Xu and A. J. Steckl, "Fabrication of visibly photoluminescent Si microstructures by focused ion beam implantation and wet etching," *Appl. Phys. Lett.*, **65** (16), pp. 2081-2083, 1994.

[251] M. Nahidi and K. W. Kolasinski, "Effects of stain etchant composition on the photoluminescence and morphology of porous silicon," *J. Electrochem. Soc.*, **153** (1), pp. C19-C26, 2006.

[252] B. González-Díaz, R. Guerrero-Lemus, N. Marrero, C. Hernández-Rodríguez, F. A. Ben-Hander and J. M. Martínez-Duart, "Anisotropic textured silicon obtained by stain-etching at low etching rates," *J. Phys. D: Appl. Phys.*, **39** (4), pp. 631-634, 2006.

[253] T. I. Kamins, "Structure and properties of LPCVD silicon films," *J. Electrochem. Soc.*, **127** (3), pp. 686-690, 1980.

[254] ---, *Polycrystalline Silicon for Integrated Circuit Applications* Boston, USA: Kluwer Acedemic Publishers, 1988.

[255] C. A. Zorman and M. Mehregany, "Materials for Microelectromechanical Systems," in *The MEMS Handbook: Volume II - MEMS: Design and Fabrication*, M. Gad-el-Hak (Ed.), 2nd ed., Boca Raton, USA: CRC Press, 2006, pp. 2-3-2-9.

[256] T. I. Kamins, "Resistivity of LPCVD polycrystalline-silicon films," *J. Electrochem. Soc.*, **126** (5), pp. 833-837, 1979.

[257] L. T. Canham, C. L. Reeves, D. O. King, P. J. Branfield, J. G. Crabb and M. C. L. Ward, "Bioactive polycrystalline silicon," *Adv. Mater.*, **8** (10), pp. 850-852, 1996.

[258] R. C. Anderson, R. S. Muller and C. W. Tobias, "Porous polycrystalline silicon: A new material for MEMS," *J. Microelectromech. Syst.*, **3** (1), pp. 10-18, 1994.

[259] S.-C. Bae and S.-Y. Choi, "Efficient and stable field emission from the oxidized porous polysilicon using Pt/Ti multilayer electrode," *J. Mater. Sci.*, **42** (4), pp. 1369-1375, 2007.

[260] R. He and C.-J. Kim, "On-wafer monolithic encapsulation by surface micromachining with porous polysilicon shell," *J. Microelectromech. Syst.*, **16** (2), pp. 462-472, 2007.

[261] E. J. Connolly, H. T. M. Pham, P. M. Sarro, P. J. French and G. M. O'Halloran, "Comparison of porous silicon, porous polysilicon and porous silicon carbide as materials for humidity sensing applications," *Sens. Actuators A*, **99** (1-2), pp. 25-30, 2002.

[262] P. G. Han, H. Wong and M. C. Poon, "Sensitivity and stability of porous polycrystalline silicon gas sensor," *Colloids Surf. A Physicochem. Eng. Asp.*, **179** (2-3), pp. 171-175, 2001.

[263] K. H. Jung, S. Shih, D. L. Kwong, G. G. Cho and B. E. Gnade, "Visible photoluminescence from porous Si formed by annealing and chemically etching amorphous Si," *Appl. Phys. Lett.*, **61** (20), pp. 2467-2469, 1992.

[264] A. J. Steckl and H. C. Mogul, "Crystallinity and photoluminescence in stain-etched porous Si," *J. Electrochem. Soc.*, **141** (3), pp. 674-679, 1994.

[265] A. J. Steckl, J. Xu, H. C. Mogul and S. M. Prokes, "Si oxyhydrides on stain-etched porous Si thin films and correlation with crystallinity and photoluminescence," *J. Electrochem. Soc.*, **142** (5), pp. 69-71, 1995.

[266] K. Higa, T. Asano and T. Miyasato, "Variation of photoluminescence properties of stain-etched Si with crystallinity of starting polycrystalline Si films," *Jpn. J. Appl. Phys., Part 2 Lett.*, **33** (12B), pp. L1733-L1736, 1994.

[267] P. G. Han, H. Wong, A. H. P. Chan and M. C. Poon, "A novel approach for fabricating light-emitting porous polysilicon films," *Microelectron. Reliab.*, **42** (6), pp. 929-933, 2002.

[268] G. M. Dougherty, A. P. Pisano and T. Sands, "Processing and morphology of permeable polycrystalline silicon thin films," *J. Mater. Res.*, **17** (9), pp. 2235-2242, 2002.

[269] G. M. Dougherty, T. D. Sands and A. P. Pisano, "Microfabrication using one-step LPCVD porous polysilicon films," *J. Microelectromech. Syst.*, **12** (4), pp. 418-424, 2003.

[270] H. Kahn, S. Stemmer, K. Nandakumar, A. H. Heuer, R. L. Mullen, R. Ballarini and M. A. Huff, "Mechanical properties of thick, surface micromachined polysilicon films," in *Proc. 9th IEEE International Workshop on Micro Electro Mechanical Systems (MEMS 1996)*, San Diego, CA, USA, pp. 343-348, Feb. 1996.

[271] P. Guyader, P. Joubert, M. Guendouz, C. Beau and M. Sarret, "Effect of grain boundaries on the formation of luminescent porous silicon from polycrystalline silicon films," *Appl. Phys. Lett.*, **65** (14), pp. 1787-1789, 1994.

[272] S. Beeby, G. J. Ensell, M. Kraft and N. White, *MEMS Mechanical Sensors*, 2nd ed., London, UK: Artech House, 2004.

[273] W. Kern and D. A. Poutinen, "Cleaning solution based on hydrogen peroxide for use in silicon semiconductor technology," *RCA Rev.*, **31**, pp. 187-206, 1970.

[274] G. S. May and S. M. Sze, *Fundamentals of Semiconductor Fabrication*, New York, USA: John Wiley & Sons, Inc., 2004.

[275] S. M. Sze, *Semiconductor Devices: Physics and Technology*, 2nd ed., New York, USA: John Wiley & Sons, Inc., 2002.

[276] S. Mohmad, *Intelligent Bio-Sensing and Drug Delivery from Nanoporous Silicon*, MSc. Dissertation, University of Southampton, 2004.

[277] SILVACO International, *ATHENA User's Manual*, Santa Clara, USA, 2006.

[278] ---, *Virtual Wafer FAB (VWF) Interactive Tools User's Manual*, Santa Clara, USA, 2005.

[279] V. V. Doan and M. J. Sailor, "Luminescent color image generation on porous silicon," *Science*, **256** (5065), pp. 1791-1792, 1992.

[280] J. I. Goldstein, D. E. Newbury, D. C. Joy, C. E. Lyman, P. Echlin, E. Lifshin, L. Sawyer and J. R. Michael, *Scanning Electron Microscopy and X-Ray Microanalysis*, 3rd ed., New York, USA: Springer, 2003.

[281] A. Grosman and C. Ortega, "Chemical composition of 'fresh' porous silicon," in *Properties of Porous Silicon (EMIS Datareview Series No. 18)*, L. T. Canham (Ed.), London, UK: INSPEC, the Institution of Electrical Engineers, 1997, pp. 145-153.

[282] R. Guerrero-Lemus, F. A. Ben-Hander, J. L. G. Fierro, C. Hernández-Rodríguez and J. M. Martínez-Duart, "Compositional and photoluminescent properties of anodically and stain etched porous silicon," *Phys. Status Solidi A*, **197** (1), pp. 137-143, 2003.

[283] S. D. Campbell, L. A. Jones, E. Nakamichi, F. X. Wei, L. D. Zajchowski and D. F. Thomas, "Spectral and structural features of porous silicon prepared by chemical and electrochemical etching processes," *J. Vac. Sci. Technol. B Microelectron. Nanometer. Struct.*, **13** (3), pp. 1184-1189, 1995.

[284] G. Binnig, C. F. Quate and C. Gerber, "Atomic force microscope," *Phys. Rev. Lett.*, **56** (9), pp. 930-933, 1986.

[285] Veeco Instruments Inc., *A Practical Guide to SPM: Scanning Probe Microscopy*, http://www.veeco.com/pdfs.php/166, last accessed in Nov. 2008.

[286] G. Mauckner, T. Walter, T. Baier, K. Thonke, R. Sauer, R. Houbertz, U. Memmert and R. J. Behm, "Luminescence properties and surface topography of porous silicon," *J. Lumin.*, **57** (1-6), pp. 211-215, 1993.

[287] M. Hatzakis, B. J. Canavello and J. M. Shaw, "Single-step optical lift-off process," *IBM J. Res. Dev.*, **24** (4), pp. 452-460, 1980.

[288] M. E. Nasir, *Fabrication and Spectroscopy of Nanostructured Surfaces on Silicon*, Ph.D. Dissertation, University of Manchester, 2008.

[289] Y. Tao and M. Esashi, "Local formation of macroporous silicon through a mask," *J. Micromech. Microeng.*, **14** (10), pp. 1411-1415, 2004.

[290] V. Lehmann, "Physics of macroporous silicon formation," *Thin Solid Films*, **255** (1-2), pp. 1-4, 1995.

[291] S. Shingubara, "Fabrication of nanomaterials using porous alumina templates," *J. Nanoparticle Res.*, **5** (1-2), pp. 17-30, 2003.

[292] H. Asoh and S. Ono, "Fabrication of ordered anodic nanoporous alumina layers and their application to nanotechnology," in *Electrocrystallization in Nanotechnology*, G. T. Staikov (Ed.), Weinheim, Germany: Wiley-VCH Verlag, 2007, pp. 138-166.

[293] G. D. Sulka, "Highly ordered anodic porous alumina formation by self-organized anodizing," in *Nanostructured Materials in Electrochemistry*, A. Eftekhari (Ed.), Weinheim, Germany: Wiley-VCH Verlag, 2008, pp. 1-116.

[294] Y. Xia, B. Gates, Y. Yin and Y. Lu, "Monodispersed colloidal spheres: Old materials with new applications," *Adv. Mater.*, **12** (10), pp. 693-713, 2000.

[295] S.-M. Yang, S. G. Jang, D.-G. Choi, S. Kim and H. K. Yu, "Nanomachining by colloidal lithography," *Small*, **2** (4), pp. 458-475, 2006.

[296] H. Masuda and K. Fukuda, "Ordered metal nanohole arrays made by a two-step replication of honeycomb structures of anodic alumina," *Science*, **268** (5216), pp. 1466-1468, 1995.

[297] A. D. Franklin, M. R. Maschmann, M. DaSilva, D. B. Janes, T. S. Fisher and T. D. Sands, "In-place fabrication of nanowire electrode arrays for vertical nanoelectronics on Si

substrates," *J. Vac. Sci. Technol. B Microelectron. Nanometer. Struct.*, **25** (2), pp. 343-347, 2007.

[298] S. Mátéfi-Tempfli, M. Mátéfi-Tempfli, A. Vlad, V. Antohe and L. Piraux, "Nanowires and nanostructures fabrication using template methods: a step forward to real devices combining electrochemical synthesis with lithographic techniques," *J. Mater. Sci. Mater. Electron.*, **20** (Supp. 1), pp. S249-S254, 2009.

[299] J. Liang, H. Chik and J. Xu, "Nonlithographic fabrication of lateral superlattices for nanometric electromagnetic-optic applications," *IEEE J. Sel. Top. Quantum. Electron.*, **8** (5), pp. 998-1008, 2002.

[300] S.-K. Hwang, J. Lee, S.-H. Jeong, P.-S. Lee and K.-H. Lee, "Fabrication of carbon nanotube emitters in an anodic aluminium oxide nanotemplate on a Si wafer by multi-step anodization," *Nanotechnology*, **16** (6), pp. 850-858, 2005.

[301] H. Masuda and K. Nishio, "Synthesis and applications of highly ordered anodic porous alumina," in *Self-Organized Nanoscale Materials*, M. Adachi and D. J. Lockwood (Eds.), New York, USA: Springer, 2006, pp. 296-312.

[302] D. T. Crouse, Y.-H. Lo, A. E. Miller and M. M. Crouse, "Self-ordered pore structure of anodized aluminum on silicon and pattern transfer," *Appl. Phys. Lett.*, **76** (1), pp. 49-51, 2000.

[303] J. P. O'Sullivan and G. C. Wood, "The morphology and mechanism of formation of porous anodic films on aluminium," *Proc. R. Soc. Lond. A Math. Phys. Sci.*, **317** (1531), pp. 511-543, 1970.

[304] O. Jessensky, F. Müller and U. Gösele, "Self-organized formation of hexagonal pore structures in anodic alumina," *J. Electrochem. Soc.*, **145** (11), pp. 3735-3740, 1998.

[305] M. Kokonou, A. G. Nassiopoulou and K. P. Giannakopoulos, "Ultra-thin porous anodic alumina films with self-ordered cylindrical vertical pores on a p-type silicon substrate," *Nanotechnology*, **16** (1), pp. 103-106, 2005.

[306] L. E. Fratila-Apachitei, H. Terryn, P. Skeldon, G. E. Thompson, J. Duszczyk and L. Katgerman, "Influence of substrate microstructure on the growth of anodic oxide layers," *Electrochim. Acta.*, **49** (7), pp. 1127-1140, 2004.

[307] A. Cai, H. Zhang, H. Hua and Z. Zhang, "Direct formation of self-assembled nanoporous aluminium oxide on SiO_2 and Si substrates," *Nanotechnology*, **13** (5), pp. 627-630, 2002.

[308] S.-K. Hwang, S.-H. Jeong, H.-Y. Hwang, O.-J. Lee and K.-H. Lee, "Fabrication of highly ordered pore array in anodic alumina oxide," *Korean J. Chem. Eng.*, **19** (3), pp. 467-473, 2002.

[309] F. Li, L. Zhang and R. M. Metzger, "On the growth of highly ordered pores in anodized aluminum oxide," *Chem. Mater.*, **10** (9), pp. 2470-2480, 1998.

[310] A. Yin, M. Tzolov, D. Cardimona, L. Guo and J. Xu, "Fabrication of highly ordered anodic aluminium oxide templates on silicon substrates," *IET Circuits Devices Syst.*, **1** (3), pp. 205-209, 2007.

[311] S.-Z. Chu, K. Wada, S. Inoue, M. Isogai and A. Yasumori, "Fabrication of ideally ordered nanoporous alumina films and integrated alumina nanotubule arrays by high field anodization," *Adv. Mater.*, **17** (17), pp. 2115-2119, 2005.

[312] A. P. Li, F. Müller, A. Birner, K. Nielsch and U. Gösele, "Hexagonal pore arrays with a 50–420 nm interpore distance formed by self-organization in anodic alumina," *J. Appl. Phys.*, **84** (11), pp. 6023-6026, 1998.

[313] M. M. Crouse, A. E. Miller, D. T. Crouse and A. A. Ikram, "Nanoporous alumina template with in situ barrier oxide removal, synthesized from a multilayer thin film precursor," *J. Electrochem. Soc.*, **152** (10), pp. D167-D172, 2005.

[314] K. Nielsch, J. Choi, K. Schwirn, R. B. Wehrspohn and U. Gosele, "Self-ordering regimes of porous alumina: The 10% porosity rule," *Nano Lett.*, **2** (7), pp. 677-680, 2002.

[315] H. Masuda, F. Hasegwa and S. Ono, "Self-ordering of cell arrangement of anodic porous alumina formed in sulfuric acid solution," *J. Electrochem. Soc.*, **144** (5), pp. L127-L130, 1997.

[316] H. Masuda and M. Satoh, "Fabrication of gold nanodot array using anodic porous alumina as an evaporation mask," *Jpn. J. Appl. Phys. Part 2 Lett.*, **35** (1B), pp. L126-L129, 1996.

[317] H. Masuda, K. Yada and A. Osaka, "Self-ordering of cell configuration of anodic porous alumina with large-size pores in phosphoric acid solution," *Jpn. J. Appl. Phys. Part 2 Lett.*, **37** (11A), pp. L1340-L1342, 1998.

[318] A. P. Li, F. Müller and U. Gösele, "Polycrystalline and monocrystalline pore arrays with large interpore distance in anodic alumina," *Electrochem. Solid-State Lett.*, **3** (3), pp. 131-134, 2000.

[319] Y. Li, M. Zheng, L. Ma and W. Shen, "Fabrication of highly ordered nanoporous alumina films by stable high-field anodization," *Nanotechnology*, **17** (20), pp. 5101-5105, 2006.

[320] W. Lee, R. Ji, U. Gösele and K. Nielsch, "Fast fabrication of long-range ordered porous alumina membranes by hard anodization," *Nature Mater.*, **5** (9), pp. 741-747, 2006.

[321] Y. Li, Z. Y. Ling, S. S. Chen and J. C. Wang, "Fabrication of novel porous anodic alumina membranes by two-step hard anodization," *Nanotechnology*, **19** (22), pp. 225604 (6pp), 2008.

[322] K. Schwirn, W. Lee, R. Hillebrand, M. Steinhart, K. Nielsch and U. Gösele, "Self-ordered anodic aluminum oxide formed by H_2SO_4 hard anodization," *ACS Nano*, **2** (2), pp. 302-310, 2008.

[323] H. Masuda, K. Kanezawa and K. Nishio, "Fabrication of ideally ordered nanohole arrays in anodic porous alumina based on nanoindentation using scanning probe microscope," *Chem. Lett.*, **31** (12), pp. 1218-1219, 2002.

[324] C. Y. Liu, A. Datta and Y. L. Wang, "Ordered anodic alumina nanochannels on focused-ion-beam-prepatterned aluminum surfaces," *Appl. Phys. Lett.*, **78** (1), pp. 120-122, 2001.

[325] S.-H. Hong, K.-S. Han, H. Lee, J. U. Cho and Y. K. Kim, "Fabrication of nano-porous structure on silicon substrate using nanoimprint lithography with an anodic aluminum oxide nano-template," *Jpn. J. Appl. Phys., Part 1 Regul. Pap. Short Note Rev. Pap.*, **46** (9B), pp. 6375-6377, 2007.

[326] H. Masuda, H. Yamada, M. Satoh, H. Asoh, M. Nakao and T. Tamamura, "Highly ordered nanochannel-array architecture in anodic alumina," *Appl. Phys. Lett.*, **71** (19), pp. 2770-2772, 1997.

[327] Y. Matsui, K. Nishio and H. Masuda, "Highly ordered anodic porous alumina with 13-nm hole intervals using a 2D array of monodisperse nanoparticles as a template," *Small*, **2** (4), pp. 522-525, 2006.

[328] J. Zou, X. Qi, L. Tan and B. J. H. Stadler, "Large-scale ordering of porous Si using anodic aluminum oxide grown by directed self-assembly," *Appl. Phys. Lett.*, **89** (9), pp. 093106 (3pp), 2006.

[329] F. Zacharatos, V. Gianneta and A. G. Nassiopoulou, "Highly ordered hexagonally arranged nanostructures on silicon through a self-assembled silicon-integrated porous anodic alumina masking layer," *Nanotechnology*, **19** (49), pp. 495306 (5 pp), 2008.

[330] H. Asoh, K. Sasaki and S. Ono, "Electrochemical etching of silicon through anodic porous alumina," *Electrochem. Commun.*, **7** (9), pp. 953-956, 2005.

[331] A. Oide, H. Asoh and S. Ono, "Natural lithography of Si surfaces using localized anodization and subsequent chemical etching," *Electrochem. Solid-State Lett.*, **8** (7), pp. G172-G175, 2005.

[332] H. Asoh, M. Matsuo, M. Yoshihama and S. Ono, "Transfer of nanoporous pattern of anodic porous alumina into Si substrate," *Appl. Phys. Lett.*, **83** (21), pp. 4408-4410, 2003.

[333] S. Z. Chu, K. Wada, S. Inoue and S. Todoroki, "Formation and microstructures of anodic alumina films from aluminum sputtered on glass substrate," *J. Electrochem. Soc.*, **149** (7), pp. B321-B327, 2002.

[334] B. Das, "Investigation of nanoporous thin-film alumina templates," *J. Electrochem. Soc.*, **151** (6), pp. D46-D50, 2004.

[335] P. G. Miney, P. E. Colavita, M. V. Schiza, Ryan J. Priore, F. G. Haibach and M. L. Myrick, "Growth and characterization of a porous aluminum oxide film formed on an electrically insulating support," *Electrochem. Solid-State Lett.*, **6** (10), pp. B42-B45, 2003.

[336] S. K. Thamida and H.-C. Chang, "Nanoscale pore formation dynamics during aluminum anodization," *Chaos*, **12** (1), pp. 240-251, 2002.

[337] V. P. Parkhutik and V. I. Shershulsky, "Theoretical modelling of porous oxide growth on aluminium," *J. Phys. D Appl. Phys.*, **25** (8), pp. 1258-1263, 1992.

[338] Z. Wu, C. Richter and L. Menon, "A study of anodization process during pore formation in nanoporous alumina templates," *J. Electrochem. Soc.*, **154** (1), pp. E8-E12, 2007.

[339] M. Kokonou and A. G. Nassiopoulou, "Nanostructuring Si surface and Si/SiO_2 interface using porous-alumina-on-Si template technology. Electrical characterization of Si/SiO_2 interface," *Physica E*, **38** (1-2), pp. 1-5, 2007.

[340] S. Ono, A. Oide and H. Asoh, "Nanopatterning of silicon with use of self-organized porous alumina and colloidal crystals as mask," *Electrochim. Acta.*, **52** (8), pp. 2898-2904, 2007.

[341] S.-J. Hwang, Y.-D. Lee, Y.-B. Park, J.-H. Lee, C.-O. Jeong and Y.-C. Joo, "In situ study of stress relaxation mechanisms of pure Al thin films during isothermal annealing," *Scr. Mater.*, **54** (11), pp. 1841-1846, 2006.

[342] K. A. Koh and S. J. Chua, "Electromigration in aluminum/silicon/copper metallization due to the presence of a thin oxide layer," *Journal of Electronic Materials*, **26** (9), pp. 1070-1075, 1997.

[343] A. Yin, R. S. Guico and J. Xu, "Fabrication of anodic aluminium oxide templates on curved surfaces," *Nanotechnology*, **18** (3), pp. 035304 (6pp), 2007.

[344] H. W. Deckman and J. H. Dunsmuir, "Natural lithography," *Appl. Phys. Lett.*, **41** (4), pp. 377-379, 1982.

[345] J. C. Hulteen and R. P. Van Duyne, "Nanosphere lithography: A materials general fabrication process for periodic particle array surfaces," *J. Vac. Sci. Technol. A*, **13** (3 pt 2), pp. 1553-1553, 1995.

[346] J. C. Hulteen, D. A. Treichel, M. T. Smith, M. L. Duval, T. R. Jensen and R. P. Van Duyne, "Nanosphere lithography: Size-tunable silver nanoparticle and surface cluster arrays," *J. Phys. Chem. B*, **103** (19), pp. 3854-3863, 1999.

[347] T. R. Jensen, M. D. Malinsky, C. L. Haynes and R. P. Van Duyne, "Nanosphere lithography: Tunable localized surface plasmon resonance spectra of silver nanoparticles," *J. Phys. Chem. B*, **104** (45), pp. 10549-10556, 2000.

[348] C. L. Haynes and R. P. Van Duyne, "Nanosphere lithography: A versatile nanofabrication tool for studies of size-dependent nanoparticle optics," *J. Phys. Chem. B*, **105** (24), pp. 5599-5611, 2001.

[349] C. L. Haynes, A. D. McFarland, M. T. Smith, J. C. Hulteen and R. P. Van Duyne, "Angle-resolved nanosphere lithography: Manipulation of nanoparticle size, shape, and interparticle spacing," *J. Phys. Chem. B*, **106** (8), pp. 1898-1902, 2002.

[350] A. D. Ormonde, E. C. M. Hicks, J. Castillo and R. P. Van Duyne, "Nanosphere lithography: Fabrication of large-area Ag nanoparticle arrays by convective self-assembly and their characterization by scanning UV - Visible extinction spectroscopy," *Langmuir*, **20** (16), pp. 6927-6931, 2004.

[351] X. Zhang, A. V. Whitney, J. Zhao, E. M. Hicks and R. P. Van Duyne, "Advances in contemporary nanosphere lithographic techniques," *J. Nanosci. Nanotechnol.*, **6** (7), pp. 1920-1934, 2006.

[352] Z. P. Huang, D. L. Carnahan, J. Rybczynski, M. Giersig, M. Sennett, D. Z. Wang, J. G. Wen, K. Kempa and Z. F. Ren, "Growth of large periodic arrays of carbon nanotubes," *Appl. Phys. Lett.*, **82** (3), pp. 460-462, 2003.

[353] A. Kosiorek, W. Kandulski, H. Glaczynska and M. Giersig, "Fabrication of nanoscale rings, dots, and rods by combining shadow nanosphere lithography and annealed polystyrene nanosphere masks," *Small*, **1** (4), pp. 439-444, 2005.

[354] Y. Li, W. Cai, B. Cao, G. Duan, C. Li, F. Sun and H. Zeng, "Morphology-controlled 2D ordered arrays by heating-induced deformation of 2D colloidal monolayer," *J. Mater. Chem.*, **16** (6), pp. 609-612, 2006.

[355] C. L. Cheung, R. J. Nikolic, C. E. Reinhardt and T. F. Wang, "Fabrication of nanopillars by nanosphere lithography," *Nanotechnology*, **17** (5), pp. 1339-1343, 2006.

[356] K. Seeger and R. E. Palmer, "Fabrication of ordered arrays of silicon nanopillars," *J. Phys. D: Appl. Phys.*, **32** (24), pp. L129-L132, 1999.

[357] A. Sinitskii, S. Neumeier, J. Nelles, M. Fischler and U. Simon, "Ordered arrays of silicon pillars with controlled height and aspect ratio," *Nanotechnology*, **18** (30), pp. 305307 (6 pp), 2007.

[358] C. Haginoya, M. Ishibashi and K. Koike, "Nanostructure array fabrication with a size-controllable natural lithography," *Appl. Phys. Lett.*, **71** (20), pp. 2934-2936, 1997.

[359] N. Nagy, A. E. Pap, E. Horváth, J. Volk, I. Bársony, A. Deák and Z. Hórvölgyi, "Large area self-assembled masking for photonic applications," *Appl. Phys. Lett.*, **89** (6), pp. 63104 (3pp), 2006.

[360] M. Manso Silván, M. Arroyo Hernández, V. Torres Costa, R. J. Martín-Palma and J. M. Martínez-Duart, "Structured porous silicon sub-micrometer wells grown by colloidal lithography," *Europhy. Lett.*, **76** (4), pp. 690-695, 2006.

[361] D. F. Liu, Y. J. Xiang, Q. Liao, J. P. Zhang, X. C. Wu, Z. X. Zhang, L. F. Liu, W. J. Ma, J. Shen, W. Y. Zhou*, et al.*, "A simple route to scalable fabrication of perfectly ordered ZnO nanorod arrays," *Nanotechnology*, **18** (40), pp. 405303 (5pp), 2007.

[362] K. Peng, M. Zhang, A. Lu, N.-B. Wong, R. Zhang and S.-T. Lee, "Ordered silicon nanowire arrays via nanosphere lithography and metal-induced etching," *Appl. Phys. Lett.*, **90** (16), pp. 163123 (3pp), 2007.

[363] K. Kempa, B. Kimball, J. Rybczynski, Z. P. Huang, P. F. Wu, D. Steeves, M. Sennett, M. Giersig, D. V. G. L. N. Rao, D. L. Carnahan*, et al.*, "Photonic crystals based on periodic arrays of aligned carbon nanotubes," *Nano Lett.*, **3** (1), pp. 13-18, 2003.

[364] N. D. Denkov, O. D. Velev, P. A. Kralchevsky, I. B. Ivanov, H. Yoshimura and K. Nagayama, "Mechanism of formation of two-dimensional crystals from latex particles on substrates," *Langmuir*, **8** (12), pp. 3183-3190, 1992.

[365] N. D. Denkov, O. D. Velev, P. A. Kralchevsky, I. B. Ivanov, H. Yoshimura, K. Nagayama, T. Enoch, A. Carr and P. Nurse, "Two-dimensional crystallization," *Nature*, **361** (6407), pp. 26, 1993.

[366] A. S. Dimitrov and K. Nagayama, "Continuous convective assembling of fine particles into two-dimensional arrays on solid surfaces," *Langmuir*, **12** (5), pp. 1303-1311, 1996.

[367] C. D. Dushkin, H. Yoshimura and K. Nagayama, "Nucleation and growth of two-dimensional colloidal crystals," *Chem. Phys. Lett.*, **204** (5-6), pp. 455-460, 1993.

[368] K. Nagayama, "Two-dimensional self-assembly of colloids in thin liquid films," *Colloids Surf. A Physicochem. Eng. Asp.*, **109**, pp. 363-374, 1996.

[369] R. Micheletto, H. Fukuda and M. Ohtsu, "A simple method for the production of a two-dimensional, ordered array of small latex particles," *Langmuir*, **11** (9), pp. 3333-3336, 1995.

[370] V. Ng, Y. V. Lee, B. T. Chen and A. O. Adeyeye, "Nanostructure array fabrication with temperature-controlled self-assembly techniques," *Nanotechnology*, **13** (5), pp. 554-558, 2002.

[371] L. M. Goldenberg, J. Wagner, J. Stumpe, B.-R. Paulke and E. Görnitz, "Ordered arrays of large latex particles organized by vertical deposition," *Langmuir*, **18** (8), pp. 3319-3323, 2002.

[372] L. K. Teh, N. K. Tan, C. C. Wong and S. Li, "Growth imperfections in three-dimensional colloidal self-assembly," *Appl. Phys. A*, **81** (7), pp. 1399-1404, 2005.

[373] Z. Zheng, X. Liu, Y. Luo, B. Cheng, D. Zhang, Q. Meng and Y. Wang, "Pressure controlled self-assembly of high quality three-dimensional colloidal photonic crystals," *Appl. Phys. Lett.*, **90** (5), pp. 051910 (3 pp), 2007.

[374] B. J. Y. Tan, C. H. Sow, K. Y. Lim, F. C. Cheong, G. L. Chong, A. T. S. Wee and C. K. Ong, "Fabrication of a two-dimensional periodic non-close-packed array of polystyrene particles," *J. Phys. Chem. B*, **108** (48), pp. 18575-18579, 2004.

[375] P. Jiang and M. J. McFarland, "Large-scale fabrication of wafer-size colloidal crystals, macroporous polymers and nanocomposites by spin-coating," *J. Am. Chem. Soc.*, **126** (42), pp. 13778-13786, 2004.

[376] R. Aveyard, J. H. Clint, D. Nees and V. N. Paunov, "Compression and structure of monolayers of charged latex particles at air/water and octane/water interfaces," *Langmuir*, **16** (4), pp. 1969-1979, 2000.

[377] J. Rybczynski, U. Ebels and M. Giersig, "Large-scale, 2D arrays of magnetic nanoparticles," *Colloids Surf. A Physicochem. Eng. Asp.*, **219** (1-3), pp. 1-6, 2003.

[378] S. M. Weekes, F. Y. Ogrin, W. A. Murray and P. S. Keatley, "Macroscopic arrays of magnetic nanostructures from self-assembled nanosphere templates," *Langmuir*, **23** (3), pp. 1057-1060, 2007.

[379] L. M. Goldenberg, J. Wagner, J. Stumpe, B.-R. Paulke and E. Görnitz, "Simple method for the preparation of colloidal particle monolayers at the water/alkane interface," *Langmuir*, **18** (14), pp. 5627-5629, 2002.

[380] M. G. Nikolaides, A. R. Bausch, M. F. Hsu, A. D. Dinsmore, M. P. Brenner, C. Gay and D. Weltz, "Electric-field-induced capillary attraction between like-charged particles at liquid interfaces," *Nature*, **420** (6913), pp. 299-301, 2002.

[381] W. Chen, S. Tan, T.-K. Ng, W. T. Ford and P. Tong, "Long-ranged attraction between charged polystyrene spheres at aqueous interfaces," *Phys. Rev. Lett.*, **95** (21), pp. 218301 (4pp), 2005.

[382] M. E. Abdelsalam, P. N. Bartlett, J. J. Baumberg and S. Coyle, "Preparation of arrays of isolated spherical cavities by self-assembly of polystyrene spheres on self-assembled pre-patterned macroporous films," *Adv. Mater.*, **16** (1), pp. 90-93, 2004.

[383] R. Legtenberg, H. V. Jansen, M. J. de Boer and M. Elwenspoek, "Anisotropic reactive ion etching of silicon using $SF_6/O_2/CHF_3$ gas mixtures," *J. Electrochem. Soc.*, **142** (6), pp. 2020-2028, 1995.

[384] B. S. Flavel, J. G. Shapter and J. S. Quinton, "Nanosphere lithography using thermal evaporation of gold," in *Proc. SPIE - Micro- and Nanotechnology: Materials, Processes, Packaging, and Systems III* Adelaide, Australia, pp. 64151J (8 pp), Dec. 2006.

[385] U. M. Mescheder and C. Koetter, "Optical monitoring and control of Si wet etching," *Sensors and Actuators A: Physical*, **76** (1-3), pp. 425-430, 1999.

[386] H. Tosaka, K. Minami and M. Esashi, "Optical *in situ* monitoring of silicon diaphragm thickness during wet etching," *Journal of Micromechanics and Microengineering*, **5** (1), pp. 41-46, 1995.

[387] M. W. Dewhirst, B. L. Viglianti, M. Lora-Michiels, M. Hanson and P. J. Hoopes, "Basic principles of thermal dosimetry and thermal thresholds for tissue damage from hyperthermia," *International Journal of Hyperthermia*, **19** (3), pp. 267 - 294, 2003.

[388] T. R. Kuphaldt, *Lessons in Electric Circuits: Volume V - Reference*, http://www.ibiblio.org/kuphaldt/electricCircuits/, last accessed in Mar. 2009

[389] E. A. Brandes and G. B. Brook (Eds.), *Smithells Metals Reference Book*, 7th ed. Oxford, UK: Butterworth-Heinemann, 1992.

[390] F. P. Incropera, D. P. DeWitt, T. L. Bergman and A. S. Lavine, *Fundamentals of Heat and Mass Transfer*, 6th ed., New York, USA: John Wiley & Sons, Inc., 2007.

[391] P. Yuan, "Numerical analysis of an equivalent heat transfer coefficient in a porous model for simulating a biological tissue in a hyperthermia therapy," *International Journal of Heat and Mass Transfer*, **52** (7-8), pp. 1734-1740, 2009.

[392] V. Lehmann, F. Hofmann, F. Möeller and U. Grüening, "Resistivity of porous silicon: A surface effect," *Thin Solid Films*, **255** (1-2), pp. 20-22, 1995.

[393] A. Wolf and R. Brendel, "Thermal conductivity of sintered porous silicon films," *Thin Solid Films*, **513** (1-2), pp. 385-390, 2006.

[394] C. Chang, Y.-F. Wang, Y. Kanamori, J.-J. Shih, Y. Kawai, C.-K. Lee, K.-C. Wu and M. Esashi, "Etching submicrometer trenches by using the Bosch process and its application to the fabrication of antireflection structures," *J. Micromech. Microeng.*, **15** (3), pp. 580-585, 2005.

[395] X. Wang, W. Zeng, G. Lu, O. L. Russo and E. Eisenbraun, "High aspect ratio Bosch etching of sub-0.25 μm trenches for hyperintegration applications," *Journal of Vacuum Science & Technology B: Microelectronics and Nanometer Structures*, **25** (4), pp. 1376-1381, 2007.

[396] Y.-F. Chang, Q.-R. Chou, J.-Y. Lin and C.-H. Lee, "Fabrication of high-aspect-ratio silicon nanopillar arrays with the conventional reactive ion etching technique," *Appl. Phys. A Mater. Sci. Processing*, **86** (2), pp. 193-196, 2007.

[397] A. Tserepi, E. Gogolides, C. Cardinaud, L. Rolland and G. Turban, "Highly anisotropic silicon and polysilicon room-temperature etching using fluorine-based high density plasmas," *Microelectron. Eng.*, **41-42**, pp. 411-414, 1998.

[398] L. Petrossian, S. J. Wilk, P. Joshi, S. Hihath, S. M. Goodnick and T. J. Thornton, "Fabrication of cylindrical nanopores and nanopore arrays in silicon-on-insulator substrates," *J. Microelectromech. Syst.*, **16** (6), pp. 1419-1428, 2007.

[399] M. J. de Boer, H. V. Jansen, E. Smulders, M.-J. Gilde, G. Roelofs, J. N. Sasserath, M. Elwenspoek and J. G. E. Gardeniers, "Guidelines for etching silicon MEMS structures using fluorine high-density plasmas at cryogenic temperatures," *J. Microelectromech. Syst.*, **11** (4), pp. 385-401, 2002.

[400] N. Maluf and K. Williams, *An Introduction to Microelectromechanical Systems Engineering*, 2nd ed., London, UK: Artech House, 2004.

[401] J. K. Bhardwaj, H. Ashraf and A. McQuarrie, "Dry etching for MEMS," in *Proc. Symposium on Microstructures and Microfabricated Systems at the Annual Meeting of the Electrochemical Society*, Montreal, Quebac, Canada, May 1997.

[402] H. V. Jansen, M. J. de Boer, S. Unnikrishnan, M. C. Louwerse and M. C. Elwenspoek, "Black silicon method X: a review on high speed and selective plasma etching of silicon with profile control: an in-depth comparison between Bosch and cryostat DRIE processes as a roadmap to next generation equipment," *J. Micromech. Microeng.*, **19** (3), pp. 033001 (41pp), 2009.

[403] M. Wasilik and A. P. Pisano, "Low-frequency process for silicon-on-insulator deep reactive ion etching," in *Proc. SPIE - Device and Process Technologies for MEMS and Microelectronics II*, Adelaide, Australia, pp. 462-472, Dec. 2001.

[404] J. Hopkins, H. Ashraf, J. K. Bhardwaj, A. M. Hynes, I. Johnston and J. N. Shepherd, "The benefits of process parameter ramping during the plasma etching of high aspect ratio silicon structures," in *Proc. Mater. Res. Soc. Fall Meeting - Symposium AA: Materials Science of Microelectromechanical Systems (MEMS) Devices*, Boston, MA, USA, pp. 63-68, Dec. 1998.

[405] M. Bahrami, *Micro-Opto-Fluidic Device for PCR Application*, Ph.D. Dissertation, University of Southampton, 2006.

[406] F. Warkusz, "The size effect and the temperature coefficient of resistance in thin films," *J. Phys. D: Appl. Phys.*, **11** (5), pp. 689-694, 1978.

[407] A. L. Doadrio, E. M. B. Sousa, J. C. Doadrio, J. Pérez Pariente, I. Izquierdo-Barba and M. Vallet-Regí, "Mesoporous SBA-15 HPLC evaluation for controlled gentamicin drug delivery," *J. Controlled Release*, **97** (1), pp. 125-132, 2004.

[408] S. W. Song, K. Hidajat and S. Kawi, "Functionalized SBA-15 materials as carriers for controlled drug delivery: Influence of surface properties on matrix-drug interactions," *Langmuir*, **21** (21), pp. 9568-9575, 2005.

[409] C. Charnay, S. Bégu, C. Tourné-Péteilh, L. Nicole, D. A. Lerner and J. M. Devoisselle, "Inclusion of ibuprofen in mesoporous templated silica: Drug loading and release property," *Eur. J. Pharm. Biopharm*, **57** (3), pp. 533-540, 2004.

[410] M. Vallet-Regí, A. Rámila, R. P. del Real and J. Pérez Pariente, "A new property of MCM-41: Drug delivery system," *Chem. Mater.*, **13** (2), pp. 308-311, 2001.

[411] L. M. Karlsson, P. Tengvall, I. Lundstrom and H. Arwin, "Penetration and loading of human serum albumin in porous silicon layers with different pore sizes and thicknesses," *J. Colloid Interface Sci.*, **266** (1), pp. 40-47, 2003.

[412] I. Batra, J. L. Coffer and L. T. Canham, "Electronically-responsive delivery from a calcified mesoporous silicon structure," *Biomed. Microdevices*, **8** (2), pp. 93-97, 2006.

[413] K. L. Holmes and L. M. Lantz, "Protein labeling with fluorescent probes," in *Methods in Cell Biology*, vol. 63: Cytometry Part 1, Z. Darzynkiewicz, H. A. Crissman and J. P. Robinson (Eds.), New York, USA: Academic Press, 2001, pp. 185-204.

[414] T. H. The and T. E. W. Feltkamp, "Conjugation of fluorescein isothiocyanate to antibodies I. Experiments on the conditions of conjugation," *Immunology*, **18** (6), pp. 865-873, 1970.

[415] R. E. J. Mitchel, I. M. Chaiken and E. L. Smith, "The complete amino acid sequence of Papain. (ADDITIONS AND CORRECTIONS)," *J. Biol. Chem.*, **245** (14), pp. 3485-3492, 1970.

[416] R. Arnon, "Papain," in *Methods in Enzymology*, vol. 19: Proteolytic Enzymes, E. P. Gertrude and L. Laszlo (Eds.), New York, USA: Academic Press, 1970, pp. 226-244.

[417] A. N. Glazer and E. L. Smith, "Phenolic hydroxyl ionization in Papain," *J. Biol. Chem.*, **236** (11), pp. 2948-2951, 1961.

[418] Sigma-Aldrich Inc., *Product Information Sheet: Papain (Product No. P 4762)*, http://www.sigmaaldrich.com/etc/medialib/docs/Sigma/datasheet5/p4762dat.pdf, last accessed in Apr. 2009.

[419] A. Kilara, K. M. Shahani and F. W. Wagner, "Preparation and properties of immobilized papain and lipase," *Biotechnol. Bioeng.*, **19** (11), pp. 1703-1714, 1977.

[420] P. R. Banks and D. M. Paquette, "Comparison of three common amine reactive fluorescent probes used for conjugation to biomolecules by capillary zone electrophoresis," *Bioconjug. Chem.*, **6** (4), pp. 447-458, 1995.

[421] Roche Applied Science, "Product Information Sheet: Fluorescein Labeling Kit (Cat. No. 11386093001)," 2005.

[422] Thermo Fischer Scientific Inc., *Product Instructions: NHS-Fluorescein (Product No. 46409 and 46410)*, http://www.piercenet.com/files/2082as4.pdf, last accessed in Apr. 2009.

[423] C. V. Sapan, R. L. Lundblad and N. C. Price, "Colorimetric protein assay techniques," *Biotechnol. Appl. Biochem.*, **29** (Part 2), pp. 99-108, 1999.

[424] C. M. Stoscheck, "Quantitation of Protein," in *Methods in Enzymology*, vol. 182: Guide to Protein Purification, M. P. Deutscher (Ed.), New York, USA: Academic Press, 1990, pp. 50-68.

[425] T. J. Mantle and D. A. Harris, "Spectrophotometric Assays," in *Spectrophotometry and Spetrofluorimetry: A Practical Approach*, M. G. Gore (Ed.), 2nd ed., Oxford, UK: Oxford University Press, 2000, pp. 183-208.

[426] G. R. Grimsley and C. N. Pace, "Spectrophotometry determination of protein concentration," in *Current Protocols in Protein Science*, J. E. Coligan, B. M. Dunn, D. W. Speicher and P. T. Wingfield (Eds.), New York, USA: John Wiley & Sons, Inc., 2003, pp. Unit 3.1 (9 pp).

[427] T. Okubo, D. Onoshima and A. Tsuchida, "Drying dissipative patterns of biological polyelectrolyte solutions," *Colloid Polymer Sci.*, **285** (9), pp. 999-1007, 2007.

[428] J. Stoer and R. Bulirsch, *Introduction to Numerical Analysis (translated from Einführung in die Numerische Mathematik)*, 2nd ed., New York, USA: Springer-Verlag, 1993.

[429] V.-P. Lehto, K. Vaha-Heikkila, J. Paski and J. Salonen, "Use of thermoanalytical methods in quantification of drug load in mesoporous silicon microparticles," *J. Therm. Anal. Calor.*, **80** (2), pp. 393-397, 2005.

[430] COMSOL AB, *AC / DC Module User's Guide*, Stockholm, Sweden, 2006.

[431] ---, *Heat Transfer Module User's Guide*, Stockholm, Sweden, 2006.